In Pursuit of New Worlds: Searches for and Studies of Transiting Exoplanets from Three Space-Based Observatories

Thesis Advisor: Professor David Charbonneau Sarah Ashley Ballard

In Pursuit of New Worlds: Searches for and Studies of Transiting Exoplanets from Three Space-Based Observatories

Abstract

This thesis presents studies of transiting exoplanets using observations gathered in large part from space, with the NASA *EPOXI* Mission, the *Spitzer* Space Telescope, and the *Kepler* Mission.

The first part of this thesis describes searches for additional transiting planets in known exoplanet systems, using time series photometry gathered as part of the NASA *EPOXI* Mission. Using the *EPOXI* light curves spanning weeks for each star, we searched six exoplanetary systems for signatures of additional transiting planets. These six systems include five hosts to hot Jupiters: HAT-P-4, TrES-3, TrES-2, WASP-3, and HAT-P-7, and one host to a hot Neptune: GJ 436. We place upper limits on the presence of additional transiting planets in the super-Earth radius range for GJ 436 in Chapter 2, and in the Neptune-to-Saturn radius range for the other five systems in Chapter 4. Chapter 3 details a search for additional transits of a hypothesized planet smaller than the Earth, whose presence was suggested by the *EPOXI* observations of GJ 436. In that study, we demonstrate the sensitivity of Warm *Spitzer* observations to transits of a sub-Earth-sized planet.

The fifth chapter details the characterization and validation of the Kepler-19 system, which hosts a transiting 2.2 $R_\oplus$ planet, Kepler-19b. We demonstrate the planetary nature of the transit signal with an analysis that combines information from high-resolution spectroscopy, the shape of the transit light curve, adaptive optics imaging, and near-infrared transits of the planet. The sinusoidal variation in the transit times of Kepler-19b indicates the presence of an additional perturbing body, and comprises the first definitive detection of a planet using the transit timing variation method. While we cannot uniquely determine the mass and orbital period of Kepler-19c, we establish that its mass must be less than 6 times the mass of Jupiter.

The sixth chapter presents evidence for the validation of a 2.0 $R_\oplus$ planet residing in the habitable zone of a low-mass star, Kepler Object of Interest 1361.01. We discuss the theoretical composition of the planet, and address issues specific to habitability of planets orbiting M dwarfs.

Contents

Acknowledgments

I thank my family for their loving support. During the best times, and during the very worst, I am profoundly grateful for their presence in my life. Thank you to my father for modeling for me what hard work and dedication can accomplish. Thank you to my mother for reminding me, again and again, to find balance. Thank you to my brother for believing that I'm "the best", and telling me so. Thank you to my sister for her insight and advice, which is somehow *always* right. Thank you also to my extended family for their love. Thank you to Melinda for being the older sister that I never had, and in my third year of graduate school, introducing me to my goddaughter, Savera.

I thank Prof. David Charbonneau for his guidance: for encouraging me to pursue the exciting field of exoplanets, for carefully guiding my scientific voice in publications and conference talks, for providing me with thoughtful career advice, and for patiently helping me to navigate the hardest parts. Thank you also to Dave for validating my interest in issues affecting women and minorities in science, and for giving me the example of a scientist who devotes his time both to science, and to the creation of a better scientific community.

I thank Dr. Jennifer Strong for helping me create a scientific identity that is still "Sarah" at heart. I could not have navigated this path without her.

I thank the other scientists I've worked closely with at the Center for Astrophysics, including team members Jessie Christiansen, David Weldrake, Jean-Michel Désert, and Francois Fressin. Guillermo Torres and Jonathan Irwin

have provided invaluable insight and advice, often when I came by their offices to pester them unannounced. Prof. Matthew Holman and Prof. Drake Deming have also provided me with advice and support as advisors and colleagues.

Thank you to Prof. Andrew West for lunches at Boston University, and for helping me navigate the trickier parts with his wisdom and humor.

Thank you to Dr. David Schlegel and Dr. Lori Allen for advising me as an undergraduate, and encouraging me to continue in astronomy.

I thank Jean Collins, Peg Herlihy, and Donna Adams for keeping the department running so smoothly. Thanks especially to Jean for her quiet insight into officemate selection. I don't know what I would have done without Laura Blecha to turn to, first in A-112 and then in P-301. Thanks to Laura especially for helping me through the hardest moments of the past five years.

Thanks to the other graduate students who have shared this adventure with me. Thank you to Robert Harris, Sarah Rugheimer, Elizabeth Newton, Gurtina Besla, Zach Berta, Wen-Fai Fong, Diego Muñoz, Eliza Kempton, and Bekki Dawson for making the Center for Astrophysics a wonderful place to work. Underneath the jokes and the companionable walks to Hi-Rise, we know we are there for one another, which makes all the difference.

For my family

Chapter 1

Introduction

The landscape of exoplanet science has changed profoundly over the past five years. While these changes have included novel means of exoplanet detection, detailed characterization of exoplanetary properties and atmospheres, and new means of validating the planetary nature of exoplanet candidates, the shifting landscape can largely be summarized by a single idea. We began 2007 in the era of hot Jupiters, two dozen of which transited their host stars, while we began 2012 in the era of habitable-zone super Earths, with hundreds of transiting exoplanets and thousands more candidates. There is every reason to believe that habitable Earth-sized planets will follow, a crucial benchmark on the road to discovering other habitable (and eventually, *in*habited) worlds.

This thesis is reflective of the shifting nature of exoplanetary science. It comprises analyses that address the single, "lonely" nature of hot Jupiter systems (which we now know are overwhelmingly likely to lack other coplanar planets).

One of these analyses, given in Chapter 2, was the first work to demonstrate the detectability of transits of planets as small as 1.5 $R_\oplus$ in mean-motion resonances with gas giant planets. Chapter 4 details another search for transiting companions around five additional known exoplanet host stars. I contextualize these results in §1.1. It includes a demonstration of the detectability of sub-Earth-sized transiting exoplanets, which predated by a year the deluge of planetary candidates in the range < 1.25 $R_\oplus$ identified after the 2009 launch of the *Kepler* Mission, given in Chaper 3. I discuss the overwhelming shift toward smaller exoplanet detections, coupled with the relationship between planet and host star size, in §1.2 of this introduction. Chapter 5 includes the first robust detection of an exoplanet using the "transit timing variation" (TTV) method, bearing out a 2005 theoretical prediction for the existence of such signals. This system also comprised one of the first exoplanetary "validations", a novel statistical means of authenticating a planetary signal without a mass measurement. The discovery of new planets, whose nature is determined by photo-dynamics or a statistical argument, is itself a novel idea from the last five years that I address in §1.3. Finally, Chapter 6 presents evidence for a planet whose characteristics are representative on four frontiers of the recent changes in exoplanetary science. First, it resides in the habitable zone of its host star. Second, it is small enough that a rocky composition is plausible. Third, it orbits a low-mass star. And fourth, its nature will be validated statistically, without measurement of the planetary mass. I comment on future prospects in the field of transiting exoplanets in §1.4, including the challenges presented by low-mass stellar characterization.

1.1 The Solitary Nature of Hot Jupiters

1.1.1 The Single Transiting Hot Neptune

The profound transition in exoplanet science over the past five years is well exemplified by the story of a single exoplanet: GJ 436. This hot Neptune was first discovered via radial velocity measurements by Butler et al. (2004), but was discovered to transit its host star, an M dwarf, in 2007 (Gillon et al. 2007b). At the time of its discovery, it was the smallest known transiting exoplanet, a fact which is remarkable to consider in light of the fact that the most recent *Kepler* data release (Batalha et al. 2012, including all candidates found within the first 16 months of observations) reported 421 such objects, in addition to the 662 that had already been identified in the first four months of *Kepler* observations (Borucki et al. 2011). However, in 2007, GJ 436 was singularly fascinating, not least because Deming et al. (2007) observed, via the second eclipse of the planet, that its orbit was significantly eccentric at $e = 0.15$. Given tidal circulatization properties similar to Neptune in our own solar system, the circularization timescale should already have elapsed, given the age of the system of 6 Gyr (Torres et al. 2008). The literature on GJ 436b reflects the intense interest in the planet's nature. Its transit times were gathered over a series of 4 years with the *Spitzer* and *Hubble* Space Telescopes, as well as from the ground, with at least one (later-retracted) claim of a detection of a GJ 436c (Ribas et al. 2008). Chapter 1 and 2 of the enclosed thesis reflects the avid interest in GJ 436, and describe a general search for additional transiting planets in the NASA $EPOXI$

observations of the system, as well as a pointed search for a sub-Earth-sized planet whose presence was suggested by *EPOXI* and cryogenic *Spitzer* observations. It is worth nothing that such a planet is, today, literally only one in a thousand Neptune-sized worlds which are now known to transit.

1.1.2 Dark and Puzzling Worlds

The properties of Hot Jupiters have also proven to be varied and unpredictable. First, with the exception of Kepler-7, with a geometric albedo of 0.38 ± 0.12 (Kipping & Bakos 2011a), hot Jupiters are remarkably dark. Snellen et al. (2009); Alonso et al. (2009b) found that CoRoT-1 has an albedo <0.2, which is a similar upper limit to that provided by the Microvariability and Oscillations of STars (MOST) telescope for HD 209458 of $A_g < 0.17$ (Rowe et al. 2008). CoRoT-2b, with albedo of 0.06 ± 0.06 (Alonso et al. 2009a) and TrES-2b, with albedo of 0.0253±0.0072 (Kipping & Spiegel 2011), are so dark as to be almost black. Such low albedos were predicted for highly irradiated gas giant planets by Sudarsky et al. (2000), and are attributable to the high equilibrium abundances of alkali metals high in the atmosphere. The broad absorption features of sodium and potassium dominate their visible spectra, preventing photons from reaching the more reflective silicon clouds that exist at lower altitudes (Sudarsky et al. 2000). Other searches for the secondary eclipses of hot Jupiters turned up upper limits, which is consistent with the generally very low albedos of this class of planets. An investigation by the *EPOXI* Mission, detailed by Christiansen et al. (2011), was the search for reflected light from six gas giant exoplanets (HAT-P-4, TrES-3,

GJ 436, TrES-2, WASP-3, and HAT-P-7), though only for two of these targets (TrES-3 and HAT-P-7) was the photometric precision high enough to rule out a plausible albedo (i.e., <1).

Additionally, the diversity of hot Jupiter atmospheres has continued to be a source of surprise and active debate. The appearance of temperature inversions in the atmospheres of the hot Jupiters (e.g. HD 209458, Knutson et al. 2008) have manifested as atmospheric features appearing in emission, rather than absorption. While stellar isolation was posited as a possible indicator of inversion (linked to the presence of the gas-phase of an absorber such as titanium oxide, creating the inversion), in actuality the division between hot Jupiters with inversions and without must be more subtle. XO-1, for example, possesses a temperature inversion but is cooler than the majority of planets without one (Machalek et al. 2008), while TrES-3 is hot enough that TiO in the atmosphere would be gaseous, but shows no inversion (Fressin et al. 2010). Rather, Knutson et al. (2010) found that chromospheric activity is a more accurate indicator of the presence of inversion. Madhusudhan et al. (2011a) has suggested that carbon-rich giant (CRG) planets, defined as planets with C/O≥1, will not host temperature inversions even in the most highly irradiated cases. This class of carbon-rich giant planets, exemplified by WASP-12 (Madhusudhan et al. 2011b), is itself fascinating.

However, though the study of hot Jupiters is a rich and rewarding field, attention has shifted in large part to searches for smaller, potentially rocky planets. Many of these searches took place first in systems with a known hot

Jupiter.

1.1.3 Searches for Companions to Hot Jupiters

The characterization of hot Jupiters extended to searches for companions, which employed radial velocity measurements, and in known transiting systems, searches for the transits of additional planets and for variations in the times of the transits of the hot Jupiters themselves. The window function of ground-based surveys, which precludes their completeness to periods longer than several days, is such that detecting exterior companions to hot Jupiters is already challenging. Many of the first searches for longer period transiting planets in known transiting systems were conducted from space. The MOST spacecraft was among the first to obtain the high-duty-cycle photometry over long durations that were amenable to detections of longer-period planets. These analyses were often coupled with searches for transit timing variations. A representative example of these analyses employed the 2004 and 2005 MOST data sets of HD 209458 (host to a hot Jupiter in a 3.5-day orbit). These data represented unprecedented time coverage at that point, with continuous observations spanning 14 and 43 days (Croll et al. 2007a). The precision of the MOST photometry of HD 209458 (3.5 mmag over 10 s exposures), allowed the authors to rule out additional transiting planets larger than 2.2 $R_\oplus$ in 0.5-day orbits, and 3 $R_\oplus$ at the exterior 2:1 mean motion resonance with the hot Jupiter. The string of consecutive transits of the hot Jupiter also allowed for constraints on non-transiting planets from the lack of transit timing variations (Miller-Ricci et al. 2008b). The MOST and HST (Agol

& Steffen 2007) transit data exclude sub-Earth mass planets (>0.3 $M_{\oplus}$) in the exterior 3:2 and 2 :1 mean-motion resonances. Until the launch of the *Kepler* Mission, every search of this nature to identify additional planets in hot Jupiter systems resulted in upper limits. As I discuss in additional detail in the following section, the assumption of systems of multiple planets residing in coplanar mean motion resonance orbits with hot Jupiters has proven broadly incorrect.

However, before *Kepler* addressed the question of transiting exoplanet multiplicity, exoplanetary astronomers conducted dozens of searches of known transiting exoplanet systems for additional transits or TTVs indicating other planets in mean-motion resonances. The *EPOXI* observations, described in Chapters 1 and 2, similarly resulted in more and more refined upper limits to the presence of additional planets in such systems. Ultimately, the exquisite phase coverage and precision of *Kepler* showed that hot Jupiters are indeed, overwhelmingly alone. The reason so many searches of hot Jupiters for additional planets resulted in upper limits is because few such coplanar planets exist to be found. Contemporaneous with searches for companions to hot Jupiters were many obliquity measurements of their orbits via the Rossiter-McLaughlin effect. Hot Jupiters have a high likelihood of being misaligned (with a projected spin-orbit angle, λ, more than 10° removed from the stellar rotation axis with 3σ confidence): 18% of planets around cooler stars are significantly misaligned, compared with 75% around hotter stars ($T_{\rm eff} > 6250$ K) (Winn et al. 2008). Planet-planet scattering during the formation history of these systems (one possible mechanism of spin-orbit misalignment explored by Chatterjee et al. 2008)

is consistent with the lack of additional coplanar planets. Yet, at the time of the *EPOXI* observations, the multiplicity of planets in hot Jupiter systems was as-yet unanswered.

1.2 The Shift Toward Super Earths

As late as 2009, the list of transiting super-Earths (exoplanets intermediate in size between Earth and Neptune) comprised two planets: CoRoT-7b (Léger et al. 2009; Queloz et al. 2009), and GJ 1214b (Charbonneau et al. 2009). The tendency of the ground-based surveys that preceded *Kepler* was to larger planets at shorter orbital periods (which we know now to be remarkably alone). Therefore, it is unsurprising that the the sheer number of multiply-transiting systems, comprising super-Earths, awaiting a detector with a duty cycle sensitive to longer periods, and a photometric sensitivity to smaller planets. However, Chapter 3 details a demonstration of the sensitivity of the *Spitzer* Space Telescope to transits of a hypothetical 0.75 $R_\oplus$ planet, with observations gathered more than three years before the definitive discovery of the first sub-Earth-sized planets orbiting KOI 961 (Muirhead et al. 2012).

With the additions of Kepler-9d (Torres et al. 2011), Kepler-10bc (Batalha et al. 2011; Fressin et al. 2011), Kepler-11bcdf (Lissauer et al. 2011), 55 Cancri b (Winn et al. 2011), and Kepler-19b (Ballard et al. 2011), by late 2011 astronomers had begun in earnest to probe this radius regime of exoplanets, for which no Solar System analog exists. Batalha et al. (2012) presents a catalog of 1235 transiting

planetary candidates, of which nearly 300 have a radius estimate in the range $1.25 < R_p < 2.0\ R_\oplus$. While most of these candidates have not yet been confirmed as authentic planets, Morton & Johnson (2011) have shown that the rate of false positives is expected to be low for the *Kepler*-identified sample. Howard et al. (2010) note that the regime of planets between 5 and 30 $M_\oplus$ in periods less than 30 days was recently anticipated (from planet formation synthesis models, such as Ida & Lin 2004) to be largely empty. As with many expectations about the nature of exoplanets, this hypothesis was disproven, in this case by the deluge of planets in this mass and period range discovered by both the radial velocity and transit methods.

1.2.1 Multiplicity and Architecture of Multiple Systems

A complete discussion of super Earths merits a discussion of their remarkable multiplicity. A commonly cited prediction, at the time that many astronomers were searching for additional transiting planets in known hot Jupiter systems, is that they would have companions captured in mean motion resonances. Such planets, posited to be Earth- or super-Earth-sized, were predicted to have entered these resonances during the migrations of the current hot Jupiters to their present locations (Raymond et al. 2006; Mandell et al. 2007) . We now know, rather, that planet pairs are rarely in resonance (Fabrycky et al. 2012a), so that planets near MMR are the exception to the rule. Even those isolated systems lying close to mean-motion resonances were not necessarily sheparded there by migration mechanisms. Rather, with non-trivial probability, as in the

illustrative case of KOI 2086 (with two planets near the 5:4 and 4:3 MMR), its planetary distribution lies sufficiently far from exact resonance to simple be reflective of a random distribution of periods, with a 25% probability. There does exist a statisically significant preponderance of resonances just outside of 2:1 and (to a greater extent) 3:2 mean motion resonances, which is accompanied by a dearth of planets exactly in resonance as well as just below the resonance (e.g., a period ratio of 1.95). Fabrycky et al. (2012a) suggest that these observed characteristics of the ensemble of multiples, namely, the lack of planets very close to the resonances, might have explained by the same mechanism as explains the "Kirkwood Gaps" in the asteroid belt. Bodies very near resonances are likely to have their eccentricities excited, and are then subsequently scattered by other planetestimals. It's also a possibility that the tidal interactions between these planets and their stars result in the planets' shifting toward the stars and slightly out of the mean motion resonances (Fabrycky et al. 2012a).

Another remarkable fact of transiting multiple systems is their coplanarity. An analysis by Fabrycky et al. (2012a) employs transit durations as a probe of mutual inclination. They compare the expected transit durations, assuming circular orbits and perfect coplanarity, with the measured transit durations. Variations in eccentricity and inclination will produce a marked departure from the expected duration ratios between outer and inner planets. They manufacture populations of multiple planet systems, drawing e and i from Rayleigh distributions widths, and compare the ratios of inferred transit durations to what is observed in the *Kepler* sample. They find that the best-fit to the

observations is derived using mutual inclinations of 1–2.3°, though eccentricity is not well constrained by this exercise. Transit durations change by order unity for inclination changes of 1%, while a change in eccentricity of 1% will produce a corresponding duration change of 1% (Fabrycky et al. 2012a). *Kepler*'s multiple planet systems are therefore remarkably coplanar, in which way *Kepler* multiple stellar systems are similar to our Solar System.

1.2.2 Host Star Dependence

Two and a half years post-launch, the *Kepler* mission has revolutionized our understanding of the frequency of extrasolar planets as a function of spectral type. As the baseline of observations has increased, the sample of *Kepler* planet candidates has grown to include smaller planet candidates at larger orbital periods, such that we are able to make statements about the frequency of planets larger than 2 $R_\oplus$ in periods less than 50 days. The results from Howard et al. (2011a) about the occurrence rates of planets as a function of planetary radius and of host star temperature indicate: (1) that the number of planets per star is an order of magnitude larger for 2 $R_\oplus$ planets than it is for 4 $R_\oplus$ Neptune analogs, with larger planets increasingly less abundant. Although the sample of *Kepler* candidates is incomplete in the radius regime below 2 $R_\oplus$, it's plausible that Earth-size planets will follow the same trend of increasing in frequency with decreasing size. And (2), stellar type is correlated with the number of planets per star, such that M0 stars (among the smallest in the *Kepler* sample) host twice the number of planets per star (in the 2-4 $R_\oplus$ radius range) when compared to

solar-type stars (Howard et al. 2011a). I remark in more detail on the challenge and promise of this result, namely, that M dwarfs are more commonly hosts to small planets, in §1.4.2.

1.2.3 Atmospheric Contraints

The composition of such super-Earth planets may be widely variable, as exemplified by the single case of GJ 1214b (Charbonneau et al. 2009), for which the measured radius and mass were consistent with both a hydrogen envelope or a pure CO_2 or H_2O atmosphere (Miller-Ricci & Fortney 2010). At the time of its discovery in 2009, it was the second-smallest known exoplanet, with a radius of 2.7 $R_\oplus$. While CoRoT-7b, with a radius of 1.7 $R_\oplus$ was smaller, the proximity of GJ 1214 (only 13 pc away), coupled with the small size of the star, enabled unprecedented atmospheric characterization of a super-Earth (the mass measurement of GJ 1214 is also much more certain than that of CoRoT-7b, which was detected at only 1.2σ confidence in one analysis by Pont et al. 2011). In the post-*Kepler* era, GJ 1214 is still singular for the same reasons. While *Kepler* may find hundreds of planets near the radius of GJ 1214, none of their host stars are bright enough, nor the stars small enough, to allow for similar constraints on atmospheric composition. The observational resources lavished on GJ 1214 have included ground-based data from the VLT (Bean et al. 2010, Bean et al. 2011, from 0.6-1 μm), Magellan (Bean et al. 2011, 2.0-2.3 μm), Keck (Crossfield et al. 2011, from 2.1-2.4 μm) and the Canada France Hawaii Telescope (Croll et al. 2011, at J and K bands), as well as space-based data from the Hubble

Space Telescope (Berta et al. 2012, from 1.1 to 1.7 μm) and Warm *Spitzer*(Désert et al. 2011, at 3.6 and 4.5 μm). The flatness of the transit depth as a function of wavelength strongly disfavors a hydrogen-rich atmosphere in favor of a steam atmosphere, both of which were plausible options at the time of discovery of GJ 1214b (Miller-Ricci & Fortney 2010).

With GJ 1214 is currently the only data point, theoretical predictions for their atmospheres await discovery of additional nearby planets within the super-Earth radius range. I comment on future prospects of the detection of such planets in Section §1.4.1. Some analyses, such as Miller-Ricci et al. (2009), allow for a variety of atmospheric compositions and provide observational tools that might be applied to directly constrain quantities such as the mean molecular weight of the atmosphere. Others, such as Rogers et al. (2011), posit that only a subset atmospheric compositions are physically plausible, given the planetary radius and equilibrium temperature. Still others, such as Heng & Kopparla (2012), comment on atmospheric stability of super-Earths as a function of stellar type.

1.3 Photodynamical and Statistical Validation of Exoplanets

Confirming many of the smallest, possibly terrestrial individual *Kepler* candidates as authentic planets has proved challenging with traditional techniques. The

limiting precision of the current state-of-the-art radial velocity observations (meters per second) precludes the dynamical confirmation of these small planets, except in exceptional cases where the planet lies extremely close to the star (Queloz et al. 2009; Batalha et al. 2011). In all but the most favorable circumstances (e.g. Kepler-10b, with a period <1 day, Batalha et al. 2011), radial velocity confirmation and thus mass measurements of super Earth candidates is untenable with the current precision of meters per second. For comparison, the radial velocity signal induced on the Sun by the Earth is an order of magnitude smaller at 9 cm s^{-1}. There exist two alternative options for the individual validation of candidates as authentic planets without radial velocity confirmation.

1.3.1 Photodynamics of Exoplanets

The first is available only for multiply transiting systems, where we are able to observe the mutual gravitational interaction of planets through the methods of transit timing and transit duration variation. Such measurements allow for independent mass constraints on the candidate planets in question, which confirms their planethood if the masses lie within the planetary regime (Ragozzine & Holman 2010). The first planetary system discovered to host two transiting planets, Kepler-9 (Holman et al. 2010), was also the first to definitively display transit timing variations. The mutual gravitational forces exerted by the two Saturn-sized planets on one another cause them to alternately speed up and slow down in their orbits, with the result that the times of transit of the planets vary by up to 39 minutes and 4 minutes for the inner and outer planets, respectively.

This effect in multiply-transiting systems was posited in papers by both Agol et al. (2005) and Holman & Murray (2005), and was finally borne out with the detection in the Kepler-9 system. This transiting timing variation (TTV) signature both confirmed the planetary nature of the transiting planet candidates (since their transit times varied in an anti-correlated fashion, it was clear that the planets were exchanging angular momentum and therefore orbiting the same star) and allowed for a mass measurement of the planets independent of radial velocity measurements of the host star. It has also been applied to infer the presence of additional non-transiting planets, as was first demonstrated for Kepler-19c and discussed in Chapter 4.

Transit timing variation analyses have also been applied to validate planets in systems for which no radial velocity confirmation is possible (unlike for the Kepler-9 case, where the planetary nature of 9b and c was independently proven with radial velocity measurements). The promise of this methodology is three fold. First, it enables the validation of planetary systems around much dimmer than have been previously been examined. Fabrycky et al. (2012b), in one of a set of three papers devoted to the use of TTVs to validation *Kepler* candidates, showed that that average magnitude of the *Kepler* target stars within this TTV-validated sample was 16. This is two magnitudes dimmer than the mean of the previous sample, and much more reflective of the underlying distribution of *Kepler* target stars. Secondly, it allows for the validation of planets for which radial velocity mass confirmation is not possible. Thirdly, it can provide mass measurements of planets from photodynamics alone. However, a mass measurement isn't

strictly required to validate transiting planets showing TTVs. Rather, dynamical stability arguments alone, coupled with the measured radius of the planet, can be combined to place upper limits on the planetary masses, as was done in Fabrycky et al. (2012b), Ford et al. (2012), and Steffen et al. (2012).

One of the most promising prospects of the *Kepler* multiply transiting systems generally is their fidelty, even with the lack of transit timing variations. While a background eclipsing binary can mimic a single transiting planet candidate, as I discuss in greater detail in the following section, it is much more difficult to create a scenario in which two or more transit signals are not attributable to authentic planets. Lissauer et al. (2011), analyzing *Kepler* multiples from the first four months of observations, found a false positive rate of 2%. This false positive probability (FPP) may be compared with the FPP for single planet transits, which Morton & Johnson (2011) found to already be <10% for the majority of *Kepler* planet candidates. Fabrycky et al. (2012a) recently revisited the statistics of *Kepler*'s multiply transiting systems. He analyzed Kepler's 885 multiple transiting exoplanet candidate systems, making use of the most recently updated list of planets from Batalha et al. (2012). In light of predictions about multiple planet systems from theory and from radial velocity, it's interesting to consider the plethora of transiting multiple systems. Of the 885 systems, only two (with period ratios very near to 1) are nominally dynamically unstable. This fact indicates the likelihood of the vast majority of these systems being comprised of real planets. In contrast, if systems were randomly populated with planets with the periods and masses (assuming a simple mass scaling law for mapping radii to

masses) of the multiple systems, fully 6.4% (57 of the 885 systems) would appear dynamically unstable. The fact that only 2, in fact, are unstable (which may be attributable to their being false positives), indicates that the FPP for multiply transiting systems lies somewhere between 1.1 and 13%, with 95% probability. This analysis finds an FPP for multiples which is slightly higher than the 2% found by Lissauer et al. (2011), but the estimate of dynamical stability is subject to the exact mass-radius relationship assumed to conduct the analysis.

Speaking to Stellar Characterization with Photodynamics

It is also worth nothing that one of the single outstanding problems toward characterizing many of the most exciting exoplanets, namely, accurately deriving the properties of M dwarf stars, has also benefitted from photodynamics. There are two key examples here, the first of which is a multiply-transiting hierarchical systems of stars (Carter et al. 2011), and the second of which is a circumbinary planet that transits both of its host stars (Doyle et al. 2011). The leverage from these systems in that they comprises at least one very low-mass star and another, coeval companion at a large mass ratio. As discussed in more detail in §1.4.2, stellar models at the low-mass end of the main sequence are largely uncalibrated, and they systems offer the ability to measure the stellar masses and radii by their transit timing and their transit depths, respectively.

1.3.2 Statistical Validation

In the absence of such dynamical validation (which applies only in multiply transiting systems), it is still possible to make a statistical argument for the planetary nature of the candidate, if the combined likelihood of all false positive scenarios (namely, blends of stars containing an eclipsing member) is sufficiently smaller than the planet scenario. The large majority of false positives are caused by blends of with eclipsing binaries, or by gazing binaries (Brown 2003). In the former scenario, which is much more likely, the presence of the bright foreground star dilutes the transit of the background eclipsing binary (BGEB), so that the transit depth appears consistent with a planet-like, as opposed to a star-like, object. For super Earths, the background eclipsing system may comprise a star and a Jupiter-like planet, with the signal diluted to look consistent with the transit of a small, rocky planet. The *Kepler* team has described the methods they employ to vet candidates even before the spectroscopic stage in Batalha et al. (2010). The *Kepler* astrometry alone can be effective at identifying BGEBs from the photocentroid shift that occurs during transit. For example, the BGEB nature of *Kepler* Object of Interest 140 (KOI-140) was determined from this photocentroid shift. The long cadence (30 minute) observations have an astrometric precision of 0.3 millipixels, and 83 μpixels over 6.5 hours, and so the 3 millipixel astrometric shift of KOI-140 during transit was readily identifiable (Batalha et al. 2010). However, this method relies on the background eclipsing system being sufficiently removed in angle from the host star in order for the photocentroid shift to be detectable: this criterion is more likely to be met when

the background system is not physically associated with the target star. In addition to the photocentroid shift, the *Kepler* team compares the depths of even and odd transit events. If the depths of every other transit are inconsistent, then the occultations are due instead to a BGEB with half the period of the putative planet (with a "transit" occurring at both transit and secondary eclipse of each star). *Kepler* also checks for a decrement in the light curve at a phase of 0.5. Some secondary eclipses of authentic planets are indeed detectable by *Kepler*, such as that of HAT-P-7b (Borucki et al. 2010). However, the detection of a secondary eclipse for a cooler planetary candidate whose orbit is too far removed from the host star to account for the decrement either (1) in reflected light from the host star or (2) the short-wavelength end of the blackbody luminosity of the planet itself, must be due to the secondary eclipse of a self-luminous body rather than a planet (Batalha et al. 2010). Candidates with no photocentroid shift during transit and no secondary eclipse are then vetted by other ground-based and space-based instruments.

These procedures (as described in Borucki et al. 2010) are (1) high-resolution imaging of the host star, to identify background stars too close to be identified by photocentroid shift, (2) medium-precision radial velocity measurements to rule out high mass companions such as brown dwarfs, (3) comparison of the *Kepler* photometry to stellar blend models, to identify whether the shape and duration of transit are consistent with a blend of the host star and a BGEB, and (4) high-precision radial velocity measurements, to verify the phase and period of the candidate (and ultimately the mass and eccentricity). Authentic

transit signals should also be achromatic to first order, because the depth is determined geometrically from the area of the stellar disk blocked by the planet during transit. The presence of absorbers in the atmosphere of the planet can change the optical depth of the atmosphere, producing an effectively differently sized planet at different wavelengths, but this effect is tiny even for hot Jupiters (for example, Swain et al. 2008 claimed the detection of methane features in the atmosphere of HD189733 at the level of only 200 ppm as compared to a transit depth of 2.4%). A stellar blend would need to be comprised of nearly identical stars, a quantifiably unlikely scenario, to produce no wavelength dependence of the transit depth. For this reason, a comparison of the transit depth at near-infrared wavelengths as measured by Warm *Spitzer* (the only near-infrared facility with the photometric precision necessary to measure the transits of most super-Earth-sized *Kepler* candidates) may help to identify false positives when compared with the transit depth at optical wavelengths derived from *Kepler*. Chapter 4 presents the validation of Kepler-19b, for which we applied both the `BLENDER` and *Spitzer* results to determine that the planet scenario was 7000 times more likely than a blend. Additionally, `BLENDER` was applied to validate Kepler-9d (Torres et al. 2011), Kepler-11f (Lissauer et al. 2011), Kepler-10c (Fressin et al. 2011), Kepler-22b (Borucki et al. 2012), and Kepler-20 e & f (Fressin et al. 2012).

1.4 Looking Ahead

1.4.1 Detection of Nearby Rocky Planets in their Habitable Zones

The most recent six months in exoplanets have marked an acceleration toward the goal of identifying a transiting terrestrial planet in the habitable zone of its host star. Kepler 22b is the first super Earth with a measured radius to reside in the habitable zone of a sun-like star outside of the Solar System, though it is likely too large, at 2.4 $R_{\oplus}$, to have a rocky composition (Borucki et al. 2011) The Kepler-20 (Fressin et al. 2012) and KOI 961 (Muirhead et al. 2012) exoplanetary systems each comprise multiple planets that are Earth-sized or smaller, with KOI 961.03 as small as Mars. However, though these planets are likely more terrestrial in composition than Kepler-22b, they orbit too close to their host stars to be habitable. The most recent release of *Kepler* exoplanetary candidates (Batalha et al. 2012) contains 10 members, though as-yet unvalidated as authentic planets, which are have planetary radii <2 $R_{\oplus}$ and with equilibrium temperatures between 185 and 303 K, which range is a generous definition of the habitable zone proposed by Kasting (2012). Our characterization and forthcoming validation of of KOI 1361.01, a 2 $R_{\oplus}$-sized planet candidate in the habitable zone of its M star and described in Chapter 5, will be another member of this group of planets that edge closer to the "habitable and terrestrial" marker.

However, the atmospheric characterization of KOI 1361.01 through

transmission spectroscopy, though favored by the small size of the host star, will be untenable even for JWST– the types of atmospheric studies lavished on GJ 1214 are enabled by its lying so close to the sun. At 30 pc, it is an order of magnitude closer than KOI 1361.01. This comparison speaks to the necessity of identifying *nearby* and *small* stellar hosts to terrestrial planets, for the purpose of addressing questions of habitability with atmospheric characterization. While *Kepler* will identify perhaps hundreds of super-Earth candidates in the habitable zones of their host stars, the mission is statistical in nature– these candidates' host stars will not be bright enough for the follow-up required to search for biomarkers (the chemical signatures of life, at least as we understand it on Earth) in the planetary atmospheres. For this reason, we must turn to dedicated searches of nearby stars for the possibility of detecting a rocky world in the habitable zone of its star, which also lies within our solar neighborhood and is therefore more amenable to atmospheric follow-up. There are four such efforts underway at present: the MEarth Observatory (Irwin et al. 2009), the Transiting Exoplanet Survey Satellite (TESS), Project MINERVA, and ExoplanetSAT (Smith et al. 2010), only one of which (MEarth) is currently operational. The project designs are varied: MEarth is a ground-based network of small telescopes gathering photometry of nearby, high-proper motion M dwarfs, TESS is a proposed NASA Small Explorer spacecraft that will monitor very nearby and bright G and K-type stars, as well as the M dwarfs within 30 pc, Project MINERVA will be a ground-based combined radial-velocity and photometric effort that will monitor the quietest and brightest FGK stars already identified as such by the

California Planet Survey, and the ExoplanetSAT design envisions a flotilla of small photometers, each less than 10 kg, which will fly in a low-Earth orbit and also monitor the nearest and brightest stars for transits.

1.4.2 The Challenges of Low-Mass Stellar Characterization

As mentioned above in §1.2.2, the results to date from the *Kepler* Mission point to the increased frequency of small (2–4 $R_\oplus$) planets around smaller stars. Though *Kepler* is not yet complete for "Earth-sized" transit candidates < 1.25 $R_\oplus$, if this relationship holds for smaller planets, then the nearest terrestrial and potentially habitable planet to the Solar System likely orbits an M star. However, the traditional procedures for deriving the physical parameters of exoplanet host stars, such as mass and radius (and by extension, the physical parameters of the planets themselves) are robust only where stellar evolution models are trustworthy: namely, outside of the M dwarf regime ($T_{\rm eff}$ >4000 K, $M_\star$ >0.5 $M_\odot$). Models for the atmospheres of low-mass stars differ substantially, and constraints on the radii of M dwarfs from eclipsing binaries are inconsistent with modeled radii (Ribas 2006; Torres 2011). While a subset of the nearest M dwarfs will be close enough for direct interferometric measurement of the radius (Berger et al. 2006) or for parallax measurements, which directly constrain the luminosity of the star (Ségransan et al. 2003), our characterization of many other M dwarfs is reliant on (as yet uncertain) stellar models. Herein lies a tremendous challenge, since the ability to characterize the radius of the host star is the limiting factor toward measuring the planetary radius. For example, an error bar of 0.5 $R_\oplus$ for

a 1.5 $R_\oplus$ planet at 500 K encloses both the possibility of a substantial hydrogen and helium envelope (comprising 0.1% the mass of the planet) and a composition of ice and heavy elements with no substantial hydrogen/helium envelope (Rogers et al. 2011), with the latter considered more favorable for habitability. Measuring the equilibrium temperature of a planet to deduce whether its surface could support the existence of liquid water also depends critically on knowledge of the stellar temperature.

However, there exist promising inroads in the spectral constraints on M dwarfs from near-infrared spectral features and colors. In K-band wavelengths, Covey et al. (2010) demonstrated the ability to derive effective temperature from some continuum regions of the spectra, while Rojas-Ayala et al. (2010) identified absorption features in sodium and calcium that enable constraints on the stellar metallicity. Muirhead et al. (2012) combined these techniques to measure the effective temperatures and metallicities of 84 Kepler Objects of Interest orbiting low-mass stars, and concluded that the stellar temperatures were in most cases several hundred Kelvin cooler than what had been inferred from the *Kepler* Input Catalog. However, a physical interpretation of these revised temperatures and metallicities relies upon trustworthy stellar evolutionary models. Cooler stars translate in a general sense to smaller radii, which is especially compelling in the case of the Kepler candidates, since a smaller stellar radius translates to a smaller planetary radius. In Chapter 6, I compare the known exoplanets with $R_p < 3R_\oplus$ and dynamically measured masses (9 such planets are currently compiled in the literature). Though this relationship is undersampled, smaller

planets in this radius range have higher densities, and so a smaller planetary radii may also imply a more terrestrial composition. For this reason, careful treatment of stellar characterization of the cool KOIs is imperative. I plan to undertake such a study as a postdoctoral fellow at the University of Washington, combining infrared spectroscopy (for measurements of stellar temperature and metallicity as described above) and optical spectroscopy (for corroboration of stellar type, in addition to probing stellar activity via the presence of $H\alpha$ in emission or absorption), enabled by instruments at the Apache Point Observatory. I am hopeful that an increased expertise in M dwarfs will be a highly valued trait in an exoplanetary scientist in the next 5 years, since our nearest neighboring habitable exoplanet likely orbits such a star.

Chapter 2

A Search for Additional Planets in the NASA *EPOXI* Observations of the Exoplanet System GJ 436

S. Ballard, J. L. Christiansen, D. Charbonneau, D. Deming, M. J. Holman, D. Fabrycky, M. F. A'Hearn, D. D. Wellnitz, R. K. Barry, M. J. Kuchner, T. A. Livengood, T. Hewagama, J. M. Sunshine, D. L. Hampton, C. M. Lisse, S. Seager, J. F. Veverka *The Astrophysical Journal*, Vol. 716, pp. 1047-1059, 2010

Abstract

We present time series photometry of the M dwarf transiting exoplanet system GJ 436 obtained with the EPOCh (Extrasolar Planet Observation and

Characterization) component of the NASA *EPOXI* mission. We conduct a search of the high-precision time series for additional planets around GJ 436, which could be revealed either directly through their photometric transits, or indirectly through the variations these second planets induce on the transits of the previously known planet. In the case of GJ 436, the presence of a second planet is perhaps indicated by the residual orbital eccentricity of the known hot Neptune companion. We find no candidate transits with significance higher than our detection limit. From Monte Carlo tests of the time series, we rule out transiting planets larger than 1.5 $R_\oplus$ interior to GJ 436b with 95% confidence, and larger than 1.25 $R_\oplus$ with 80% confidence. Assuming coplanarity of additional planets with the orbit of GJ 436b, we cannot expect that putative planets with orbital periods longer than about 3.4 days will transit. However, if such a planet were to transit, we rule out planets larger than 2.0 $R_\oplus$ with orbital periods less than 8.5 days with 95% confidence. We also place dynamical constraints on additional bodies in the GJ 436 system, independent of radial velocity measurements. Our analysis should serve as a useful guide for similar analyses of transiting exoplanets for which radial velocity measurements are not available, such as those discovered by the *Kepler* mission. From the lack of observed secular perturbations, we set upper limits on the mass of a second planet as small as 10 $M_\oplus$ in coplanar orbits and 1 $M_\oplus$ in non-coplanar orbits close to GJ 436b. We present refined estimates of the system parameters for GJ 436. We find $P = 2.64389579 \pm 0.00000080$ d, $R_\star = 0.437 \pm 0.016$ $R_\odot$, and $R_p = 3.880 \pm 0.147$ $R_\oplus$. We also report a sinusoidal modulation in the GJ 436 light curve that we attribute to star spots. This

signal is best fit by a period of 9.01 days, although the duration of the EPOCh observations may not have been long enough to resolve the full rotation period of the star.

2.1 Introduction

EPOXI (EPOCh + DIXI) is a NASA Discovery Program Mission of Opportunity using the Deep Impact flyby spacecraft (Blume 2005). From January through August 2008, the EPOCh (Extrasolar Planet Observation and Characterization) Science Investigation used the HRI camera (Hampton et al. 2005) with a broad visible bandpass to gather precise, rapid cadence photometric time series of known transiting exoplanet systems. The majority of these targets were each observed nearly continuously for several weeks at a time. In Table 1 we give basic information about the seven EPOCh targets and the number of transits of each that EPOCh observed.

One of the EPOCh science goals is a search for additional planets in these systems. Such planets would be revealed either through the variations they induce on the transits of the known exoplanet, or directly through the transit of the second planet itself. This search is especially interesting in the case of the GJ 436 system, since the non-zero eccentricity of the known Neptune-mass planet, first measured by Butler et al. (2004), may indicate the presence of a second planetary companion (Maness et al. 2007). Because GJ 436 is a nearby M dwarf, it is also the only EPOCh target for which we are sensitive to planets as small as 1.0 $R_{\oplus}$.

We will describe the searches for additional planets conducted on the remaining EPOCh targets in subsequent papers.

The search for transiting Earth-sized planets in the GJ 436 light curve is scientifically compelling for the following four reasons. First, theoretical predictions of the mass-radius relation for "super Earths" are still largely observationally unconstrained, with the exciting exceptions of the two known transiting super Earths CoRoT-7b (Léger et al. 2009) and GJ 1214b (Charbonneau et al. 2009). Depending on the level of observational uncertainty, a measurement of the mass and radius of a super Earth could point to the presence of a large amount of water or iron (enabled with 10% uncertainty), or allow us to distinguish between a planet composed predominately of water ice, silicates, or iron (enabled with 5% uncertainty; Seager et al. 2007). Second, the discovery of two transiting bodies in the same system would permit the direct observation of their mutual dynamical interactions. This would enable constaints on the masses of the two bodies independent of any radial velocity measurement (Holman & Murray 2005; Agol et al. 2005). Since radial velocities can only be observed for planets above a certain mass limit, this is an important tool for future surveys of stars too faint for radial velocity measurements. Third, the discovery of an Earth-sized planet at an orbital radius outside that of a giant planet would inform theories of planet formation. Hot Earths are predicted to be captured in low order mean motion resonances with migrating giant planets (Raymond et al. 2006; Mandell et al. 2007). Since the phenomenon of Earth-sized planets at larger orbital radii than Jovian planets is not observed in our own solar system, observations of exoplanet

systems are particularly important for this question.

Finally, the eccentricity of the known transiting Neptune-mass planet, GJ 436b (Butler et al. 2004), may indicate the presence of an additional perturbing planet, since the assumed circularization timescale for the known planet is much less than the age of the system (Maness et al. 2007; Deming et al. 2007; Demory et al. 2007). Ribas et al. (2008) claimed evidence for a 5 $M_{\oplus}$ super Earth in radial velocity observations of GJ 436, but this proposed planet was ruled out by subsequent investigations (Alonso et al. 2008; Bean & Seifahrt 2008). The absence of this additional perturbing body in the GJ 436 system would also be very scientifically interesting. If no other body is present to explain the eccentricity of GJ 436b, the observed eccentricity requires a very high tidal dissipation parameter, Q. The current estimate of the circularization timescale assumes a Q value for the hot Neptune similar to the value derived for the ice giant planets in our own solar system, so a substantially different Q would indicate physical properties of GJ 436b very different from these ice giants (Deming et al. 2007). Jackson et al. (2008b) show that a ratio of planetary tidal dissipation parameter to planetary Love number Q/k_2 for GJ 436b greater than $10^{6.3}$ can explain the system's eccentricity (the Love number k_2 is theoretically between 3/2, in the case of a homogeneous body, and 0, in the case of a centrally condensed body, but ranges between 0.3 and 0.6 for gas giants in the Solar System; Bursa 1992). In contrast, Uranus and Neptune, the solar system bodies presumably most similar in composition and mass to GJ 436b, have tidal Q parameters estimated at $Q_U < 3.9 \times 10^4$ and $1.2 \times 10^4 < Q_N < 3.3 \times 10^5$

respectively (Tittemore & Wisdom 1989; Banfield & Murray 1992)— several orders of magnitude smaller than the Q necessary to explain the eccentricity of GJ 436b . If the eccentricity is not attributable to a high Q, there may instead be an additional perturbing body maintaining the system's eccentricity. The possibility of a close-in resonant companion in 2:1 or 3:1 resonance with GJ 436b is strongly disfavored by transit timing measurements (Pont et al. 2009). Batygin et al. (2009) proposed possible secular perturbers to GJ 436b, the presence of which would be consistent with observed radial velocities, transit timing measurements, and the non-zero eccentricity of the system. Bean & Seifahrt (2008) also quantified the improvement to the goodness-of-fit of the GJ 436 radial velocity data with the addition of perturbing planets to the model—the parameter space they investigated included putative planets of lower mass and eccentricity than those suggested by Batygin et al. (2009). The existence and possible orbital parameters of this putative planet are still open questions. In addition, the recent discovery of the second transiting hot Neptune, HAT-P-11b, also makes this question timely, since the planetary orbit is also eccentric (Bakos et al. 2010).

The remainder of this paper is organized as follows. In Section 2, we describe the photometry pipeline we created to produce the time series. In Section 3, we detail the refinement of system parameters and the search we conduct for additional planets around GJ 436, both for additional transits and for dynamical perturbations to GJ 436b. We present a Monte Carlo analysis of the EPOCh observations of GJ 436 and demonstrate the sensitivity to detect a transiting planet as small as 2.0 times the size of Earth for all periods less than 8.5 days with

high confidence. We discuss the upper limits on the mass of additional coplanar and non-coplanar planets with periods between 0.5 and 9 days from dynamical constraints. We also discuss the constraints we place on the rotation period of GJ 436. In Section 4, we present our best candidate transit signal, and from the search for additional transits we place upper limits on the radius and mass of the putative planet GJ 436c.

2.2 Observations and Data Reduction

We acquired observations of GJ 436 nearly continuously during 2008 May 5 – 29, interrupted for several hours at approximately 2-day intervals for data downloads. The basic characteristics of the targets and observations are given in Tables 1 and 2. Observations of this type were not contemplated during development of the original Deep Impact mission; the spacecraft was not designed to maintain very precise pointing over the timescale of a transit (Table 2.2). Furthermore, the available onboard memory precludes storing the requisite number of full-frame images (1024×1024 pixels). Hence the observing strategy used 256×256 sub-array mode for those times spanning the transit, and 128×128 otherwise. This strategy assured complete coverage at transit, with minimal losses due to pointing jitter exceeding the 128×128 sub-array at other times.

We use the existing Deep Impact data reduction pipeline to perform bias and dark subtractions, as well as preliminary flat fielding (Klaasen et al. 2005). The image motion from pointing jitter produces a significant challenge for photometry

Table 2.1. EPOCh Targets

Name	V Magnitude	Number of Transits Observed[a]	Dates Observed [2008]
HAT-P-4	11.22	10	Jan 22–Feb 12, Jun 29–Jul 7
TrES-3	11.18	7	Mar 8–March 10, March 12–Mar 18
XO-2	12.40	3	Mar 11, Mar 23–Mar 28
GJ 436	10.67	8	May 5–May 29
TrES-2	11.41	9	Jun 27–Jun 28, Jul 9–Jul 18, Jul 21–Aug 1
WASP-3	10.64	8	Jul 18–Jul 19, Aug 1–Aug 9, Aug 11–Aug 17
HAT-P-7	10.50	8	Aug 9–Aug 10, Aug 18–Aug 31

[a]Some transits are partial.

Table 2.2. Characteristics of the EPOCh Observations

Instrument Parameter	Value
Telescope aperture	30 cm
Spacecraft memory	300 Mb
Bandpass	350-1000 nm
Integration time	50 seconds
Pointing jitter	± 20 arc-sec per hour
Defocus	4 arc-sec FWHM
Pixel scale	0.4 arc-sec per pixel
Subarray size	256×256 pixels spanning transit, 128×128 otherwise

at our desired level of precision. The flat field calibration that was obtained on the ground before launch is not successful at the level of precision needed here, because spatial variation of the sensitivity of the CCD has changed modestly since launch in 2005. Our observing sequences included observations of a green stimulator LED ("stim lamp") that could be switched on to illuminate the CCD. The stim lamp illumination is neither flat nor stable in an absolute sense, but its spatial pattern was designed to be stable. Hence it is useful to define and monitor changes in the flat field response pattern of the CCD. But since the stim lamp has a different effective wavelength than the stars, it is not a perfect calibrator for flat field changes. For this reason we also use a 2D spatial-spline fit to the actual data, as a bootstrap flat field method as described below.

We extract the photometric time series as follows. We determine the position of the star on the CCD using PSF fitting, by maximizing the goodness-of-fit (with the χ^2 statistic as an estimator) between an image and a model PSF with variable position, additive sky background, and multiplicative brightness scale factor. We take advantage of a defocused aperture; given our limited on-board memory, defocusing enables us to spread the starlight over more pixels and extend our duty cycle. The PSF itself has a donut-like shape with a roughly 10 pixel FWHM. A model of the PSF is produced from the drizzle of more than 1200 60×60 pixel cutouts, filtered to eliminate cosmic ray hits before drizzle. The final PSF model is sampled to a tenth of a pixel. A bilinear interpolation of this PSF increases the sampling to a hundredth of a pixel, which is the accuracy to which we estimate the position from the χ^2 grid. At this point, we perform cosmic ray

filtering by removing images from the sample with a larger than 15σ outlier in the residuals between image and best-fit PSF model. Because of the high cadence of the EPOCh observations, we simply reject the approximately 30 images ($\approx$0.1% of the total) containing a cosmic ray overlying the stellar PSF from the time series.

From each image we subtract a bias determined from the sigma-clipped median of the overclock pixels in each of the four quadrants of the CCD. These are not true pixels that lie on an unilluminated part of the CCD, but rather the bias values read out after the true pixels and then recorded to pixels on the outside of the FITS images. We subtract a bias independently for each quadrant, since the original Deep Impact reduction pipeline does not account for time-dependent bias variations of the CCD.

We then process the images to remove several sources of systematic error.

1. We scale down the two central rows by a constant value. Due to the CCD read-out electronics, there is a reduction in signal in the pixels at the internal boundary of the two upper and lower imaging regions. However, because the Deep Impact pipeline flat fields these pixels in the same way as the others, we observe the brightness of the star to increase by about 3% when the stellar PSF lies on the central rows if we do not apply this correction.

2. We scale down the central columns by a separate constant value. We observe an increase in brightness on the order of 0.25% when the stellar PSF overlies the central columns if this correction is not applied. We interpret the

physical origin of this sensitivity variation to be the serial read-out register, which is split in the middle of the CCD to allow the rows to be read out at both ends of the register.

3. We scale the entire image by a multiplicative factor determined by the size of the sub-array. We gathered observations using two sub-arrays of the 1024×1024 CCD as mentioned above: one in 128×128 mode and another in 256×256. We observed an offset in the average out-of-transit brightness between the two sub-arrays of 8.5×10^4. We correct for the offset in 256×256 mode by performing the photometric extraction of the time series, determining the decrement in brightness observed in 256×256 mode, uniformly dividing the 256×256 images by this value, and repeating this process until the out-of-transit brightness shows no offset between the two observing modes.

4. We divide the images by a "stim", described above. We first bias-correct the stims using the same prescription as we apply to the images. We then process the stims to remove the asymmetrical illumination pattern, which we model as a plane surface in x and y position.

We then perform aperture photometry on the corrected images. We choose an optimal aperture radius based on analysis of the standard deviation of the out-of-transit time series. We find that this standard deviation is minimized for an aperture radius of 10 pixels, corresponding to twice the HWHM of the PSF. After performing the bias subtraction, scaling of the two middle columns and rows, scaling of the 256×256 sub-array images, and division by a stim, the

time series still suffers from significant red noise due to the interpixel sensitivity variations on the CCD. At this point, we implement a 2D spline fit to the data with position by fitting a surface, with the same resolution as the CCD, to the brightness variations on the array. We randomly draw a subset of several thousand out-of-transit and out-of-eclipse points from the light curve (from a data set of ∼29,988 points) and find a robust mean of the brightness of the 30 nearest neighbors for each. We then fit a spline surface to these samples, and correct each data point individually by linearly interpolating on this best-fit surface. We use only a small fraction of the observations to create the spline surface in order to minimize the potential transit signal suppression introduced by flat fielding the data by itself.

To produce the final time series, we iterate the above steps, fitting for the row and column multiplicative factors, the 256 mode scaling factor, and the 2D spline surface that minimize the out-of-transit white noise of the photometric time series. We include one additional step to create the final 2D spline, which is to iteratively remove an overall modulation from the GJ 436 light curve, which has a roughly sinusoidal shape with an amplitude of a few parts in 10^4. We attribute this modulation to star spots, and discuss this signal in Section 3. After performing the 2D spline, we fit a polynomial to the corrected and binned flux, divide this polynomial from the pre-splined time series, and repeat the spline fit. Otherwise, we expect the modulation signal to introduce red noise to the time series, since we correct for interpixel variations with the assumption that the star's intrinsic brightness is constant outside of times of eclipse and transit.

After we take these steps to address the systematics associated with the observations, the red noise is largely removed. Figure 2.1 shows the GJ 436 time series before and after this 2D spline correction. In the bottom panel, we show that the time series after the 2D spline bins down roughly as predicted for Gaussian noise over timescales less than 4 hours. In the corrected time series, we attribute the scatter to photon noise and low-level cosmic rays. We compare the sigma-clipped standard deviation of the out-of-transit and out-of-eclipse flux to the expected value of the photon noise-limited precision, and find that we are 56% above the Poisson limit.

We also investigate the transit signal suppression introduced by using a flat field created from the out-of-transit and out-of-eclipse data itself. We avoid the suppression of transits of GJ 436b by excluding those observations from the points used to generate the flat field surface, so that we only use the presumably constant out-of-transit and out-of-eclipse observations to sample the CCD sensitivity. However, if the transit of an additional planet occurs while the stellar PSF is lying on a part of the CCD that is never visited afterward, the 2D spline algorithm instead treats the transit as a dark pixel. To quantify the suppression of additional transits that result from using the 2D spline, we inject transit light curves with periods ranging from 0.5 days to 20 days in intervals of 30 minutes in phase (ranging from a phase of zero to a phase equal to the period) into the EPOCh light curve just prior to the 2D spline step. After performing the 2D spline, we then phase the data at the known injected period and fit for the best radius, using χ^2 as the goodness-of-fit statistic. We find that the best-fit

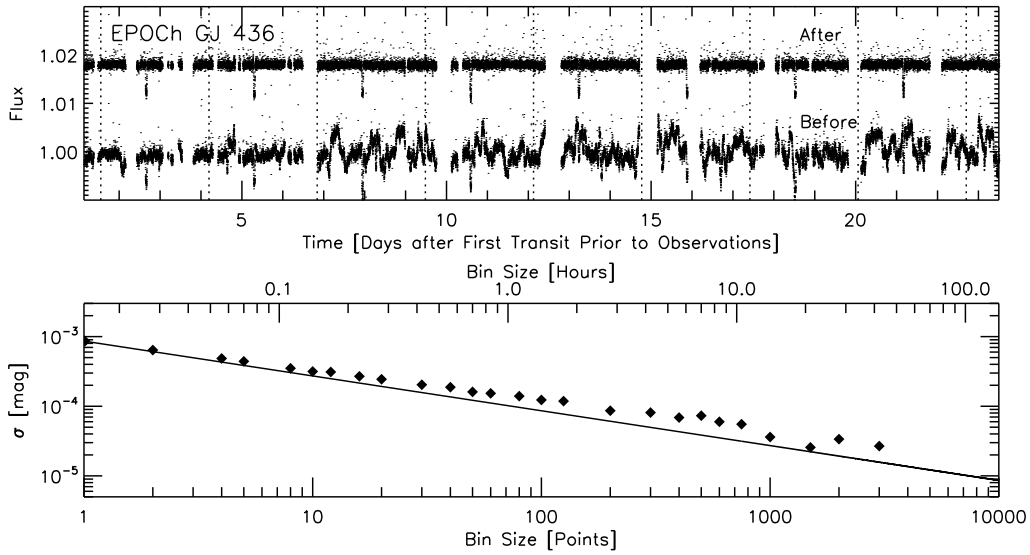

Figure 2.1.—: *Top panel:* GJ 436 time series before (lower curve) and after (upper curve) 2D spline correction. The uncorrected time series (lower curve) has had the two middle rows and columns in each image, and the entire image if taken in 256×256 observing mode, scaled by a multiplicative factor to reduce the flux dependence on position and sub-array size. The images were also divided by a flat field constructed from a stim. We have used the 2D spline to correct for additional interpixel variation in the upper curve. *Bottom panel:* The data (diamond symbols) bin down consistently with the expectation for Gaussian noise (shown with a line, normalized to match the value at N=1).

radius is suppressed to a mean value of 73% at all periods, with the standard deviation from that value increasing with period from 3% at at period of 1 day to 16% at a period of 10 days. We describe our incorporation of signal suppression into our search for additional planets in greater detail in Section 3.2.

2.3 Analysis

2.3.1 Transit Parameters

We describe here our refinement of the GJ 436 system parameters. When conducting our analysis, we were careful to account for the effects of remaining correlated noise on the parameters and their uncertainties. In the final calibrated GJ 436 light curve, we still observe evidence of correlated noise and trends that have not been corrected by the reduction process. For each transit, we fit a line to the out-of-transit data on both sides of the transit (from 3 minutes outside of transit to half an hour outside of transit) and divide the time series by this line.

We investigate the effects of limb-darkening using several different methods. In the first instance, we use stellar atmosphere models to fix the limb-darkening coefficients to a set of theoretical values. Initially, we use a model atmosphere produced by R. Kurucz (Kurucz 1994, 2005) corresponding to $T_{\rm eff} = 3500K$, $\log\, g = 4.5$, [M/H] = 0.0 and $v_{\rm turb} = 0.0$ km/s. We fit the four coefficients of the non-linear limb-darkening law of Claret (2000) to 17 positions across the stellar limb. We repeat this fit in 0.2 nm intervals across the *EPOXI* bandpass, weighted for the total sensitivity (including filter, optics and CCD response) and photon count at each wavelength. We calculate the final set of coefficients as the average of the weighted sum across the bandpass, for which we find $c_1 = 0.97$, $c_2 = -0.50$, $c_3 = 0.54$, and $c_4 = -0.17$. In order to understand the effect of the stellar atmosphere model choice on the final derived transit parameters, we

also generate a set of coefficients from the PHOENIX model (Hauschildt et al. 1999) with $T_{\rm eff} = 3300K$, $\log g = 4.5$, [M/H] = 0.0 and $v_{\rm turb} = 0.0$ km/s (private communication), and find $c_1 = 0.97$, $c_2 = 0.35$, $c_3 = -0.21$, and $c_4 = -0.03$. As a final test, we also run a parallel analysis where quadratic limb-darkening coefficients are allowed to vary in the fit described below, to see if the data are sufficiently precise to break the degeneracy of the transit shape with geometric parameters and limb-darkening. This is discussed further below.

For each of the three limb-darkening treatments, we fit the transit using the analytic algorithms of Mandel & Agol (2002). Using the Levenberg-Marquardt algorithm with χ^2 as the goodness-of-fit estimator, we fit for three geometric parameters: $R_p/R_\star$, $R_\star/a$ and $\cos i$. Initially we fix the period to the Bean et al. (2008) value of $P = 2.643904$ days and allow the times of the center of transit to vary independently for each of the eight transits, for a total of eleven free parameters. In addition, there are two quantities that parametrize quadratic limb darkening. These are set as two orthogonal linear combinations of the coefficients $2\gamma_1 + \gamma_2$ and $2\gamma_2 - \gamma_1$. In all three cases we find results that are internally consistent at the 1σ level, demonstrating that the choice of limb-darkening treatment does not significantly alter the derived parameters. We note that we can only constrain one linear combination of the limb-darkening coefficients in the quadratic limb-darkening case, the other being degenerate with the geometric parameters to within the precision of the light curve. Due to this degeneracy, the error bars on the geometric parameters are larger in the case where the limb-darkening coefficients are allowed to vary; the uncertainty on the planetary

radius R_p is larger by a factor of 2.5 and the uncertainty on the stellar radius $R_\star$ is larger by a factor of 2.2.

For the Kurucz stellar atmosphere limb-darkening coefficients, we find $R_p/R_\star = 0.08142 \pm 0.00085$, $R_\star/a = 0.0707 \pm 0.0025$ and $\cos i = 0.0594 \pm 0.0030$. The light curve is phased and binned into 2 minute intervals with this best-fit model overplotted and shown in Figure 2.2. Since there are significant time-correlated systematic errors in the light curve, we calculate the errors on the parameters using the "rosary bead" method, in the fashion described by Winn et al. (2008). First, we subtract the best-fit model from the light curve and compile a set of initial residuals. We then shift the residuals along the light curve to the next time stamp in each case, preserving the temporal correlation, add the model back to the residuals, and fit the new light curve as above. For GJ 436, we repeat this process 200 times, which corresponded to a total shift of over three hours, more than three times the duration of the GJ 436 transit. This is sufficient to sample the systematics, which on short timescales vary on the order of 10–30 minutes. The error bars on the parameters are then calculated as the range required to encompass 68% of the results. Increasing the number of shifts to the residuals does not increase the resulting error bars. We also use the Monte Carlo Markov Chain method, as adapted to transit light curve analysis by e.g. Holman et al. (2006), and find that it results in significantly smaller error bars (30–40%) than the rosary bead analysis, due to the inability to factor in systematic errors in the light curve. The Monte Carlo Markov Chain method remains a useful tool, however, for assessing the impact of systematic errors on the derived parameters.

Using the stellar mass from Torres (2007), $M_\star = 0.452 \pm 0.013$, we find $R_\star = 0.437 \pm 0.016\ R_\odot$, $R_p = 3.880 \pm 0.147\ R_\oplus$, and $i = 86.60 \pm 0.17°$. Our measurement of the planetary radius is consistent at the 1σ level with the measurements of Gillon et al. (2007b), Pont et al. (2009), and Southworth (2008), and only marginally inconsistent (at the level of 1.3σ and 1.4σ) with the values measured by Shporer et al. (2009) and Gillon et al. (2007a). It is significantly smaller than the values obtained by Torres (2007), Deming et al. (2007), and Bean et al. (2008). Although different treatments of limb darkening may partly account for the discrepancy, in all three cases of limb darkening analysis described above, we find internally consistent results. Our smaller value of the planetary radius would require a reduced mass of the H/He envelope of GJ 436b. Coughlin et al. (2008) tentatively suggested that the GJ 436 inclination, transit width and transit depth were increasing with time as the eccentric orbit precessed. Although we do find an slight increase in inclination, again consistent with previous published values, we find a shorter (58.5 ± 2.5 min) and shallower (6.173 ± 0.037 mmag) transit than expected from the predicted increase. These findings weaken the trends observed by Coughlin et al. (2008) and we therefore cannot confirm any parameter variation with these data.

We fix the times of the centers of transit at the values returned by the least-squares fit described above. These times are shown in Table 2.3 in UTC. Adding our eight transit times to those published by Pont et al. (2009), Caceres et al. (2009), Shporer et al. (2009), Gillon et al. (2007a,b), Coughlin et al. (2008), Bean et al. (2008), Deming et al. (2007) and Alonso et al. (2008) we find a

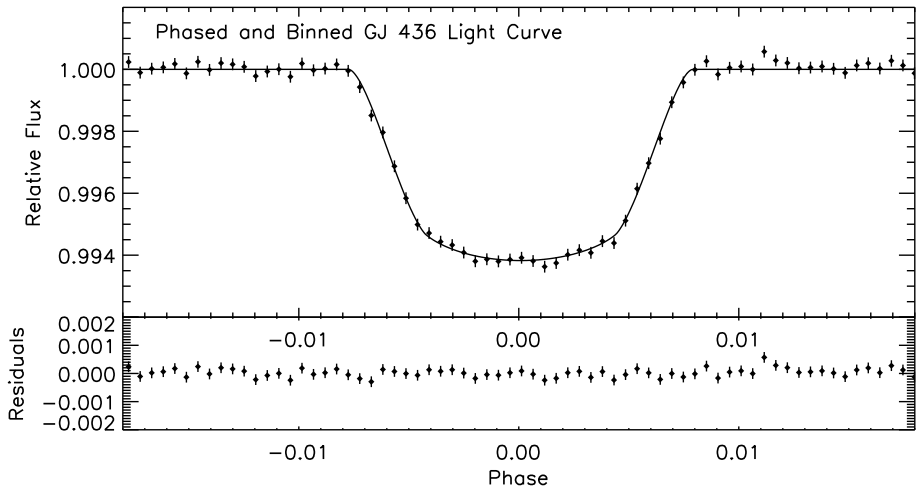

Figure 2.2.—: Phased and binned GJ 436 light curve with the best-fit model overplotted. The error bars are the rms errors in the bins.

new linear, weighted ephemeris of $T_c(\mathrm{BJD}) = 2,454,600.693205 \pm 0.000040$ and $P = 2.64389579 \pm 0.00000080$ d.

2.3.2 Search for Additional Transiting Planets

We perform a robust search of the GJ 436 time series for evidence of additional planets using two methods. The first is a search for additional shallow transits in the light curve. We developed software to search for these additional transits partly modeled on the methods employed on the MOST photometry (Croll et al. 2007b,a). The steps involved in the procedure are described in this section.

The photometric precision of the GJ 436 time series (with S/N≈65 for each

Table 2.3. EPOCh Derived Stellar and Planetary Parameters for GJ 436

Parameter	Value
Light curve Parameters	
P (days)	$2.64389579 \pm 0.00000080$
Transit Times (BJD)	$2,454,592.76134 \pm 0.00022$
	$2,454,595.40458 \pm 0.00026$
	$2,454,598.04822 \pm 0.00021$
	$2,454,600.69271 \pm 0.00045$
	$2,454,603.33657 \pm 0.00017$
	$2,454,605.98079 \pm 0.00035$
	$2,454,608.62326 \pm 0.00026$
	$2,454,611.27015 \pm 0.00040$
$R_p/R_\star$	0.08142 ± 0.00085
$R_\star/a$	0.0707 ± 0.0025
i (deg)	86.60 ± 0.17
Stellar and Planet Parameters[a]	
$R_\star$ ($R_\odot$)	0.437 ± 0.016
R_p ($R_\oplus$)	3.880 ± 0.147

[a]Using the stellar mass from Torres (2007).

transit event) should enable a detection of a 1.5 $R_\oplus$ planet with S/N≈10 and a 2 $R_\oplus$ with S/N≈17, even if the planet produces only a single transit event. In order to test this prediction, we conduct a Monte Carlo analysis to assess how accurately we could recover an injected planetary signal in the GJ 436 light curve. We evaluate our sensitivity to transit signals on a grid in radius and period space sampled at regular intervals in R_P^2 and regular frequency spacing in P. We create an optimally spaced grid as follows: for the lowest period at each radius, we determine the radii at which to evaluate the adjacent periods by solving for the radius at which we achieve equivalent signal-to-noise (for this reason, we expect significance contours to roughly coincide with the grid spacing). We use the Mandel & Agol (2002) routines for generating limb-darkened light curves given these parameters to compute a grid of models corresponding to additional possible planets. If we make the simplifying assumptions of negligible limb darkening of the host star, a circular orbit, and an orbital inclination angle i of 90°, the set of light curves for additional transiting bodies is a three parameter family. These parameters are radius of the planet R_p, orbital period of the planet P, and orbital phase ϕ. At each test radius and period, we inject planetary signals with 75 randomly assigned phases into the residuals of GJ 436 EPOCh light curve with the best GJ 436b transit model divided out, and then attempt to recover blindly the injected signal by minimizing the χ^2 statistic. We first conduct a coarse χ^2 grid search in radius, period, and phase. We select the spacing of this grid to minimize processing time while ensuring that the transit was not missed. We sample the χ^2 space at 300 points in period space (at even frequency intervals

between 0.5 and 8.5 days), 50 points in radius space (between 0.5 and 5.5 Earth radii) and a variable number of points in phase space from around 30 to nearly 200 (sampled at half a transit duration for each period). We use an expression for the transit duration τ given by Seager & Mallén-Ornelas (2003):

$$\sin i \sin\left(\frac{\pi\tau}{P}\right) = \sqrt{\left(\frac{R_\star + R_P}{a}\right)^2 - \cos^2 i}. \tag{2.1}$$

For each test model, we compute the χ^2, using the out-of-transit standard deviation to estimate the error in each point. The grid search requires about 24 CPU hours on a 2.66 GHz processor for each radius and period (75 light curves with randomly injected phases). After the grid χ^2 minimum is determined, we use the `amoeba` minimization routine (Nelder & Mead 1965) to more finely sample the χ^2 space in order to find the χ^2 minimum from the specified nearest grid point. We also investigate whether aliases of the best-fit period from the χ^2 grid improve the fit. We find that roughly half of the best solutions from the grid are aliases of the injected period, most at either half or twice the value of the injected period, but we test aliases at every integer ratio from 1/35 to 35 times the given period (these other aliases occur less than one percent of the time). We also repeat the finer grid search at the three next lowest χ^2 minima, in case the best solution (or an alias of the best solution) lies closer to that grid point. For all 3600 injected signals, we recover a solution which is a better fit (in the χ^2 sense) than the exact injected signal. For injected radii greater than 1 $R_\oplus$, we recover the period to within 1% for all injected periods less than 7 days (with the exception of one

signal[1]). For these reasons, we are confident that we are sampling the χ^2 space sufficiently finely to locate the best solution.

We quantify the success of this analysis by how well the search blindly recovers the known injected transit signal. We define the error on the recovered parameter, for instance period, to be $\mid P_{injected} - P_{observed} \mid / P_{injected}$. We set an approximate error of one sigma for a given parameter at the value that includes 51 of the 75 errors at that point in radius and period (roughly 68% of all values). Figure 2.3 shows this relative error in radius for all searches. We shift the location of the points at which we evaluate our sensitivity, shown as diamonds, to conservatively incorporate the expected level of signal suppression from a planetary transit. As we note in the last paragraph of Section 1, we anticipate suppression of additional transit signals from the bootstrap flat field treatment of the *EPOXI* data. We evaluate the suppression we expect at all eight periods on the grid shown in Figure 2.3. We inject planetary transits into the pre-flat fielded light curve in intervals of 30 minutes in phase (from a phase of zero to a phase equal to the period), apply the 2D spline flat field, phase to the known period, and fit for the suppressed transit depth. In this way, we obtain a complete understanding of the suppression at each period, and we can evaluate the level of suppression that we expect with a given confidence. In particular, with 95%

[1]In this injected signal with a period of 7 days, only one transit event occurred over the baseline of the observations. Although the radius of the planet corresponding to the single transit event was recovered to 1%, more than a single transit event is required to accurately recover the period itself.

confidence, we expect suppression to be no worse than 71% the injected radius at 0.55 days, 68% at 0.79 days, 65% at 1.13 days, 67% at 1.63 days, 63% at 2.35 days, 65% at 3.38 days, 53% at 4.86 days, and 55% at 6.98 days. We incorporate this expected suppression by shifting the effective radius values of the grid points at which we evaluate our sensitivity to additional transits. For example, at 1.63 days, all grid points have been shifted upward in radius by a value of 1/0.67, or 1.49. Because we anticipate no more than 67% radius suppression at this period (with 95% confidence), an authentic transit signal would pessimistically appear only 67% its original radius value after we process the data. For this reason, the recovery statistics corresponding to a 1.0 $R_\oplus$ transit depth in the final light curve would be accurate for an original transit signal of a 1.49 $R_\oplus$ planet once we fold our expectation of signal suppression. For a planet with 2.0 times the Earth's radius, we are able to recover the radius to better than 5% accuracy at least 68% of the time for all periods less than 4 days, and better than 10% at least 95% of the time in the same period interval.

We also evaluate the overall detection probability for putative transiting planets. Given the cadence and coverage of the *EPOXI* observations, we determine the number of in-transit points we expect for a given radius, period, and phase (where the phase is evaluated from 0 to 1 periods, in increments of 30 minutes). We then evaluate the expected significance of the detection, assuming a boxcar-shaped transit at the depth of $(R_P/R_\star)^2$, and the noise of the actual GJ 436 time series. At each phase and period individually, we scale down R_P to incorporate the signal suppression at that ephemeris. We use the improvement

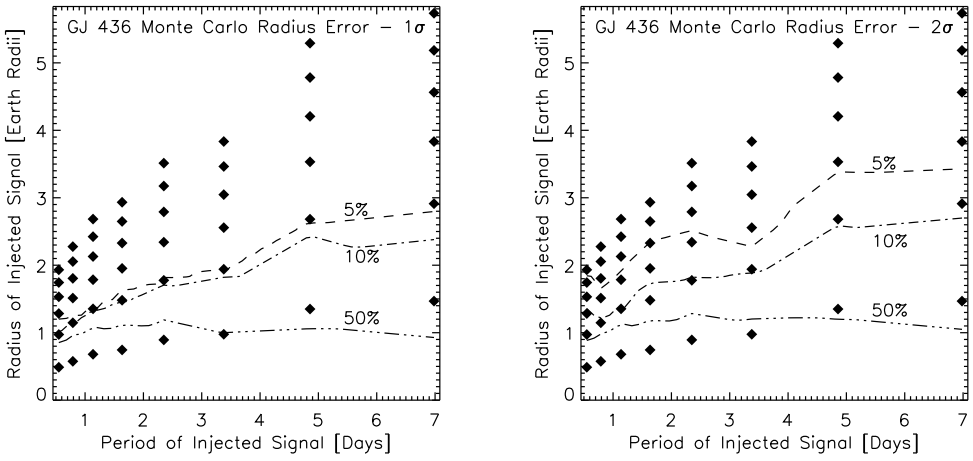

Figure 2.3.—: Constraints on radius from the Monte Carlo analysis. For each point in radius and period, we create 75 light curves with random orbital phases, inject them into the GJ 436 residuals, and attempt to recover them blindly. The diamonds indicate the grid of radii and periods at which we evaluate our sensitivity; the contours are produced by interpolating between these points. At left, contours indicate the relative error in radius (absolute value of recovered-injected/injected radius) that encloses 68% of the results. At right, contours indicate the relative error in radius that encloses 95% of the results. The radius values of the grid points have been upwardly adjusted to incorporate conservative expectations of signal suppression at each period.

in the χ^2 over the null hypothesis to define a positive detection, after we have removed the best candidate transit signal (presented in Section 4.1). If we do not first remove this signal, then we are a priori defining a "detectable" signal to be any signal more prominent than the best candidate signal, and we would

be unable to evaluate this signal's authenticity. We set our detection limit at an improvement in χ^2 over the null hypothesis of 250. This level is set by the results of the Monte Carlo analysis; we observe a χ^2 improvement of 250 compared to the null hypothesis only at radii and periods at which we correctly recover the injected period (with the exception again of the single signal which presented only one transit event). Although we use the χ^2 as a detection statistic, we do not assign a percent significance to a $\Delta\chi^2$ of 250 because of the presence of red noise in the time series. We then determine the fraction of phases for which the signal would be significant enough for *EPOXI* to detect, which is shown in Figure 2.4. For planets larger than about 2.0 times the size of Earth, we would detect the planet with 95% probability for all periods less than 8.5 days, and we would detect the planet with nearly 100% probability at periods less than 6 days— this includes the 2:1 resonance with the known Neptune-mass planet. We would also have a good chance (80% certainty) of detecting a 1.5 $R_\oplus$ planet with a period corresponding to the 2:1 resonance or shorter. Our sensitivity to 1 $R_\oplus$ planets is limited to periods of 1.5 days or less for greater than 50% confidence. Although planets with longer periods are much less likely to transit, we are still sensitive to planets larger than 2.0 $R_\oplus$ with 80% certainty at a period of 15 days, and 70% certainty at a period of 20 days.

2.3.3 Dynamical Constraints on Second Planets

Over the past few years, many researchers have pointed out that the excellent precision of transit data can reveal second planets. Such a detection would rely

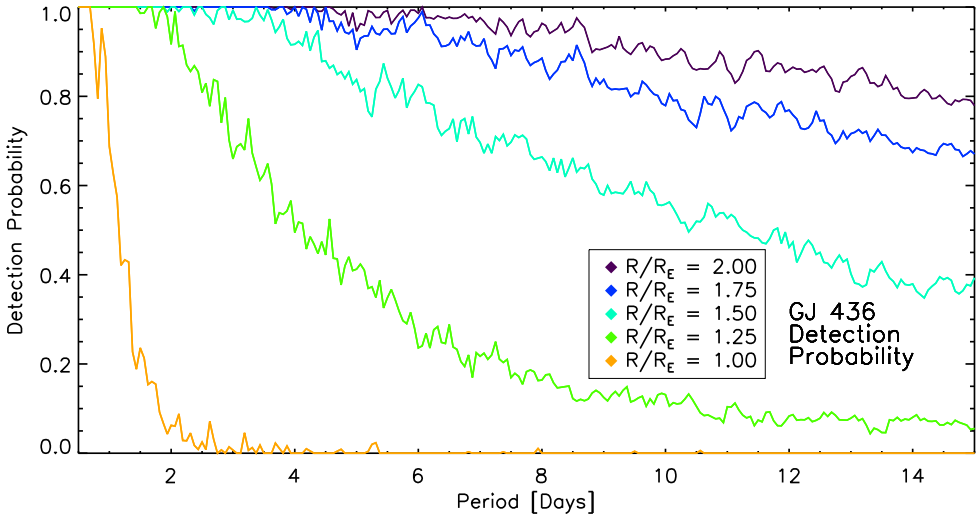

Figure 2.4.—: Detection probability versus period for planets ranging in size from 1 to 2 $R_\oplus$. The detection criteria is set by the percentage of phases at a given period for which the number of points observed in transit produces a χ^2 improvement of 250, compared to the null hypothesis. We assume a boxcar-shaped transit at the depth of $(R_P/R_\star)^2$, where R_P at each period and phase includes the expected level of signal suppression.

on the deviation of the known planet from a Keplerian orbit; in particular, the orbit and light curve would no longer be perfectly periodic. We may sort such effects into several categories.

First, on orbital timescales the two (or more) planets exchange small amounts of angular momentum and energy as they approach and recede from mutual conjunctions. This effect is imprinted on fluctuations of the transit-to-transit orbital period (Agol et al. 2005; Holman & Murray 2005), which might be seen in

a short string of consecutive transits, like those we are reporting. Each of the 8 EPOCh transit times of GJ 436b is plotted in Figure 2.5, and given in Table 2.3. We consider variation around a constant period of > 100 s to be ruled out by our data. We introduce a small second planet in a series of numerical integrations spanning the transits that *EPOXI* measured, to see what mass planet would have been detectable. For each period of a hypothetical planet of mass 0.01 $M_{\rm Jup}$, we chose a circular orbit, coplanar with the known planet, and a grid of initial orbital phases. We recorded the time of minimum separations between the star and planet b, representing the *EPOXI* mid-transit times, and found their standard deviation from a linear ephemeris. We examined the minimum and the median (on the grid of phases) of those standard deviations. The minimum was generally considerably higher than the limits from other effects, quoted below. The median, however, was smaller than 100 s in orbits close to planet b. Even where it was not, as the short-term perturbations are linear in the mass of the perturber, we scale the value of the computed perturbations and the mass to 100 s and a "typical" mass that could have been seen in our data. We plot that typical mass in Figure 2.6 as a thin line.

Second, on timescales of several tens of orbital periods (for the mass of GJ 436b), orbit-orbit resonances between planets can cause the periods to oscillate, the eccentricities to fluctuate, and the apses to precess. Our data alone does not have the requisite time span to sample all of such oscillations, although resonant effects do cause the short-term constraints of Figure 2.6 to appear jagged, as a function of period. In combination with light curves taken

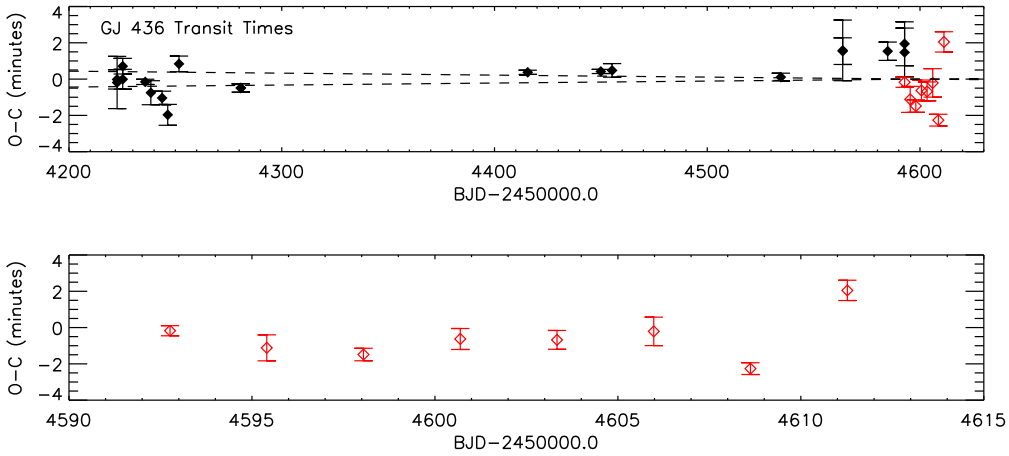

Figure 2.5.—: Transit timing residuals from the new ephemeris. The solid diamonds are the previously published times from sources listed in the text; the hollow diamonds are the EPOCh times. The propagated error in the new period is overplotted as dashed lines.

over several seasons, the data gathered by *EPOXI* allow very deep constraints on planets in resonance. We defer this analysis to future work, as sampling of the relevant timescales is not yet complete using available data. Similar analyses have already been performed on TrES-1b (Steffen & Agol 2005), HD 189733b (Miller-Ricci et al. 2008a), HD 209458b (Agol & Steffen 2007; Miller-Ricci et al. 2008b), CoRoT-Exo-1b (Bean 2009), and TrES-3b (Gibson et al. 2009). The only considerable difference in the case of GJ 436b is that, because of its small mass, its response to resonant perturbations is proportionally bigger, so the current non-detections of perturbations allow surprisingly low-mass planets to be ruled out. For instance, once the 6 month timescale is well sampled by transit times

with precisions of 7 seconds, then the data could detect or rule out a $\gtrsim 0.05 M_{\rm Earth}$ planet librating with large amplitude in the 2:1 resonance (Pont et al. 2009).

Third, on timescales of thousands of orbital periods, the planets torque each other's orbits into different orientations and eccentricities, exchanging angular momentum, but not energy. These secular effects therefore do not change the semimajor axes and periods of the planets, but several recent papers have shown that these changes would still manifest themselves in transit data. For some effects, an eccentric planet is required and a large impact parameter is desirable, so GJ 436b (with an impact parameter of 0.85) provides a suitable laboratory to search for them. The remainder of this section evaluates these constraints in detail.

Apsidal motion causes the longitude of transit to move either towards the periastron or towards the apastron of the orbit, depending on ω and the sign of $\dot{\omega}$ (here ω is the angle between the ascending node on the plane of the sky and the periastron of the orbit). The precession period is expected to be considerably longer than the observational baseline, $P_{\rm prec} = 2\pi/\dot{\omega} \gg \tau_{\rm obs}$, so we expect to detect at most a linear change in ω. One consequence of precession is that the observed period of transits generally differs from the true (sidereal) orbital period. However, because the true period is known only from radial velocity observations, which are several orders of magnitude less precise than transit data for this purpose, in practice this method is not constraining. On the other hand, the period of transits would differ from the period of occultations, so multi-epoch secondary eclipse observations should be able to place a tight constraint on $\dot{\omega}$

from this technique (Miralda-Escudé 2002; Heyl & Gladman 2007). Currently, the technique with the highest precision is to use transit *durations* to constrain $\dot{\omega}$, as the duration changes linearly in time depending on the true planet-star separation at transit. This dependence comes in two forms: (1) the impact parameter is directly proportional to this separation and (2) the tangential velocity is inversely proportional to this separation, according to Kepler's second law. It has been shown (Kopal 1959) that these two effects cancel, for linear changes in ω, at an impact parameter of $b = 1/\sqrt{2}$. At the impact parameter of GJ 436b, the dependence of the impact parameter is more important, as has been emphasized by Shporer et al. (2009). Both effects together cause the duration to change at a rate:

$$\frac{d\omega}{dt} = \frac{dT/dt}{T} \frac{1 + e\sin\omega}{e\cos\omega} \frac{1 - b^2}{1 - 2b^2} \tag{2.2}$$

(Pál & Kocsis 2008; Jordán & Bakos 2008), where T is the duration between the times when the projected centers of the planet and star are separated by $R_\star$. We combined the transit duration of our combined light curve, considered as a "single epoch" measurement of extremely high quality, with the transit durations reported over the last two years. Here and below, we take the values from the compilation and homogeneous analysis of Coughlin et al. (2008).[2] We measure $dT/dt = (1.9 \pm 3.7) \times 10^{-3}$ min/day, so infer $\dot{\omega} = (-8 \pm 15) \times 10^{-3}$ deg/day by equation 2.2. Taking $|\dot{\omega}| \lesssim 4.5 \times 10^{-2}$ deg/day to be a conservative upper limit, we now consider what constraints this puts on additional planets in the

[2]Coughlin et al. (2008) analyzed the data in two ways; we use the results assuming fixed stellar and planetary radii for all the data sets.

GJ 436 system. As Heyl & Gladman (2007) pointed out, the asymptotic formulae (Miralda-Escudé 2002) for apsidal rate due to second planets underestimates their strength by a factor of > 2 when the perturbing planet is within a factor of 2 in semi-major axis of the transiting planet. Thus we use the full formula for apsidal motion caused by a perturbing planet on a circular orbit (Heyl & Gladman 2007; Murray & Dermott 1999):

$$\frac{d\omega}{dt} = \frac{\pi}{2P_b}\frac{M_c}{M_\star} \times \left\{ \begin{array}{ll} (a_c/a_b)b^{(1)}_{3/2}(a_c/a_b) & a_c < a_b \\ (a_b/a_c)^2 b^{(1)}_{3/2}(a_b/a_c) & a_c > a_b \end{array} \right\} \tag{2.3}$$

where

$$b^{(1)}_{3/2}(x) = \frac{1}{\pi}\int_0^{2\pi} \frac{\cos\psi d\psi}{(1+2x\cos\psi+x)^{3/2}} \tag{2.4}$$

is the Laplace coefficient, which we compute numerically. We may invert this formula to obtain a constraint on the mass of a second planet, as a function of its semimajor axis, given the previously quoted constraint on $\dot{\omega}$; this is plotted in Figure 2.6. Perturbing planets on currently eccentric orbits can torque planet b at somewhat different rates, depending on the relative apsidal orientation, an effect we neglect here.

Another secular effect is nodal precession, which changes both the node and the inclination of the orbit. The former is measurable in principle by comparing Rossiter-McLaughlin (R-M) observations spanning many years, but GJ 436 is a slow rotator ($P_{\rm rot} \approx 48$ days; Demory et al. 2007) and thus not a favorable R-M target. The latter, however, is exquisitely measurable due to the large impact parameter of GJ 436b. In fact, detections of an inclination change have already been suggested (Ribas et al. 2008; Coughlin et al. 2008), which would imply a

several Earth-mass planet in a nearby orbit, and the specific orbits and masses of allowable planets have been debated (Alonso et al. 2008; Demory et al. 2009; Bean & Seifahrt 2008). We measured $di/dt = (-6 \pm 31) \times 10^{-5}$ deg/day by producing a weighted linear ephemeris to our inclination and the ones presented in Coughlin et al. (2008), Gillon et al. (2007a,b), Bean et al. (2008), Deming et al. (2007), Shporer et al. (2009), and Alonso et al. (2008). We find a a conservative upper limit of $|di/dt| \lesssim 9 \times 10^{-4}$ deg/day. The shape of the light curve is much more sensitive to inclination change than to apsidal motion. Next, we convert this to a mass constraint on second planets. The secular theory of Murray & Dermott (1999, §7.2), gives the rate of inclination change due to a perturbing planet, as the nodes of the planets precess:

$$\frac{di}{dt} = -\frac{d\omega}{dt}\Delta\Omega_{\rm sky}, \tag{2.5}$$

where $d\omega/dt$ is given by Equation 2.3 and $\Delta\Omega_{\rm sky}$ is the ascending node of the second planet relative to the ascending node of the known planet, measured clockwise on the plane of the sky. (This latter quantity is the sky-projected mutual inclination, similar to the sky-projected spin-orbit angle from the R-M literature.) Equation 2.5 assumes small eccentricities and mutual inclination. We have tested it against numerical integrations for the known planet and a second planet that would be marginally detectable and is far from resonance ($M_c = 35 M_\oplus$, $P_c = 2.818 P_b$), and find it to be accurate to 20% over the timespan of the data if the perturbing planet begins on a circular orbit and is inclined less than 20° from the orbit of planet b. The resulting mass limit is plotted in Figure 2.6 for

$|\Delta\Omega_{\rm sky}| \geq 10^\circ$. Because of the lightcurve's sensitivity to inclination change, only a small $\Delta\Omega_{\rm sky}$ is needed for an inclination change over a certain angle to be as detectable as apsidal motion through the same angle. For $\Delta\Omega_{\rm sky} = 0.37^\circ$, the inclination constraint has the same magnitude as the apsidal motion constraint. According to Equation 2.5 it also has the same form.

We note a degeneracy between the effects of apsidal motion and nodal precession. The light curve is most sensitive to both via transit duration change, so with a judiciously chosen orbit for a second planet, the two effects mostly cancel at the present time (Miralda-Escudé 2002). In such a case, the precession of the planet in its plane causes the impact parameter to increase at the same rate the precession of the planet out of its plane causes the impact parameter to decrease. This happens for $\Delta\Omega_{\rm sky} = -0.37^\circ$, so a much larger M_c is possible for that particular orbit. The degeneracy could be broken by the shape of the light curve, as the changing velocity accompanying apsidal motion is not canceled, so the change in the ingress/egress duration and the depth of the transit due to the limb-darkened star may be observable. However, in practice the radial velocity constraint provides a stronger limit for such orbits.

We have also plotted as a gray area in Figure 2.6 the orbits near GJ 436b that are not guaranteed to be stable by Hill's criterion (e.g., Gladman 1993). We took account of the eccentricity of b, so the stability criterion is approximately

$$\frac{a_{\rm outer} - a_{\rm inner}}{a_{\rm inner}} > \sqrt{\frac{8}{3}e_b^2 + 5.76\Big(\frac{M_{\rm inner} + M_{\rm outer}}{M_\star}\Big)^{2/3}}. \qquad (2.6)$$

There is only a narrow region that both satisfies the stability criterion and is

ruled out by these secular constraints more strongly than by the radial velocity measurements. However, these dynamical constraints will certainly tighten in the future with both longer observing baselines and the measurement of the occultation period, to be compared with the transit period. The secular limits given above will improve approximately linearly in time, until 1 radian of the secular cycle has elapsed. This timescale may be computed using Equation 2.3 with $\max(M_b, M_c)$ substituted for M_b, and is typically decades. In contrast, most relevant short-term and resonant timescales are shorter than the several-year time span of data collected so far, so apart from sampling all the timescales, those constraints have saturated. Thus, they will only improve considerably with improved precision of transit data.

In the case of GJ 436, excellent radial velocity data was in hand before transits were ever discovered, so it is not surprising that radial velocity constraints are stronger than the transit timing constraints for a wide range of periods of perturbers. However, soon exquisite transit data will be available from the *Kepler* mission, with little or no useful constraints from radial velocity. Therefore, the techniques illustrated here for GJ 436 are expected to be very useful in those cases.

Finally, there are still several potentially confounding effects which are well below the sensitivity of the data. The apsidal line may precess not by a second planet, but by either the post-Newtonian relativistic correction, by a tidal bulge raised on the planet (Ragozzine & Wolf 2009), or by rotational oblateness of the star (Miralda-Escudé 2002). These effects have expected magnitude

Figure 2.6.—: (Following page) Limits in the mass - period plane for a hypothetical companion planet GJ 436c. The secular limits are given due to a lack of observed transit inclination and duration change, assuming the companion is currently on a circular orbit. A coplanar second planet must have a mass below the long-dashed line, due to our upper limit on apsidal motion of b. A non-coplanar second planet must have M_2 below the thick solid line for $|\Delta\Omega_{\rm sky}| \geq 10^\circ$, with the limit scaled up or down in proportion with the actual value of $|\Delta\Omega_{\rm sky}|$. Such planets could be stable; according to Hill's criterion (Gladman 1993) second planets on initially circular orbits are certainly stable outside of the gray area. The approximate radial velocity limit is given as a critical semi-amplitude K (short-dashed line) that would have been detectable according to the simulations of Bean & Seifahrt (2008). For perturbers producing short-term fluctuations that would have been detectable in *EPOXI* alone, a typical value of the detectable mass is given as a thin solid line; in contrast to the other lines, this should not be viewed as an upper limit (see text).

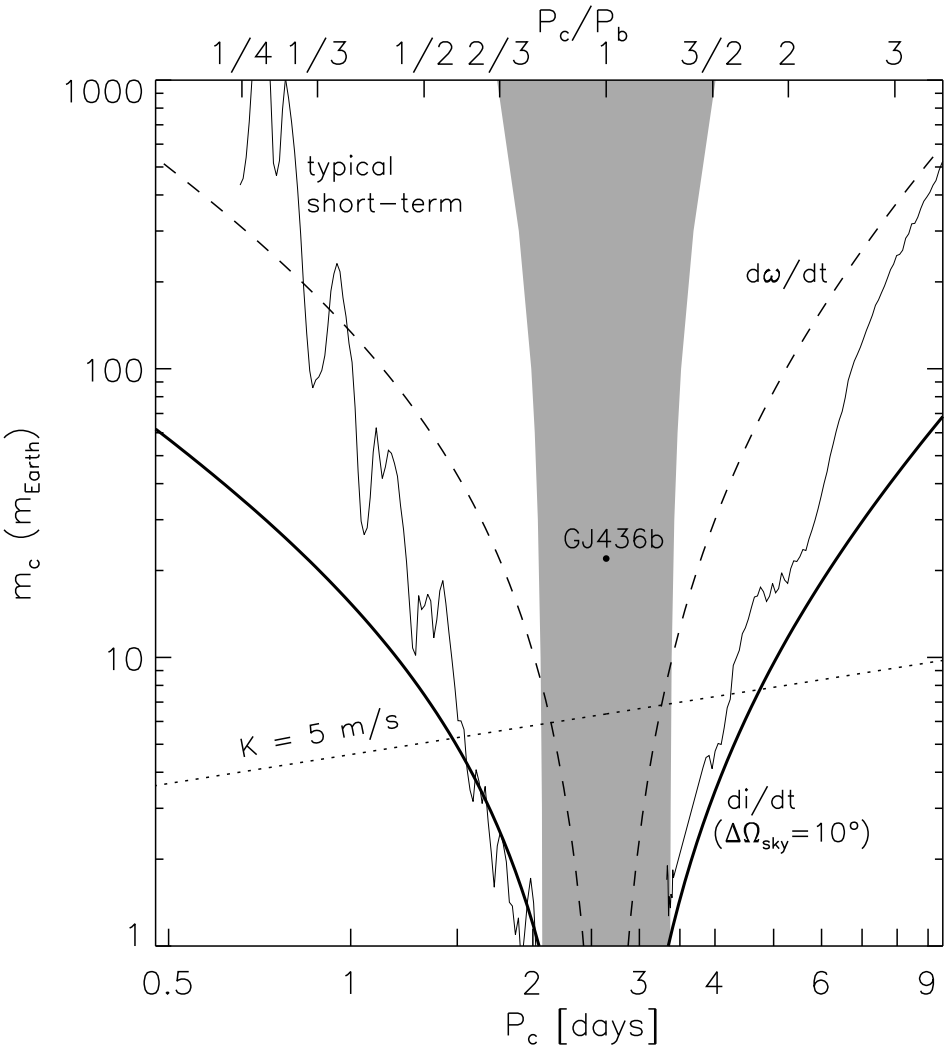

Figure 2.6.—: (Continued).

6.5×10^{-5} deg/day (Pál & Kocsis 2008; Jordán & Bakos 2008), 1.0×10^{-6} deg/day (Ragozzine & Wolf 2009), and 3×10^{-8} deg/day (Miralda-Escudé 2002) respectively, all far below the current reach of the data. Also, nodal precession may occur and be observable if the stellar spin axis and the orbit normal do not lie in the same angle as projected on the plane of the sky. Such precession is driven by rotational oblateness, so its timescale is similar to apsidal motion by the same mechanism, approximately 3×10^{-8} deg/day.

We note also that a detailed search for Trojan asteroids to the known planet GJ 436b using the transit timing method proposed by Ford & Gaudi (2006) could place interesting limits on Trojans in this system, although we do not specifically address this question in this work. However, Trojan bodies could also produce a photometric transit, so our constraints on additional transiting bodies could be applied to the detection of Trojans as well. These Trojan asteroids would have a period equal to GJ 436b (trailing or preceding the hot Neptune planet at the fixed phase set by the L4 and L5 Lagrange points), so without conducting a detailed analysis specific to Trojan asteroids, we conservatively would have been able to detect Trojans that produced a transit depth equivalent to a 1.5 $R_\oplus$ planet with nearly 100% certainty from the detection probabilities shown in Figure 2.4.

2.3.4 Rotation Period of GJ 436

As previously stated, we fit a sinusoidal modulation in the GJ 436 light curve with a polynomial and remove it in order to conduct the search for additional transits.

Here we consider the astrophysical significance of this signal, which we attribute to changes in the apparent brightness of the star due to star spots. The sinusoidal modulation has a peak amplitude near 0.5 millimagnitudes and is shown in the top panel of Figure 2.7. Butler et al. (2004) give an upper limit on V sin i of 3 km s^{-1}; if we assume rigid body rotation and a stellar radius from this work of $R_\star = 0.437 \pm 0.016\ R_\odot$, we infer a lower limit on the rotation period of ≈ 7.4 days. We investigate the periodicity of the EPOCh GJ 436 observations by binning the time series in two hour increments and creating a Lomb-Scargle periodogram of the binned observations. We find only one peak with false alarm probability significantly less than 0.01% at $P_{\rm rot}$=9.01 days; the time series is shown phased to this period in the bottom panel of 2.7. The best-fit rotational period of 9.01 days is longer than the lower limit set by V sin i. However, Demory et al. (2007) observed flux variations of GJ 436 nearly 20 times larger with amplitude of 1% which were best fit by a stellar rotation period ≈ 48 days. It is therefore possible that the baseline of the *EPOXI* observations is not long enough to resolve the full rotation period of the star, and the modulation we observe is due to multiple starspots passing into view over a period shorter than the rotation period of the star.

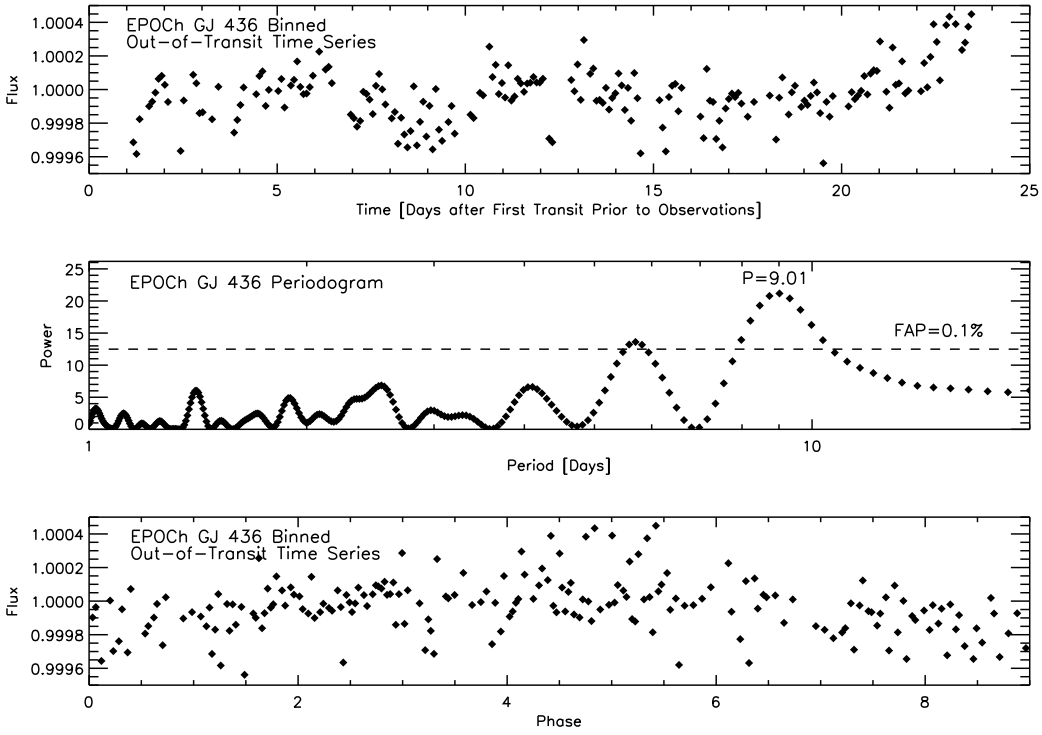

Figure 2.7.—: *Top panel:* GJ 436 out-of-transit and out-of-eclipse EPOCh observations, binned in two hour increments. *Middle panel:* Lomb-Scargle periodogram of binned observations, with false alarm probability of 0.1% overplotted. The most significant peak corresponds to a period of 9.01 days. *Bottom panel:* Time series phased to most significant period of 9.01 days.

2.4 Discussion

2.4.1 Best Candidate Transit Signal

We find no transit signals for GJ 436c at the significance limit set by $\Delta\chi^2$=250. We present our best candidate here, which corresponds to a planet with radius

1.04 $R_\oplus$ and period 8.42 days. The improvement in the χ^2 over the null hypothesis is 170. We investigate the possibility of signal suppression by masking these suspected transit points from the points used to create the 2D spline, and recreating the spline surface. We find that the candidate transit depth is unaltered, indicating that these points are well-sampled on the CCD. In Figure 2.8, we show the phased and binned best candidate signal, as well as the two observed candidate transit events separately. The gap in the middle of the first event is due to the star wandering off the bottom edge of the CCD for a period of about an hour.

We also perform an identical transit search on a flipped version of the time series (we subtract 1 from the normalized time series and multiply by -1), since we expect red noise fluctuations to introduce both positive and negative imposter transit signals. We find that the best solution to the inverted time series produces an improvement over the null hypothesis of $\Delta\chi^2 = 106$.

2.4.2 Radius constraints

From the results of our Monte Carlo analysis and phase coverage analysis, we rule out transiting planets orbiting interior to GJ 436b larger than 1.5 Earth radii with 95% confidence. We would expect to detect such a planet with 95% certainty, and recover its radius to within 15% with 95% confidence (referencing Figures 2.4 and 2.3, respectively). For planets exterior to the orbit of GJ 436, we can no longer assume that additional planets will transit the host star—since

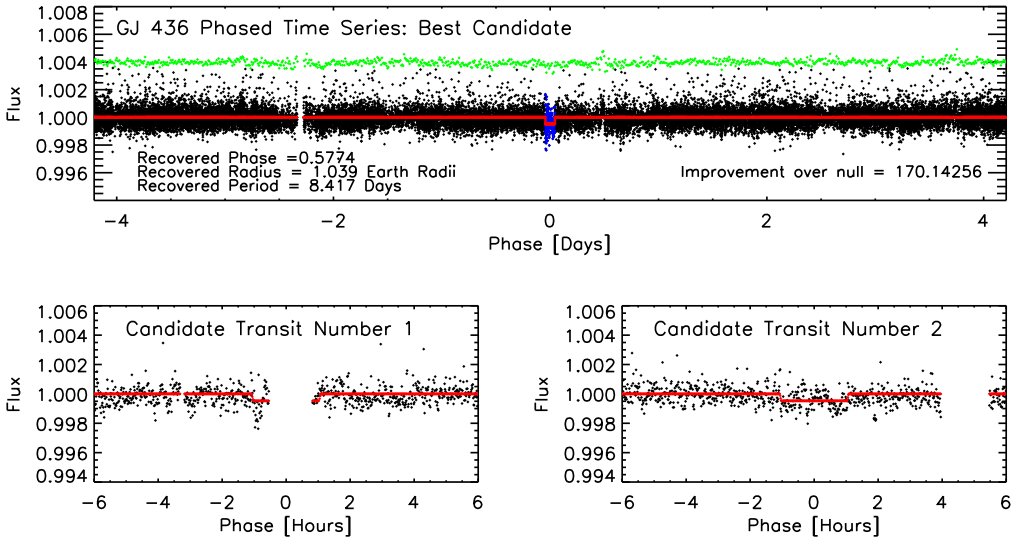

Figure 2.8.—: *Top panel:* Best transit candidate, shown phased (black points) with best-fit model overplotted in red. The green curve directly above is the phased light curve binned by a factor of 30. *Bottom panels:* The two observed candidate transit events which contribute to the best candidate signal, with best-fit model overplotted in red. The transit event at left contributes an improvement over the null χ^2 of 49, and the right transit contributes an improvement in χ^2 of 121. Since we place our significance limit at $\Delta\chi^2 = 250$, we cannot claim a positive detection.

GJ 436b itself has an inclination of $i = 86.60 \pm 0.17°$, and the host star has a radius of $R_\star = 0.437 \pm 0.016\ R_\odot$ (from this work), we would anticipate coplanar planets to transit only with periods less than about 3.4 days. However, the orbital inclination of Earth differs from the orbital inclinations of the gas giants by up to 2.5° in the case of Saturn (Cox 2000). If the putative GJ 436c had an inclination which was 2° closer to edge-on than GJ 436b, we should be able to detect transits

out to nearly 13 days. For all periods less than about 8.5 days, we would have detected the transit of a planet 2.0 $R_\oplus$ or larger with 95% probability if the planet produced a transit (shown in Figure 2.4). This includes the 2:1 resonance with GJ 436b at about 5.3 days, although NICMOS observations of the transit times of GJ 436b, with timing variations less than a few seconds, disfavor planets in the 2:1 resonance– a planet in the 2:1 resonance with GJ 436b with a mass as small as 0.01 $M_\oplus$ should produce at least 7 second variations (Pont et al. 2009). For periods less than about 20 days, we would have detected the transit of a planet of 2.0 $R_\oplus$ or larger with 70% probability.

2.4.3 Mass constraints

We use the theoretical mass-radius relationships for super Earths and hot Neptunes calculated by Fortney et al. (2007) to place approximate mass constraints, given our radius constraints derived from the search for additional transiting planets. We rule out planets larger than 1.5 $R_\oplus$ interior to GJ 436b—using the analytic formulae given in Fortney et al. (2007), such a planet would have a mass around 0.8 $M_\oplus$ if it were pure ice, 2.9 $M_\oplus$ if it were pure rock, and 4.6 $M_\oplus$ if it were pure iron. At semi-major axes larger than that of GJ 436b, since additional planets may not transit, we are unable to set firm upper limits from the lack of transits. If such a planet with a period less than 8.5 days did transit, we would be sensitive with 95% confidence to radii as small as 2.0 $R_\oplus$– even at a period of 20 days, although the transit probability is much less likely, we would still detect a planet this size with 70% certainty. We can therefore

rule out transiting planets at periods less than 8.5 days with masses greater than 2.3 $M_\oplus$ assuming a pure ice composition, 9.6 $M_\oplus$ assuming a pure rock composition. Although a pure iron planet with a radius of 2.0 $R_\oplus$ would have a mass of 63.5 $M_\oplus$ (Fortney et al. 2007), this composition is perhaps unrealistic, even assuming a formation history with mantle-stripping collisions (Marcus et al. 2010). The maximum mass of a 2.0 $R_\oplus$ planet, using the relations derived by Marcus et al. (2010) for maximum collisional stripping, would be closer to 20 $M_\oplus$. Planets with periods less than 7 days have been ruled out in the GJ 436 system by radial velocity constraints down to about 8 $M_\oplus$ with 3σ confidence (Bean & Seifahrt 2008). Our limits on the presence of pure rock planets are therefore complementary with previous, stronger constraints.

We find that the EPOCh dynamical constraints on additional planets with periods from 0.5 to 9 days rule out coplanar secular perturbers as small as 10 $M_\oplus$ and non-coplanar secular perturbers as small as 1 $M_\oplus$, as shown in Figure 2.6. These dynamical constraints are not as strong as current radial velocity constraints, except in orbits very close to that of GJ 436b. However, we anticipate that dynamical analyses similar to those presented in this work will prove useful to the community in cases of planets with masses below current radial velocity detectability, such as those that *Kepler* will find.

2.4.4 Eccentricity of GJ 436b

The eccentricity of GJ 436b has been attributed to two possible mechanisms. First, the residual eccentricity can be attributed to excitation from the dynamical interactions of GJ 436b with an as-yet undetected additional planet. Bean & Seifahrt (2008) tested this second hypothesis by finding how well the radial velocity data could be improved by adding perturbers to the system and evolving the system forward by numerically integrating the Newtonian equations of motion. Their analysis ruled out perturbers greater than 8 $M_{\oplus}$ at periods less than about 11 days (semi-major axes less than 0.075 AU) with high confidence. They presented radial velocity solutions that improved the fit by up to 4σ at smaller masses with periods between 4 and 11 days. We rule out rocky transiting bodies down to 9.6 $M_{\oplus}$ with periods less than 8.5 days with 95% confidence in the GJ 436 system. However, this doesn't preclude the possibility of an additional planet at these periods which does not transit. Batygin et al. (2009) compiled a list of possible dynamically stable secular perturbers which are consistent with the transit times, radial velocities, and observed eccentricity of GJ 436b. These proposed additional planets all have periods greater than 16 days, however. *EPOXI* would be sensitive to a transiting planet larger than 2.0 $R_{\oplus}$ with close to 80% probability at 15 days (see Figure 2.4).

The second possible explanation for the eccentricity of GJ 436b is a tidal Q parameter that is much larger than that of the ice giants in our solar system (thereby increasing the circularization time to greater than the age of the

system)—such a Q would need to be 1–2 orders of magnitude larger than that measured for Neptune (Batygin et al. 2009; Banfield & Murray 1992). However, the tidal Q for Jupiter may be as high as 2×10^6 with the assumption that Jupiter and Io are orbiting in a steady-state configuration; and may be even higher if that assumption is false (and tides on Io are currently dominant) (Jackson et al. 2008b). In fact, Ogilvie & Lin (2004) find that hot Jupiters may typically have Q values near 5×10^6, so a value of $10^{6.3}$ for GJ 436b for Q/k_2, proposed by Jackson et al. (2008b), may not be unreasonable (the Love number k_2 is typically near 0.5 for Solar System gas giants; Bursa 1992). However, Batygin et al. (2009) suggest that the actual Q for GJ 436b must be higher still.

A definitive explanation for the eccentricity of GJ 436b is so far undetermined, but a resolution to this question is observationally tractable. Batygin et al. (2009) provide a thorough discussion of follow-up observations that could measure the signal of a secular perturber to GJ 436b: radial velocity measurements are sensitive enough at their current level to resolve the periodogram signature of such a perturber, and a long baseline of transit times at the level of $\Delta t < 10$ s could also confirm its presence (Batygin et al. 2009). If these methods find no signal corresponding to a perturbing body, then the tidal Q of GJ 436b may indeed be much higher than those for the ice giants in our solar system. The explanation proposed by Jackson et al. (2008b) may alternatively be correct– the Q values for solar system giant planets are current underestimations of the true Q value for these planets, in which case the tidal Q necessary to explain GJ 436b may not be inconsistent with that of Neptune.

2.5 Acknowledgments

We are extremely grateful to the *EPOXI* Flight and Spacecraft Teams that made these difficult observations possible. At the Jet Propulsion Laboratory, the Flight Team has included M. Abrahamson, B. Abu-Ata, A.-R. Behrozi, S. Bhaskaran, W. Blume, M. Carmichael, S. Collins, J. Diehl, T. Duxbury, K. Ellers, J. Fleener, K. Fong, A. Hewitt, D. Isla, J. Jai, B. Kennedy, K. Klassen, G. LaBorde, T. Larson, Y. Lee, T. Lungu, N. Mainland, E. Martinez, L. Montanez, P. Morgan, R. Mukai, A. Nakata, J. Neelon, W. Owen, J. Pinner, G. Razo Jr., R. Rieber, K. Rockwell, A. Romero, B. Semenov, R. Sharrow, B. Smith, R. Smith, L. Su, P. Tay, J. Taylor, R. Torres, B. Toyoshima, H. Uffelman, G. Vernon, T. Wahl, V. Wang, S. Waydo, R. Wing, S. Wissler, G. Yang, K. Yetter, and S. Zadourian. At Ball Aerospace, the Spacecraft Systems Team has included L. Andreozzi, T. Bank, T. Golden, H. Hallowell, M. Huisjen, R. Lapthorne, T. Quigley, T. Ryan, C. Schira, E. Sholes, J. Valdez, and A. Walsh.

Support for this work was provided by the *EPOXI* Project of the National Aeronautics and Space Administration's Discovery Program via funding to the Goddard Space Flight Center, and to Harvard University via Co-operative Agreement NNX08AB64A, and to the Smithsonian Astrophysical Observatory via Co-operative Agreement NNX08AD05A.

DF gratefully acknowledges support from the Michelson Fellowship, supported by the National Aeronautics and Space Administration and administered by the Michelson Science Center.

Chapter 3

Search for a Sub-Earth-Sized Companion to GJ 436 and a Novel Method to Calibrate Warm *Spitzer* IRAC Observations

S. Ballard, D. Charbonneau, D. Deming, H. A. Knutson, J. L. Christiansen, M. J. Holman, D. Fabrycky, S. Seager, & M. F. A'Hearn *Publications of the Astronomical Society of the Pacific*, Vol. 122, pp. 1341-1352, 2010

Abstract

We discovered evidence for a possible additional 0.75 $R_\oplus$ transiting planet in the NASA *EPOXI* observations of the known M dwarf exoplanetary system GJ 436. Based on an ephemeris determined from the *EPOXI* data, we predicted a transit event in an extant *Spitzer Space Telescope* 8 μm data set of this star. Our subsequent analysis of those *Spitzer* data confirmed the signal of the predicted depth and at the predicted time, but we found that the transit depth was dependent on the aperture used to perform the photometry. Based on these suggestive findings, we gathered new Warm Spitzer Observations of GJ 436 at 4.5 μm spanning a time of transit predicted from the *EPOXI* and *Spitzer* 8 μm candidate events. The 4.5 μm data permit us to rule out a transit at high confidence, and we conclude that the earlier candidate transit signals resulted from correlated noise in the *EPOXI* and *Spitzer* 8 μm observations. In the course of this investigation, we developed a novel method for correcting the intrapixel sensitivity variations of the 3.6 and 4.5 μm channels of the Infrared Array Camera (IRAC) instrument. We demonstrate the sensitivity of Warm *Spitzer* observations of M dwarfs to confirm sub-Earth sized planets. Our analysis will inform similar work that will be undertaken to use Warm *Spitzer* observations to confirm rocky planets discovered by the *Kepler* mission.

3.1 Introduction

With the recent discoveries of the transiting super Earths CoRoT-7b (Léger et al. 2009) and GJ 1214b (Charbonneau et al. 2009), and the launch of the *Kepler* Mission (Borucki et al. 2010), astronomers have begun to probe the regime of super-Earth exoplanets. CoRoT-7b, with a radius of 1.7 $R_\oplus$ in an orbit around a 0.87 $R_\odot$ star, produces a photometric signal of only 340 ppm (Léger et al. 2009). The radial velocity confirmation of CoRoT-7b required 70 hours of follow-up observations with the HARPS instrument (Queloz et al. 2009). A complementary approach is to use Warm *Spitzer* observations to prove that the transit depth is not color dependent (Fressin et al. 2010). Similar follow-up observations using Warm *Spitzer* to confirm candidates identified by *Kepler* are already being gathered as part of an Exploration Science Program (D. Charbonneau). In this work, we present a search for a 0.75 $R_\oplus$ transiting planet around the M dwarf GJ 436, which is already known to host the transiting hot Neptune GJ 436b in an eccentric orbit (Butler et al. 2004; Maness et al. 2007; Gillon et al. 2007b; Deming et al. 2007; Demory et al. 2007).

EPOXI is a NASA Discovery Program Mission of Opportunity using the Deep Impact flyby spacecraft (Blume 2005), comprising the Extrasolar Planet Observation and Characterization (EPOCh) investigation and the Deep Impact eXtended Investigation (DIXI). From January through August 2008, the EPOCh Science Investigation used the HRI camera (Hampton et al. 2005) with its broad visible bandpass to gather precise, rapid cadence photometric time series of known

transiting exoplanet systems (Ballard et al. 2010b; Christiansen et al. 2010). The majority of these targets were each observed nearly continuously for several weeks at a time.

One of the *EPOXI* science goals was a search for additional planets in these systems. Such planets would be revealed either through the variations they induce on the transit times of the known exoplanet, or directly through the transit of the second planet itself. This search is especially interesting in the case of the GJ 436 system. The eccentricity of the known transiting Neptune-mass planet, GJ 436b (Butler et al. 2004), may indicate the presence of an additional perturbing planet, since the assumed circularization timescale for the known planet is much less than the age of the system (Maness et al. 2007; Deming et al. 2007; Demory et al. 2007). Ribas et al. (2008) claimed evidence for a 5 $M_{\oplus}$ super-Earth in radial velocity observations of GJ 436, but this proposed planet was ruled out by subsequent investigations (Alonso et al. 2008; Bean & Seifahrt 2008). The absence of this additional perturbing body in the GJ 436 system would also be very scientifically interesting. If no other body is present to explain the eccentricity of GJ 436b, the observed eccentricity requires a very high tidal dissipation parameter, Q.

We presented our search for additional transiting planets in the *EPOXI* observations of GJ 436 in Ballard et al. (2010b). We demonstrated the sensitivity to detect additional transiting planets as small as 1.5 $R_{\oplus}$ interior to GJ 436b. We further uncovered evidence for a 0.75 $R_{\oplus}$ transiting planet, in a orbit close to a 4:5 resonance with GJ 436b, below the formal detection limit established by Ballard et al. (2010b). We first analyzed an extant 8 μm *Spitzer Space Telescope*

phase curve of GJ 436, obtained two months after the *EPOXI* observations as part of *Spitzer* Program 50056 (PI: H. Knutson). We then gathered Warm *Spitzer* 4.5 μm observations of GJ 436, which enabled us to conclusively test the planet hypothesis. We found that the current state-of-the-art reduction techniques to remove the intrapixel sensitivity variations associated with the Infrared Array Camera (IRAC) instrument (Reach et al. 2005; Charbonneau et al. 2005; Knutson et al. 2008, 2009b) were insufficient to remove correlated noise at an amplitude comparable to the depth of the putative transit. We therefore pursued a novel technique for the removal of this intrapixel sensitivity variation. When compared to the earlier method, our technique identifies and corrects for high frequency intrapixel sensitivity features which were previously missed. Our novel method enhances the sensitivity of Warm *Spitzer* observations to transits of sub-Earth sized planets.

The remainder of this paper is organized as follows. In Section 2, we describe the observations and the photometry time series extraction for the *EPOXI* and *Spitzer* data sets. Section 2.3 describes the novel technique used to reduce the 4.5 μm observations. In Section 3, we consider the evidence for the planet hypothesis in the three data sets and we demonstrate the sensitivity of the Warm *Spitzer* 4.5 μm observations of GJ 436 to detect a 0.75 $R_{\oplus}$ planet. In Section 4, we discuss the applications of this work for future transit searches, including those to confirm candidate rocky planets from the *Kepler* mission.

3.2 Observations and Time Series Extraction

3.2.1 *EPOXI* Observations

We acquired observations of GJ 436 nearly continuously during 2008 May 5—29, interrupted for several hours at approximately 2-day intervals for data downloads. A complete description of the *EPOXI* photometric extraction pipeline is given in Ballard et al. (2010b) and summarized here. We used the existing Deep Impact data reduction pipeline to perform bias and dark subtractions, as well as preliminary flat fielding (Klaasen et al. 2005). We first determined the position of the star on the CCD using PSF fitting, by maximizing the goodness-of-fit (with the χ^2 statistic as an estimator) between an image and a model PSF (oversampled by a factor of 100) with variable position, additive sky background, and multiplicative brightness scale factor. We then processed the images to remove sources of systematic error due to the CCD readout electronics. We first scaled down the two central rows by a constant value, then we scaled down the central columns by a separate constant value, and finally we scaled the entire image by a multiplicative factor determined by the size of the sub-array. We performed aperture photometry on the corrected images, using an aperture radius of 10 pixels, corresponding to twice the HWHM of the PSF. To remove remaining correlated noise due to the interpixel sensitivity variations on the CCD, we fit a 2D spline surface, with the same resolution as the CCD, to the brightness variations on the array as follows. We randomly drew a subset of several thousand out-of-transit and out-of-eclipse points from the light curve (from a data set of

$\sim$29,988 points) and found a robust mean of the brightness of the 30 nearest neighbors for each. We fit a spline surface to these samples and corrected each data point individually by linearly interpolating on this best-fit surface. We used only a small fraction of the observations to create the spline surface in order to minimize the potential transit signal suppression introduced by flat fielding the data with itself. To produce the final time series, we iterated the above steps, fitting for the row and column multiplicative factors, the sub-array size scaling factor, and the 2D spline surface that minimized the out-of-transit white noise of the photometric time series. We included one additional step to create the final 2D spline, which was to iteratively remove an overall modulation from the GJ 436 light curve which we attributed to star spots. After we took these steps to address the systematics associated with the observations, the red noise was largely removed. Figure 3.1 shows the GJ 436 time series before and after the 2D spline correction. After the correction is applied, the precision of the light curve is 56% above the photon limit. We note that the version of the *EPOXI* GJ 436 light curve presented in Ballard et al. (2010b) is very slightly different from the version used in this analysis. Because of the possibility of suppression of additional transits by the 2D spline correction method, we produced a version of the light curve which masked the points that occurred during transit times of the putative GJ 436c from contributing to the CCD sensitivity map. This set of additional masked points is 16 hours total in duration over the entire data set, consisting of 2 hours intervals centered at each of 10 candidate transit events– two of which partially coincide with transits of GJ 436b and were already masked

from the 2D spline correction.

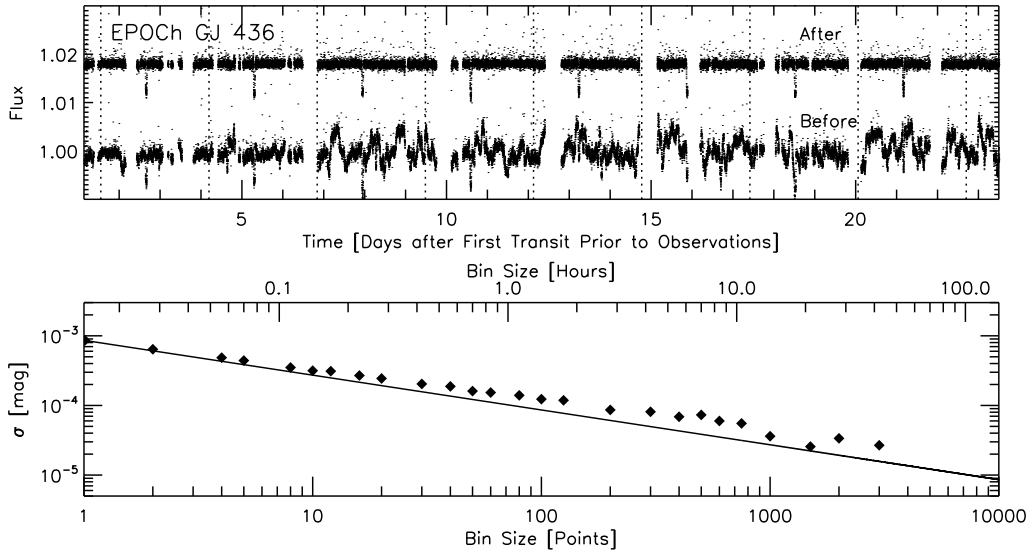

Figure 3.1.—: *Top panel:* GJ 436 time series before (lower curve) and after (upper curve) 2D spline correction. The uncorrected time series (lower curve) has had the two middle rows and columns in each image, and the entire image if observed in the large sub-array mode, scaled by a multiplicative factor to reduce the flux dependence on position and sub-array size. We have used the 2D spline to correct for additional interpixel variation in the upper curve. *Bottom panel:* The data (diamond symbols) bin down consistently with the expectation for Gaussian noise (shown with a line, normalized to match the value at N=1).

3.2.2 Cold *Spitzer* 8 μm Observations

Under *Spitzer* GO Program 50056 (PI: H. Knutson), GJ 436 was monitored for 70 hours continuously from 2008 July 12—15 by the *Spitzer Space Telescope* (Werner

et al. 2004) with the IRAC subarray (Fazio et al. 2004) in the 8 μm channel, to obtain a full phase curve of the hot Neptune GJ 436b. This observing sequence consisted of 0.4 s integration exposures in 9195 blocks of 64 images each. These data were preflashed using the same technique as the HD 149026 observations (described in Knutson et al. 2009b). Preflashing effectively removes most of the "detector ramp" effect, which is characterized by an initial upward asymptote in the measured flux, followed by a gradual downward slope (Charbonneau et al. 2008; Knutson et al. 2008, 2009a). In this case we observed a region in M17 centered at RA $18^{\rm h}20^{\rm m}28^{\rm s}$ and Dec -16°12'20" with fluxes ranging between 3500-8000 MJy/Sr for 30 minutes prior to the start of the observations. This significantly reduced the amplitude of the detector ramp in these data, although there is still a small rise in flux of approximately 0.05% visible in the first five hours of observations. The data after this point have a flux variation of less than 0.05% over the remaining 65 hours. The photometric extraction was performed by a similar method to the one described in detail in Knutson et al. (2009b), which we summarize here. We determined the position of the star on the array by centroid, taking a position-weighted sum of the flux within a circular aperture with a radius of 5 pixels. We find that using this aperture size for the position determination returned the photometric lowest rms in the resulting time series. To perform background subtraction, we first created a median image from all the observations and identified four regions in the corners of the array where the light from the point spread function (PSF) was minimized, in order to minimize contamination by diffraction spikes in our background estimates. We created a

histogram of the values of these pixels, and calculated the background from the mean of this distribution. We then performed aperture photometry with apertures ranging from 2.5 pixels in radius to 7.0 pixels in radius (the radius used for the aperture photometry affects the significance of the putative additional transit, which is explained in Section 3.2). We discarded points which lie more than 3σ from the median value within each set of 64 images (in order to remove images affected by transient hot pixels). For the purposes of addressing the additional planet hypothesis, we were concerned with only a 5 hour portion of the light curve that fell in the latter half of the 70 hour phase curve, where we no longer observe any evidence for a detector ramp. Nonetheless, we fit and divided a quadratic function in time during the window of interest in order to remove any remaining trends in the data, which could be due to spots on the star, position-dependent aperture losses, and the phase variation from the planet itself.

3.2.3 Warm *Spitzer* 4.5 μm Observations

We observed GJ 436 in subarray mode, using a 0.1 s integration time in the 4.5 μm channel. These observations span 18 hours over UT 28 Jan 2010—29 Jan 2010. The observing sequence consisted of 7640 blocks of 64 images each. We experimented with two methods of locating the position of the star on the array. We first found a flux-weighted sum of the position within a circular aperture with a radius of 3 pixels. We also experimented with determining the position of the star by fitting a PSF within a 3.5 pixel aperture (we found similar results with larger apertures). Using the 100–times–oversampled PSF provided by the

Spitzer Science Center for the 4.5 μm channel, we performed a χ^2 minimization in which we allowed the X and Y positions of the PSF, a multiplicative brightness factor, and an additive sky background value to vary. We compared a histogram of the positions to get a sense for the precision of each measurement technique, first subtracting a running median calculated individually for each point from the nearest 20 points in time (to account for positional drift). We determined that these histograms had similar width with the two methods: 6.0×10^{-3} pixels in Y with PSF-fitting versus 6.4×10^{-3} pixels in Y with centroid. However, the precision of the final time series was not improved by using the PSF-fitting measured positions; rather, the precision was degraded by 20%. We attribute this degradation to the decreased positional precision of the PSF positions: although their bulk scatter is less than the scatter from centroiding, the precision with which we measure an individual position is set by the resolution of the PSF at 0.01 pixels, rather than the 1σ error from the scatter in the centroided positions of 6.4×10^{-3} pixels. We considered the possibility of improving our positional accuracy by producing a more highly oversampled PSF with an interpolation of the *Spitzer* Science Center PSF, but found the computing time of PSF-fitting with such a large PSF to be prohibitively expensive.

We then measured the stellar brightness in each image by performing aperture photometry on the Basic Calibrated Data (BCD) products across a range of apertures from 2.1 to 6 pixels. We calculate the sky background, which is almost negligable, from a 3σ-clipped mean of the pixels inside a ring of width 10 pixels from a radius of 7 pixels to 17 pixels. We found that the precision of the

final time series was optimized at an aperture of 2.1 pixels in radius.

We then corrected for the well-known intrapixel sensitivity variation observed in IRAC Channels 1 and 2 (Reach et al. 2005; Charbonneau et al. 2005; Knutson et al. 2008, 2009b). In lieu of fitting a polynomial in X and Y to the brightness variations, we instead implemented a point-by-point correction. We first binned the light curve into 20 second bins (approximately 145 points/bin). For each binned point, we evaluate a weighted sensivity function using all unbinned points (excluding those points which occurred inside the bin in question and outliers more than 3σ from the mean of nearby points) given by:

$$W(x_i, y_i) = \frac{\sum_{j \neq i} exp\left(-\frac{(x_j - x_i)^2}{2\sigma_x^2}\right) exp\left(-\frac{(y_j - y_i)^2}{2\sigma_y^2}\right) \cdot f_j \cdot S(t_j)}{\sum_{j \neq i} exp\left(-\frac{(x_j - x_i)^2}{2\sigma_x^2}\right) exp\left(-\frac{(y_j - y_i)^2}{2\sigma_y^2}\right) \cdot S(t_j)}, \tag{3.1}$$

where f_j is the flux value of the jth observation, which is assigned a weight based on its distance in X and Y from the ith point being corrected. The function $S(t_j)$ is a boxcar function in time, which is 1 for all points which are permitted to contribute to the sensitivity map, and 0 for all points which are not. The position of this function defines a "mask" interval during which time observations do not contribute to the interpixel sensitivity map. The purpose of this mask is to exclude points that do not reflect an accurate representation of the pixel sensitivity, such as those during transit; if we were to include these points in the creation of the intrapixel sensitivity map, we would both suppress the transit and introduce additional correlated noise outside of transit. The sensitivity function

is then normalized by dividing by the Gaussian function multiplied by the boxcar $S(t_j)$. We find the best results using $\sigma_x = 0.017$ pixels and $\sigma_y = 0.0043$ pixels (the width of the Gaussian weighting function is much smaller in Y because the dependence of the flux on the Y position is much stronger). We then divide the ith binned flux value by $W(x_i, y_i)$ to remove the effects of intrapixel sensitivity. Using a point-by-point sensitivity function, we do not need to assume a functional form for the intrapixel sensitivity; however, there is the very important caveat that flat-fielding the data by itself has the effect of suppressing the depths of additional transits, if they are present. We discuss how we avoid this effect in Section 3.3 with the use of the mask function. We show in Figure 3.2 three dimensional views of the intrapixel sensitivity map given by the weighting function $W(x_i, y_i)$. The large scale features of $W(x_i, y_i)$ are well approximated by polynomials in X and Y, per previous techniques, but we also find a smaller scale "corrugation" effect in the Y direction, where the sensitivity exhibits low-level sinusoidal-like variations with a separation of approximately 5/100ths of a pixel between peaks.

We investigated the authenticity of these features using several tests. For Gaussian noise, we expect the weighting function to exhibit only smoothed random noise, with features equal in size to the smoothing kernel, and so the corrugation features in Y should have a size scale near 9/1000ths of a pixel (because σ_y is 0.0043 pixels). Futhermore, we should be able to predict the χ^2 improvement by comparing the data to $W(x_i, y_i)$ as opposed to the null hypothesis. A Gaussian time series will be better fit by a smoothed version of itself than a flat line. The χ^2 should improve by the number of smoothing kernels

Figure 3.2.—: (Following page) *Top panels:* At left, a three-dimensional view of the intrapixel sensitivity of the IRAC detector at 4.5 μm ($W(x_i, y_i)$, as computed in Equation 3.1). At right, the best fit third degree polynomial fit in X and Y. In both plots, The X axis shows the X position in pixels, the Y axis shows the Y position in pixels, and the Z axis show the fractional sensitivity. The jagged edges of the map are due to the low density of coverage in those areas; the star spent most of the time in the central region. *Bottom panels:* At left, the residuals after the best-fit 2D polynomial is divided from the weighting function $W(x_i, y_i)$. With large scale variations divided out, additional higher-frequency features are also visible. At right, a contour map of the same residuals.

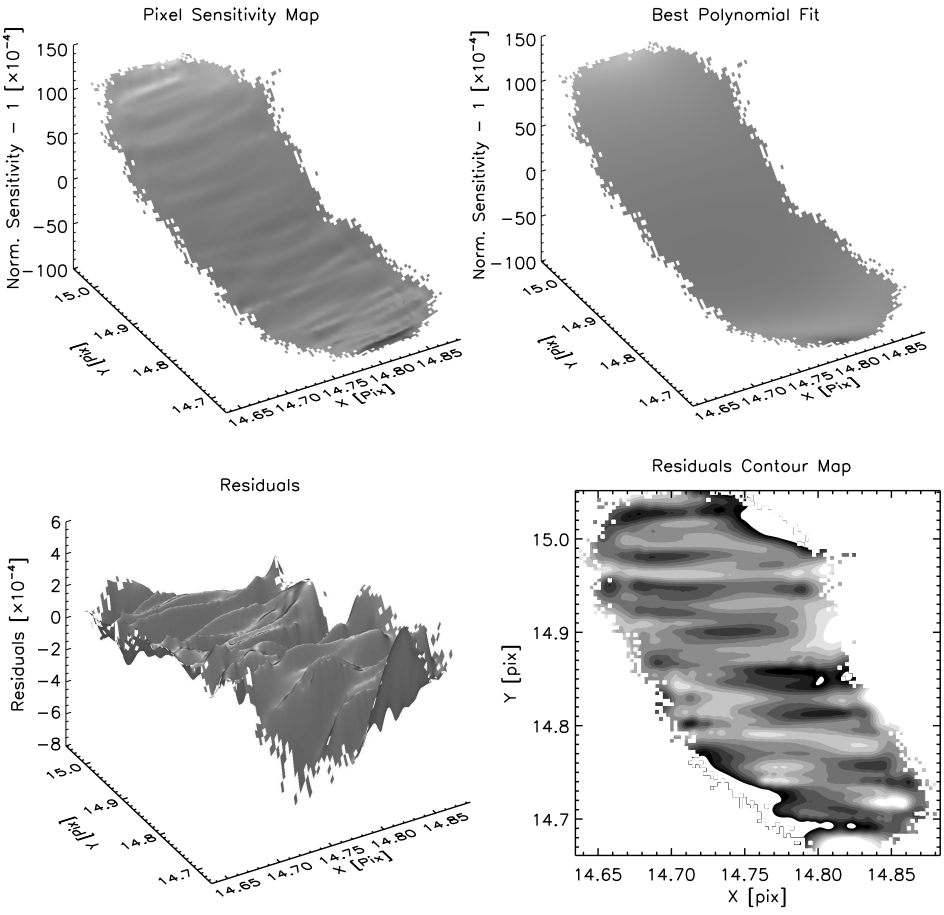

Figure 3.2.—: (Continued).

contained in the interval in question: for a time series with N_y values ranging over 0.25 of a pixel, and a smoothing kernel of σ_y=0.0043, then the number of smoothing kernels (defining 3σ from the center as the extent of the kernel) contained in the interval is approximately 10, and we should expect the χ^2 of the fake time series to improve by 10 when compared to the weighting function instead of a flat line. Conversely, in order for authentic features attributable to the intrapixel sensitivity to be believable, the features must be significantly larger than the smoothing kernel, and the weighting function must provide a much better fit to the data than predicted from a smoothed version of the data itself. To test this hypothesis, we created a random Gaussian data set sampled at the same X and Y positions on the detector, with a standard deviation equal to that of the actual time series. We then created a sensitivity function using the same kernel in X and Y as for the actual observations, and compared the results; this comparison is shown in Figure 3.3.

We find that the weighting function from the random data set looks as we expected it to look, with corrugation features near the size of the FWHM of the smoothing kernel. The improvement in χ^2, using a flat line with value 0 as compared to the binned weighting function, is 11.4 for the fake data set, very close to the predicted improvement of 10. For comparison, the improvement in χ^2 for the real data, between a flat line and the weighting function, is 24.3, and the amplitude of the features are larger. Furthermore, the peak-to-peak size scale of features is 0.05 pixels, more than 6 times the FWHM of the smoothing kernel, which argues against their being smoothing artifacts. The difference in

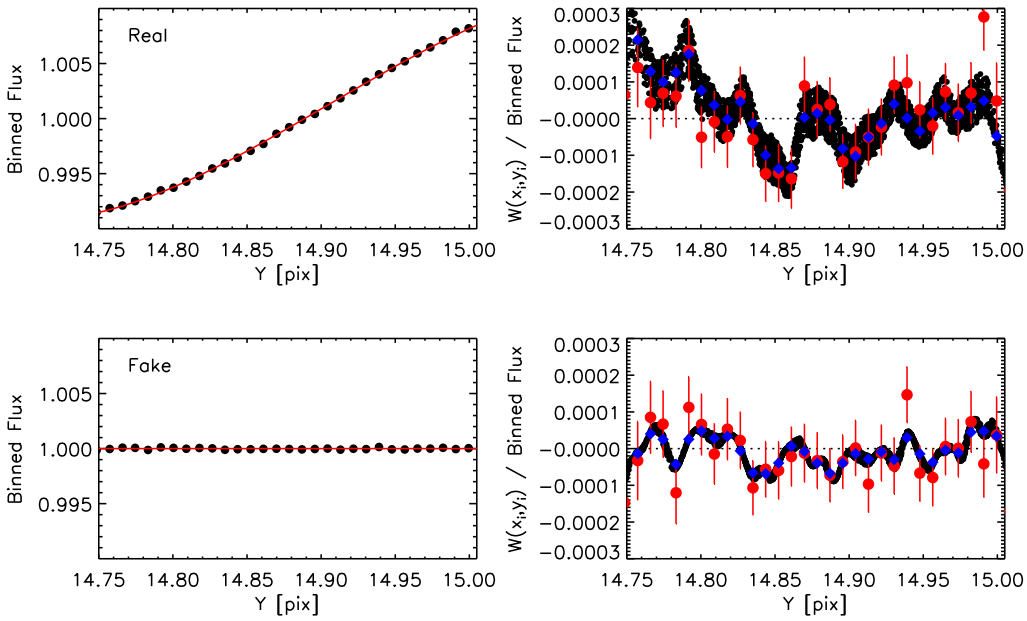

Figure 3.3.—: *Top panels:* At left, cross section of the flux as a function of Y position, holding X constant at 14.759 pixels (black points shown flux within 0.02 pixels of this X position, binned at 0.001 pixel intervals in Y; error bars are contained within the plotting symbol). Overplotted in red is the best-fit third degree polynomial. At right, the red points show the binned flux after the best-fit third degree polynomial is divided out. The black points overplotted shown the weighting function with best-fit third degree polynomial removed, and the blue points show the weighting function binned at the same intervals as the flux. *Bottom panels:* At left, cross section of fake Gaussian data set over the same Y range– no underlying structure is present. At right, the binned flux is shown in red, the weighting function is shown in black, and the binned weighting function is shown in blue.

width of the weighting function between the real and fake data sets (the thickness of the black points in the vertical direction) can be attributed to the weak X dependence of the pixel sensitivity. In the lowest right hand panel of Figure 3.2, there is evidence for pixel sensitivity variation in the X direction over a size scale comparable to the width of the 0.04 pixel cross section used to generate Figure 3.3. For these reasons, we are confident that the high-frequency features, with a period of 0.05 pixels, in the real weighting function are authentic. The amplitude of this effect is 100 ppm, 40% of the amplitude of a 0.75 $R_{\oplus}$ transit in front of a 0.438 $R_{\odot}$ star such as GJ 436 (Ballard et al. 2010b). Therefore, removing this correlation with position was crucial to our ability to rule out the putative transit of depth 250 ppm.

With this photometric reduction procedure, we achieve a precision of 0.0053 per 0.1 s exposure on the unbinned time series. Compared to the photon noise-limited precision of 0.0042, we are 26% above the photon noise limit, although the presence of remaining correlated noise means that the scatter with larger bin sizes deviates more from the ideal Gaussian limit. We achieve a sensitivity of 71 ppm per 20-minute bin, compared to the shot-noise limit of 41 ppm at that bin size.

For comparison, we also perform a reduction using a polynomial fit in X and Y to remove the intrapixel sensitivity variations in flux (Reach et al. 2005; Charbonneau et al. 2005; Knutson et al. 2008, 2009b). We express the measured flux f' in terms of the incident flux f and the X and Y position of the star on the detector with the following expression:

$$f' = f\left(b_1 + b_2(x-\bar{x}) + b_3(x-\bar{x})^2 + b_4(y-\bar{y}) + b_5(y-\bar{y})^2) + b_6(y-\bar{y})^3)\right) \quad (3.2)$$

We find that the precision we achieve using a polynomial intrapixel sensitivity function, for the same bin size of 20 minutes, is 230 ppm, as compared to a precision of 71 ppm using the weighted sensitivity map $W(x_i, y_i)$. If we divide the time series into 3 portions of 5 hours duration, and fit separate polynomial coefficients for each portion, we achieve a precision of 91 ppm for a bin size of 20 minutes– still 1.3 times times larger than the precision using $W(x_i, y_i)$. However, although we can improve the overall precision of the time series by fitting the polynomial coefficients independently for increasingly short durations, we are never able to reliably recover transits of a 0.75 $R_\oplus$ planet in a time series reduced with a polynomial sensitivity function. We discuss this analysis in Section 3.3.

3.3 Search for Photometric Evidence

3.3.1 The Suggestion from *EPOXI*

In Ballard et al. (2010b), we conducted a search for additional transiting planets in the *EPOXI* light curve of GJ 436. In that work, we demonstrate our sensitivity to additional transits by injecting light curves corresponding to additional planets with varying planetary radius, period, and phase, and then attempting to recover them by maximizing the χ^2 goodness of fit. We found, when we carefully accounted for the signal suppression introduced by reducing the data with the 2D

spatial spline method, we were sensitive to Earth-sized planets with good ($\geq$50%) probability for periods less than only 0.5 days. However, we discovered weak evidence for an additional transiting planet, which fell well below the criterion we established for a detection. In Ballard et al. (2010b), we empirically established the criterion for detection that used the improvement of χ^2 corresponding to the best fit transit signal compared to the χ^2 of the null hypothesis: we could reliably recover the correct period of any signal which produced an improvement of $\Delta\chi^2$ $\geq$250. The transit signal corresponding to a 0.75 $R_\oplus$ size planet is well below this threshold. However, we find that the largest deviations occurred with a regular period near the 4:5 resonance with the Neptune-sized planet. Five of these events produced a combined improvement to the χ^2 of 140. However, these 5 comprise only half of the transits we would expect to see with this ephemeris: Of these remaining 5 events, two coincide with transits of GJ 436b, one occurs during a gap in the phase coverage, and two show no evidence of a transit. If we include all predicted candidate transit events in our χ^2 calculation (including the two events that coincide with a transit of GJ 436b), the null hypothesis gives a better solution than any transit model. However, if points that coincide closely in time with transits of the GJ 436b are excluded from the calculation, the improvement over the null χ^2 is 70. There are two motivations to exclude these in-transit points: First, we fit a slope with time to the points immediately outside of the transit of GJ 436b (from 3 minutes to 30 minutes before the start of transit and after the end of transit) and divide this slope in order to normalize each transit before we fit for the system parameters (see Ballard et al. 2010b),

and this procedure may suppress other signals. Second, there is also the small possibility of an occultation of GJ 436c by GJ 436b.

We observed comparable $\Delta\chi^2$ improvement (within 2σ) for periods ranging between 2.1074 days (0.797 the period of GJ 436b) and 2.1145 days (0.800 the period of GJ 436b). Figure 3.4 shows the 10 events separately. We also plot a transit model corresponding to a planet with radius 0.75 $R_\oplus$ and period 2.1076 days (this period was selected by combining the *EPOXI* and *Spitzer* 8 μm observations described in the next section).

3.3.2 Corroboration by *Spitzer* at 8 μm

The constraints on the ephemeris of the putative GJ 436c from the *EPOXI* data alone meant that the accuracy with which we could predict the times of transits 1.5 years out from the *EPOXI* observations was poor. However, the extant *Spitzer* 8 μm phase curve was gathered only two months after the *EPOXI* observations took place, such that our accuracy on the predicted time was 5 hours (defined by the duration of the 2σ confidence interval from *EPOXI*). We performed a boxcar search of this light curve, allowing both the time of transit and the depth of transit to vary, since the *EPOXI* observations provided only weak constraints on the planetary radius. We discovered a transit-like signal in these data within the time window predicted from *EPOXI*, but the signal was present (that is, produced a $\Delta\chi^2$ improvement larger than any other feature during the time window of interest) only when apertures smaller than 4 pixels in radius were used to perform

Figure 3.4.—: (Following page) *Top panel: EPOXI* time series of GJ 436, after dividing out model of transits of GJ 436b, during times of transit of the putative GJ 436c discussed in text. The significance of the light curve shown overplotted is far below the criterion of a confident detection (Ballard et al. 2010b). Model light curves (Mandel & Agol 2002) with the predicted transit depth and ephemeris are shown overplotted with the solid black line; the events with positive transit depth are labeled Events 3, 7, 8, 9, and 10. A gap in the phase coverage occurs during predicted Event 4, Events 2 and 5 show negatives deviations (an increase in brightness, as opposed to a decrement), and Events 1 and 6 overlap in time with transits of GJ 436b. *Bottom panel:* All events except those that overlap in time with a GJ 436b transit (labeled 1 and 6 above), binned in 10 minute intervals.

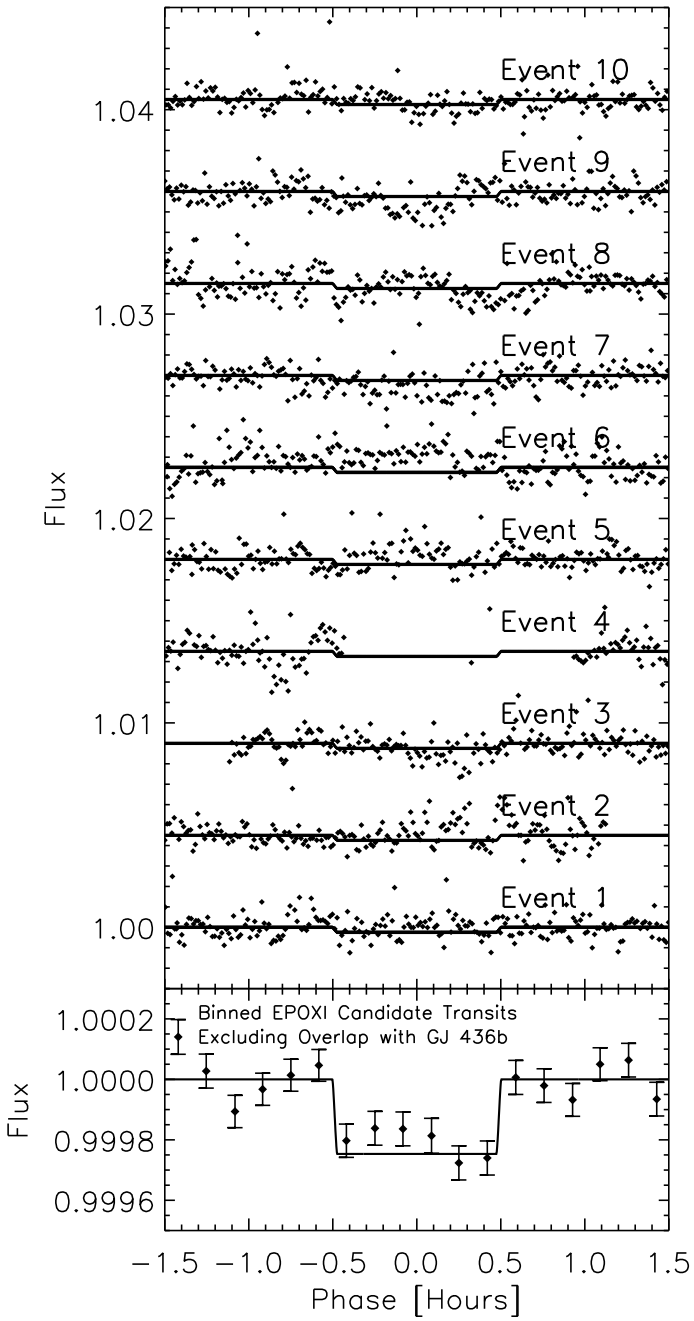

Figure 3.4.—: (Continued).

the photometry. The top panel of Figure 3.5 shows a portion of the 8 μm light curve, with 3.5 pixel aperture used to extract the photometry. The solid black curve shows the best-fit transit light curve solution, and the event at a time of BJD 2454660.4 is the secondary eclipse of the hot Neptune GJ 436b. The second panel shows the significance of the best χ^2 as a function of time. The bottom two panels show the results using a 7.0 pixel aperture to extract the photometry. While the significance of the secondary eclipse remains constant, the significance of the putative additional transit depends on aperture size.

The dependence of the putative transit signal on the size of the aperture argued against the planet hypothesis: rather, a signal that disappears at larger radii is more likely due to position-dependent flux losses. We concluded that the *Spitzer* 8 μm observations neither definitely confirmed nor refuted the planet hypothesis, so we gathered additional *Spitzer* observations at 4.5 μm, where we could obtain a higher precision light curve, to definitely resolve the question. The single candidate transit from *Spitzer* greatly decreased the possible parameter space of the planet's ephemeris, so that we were able to predict a transit to occur 1.5 years after the *EPOXI* observations within an 15 hour window. We also predicted the radius of the putative planet, from a χ^2 minimization of the combined *EPOXI* and *Spitzer* 8 μm observations, to be 0.75 $R_\oplus$.

Figure 3.5.—: (Following page) *Top two panels:* Portion of *Spitzer* 8 μm phase, photometry performed with aperture radius of 3.5 pixels, with solid line denoting the putative transit time predicted from *EPOXI* and the dashed lines indicating the 2σ confidence interval. The best-fit transit light curve solution is shown overplotted in red, with a depth of 1 $R_{\oplus}$ at this aperture, and the secondary eclipse of GJ 436b is evident at a time 17.5 hours after the candidate transit. The second panel shows the improvement of the best-fit transit light curve solution χ^2 at each time compared to the null χ^2. *Bottom two panels:* The same portion of the 8 μm phase curve, with an aperture radius of 7.0 pixels. The last panel shows the improvement of the best-fit transit light curve solution as compared to the null.

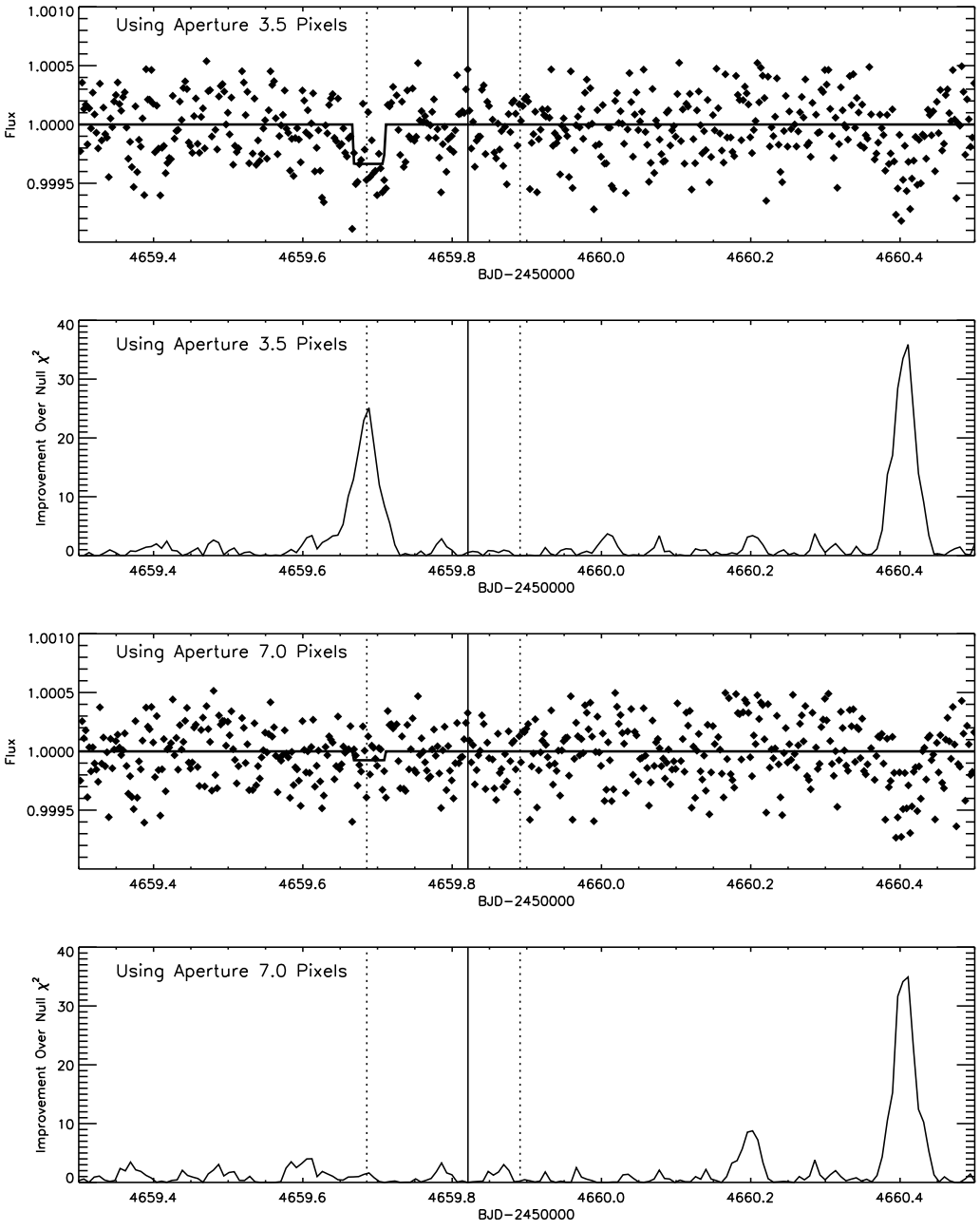

Figure 3.5.—: (Continued).

3.3.3 The Death Knell from *Spitzer* at 4.5 μm

The method we use to correct the 4.5 μm data has the possible effect of suppressing transit signals, since the point-by-point correction relies critically on the assumption that the flux variations are due *only* to the pixel sensitivity variations, and that the stellar flux is constant. If a transit occurs during the observations, then the derived value of the pixel sensitivity $W(x_i, y_i)$ in the location of the detector where the transiting points occur will be lower by a fraction that depends on the pixel sampling. If the points in transit comprise 10% of the observations in that location on the detector, then the value for the pixel sensitivity in that location will be low by 10%. This will have the effect of suppressing the transit depth by 10%, since we will incorrectly attribute a fraction of the decrement at that time to the pixel performance, rather than an astrophysical variation. Therefore, to correctly recover the true transit signal, we must iteratively identify and then mask the points which occur in transit. This presents a challenge since we do not know exactly when the transit should occur. We tested the procedure of simply masking points that occur within a transit duration of each point being corrected (so that the sensitivity function for each point is calculated using points more than half a transit duration removed in time), but found that this did not produce the highest quality time series. Although this masking procedure prevents suppression of the transit signal when the mask is corrected located over the transit, the transiting points are allowed to contribute to the sensitivity function at other times, which introduces correlated noise to the remainder of the time series. Although the depth of the transit

signal is preserved, its significance relative to other features in the time series is dimished, reducing our ability to correctly identify it. We therefore concluded that the correct procedure is to locate the position of the transit in time, and mask the set of transiting points for each individual flux correction. The challenge is to locate the true position of the transit in order to correctly place the mask. We addressed this question by producing n time series, where n is the number of tested mask positions (in this case, we tested mask positions in 30 minute intervals over a roughly 15 hour time series, resulting in 33 mask positions). We hypothesize that when the mask correctly coincides with a transit, both the depth of the transit and its significance relative to the next most significant feature in the time series should increase, thus enabling us to identify the time of transit.

In order to establish that we could reliably detect the 0.75 $R_{\oplus}$ radius planet, we injected a transit of this size into the *Spitzer* 4.5 μm observations. We attempted to blindly recover the injected transit time by varying the mask position (which was always one hour in duration) by 30 minute intervals, producing a separate time series for each mask position. Then, for each of these n time series, we evaluated the significance of a boxcar light curve function with the predicted transit depth and duration, allowing only the time of the transit to vary. We identified the time of transit from the time of most significant improvement to the χ^2 from the boxcar search among all the time series, which indeed occurred when the mask was correctly located over the injected transit. We then repeated this procedure, shifting the injected transit time in hour increments, to ensure that we could detect the transit at any time during the observations. Figure 3.6 shows

the 4.5 μm light curve, with 0.75 $R_\oplus$ transit signal injected at a location denoted by the solid line. The dashed lines mark the beginning and end of the window in time during which data are masked from the sensitivity function calculation. In this case, the significance of the detection, using the improvement over the null χ^2, increases by a factor of two when the mask is correctly located over the transit, which enabled us to blindly locate the time of the injected transit.

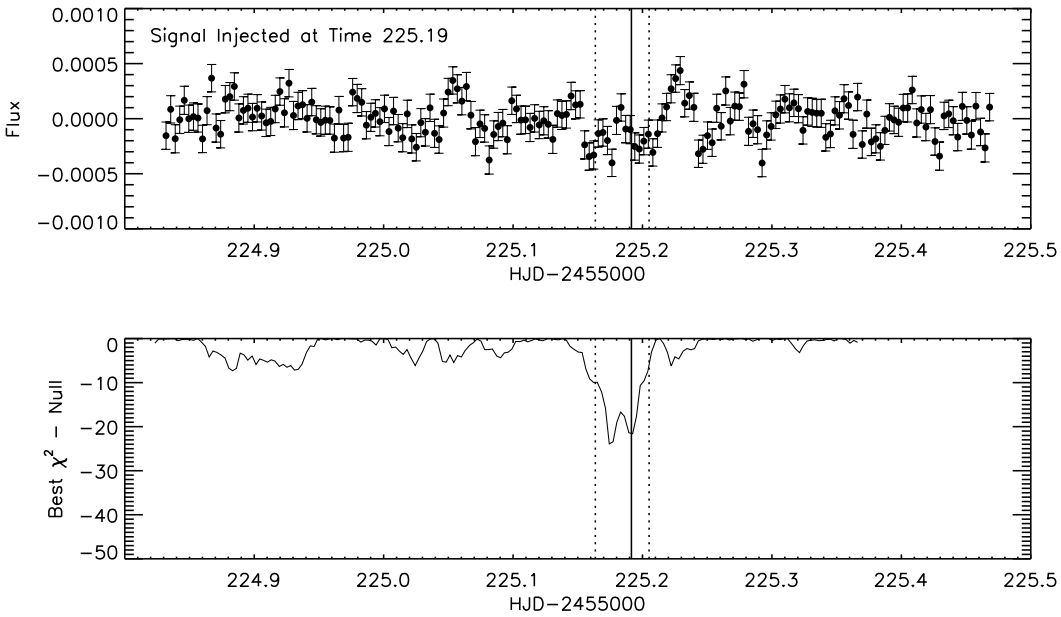

Figure 3.6.—: *Top panel: Spitzer* 4.5 μm light curve, with 0.75 $R_\oplus$ planet transit injected at time shown by the solid line. The location of the time window during which points are masked from the weighting function is shown by the dashed lines. *Bottom panel:* The improvement of the best-fit transit light curve solution χ^2 at each time compared to the null χ^2. In this case, the significance doubles when the mask is correctly placed over the transit.

We assess our sensitivity to 0.75 $R_\oplus$ planet transits by noting both the absolute significance of the detection, and the ratio of the detection significance to the significance of the next best solution, for all injected signals. We find that, for all transits occurring after a time of BJD 2455224.9 (corresponding to a period of 2.1071 days, which is safely before any ephemeris consistent with the solution from *EPOXI*), we recover the correct transit time with significance $\Delta\chi^2 \gtrsim 20$, and in all cases the significance of the transit signal (once the mask is centered over the transit time, so the suppression is minimized) is at least 60% higher than the the significance of the next highest solution. Figure 3.7 shows the recovery statistics for all injected transit times, starting at BJD 2455224.90 and ending at BJD 245525.44, in increments of 1 hour.

We note also that the average detection significance is a $\Delta\chi^2$ of 45, as compared to a predicted significance of 37 (using the scatter of 71 ppm for 20 minutes bins compared to the transit depth of 250 ppm, and assuming an hour-long transit). Having demonstrated our sensitivity to transits as small as the putative GJ 436c, we then repeated the above analysis on the actual time series—generating different versions of the time series for each mask position, while keeping the duration of the mask constant at one hour. The solution with the best improvement over the null hypothesis is shown in Figure 3.8, with the beginning and end of the interval during which data are masked from the weighting function shown by dashed lines. The best solution is actually an anti-transit in this case; when the mask is located over these points, the solution with highest significance gives an improvement over the null χ^2 of 15. The most

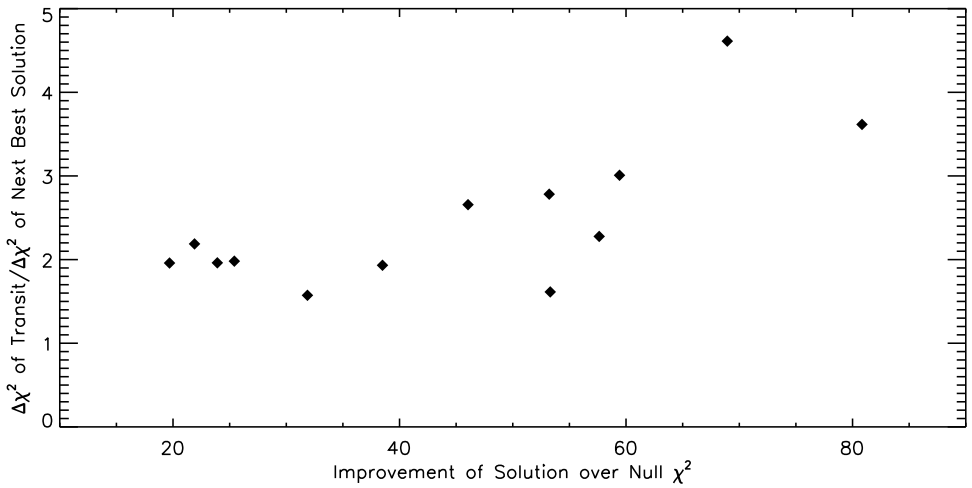

Figure 3.7.—: Recovery statistics of 0.75 $R_\oplus$ transit signals injected into *Spitzer* 4.5 μm observations. All transits times within the window allowed by the *EPOXI* and *Spitzer* 8 μm were successfully recovered. The X axis gives the absolute significance of the recovery, and the Y axis gives the ratio of the significance of the transit to the significance of the next best solution.

significant solution with a transit decrement solution has a significance of 7. We do not find any signal with the significance at which we detected injected signals of the expected depth.

We repeated this analysis on a version of the time series which was reduced using a polynomial fit to the intrapixel sensitivity variation. The standard deviation of the time series, as discussed in Section 2.3, is 30% higher than the standard deviation of the time series reduced using the weighted sensitivity function, even after we fit coefficients independently to 5-hour pieces of the time series. We find that we are able to recover the correct injected transit time only

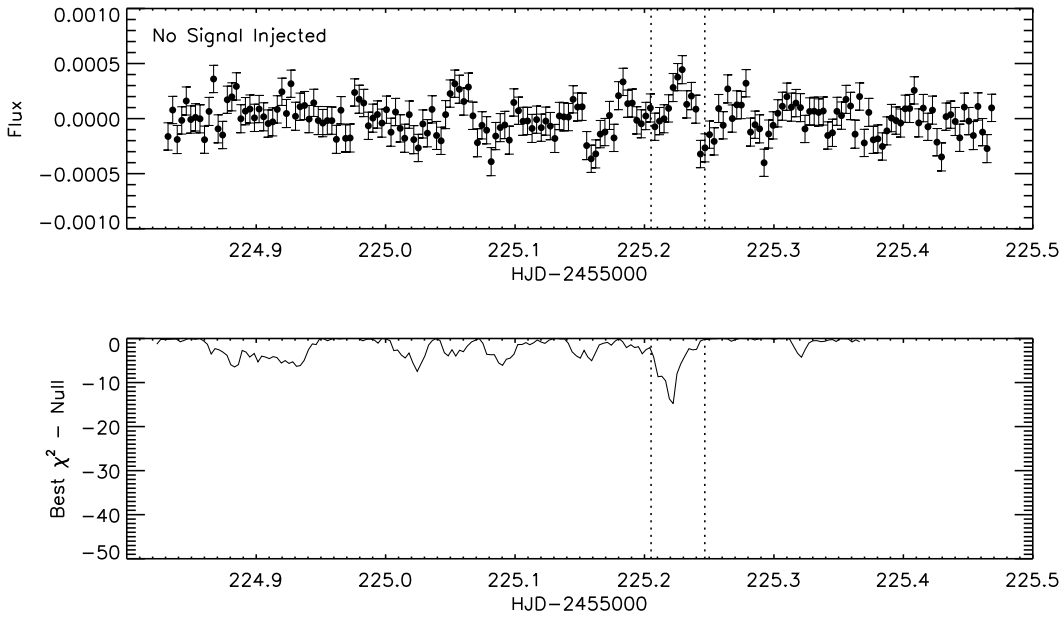

Figure 3.8.—: *Top panel: Spitzer* 4.5 μm light curve. The location of the time window during which points are masked from the weighting function is shown by the dashed lines; using this window, we find the most significant "transit" signal, which is actually an anti-transit. *Bottom panel:* The improvement of the best-fit transit light curve solution χ^2 at each time compared to the null χ^2.

20% of the time when the time series is reduced using a polynomial fit to the sensitivity function.

3.4 Discussion

We conclude that the putative transiting sub-Earth-sized GJ 436c planet, which was suggested by our *EPOXI* and *Spitzer* 8 μm data, can be conclusively ruled

out by our *Spitzer* 4.5 μm data. The periodicity of the candidate transit events within the *EPOXI* and *Spitzer* 8 μm data sets, coupled with the proximity of the hypothesized period to a resonance with the period of the known hot Neptune GJ 436b, initially merited further investigation, but the lack of a transit in the *Spitzer* 4.5 μm observations proves definitively that the candidate transit signals are not authentic.

Motivated by the intriguing eccentricity of GJ 436b, the observational campaigns to find the putative additional planet responsible have resulted in very sensitive upper limits to GJ 436c. The radial velocity analysis presented by Bean & Seifahrt (2008) ruled out perturbers greater than 8 $M_{\oplus}$ at periods less than about 11 days (semi-major axes less than 0.075 AU) with high confidence. From the *EPOXI* search for additional transits of this putative planet, we ruled out rocky transiting bodies down to 9.6 $M_{\oplus}$ with periods less than 8.5 days with 95% confidence in the GJ 436 system (Ballard et al. 2010b), in addition to definitively ruling out the 0.75 $R_{\oplus}$ planet suggested by the combined *EPOXI* and 8 μm *Spitzer* photometry. Furthermore, the possibility of a close-in resonant companion in 2:1 or 3:1 resonance with GJ 436b is strongly disfavored by transit timing measurements (Pont et al. 2009). Batygin et al. (2009) compiled a list of possible dynamically stable secular perturbers which are consistent with the transit times, radial velocities, and observed eccentricity of GJ 436b, which are observationally tractable. In light of the sensitive upper limits to this perturbing companion, the resolution to the eccentricity of GJ 436b may instead be a higher tidal dissipation factor for the hot Neptune—such a Q would need to be 1–2

orders of magnitude larger than that measured for Neptune in our solar system (Batygin et al. 2009; Banfield & Murray 1992). A value of $10^{6.3}$ for GJ 436b for Q/k_2 (where the Love number k_2 is typically near 0.5 for Solar System gas giants; Bursa 1992) proposed by Jackson et al. (2008b) could explain the eccentricity of GJ 436b without requiring the presence of an additional planet.

We demonstrate that the precision we obtain with Warm *Spitzer* observations at 4.5 μm is sufficient to detect a sub-Earth-sized planet around GJ 436. We find that the use of a polynomial to correct for the intrapixel sensitivity variation is insufficient to detect the putative 0.75 $R_\oplus$ planet. It was therefore necessary to correct for the variation with a point-by-point weighted sensitivity map in order to conclusively rule out the existence of the planet: both the rms precision and our ability to recover injected transit signals are enhanced with this correction method. We hope the methods outlined here to obtain this precision will be a useful guide for the reduction of future Warm *Spitzer* data sets of *Kepler* targets, some of which almost certainly *will* contain transits of Earth-sized planets.

Chapter 4

A Search for Additional Planets in Five of the Exoplanetary Systems Studied by the NASA *EPOXI* Mission

S. Ballard, J. L. Christiansen, D. Charbonneau, D. Deming, M. J. Holman, M. F. A'Hearn, D. D. Wellnitz, R. K. Barry, M. J. Kuchner, T. A. Livengood, T. Hewagama, J. M. Sunshine, D. L. Hampton, C. M. Lisse, S. Seager, J. F. Veverka

The Astrophysical Journal, Vol. 732, pp. 41-50, 2011

Abstract

We present time series photometry and constraints on additional planets in five of the exoplanetary systems studied by the EPOCh (Extrasolar Planet Observation and Characterization) component of the NASA *EPOXI* mission: HAT-P-4, TrES-3, TrES-2, WASP-3, and HAT-P-7. We conduct a search of the high-precision time series for photometric transits of additional planets. We find no candidate transits with significance higher than our detection limit. From Monte Carlo tests of the time series using putative periods from 0.5 days to 7 days, we demonstrate the sensitivity to detect Neptune-sized companions around TrES-2, sub-Saturn-sized companions in the HAT-P-4, TrES-3, and WASP-3 systems, and Saturn-sized companions around HAT-P-7. We investigate in particular our sensitivity to additional transits in the dynamically favorable 3:2 and 2:1 exterior resonances with the known exoplanets: if we assume coplanar orbits with the known planets, then companions in these resonances with HAT-P-4b, WASP-3b, and HAT-P-7b would be expected to transit, and we can set lower limits on the radii of companions in these systems. In the nearly grazing exoplanetary systems TrES-3 and TrES-2, additional coplanar planets in these resonances are not expected to transit. However, we place lower limits on the radii of companions that would transit if the orbits were misaligned by 2.0° and 1.4° for TrES-3 and TrES-2, respectively.

4.1 Introduction

EPOXI (EPOCh + DIXI) is a NASA Discovery Program Mission of Opportunity using the Deep Impact flyby spacecraft (Blume 2005). From January through August 2008, the EPOCh (Extrasolar Planet Observation and Characterization) Science Investigation used the HRI camera (Hampton et al. 2005) with a broad visible bandpass filter to gather precise, rapid cadence photometric time series of known transiting exoplanet systems. The majority of these targets were each observed nearly continuously for several weeks at a time. In Table 1 we give basic information about the seven EPOCh targets and the number of transits of each that EPOCh observed.

One of the EPOCh science goals is a search for additional planets in these systems. Such planets would be revealed either through the variations they induce on the transits of the known exoplanet, or directly through the transit of the second planet itself. The search for additional planets in the EPOCh observations of the M dwarf GJ 436 was presented in Ballard et al. (2010b). Because GJ 436 is a nearby M dwarf, it is the only EPOCh target for which we are sensitive to planets as small as 1.25 $R_{\oplus}$. In this work, we conduct a search for photometric transits of additional planets; the transit times of the known exoplanets observed by EPOCh are presented in Christiansen et al. (2011).

The search for transiting planets in the EPOCh light curves is scientifically compelling because the discovery of two transiting bodies in the same system permits the direct observation of their mutual dynamical interactions. This

enables constraints on the masses of the two bodies independent of any radial velocity measurement (Holman & Murray 2005; Agol et al. 2005), as has been done for the multiple transiting planet system Kepler 9 (Holman et al. 2010). There are also separate motivations for searches for additional planets around the EPOCh targets. The search for additional transits in the EPOCh observations is complementary to existing constraints on additional planets from photometric observations, radial velocity measurements, and transit timing analyses of the known exoplanet.

Here we briefly summarize such work to date for our five targets. Smith et al. (2009) investigated 24 light curves of known transiting exoplanets, including the *EPOXI* targets HAT-P-4, TrES-2, WASP-3, and HAT-P-7, and found that they were sensitive to additional transits of Saturn-sized planets with orbital periods less than 10 days with greater than 50% certainty, although that probability is less for HAT-P-4 (Kovács et al. 2007) because of decreased phase coverage. Transit timing analyses of TrES-3b (O'Donovan et al. 2007) have ruled out planets in interior and exterior 2:1 resonances (Gibson et al. 2009), although the transit times obtained by Sozzetti et al. (2009) for TrES-3b may suggest a deviation from a constant period that could be attributed to an additional body. Freistetter et al. (2009) found that a broad range of orbits around TrES-2 (O'Donovan et al. 2006) would be dynamically stable for additional planets, although the constraints presented by Rabus et al. (2009) for TrES-2 have ruled out an 5 $M_{\oplus}$ planet in the 2:1 resonance specifically, and Holman et al. (2007) found no deviations in the transit timing residuals from the predicted ephemeris. Additionally, Raetz

et al. (2009) observed a candidate transit in their photometry of TrES-2 which might be attributed to an additional body in the system in an external orbit to TrES-2b. However, Kipping & Bakos (2011b) investigated the TrES-2 *Kepler* observations and found no unexpected photometric decrements and no significant transit timing or transit duration variation. Maciejewski et al. (2010) performed an analysis of the transit times of WASP-3b (Pollacco et al. 2008), and found evidence for planet with a mass of 15 $R_{\oplus}$ in a orbit close to a 2:1 resonance with the known planet. In the HAT-P-7 (Pál et al. 2008) radial velocity measurements, Winn et al. (2009) found a drift that provides evidence for a third body. This radial velocity trend is consistent with any period longer than a few months. Finally, the light curves obtained by the *Kepler* Mission (Borucki et al. 2010) will ultimately enable exquisite constraints on the presence of additional planets in two of the systems which were also observed by *EPOXI*: TrES-2 and HAT-P-7.

The remainder of this paper is organized as follows. In Section 2, we describe the photometry pipeline we created to produce the time series. In Section 3, we describe the search we conduct for additional transiting planets. We present a Monte Carlo analysis of the EPOCh observations of HAT-P-4, TrES-3, TrES-2, WASP-3, and HAT-P-7, and demonstrate the sensitivity to detect additional planets in the Neptune-sized and Saturn-sized radius ranges. In Section 4, we present our best candidate transit signals, and from the search for additional transits we place upper limits on the radii of additional putative planet in these systems in the exterior 3:2 and 2:1 resonances with the known exoplanets.

4.2 Observations and Data Reduction

The photometric pipeline we developed for the EPOCh data is discussed at length in Ballard et al. (2010b) (concerning GJ 436 in particular), and is summarized in Christiansen et al. (2010) (concerning HAT-P-7) and Christiansen et al. (2011) (concerning HAT-P-4, TrES-3, TrES-2, and WASP-3). We outline here the basic steps we undertake to produce the final EPOCh time series. We acquired observations of the five EPOCh targets presented here nearly continuously for approximately two-week intervals. These intervals were interrupted for several hours at approximately 2-day intervals for data downloads. We also obtained for TrES-2, WASP-3, and HAT-P-7 approximately one day of "pre-look" observations, implemented to optimize pointing for each target, that predate the continuous observations by a week. The basic characteristics of the targets and observations are given in Tables 1 and 2. Observations of this type were not contemplated during development of the original Deep Impact mission; the spacecraft was not designed to maintain very precise pointing over the timescale of a transit (Table 4.2). Furthermore, the available onboard memory precludes storing the requisite number of full-frame images (1024×1024 pixels). Hence, the observing strategy during the later observations (TrES-2, WASP-3, and HAT-P-7) used 256×256 sub-array mode for those times spanning the transit, and 128×128 otherwise. This strategy assured complete coverage at transit, with minimal losses due to pointing jitter exceeding the 128×128 sub-array at other times. We elected to exclude the following EPOCh data from the search for additional transits: first, the observations of XO-2, for which we gathered only partial transits and had

relatively sparse phase coverage due to pointing jitter and data transfer losses. Second, we did not use the observations from the second EPOCh campaign for HAT-P-4 (from 29 Jun - Jul 7 2008), which we could not calibrate to the same level of precision as the original observations for reasons explained below. Our sensitivity to additional transit signals in the HAT-P-4 light curve, which should theoretically have improved with additional observations removed in time, was in reality diminished due to the increased correlated noise in the second campaign HAT-P-4 observations. For this reason, we elected to use only the original 22 days of observations in the search for additional transits.

We used the existing Deep Impact data reduction pipeline to perform bias and dark subtractions, as well as preliminary flat fielding (Klaasen et al. 2005). We first determined the position of the star on the CCD using PSF fitting, by maximizing the goodness-of-fit (with the χ^2 statistic as an estimator) between an image and a model PSF (oversampled by a factor of 100) with variable position, additive sky background, and multiplicative brightness scale factor. We then processed the images to remove sources of systematic error due to the CCD readout electronics. We first scaled down the two central rows by a constant value, then we scaled down the central columns by a separate constant value. Finally, in the case of 256×256 images, we scaled the entire image by a multiplicative factor to match the 128×128 images (the determination of the optimal correction values is performed independently for each target). We performed aperture photometry on the corrected images, using an aperture radius of 10 pixels, corresponding to twice the HWHM of the PSF. To remove remaining correlated noise due to

Table 4.1. EPOCh Targets

Name	V Magnitude	Number of Transits Observed[a]	Dates Observed [2008]
HAT-P-4	11.22	10	Jan 22–Feb 12, Jun 29–Jul 7
TrES-3	11.18	7	Mar 8–March 10, March 12–Mar 18
XO-2	12.40	3	Mar 11, Mar 23–Mar 28
GJ 436	10.67	8	May 5–May 29
TrES-2	11.41	9	Jun 27–Jun 28, Jul 9–Jul 18, Jul 21–Aug 1
WASP-3	10.64	8	Jul 18–Jul 19, Aug 1–Aug 9, Aug 11–Aug 17
HAT-P-7	10.50	8	Aug 9–Aug 10, Aug 18–Aug 31

[a]Some transits are partial.

Table 4.2. Characteristics of the EPOCh Observations

Telescope aperture	30 cm
Spacecraft memory	300 Mb
Bandpass	350-1000 nm
Integration time	50 seconds
Pointing jitter	± 20 arc-sec per hour
Defocus	4 arc-sec FWHM
Pixel scale	0.4 arc-sec per pixel
Subarray size	256×256 pixels spanning transit, 128×128 otherwise[a]

[a]With the exception of the HAT-P-4 observations during 2008 January and February and TrES-3 observations, which were conducted entirely in 128×128 subarray mode.

the interpixel sensitivity variations on the CCD, we fit a 2D spline surface to the brightness variations on the array as follows. We randomly drew a subset of several thousand out-of-transit and out-of-eclipse points from the light curve (from a data set ranging from 11,000 total points in the case of TrES-3 to 20,000 points in the case of HAT-P-4), recorded their X and Y positions, and calculated a robust mean of the brightness of the 30 nearest spatial neighbors for each selected point. To determine the robust mean, we used an iterative sigma-clipping routine that recalculates the mean after excluding outliers further than 3 sigma from the mean estimate at each iteration (the routine concludes after the iteration when no new outliers are identified). Given the set of X and Y positions and the average brightness values of the 30 points which lie nearest those positions, we fit a spline surface to the brightness variations in X and Y using the IDL routine `GRID_TPS`. This spline surface has the same resolution as the CCD, and approximates a flat field of the CCD which has been convolved by a smoothing kernel with width equal to the average distance required to enclose 30 neighboring points. We then corrected each data point individually by bilinearly interpolating on the spline surface to find the expected brightness of the star at each X and Y position. We then divide each observation by its expected brightness to remove the effects of interpixel sensitivity variations. We used only a small fraction of the observations to create the spline surface in order to minimize the potential transit signal suppression introduced by flat fielding the data with itself. To produce the final time series, we iterated the above steps, fitting for the row and column multiplicative factors, the sub-array size scaling factor, and the 2D spline surface

that minimized the out-of-transit standard deviation of the photometric time series.

We include two additional steps in the reduction of these data that were not included in the Ballard et al. (2010b) reduction of the GJ 436 EPOCh observations. First, during the second campaign observations of HAT-P-4 and TrES-2, we observed an increase in brightness when the position of the star was located in the lower right-hand quadrant of the CCD. At the image level, we observed a bright striping pattern in this quadrant that caused the measured brightness of the star to increase as soon as the PSF entered this quadrant. We found that the dependence of the brightness increase in this quadrant was correlated with the Instrument Control Board Temperature value recorded for for each image in the FITS header. For the HAT-P-4 second campaign and TrES-2 observations, we first fit a spline to the dependence of the photometric residuals (after the bootstrap flat field was applied, described below) on the Instrument Control Board Temperature, using residuals for which the entire PSF of the star fell into the CCD quadrant in question. The most egregious brightness increase is 4 mmag, when this effect was most prominent. We then performed aperture photometry again on these targets and corrected each image by interpolating the Instrument Control Board Temperature for that image onto the spline, multiplying this correction value by the fraction of the PSF core that fell into the quadrant in question, and dividing this value from the photometry. We found that this iterative procedure largely removed this quadrant-dependent effect. In the latter half of TrES-2 observations, we no longer observed the brightness increase

in this CCD quadrant. Therefore, we found that the correction procedure was only necessarily for the second campaign HAT-P-4 and the first portion of TrES-2 observations. However, because of the 6-month separation of the second campaign HAT-P-4 observations from the original HAT-P-4 observations, the behavior of the CCD had sufficiently altered to disallow the combination of the data into a single 2D spline surface. The separate 2D spline correction of the second campaign observations (spanning only 8 days), coupled with the residual striping artifacts, sufficiently decreased the precision of the second campaign observations that we elected to exclude them from the search for additional transiting planets around HAT-P-4.

Secondly, we include one final correction after we have removed the interpixel brightness variations with the 2D spline, which is to perform an additional point-by-point correction to the data taken during transit and secondary eclipse of the known exoplanets. The bootstrap flat field randomly selects a set of points to create the spline surface, instead of using all the data to create this surface; this minimizes the suppression of additional transits. Our sensitivity to additional transits is sufficiently diminished during the transits of the known planet that we are concerned more with removing correlated noise, and less concerned about avoiding additional transit suppression. The two reasons for the diminished sensitivity during transit windows are, first, that we fit a slope with time to the points immediately outside of the transit of the known exoplanet (from 3 minutes to 30 minutes before and after transit) and divide by the slope in order to normalize each transit before we fit for the system parameters (this procedure is

also detailed in Ballard et al. 2010b). This could have the possibility of removing a decrement due to an additional transit. Second, there is also the possibility of an occultation of one planet by another. We therefore elected to perform a point-by-point correction after the 2D spline for points occurring during the transit and eclipse of the known exoplanet, wherein we find a robust mean of the 30 nearest neighbors to each point (using the same iterative routine described above) and divide this value individually for each point in transit or eclipse. This has the benefit of removing additional correlated noise during transit and eclipse, while still minimizing signal suppression of additional putative planets outside of these time windows

After we take these steps to address the systematics associated with the observations, we achieve a precision for the unbinned observations which is approximately twice the photon noise limited precision for all five targets. We estimate the photon limited precision at the image level, by converting the stellar flux from watts per meter squared per steradian per micron ($W/m^2 \cdot sr \cdot \mu m$) to electron counts as follows. We first divide by the conversion factor in the FITS header (keyword RADCALV = 0.0001175 $W/m^2 \cdot sr \cdot \mu m$ per DN/s), then multiply by the exposure time (INTTIME = 50.0005 s), and finally multiply by the gain (28.80 e/DN, per Klaasen et al. 2008 for the HRI camera). We then estimate the photometric error by calculating $1/\sqrt{N}$, where N is the number of electrons. We have excluded read noise, bias, and dark current from the estimation of the photon limited precision because these quantities contribute negligibly to the total number of electrons measured within the aperture; we briefly summarize our

reasoning here. Using the results of the calibration tests on the HRI instrument shown in Klaasen et al. (2008), we estimate the read noise and dark current (given the CCD temperature of 160 K, as recorded in the image headers) to contribute less than a DN. Calculating the median bias value per pixel from the overclocked pixels associated with each image, and then multiplying this median value by the number of pixels contained within the aperture, we determine that the bias contributes less than 500 DN. When compared to the total measured DN flux contained in the aperture, which is of order 10^5 DN for the dimmest target star, TrES-3, we conclude that read noise, bias, and dark current are negligible. We repeat the photon limited precision calculation on 50 images for each target, and take the mean of these values to be our estimate for the photon limited precision. Our precision of 1.21 mmag for HAT-P-4 is 94% above the limit, 2.17 mmag for TrES-3 is 106% above the limit, 1.62 mmag for TrES-2 is 136% above the limit, 0.97 mmag for WASP-3 is 106% above the limit, and 0.86 mmag for HAT-P-7 is 91% above the limit. The EPOCh precision for GJ 436 of 0.51 mmag was only 56% above the photon noise limit, which we attribute to the longer baseline of observations with fewer gaps in phase coverage, both of which enabled us to create a higher quality 2D spline flat field (Ballard et al. 2010b). Figure 4.1 shows five EPOCh time series after the 2D spline correction is applied; these light curves are identical to the ones presented in Christiansen et al. (2010, 2011). In the right panel adjacent to each time series, we show how the time series, after the 2D spline is applied, bins down as compared to Gaussian noise over timescales of 7 hours (512 points) or less. We selected the longest contiguous portion of the

Figure 4.1.—: (Following page) *Left panels: EPOXI* time series for targets HAT-P-4, TrES-3, TrES-2, WASP-3, and HAT-P-7. For TrES-3 (second panel from top), we show the light curve with original modulation due to star spots at bottom. *Right panels:* The standard deviation versus bin size for each target, compared to the ideal Gaussian limit (shown with a line, normalized to match the value at N=1).

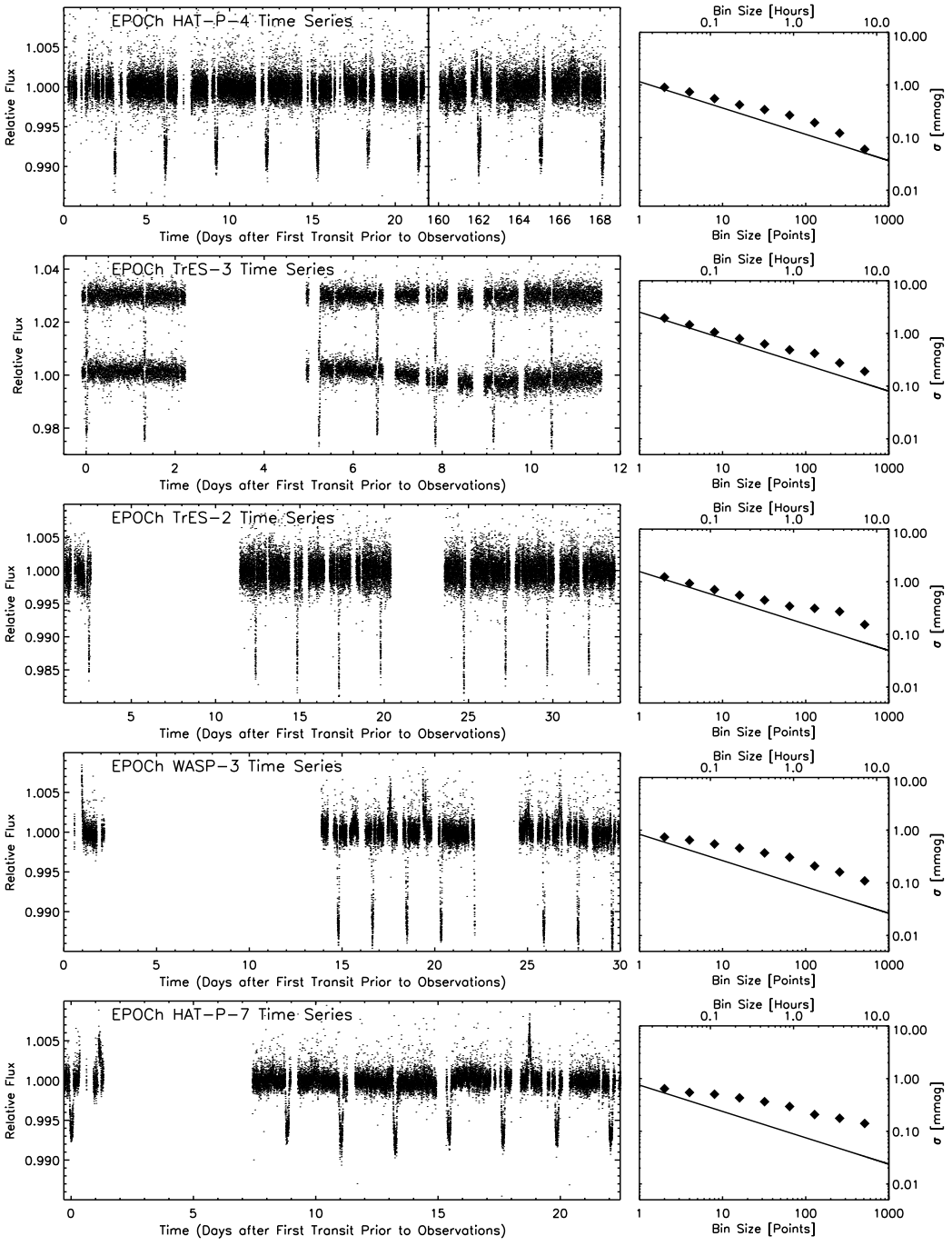

Figure 4.1.—: (Continued).

lightcurve between transits (and excluding secondary eclipse) to calculate the standard deviation as a function of binsize– this unbinned portion typically comprises about 2500 points. We compare the expected Gaussian scatter for a bin size of 1 hour (assuming that sigma decreases as $N^{-1/2}$, and normalizing to the observed rms of the unbinned data) to the measured scatter, and find that the presence of correlated noise inflates the 1σ error bar by a factor of 1.86 for HAT-P-4, 1.58 for TrES-3, 1.90 for TrES-2, 2.77 for WASP-3, and 3.14 for HAT-P-7 for 1 hour timescales.

We also investigate the transit signal suppression introduced by using a flat field created from the out-of-transit and out-of-eclipse data itself. We avoid the suppression of known transits in each data set by iteratively excluding those observations (using an ephemeris for the known planet derived from the EPOCh observations) from the points used to generate the flat field surface, so that we only use the presumably constant out-of-transit and out-of-eclipse observations to sample the CCD sensitivity. However, if the transit of an additional planet occurs while the stellar PSF is lying on a part of the CCD that is never visited again, the 2D spline algorithm instead models the transit as diminished pixel sensitivity in that CCD location. To quantify the suppression of additional transits that result from using the 2D spline, we inject transit light curves with periods ranging from 0.5 days to 7 days in intervals of 30 minutes in phase (ranging from a phase of zero to a phase equal to the period) into the EPOCh light curve just prior to the 2D spline step. After performing the 2D spline, we then phase the data at the known injected period and fit for the best radius, using χ^2 as the goodness-of-fit

statistic. We show in Figure 4.2 the radius suppression as a function of period for five EPOCh targets. The HAT-P-4 observations occur over a longer duration with less gaps in phase coverage, so even at a period of 7 days, we have 95% confidence that the radius of an additional transiting planet will not be suppressed to less than 60% its original value. For example, an additional 8 $R_\oplus$ planet orbiting HAT-P-4 will appear no smaller than 0.6×8 $R_\oplus$, or 4.8 $R_\oplus$, with 95% confidence. However, for a target with sparser phase coverage, such as WASP-3, we have 95% confidence that the radius will not be suppressed to less than 45% its original value. The same 8 $R_\oplus$ planet orbiting WASP-3 will therefore appear no smaller than 0.45×8 $R_\oplus$, or 3.6 $R_\oplus$, with the same confidence. The average (50% confidence) suppression value of 75% across all periods and for all targets reflects the average density of points on the CCD (and thus the quality of the 2D spline), which is indicative of the pointing jitter of the instrument. We describe our incorporation of signal suppression into our search for additional planets in greater detail in Section 3.2.

4.3 Analysis

4.3.1 Search for Additional Transiting Planets

We search the *EPOXI* time series for evidence for additional shallow transits. We developed software to search for these additional transits, which is discussed at length in Ballard et al. (2010b). The steps involved in the procedure are

Figure 4.2.—: (Following page) The 50% and 95% confidence values for suppression of additional transits as a function of orbital period in the EPOCh observations. We have 50% confidence that the transit signal will not be suppressed more than the value of the dashed line at that period, and 95% confidence that the transit signal will not be suppressed more than the value of the solid line.

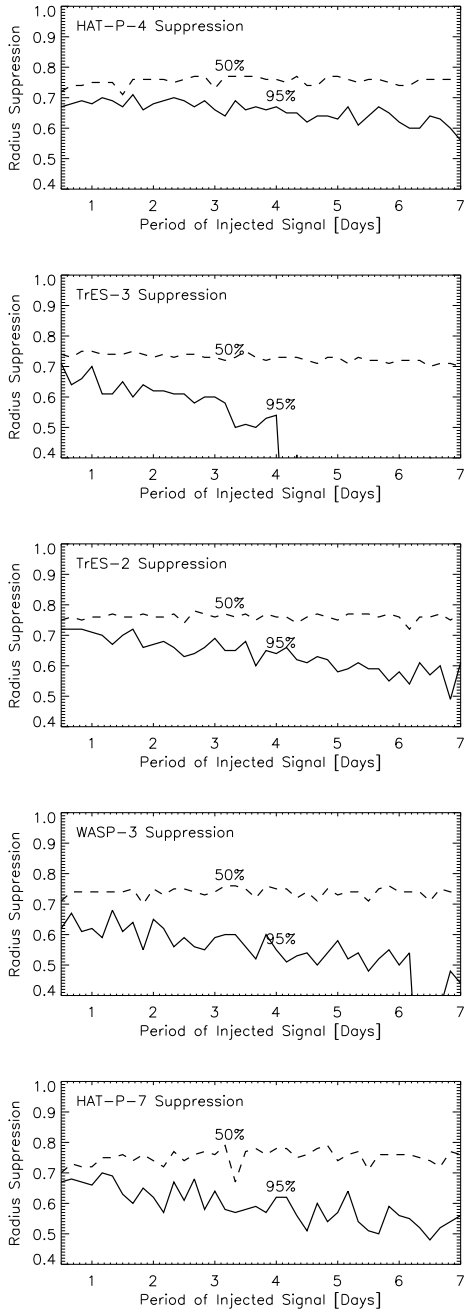

Figure 4.2.—: (Continued).

summarized in this section. We conduct a Monte Carlo analysis to assess how accurately we could recover an injected planetary signal in each of the EPOCh light curves. We evaluate our sensitivity to transit signals on a grid in radius and period space sampled at regular intervals in R_P^2 and regular frequency spacing in P. We create an optimally spaced grid as follows: for the lowest period at each radius, we determine the radii at which to evaluate the adjacent periods by solving for the radius at which we achieve equivalent signal-to-noise (for this reason, we expect significance contours to roughly coincide with the grid spacing). We use the Mandel & Agol (2002) routines for generating limb-darkened light curves given these parameters to compute a grid of models corresponding to additional possible planets. If we make the simplifying assumptions of negligible limb darkening of the host star, a circular orbit, and an orbital inclination angle i of 90°, the set of light curves for additional transiting bodies is a three parameter family. These parameters are radius of the planet R_p, orbital period of the planet P, and orbital phase ϕ. To generate these light curves, we also use the stellar radii values determined by Christiansen et al. (2010, 2011) from the *EPOXI* data, with the corresponding stellar masses, from the literature, that were used to calculate those radii. Those radius and mass values are 1.60 $R_\odot$ and 1.26 $M_\odot$ (Kovács et al. 2007) for HAT-P-4, 0.82 $R_\odot$ and 0.93 $M_\odot$ (Sozzetti et al. 2009) for TrES-3, 0.94 $R_\odot$ and 0.98 $M_\odot$ (Sozzetti et al. 2007) for TrES-2, 1.35 $R_\odot$ and 1.24 $M_\odot$ (Pollacco et al. 2008) for WASP-3, and 1.82 $R_\odot$ and 1.47 $M_\odot$ (Pál et al. 2008) for HAT-P-7. At each test radius and period, we inject planetary signals with 75 randomly assigned phases into the residuals of EPOCh light curves with the best

transit model divided out, and then attempt to recover blindly the injected signal by minimizing the χ^2 statistic. The period range of injected signals is selected for each target individually, to ensure the injected transit signal comprises at least two transits in most cases. For a target with high phase coverage, like HAT-P-4, we inject signals with periods up to 7 days, but for targets with observations of a shorter duration and sparser phase coverage, like TrES-3 or WASP-3, we inject signals up to 3.5 and 2.5 days, respectively. For planets with periods higher than these values, we may detect the planet, but with a single transit, we expect only a very weak constraint on the period.

We first conduct a coarse χ^2 grid search in radius, period, and phase. We select the spacing of this grid to minimize processing time while ensuring that the transit was not missed; we polish the parameters with a finer χ^2 search after the initial coarse search. We sample the χ^2 space at 300 points in period space (at even frequency intervals between 0.5 and 8.5 days), 50 points in radius space (between 0.5 and 5.5 Earth radii) and a variable number of points in phase space set by the resolution of the transit duration for each period. We use an expression for the transit duration τ given by Seager & Mallén-Ornelas (2003):

$$\sin i \sin\left(\frac{\pi\tau}{P}\right) = \sqrt{\left(\frac{R_\star + R_P}{a}\right)^2 - \cos^2 i}. \tag{4.1}$$

For each test model, we compute the χ^2, using the out-of-transit standard deviation to estimate the error in each point. After the grid χ^2 minimum is determined, we use the `amoeba` minimization routine (Nelder & Mead 1965)

to more finely sample the χ^2 space in order to find the χ^2 minimum from the specified nearest grid point. We also investigate whether aliases of the best-fit period from the χ^2 grid improve the fit. We find that roughly half of the best solutions from the grid are aliases of the injected period, most at either half or twice the value of the injected period, but we test aliases at every integer ratio from 1/35 to 35 times the given period (although aliases other than 1:2, 2:1, 3:1, 1:3, 2:3, or 3:2 occurs less than 3% of the time for all targets). We also repeat the finer grid search at the three next lowest χ^2 minima, in case the best solution (or an alias of the best solution) lies closer to that grid point. For all injected signals, we recover a solution which is a better fit (in the χ^2 sense) than the injected signal. For this reason, we are confident that we are sampling the χ^2 space sufficiently finely to locate the best solution.

We quantify the success of this analysis by how well the search blindly recovers the known injected transit signal. We define the error on the recovered parameter, for instance period, to be $\mid P_{injected} - P_{observed} \mid / P_{injected}$. Figure 4.3 shows this relative error in radius, with 95% confidence, for all searches. As we note in the last paragraph of Section 2, we anticipate suppression of additional transit signals from the bootstrap flat field treatment of the *EPOXI* data. We evaluate the suppression we expect at the period values used in the Monte Carlo analysis, using the results shown in Figure 4.2. We incorporate this expected suppression by vertically shifting the effective radius values of the grid points at which we evaluate our sensitivity to additional transits. For example, for HAT-P-4 at 1.63 days, all grid points have been shifted upward in radius by a

Figure 4.3.—: (Following page) Constraints on radius from the Monte Carlo analysis. For each point in radius and period, we create 75 light curves with random orbital phases, inject them into the EPOCh residuals, and attempt to recover them blindly. The diamonds indicate the grid of radii and periods at which we evaluate our sensitivity; the contours are produced by interpolating between these points. The contours indicate the relative error in radius (absolute value of recovered-injected/injected radius) that encloses 95% of the results.

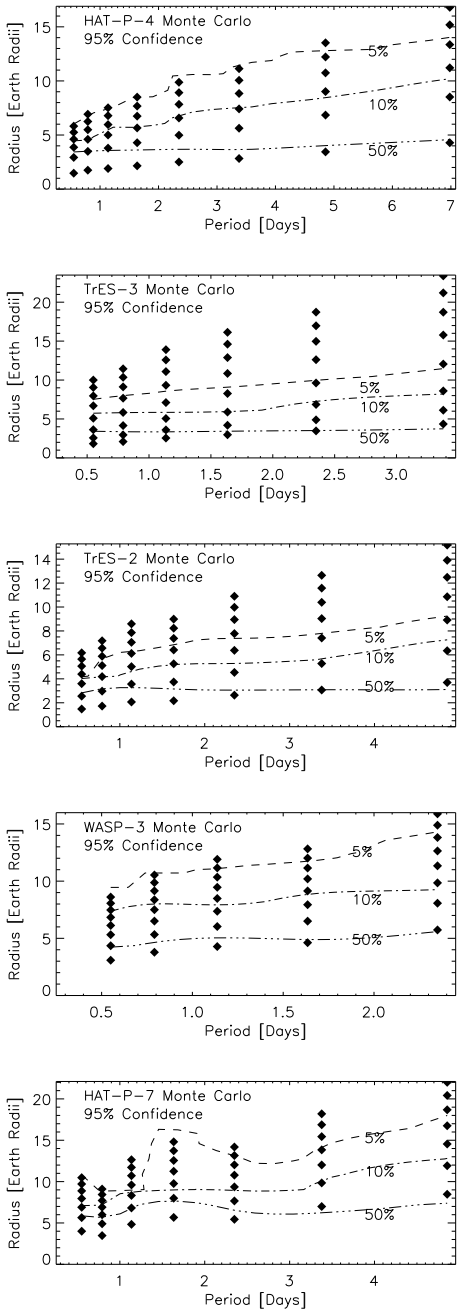

Figure 4.3.—: (Continued).

value of 1/0.7, or 1.42, because we anticipate that the radius will be suppressed to no smaller than 70% its original value. For this reason, the recovery statistics corresponding to a 3.0 $R_\oplus$ transit depth in the final light curve would be accurate for an original transit signal of a 4.3 $R_\oplus$ planet once we fold our expectation of signal suppression.

We also evaluate the overall detection probability for putative transiting planets. Given the cadence and coverage of the *EPOXI* observations, we determine the number of in-transit points we expect for a given radius, period, and phase (where the phase is evaluated from 0 to 1 periods, in increments of 30 minutes). We then evaluate the expected significance of the detection, assuming a boxcar-shaped transit at the depth of $(R_P/R_\star)^2$, and the standard deviation of the time series. At each phase and period individually, we scale down R_P to incorporate the signal suppression at that ephemeris. We use the improvement in the χ^2 over the null hypothesis to define a positive detection, after we have removed the best candidate transit signal (described in Section 4.1). If we do not first remove this signal, then we are a priori defining a "detectable" signal to be any signal more prominent than the best candidate signal, and we would be unable to evaluate this signal's authenticity. We set our detection limit at an improvement in χ^2 over the null hypothesis that signifies a correctly recovered period (which we define as a period error of <1%). This number is variable among the EPOCh targets due to the precision of the observations and the contamination of correlated noise. The detection probability of additional transiting planets, as a function of their radius and orbital period, is shown in Figure 4.4.

Figure 4.4.—: (Following page) Detection probability versus period for planets ranging in size from 3 to 10 $R_\oplus$. The detection criteria is set by the percentage of phases at a given period for which the number of points observed in transit produces a χ^2 improvement of the cutoff significance, compared to the null hypothesis ($\Delta\chi^2$ of 250 for HAT-P-4, 200 for TrES-3 and TrES-2, 400 for WASP-3, and 500 for HAT-P-7). We assume a boxcar-shaped transit at the depth of $(R_P/R_\star)^2$. The vertical lines show the positions of the 3:2 and 2:1 resonances with the known planet, and the cross-hatching shows the location of orbits which are not guaranteed to be stable by Hill's criterion per Gladman (1993).

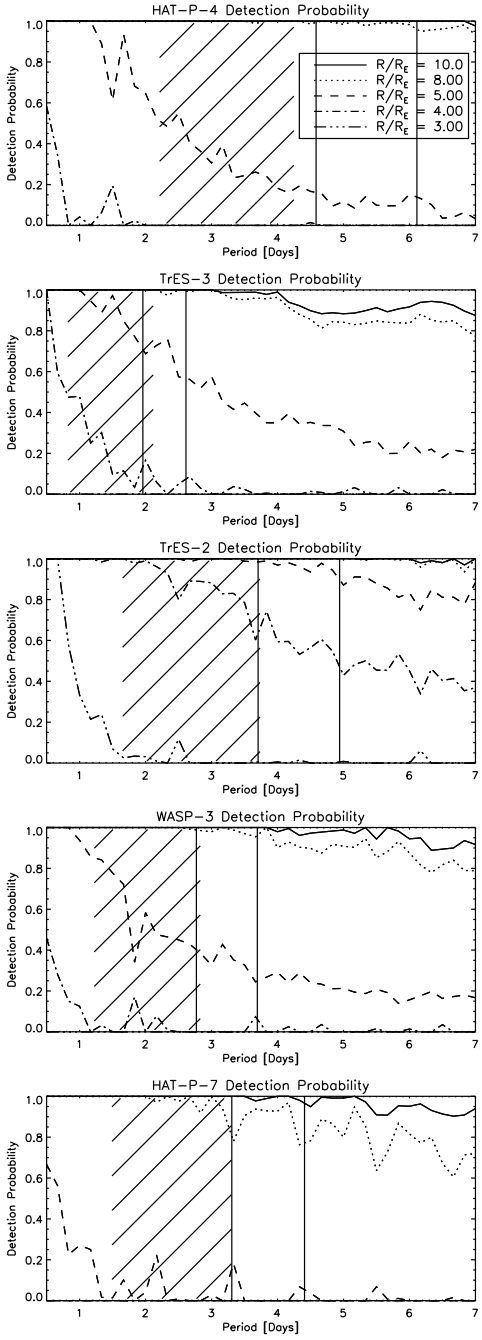

Figure 4.4.—: (Continued).

For the HAT-P-4, TrES-3, and TrES-2, the $\Delta\chi^2$ cutoff is set at 250, 200, and 200 respectively. For WASP-3, the $\Delta\chi^2$ criterion for detection is 400, and for HAT-P-7, the cutoff is 500. There are five exceptions here for these threshold values across the five targets: in our analysis of WASP-3, we find two instances of a significance higher than 400, but an incorrect period value: these signals both comprise 4 full transit events, and are recovered at a 4:1 alias of the true period of 2.34 days. Due to the same instances of correlated noise that produce two positive deviations during two of the four transit events that decrease the depths by 2 mmag, a better solution is found at an alias of 4:1 that at the true period. For HAT-P-7, we find three similar cases of a 2:1 alias providing a better solution than the injected period, although the significance of the detection is above the threshold vale of 500. For these three injected signals, which comprise three transits, two of the transits are recovered correctly, and the third overlays a single instance of correlated noise that decreases the depth of the transit by 0.5 mmag.

We investigated the true signal-to-noise ratio (including correlated noise) associated with a single detectable transit with the cutoff $\Delta\chi^2$ significance for each target. We use a method similar to the one described by Winn et al. (2008) to determine the contribution of correlated noise to the standard deviation over a transit duration timescale. We first solved for the transit depth associated with the cutoff $\Delta\chi^2$ value, assuming a single boxcar transit with standard deviation equal to the out-of-transit and out-of-eclipse standard deviation of the unbinned time series. We next found the standard deviation at a bin size corresponding to a transit duration for each target. We assume an edge-on transit

(which assumption we also used for the Monte Carlo analysis) and the shortest period where we expect mostly single transits (this period is slightly larger than the largest period used for the Monte Carlo analysis; which period range was selected so that we would expect at least two transits in nearly all cases). This approximate orbital period is 7.5 days for HAT-P-4, 4.0 days for TrES-3, 5.0 days for TrES-2, 3.0 days for WASP-3, and 5.0 days for HAT-P-7. Using the cutoff transit depth and the standard deviation associated with the transit duration for each target, we find that the signal-to-noise ratio associated with the detection criteria is approximately constant across the targets, ranging between 5 and 8. The variation in the $\Delta\chi^2$ value can be attributed in part to the varying presence of correlated noise in the different data sets (and also to the number of points associated with each transit, which depends on the transit duration). We confirm empirically that planets of these radii are detectable by examining the detection probability as a function of radius and orbital period shown in Figure 4.4. We convert the cutoff transit depth to a planetary radius, assuming the stellar radius derived from the EPOCh observations and average suppression of the radius to 0.75 its original value (roughly constant for all EPOCh targets, as shown in Figure 4.2). This radius value physically corresponds to the minimum planetary radius detectable by EPOCh from a single transit. This value is 7.1 $R_\oplus$ for HAT-P-4, 6.2 $R_\oplus$ for TrES-3, 5.3 $R_\oplus$ for TrES-2, 6.5 $R_\oplus$ for WASP-3, and 7.9 $R_\oplus$ for HAT-P-7. Comparing to the nearest radius value in Figure 4.4, we find that indeed, at the shortest orbital period where we should expect to see single transits, we can detect a planet with radius associated with the detection criteria at high significance.

At longer orbit periods, we still expect single transits, but the likelihood that the single transit occurs during a gap in the phase coverage increases.

4.4 Discussion

4.4.1 Best Candidate Transit Signals

We present our best candidate transits here, for each of the five EPOCh targets. Figure 4.5 shows each of the individual candidate transit events that comprise the best candidate signal, as well as the entire phased and binned signal. For HAT-P-4, the best candidate is a 2.7 $R_\oplus$ planet in a 3.1 day orbit; the $\Delta\chi^2$ significance is 61 (as compared to a detection criterion of 250). For TrES-3, the best candidate is a 2.9 $R_\oplus$ planet in a 2.63 day orbit; the $\Delta\chi^2$ significance is 87 (as compared to a detection criterion of 200). For TrES-2, the best candidate is a 3.6 $R_\oplus$ planet with a period of 7.22 days; the significance is $\Delta\chi^2$ of 269 (as compared to a detection criterion of 200). For WASP-3, the best candidate is a 4.2 $R_\oplus$ with a period of 5.9 days; the $\Delta\chi^2$ significance is 232 (as compared to a detection criterion of 400). For HAT-P-7, the best candidate is a 4.4 $R_\oplus$ planet with a 3.9 day orbit; the significance of the detection is a $\Delta\chi^2$ of 201 (as compared to a detection criterion of 500). The only candidate signal above the $\Delta\chi^2$ detection threshold is the one in the TrES-2 light curve; this candidate signal comprises two transit events (the other predicted events occur during gaps in the phase coverage). One of the candidate transit events occurs in a portion of the

Figure 4.5.—: (Following page) The best candidate transits for the five EPOCh targets. Each of the individual candidate transit events comprising the signal are shown at left; the phased and binned signal is shown at right. A time of zero on each X axis corresponds to the time of the first transit of the known planet observed by EPOCh. The $\Delta\chi^2$ significance of the HAT-P-4, TrES-3, WASP-3, and HAT-P-7 candidate signals fall below the detection criteria. While the significance of the TrES-2 candidate is above the detection criteria, one of the candidate transits (shown in the leftmost panel) occurs in a sparsely sampled part of the CCD, so the observations are uncalibrated and unreliable. Excising this candidate event, the significance of the remaining signal falls below the detection threshold.

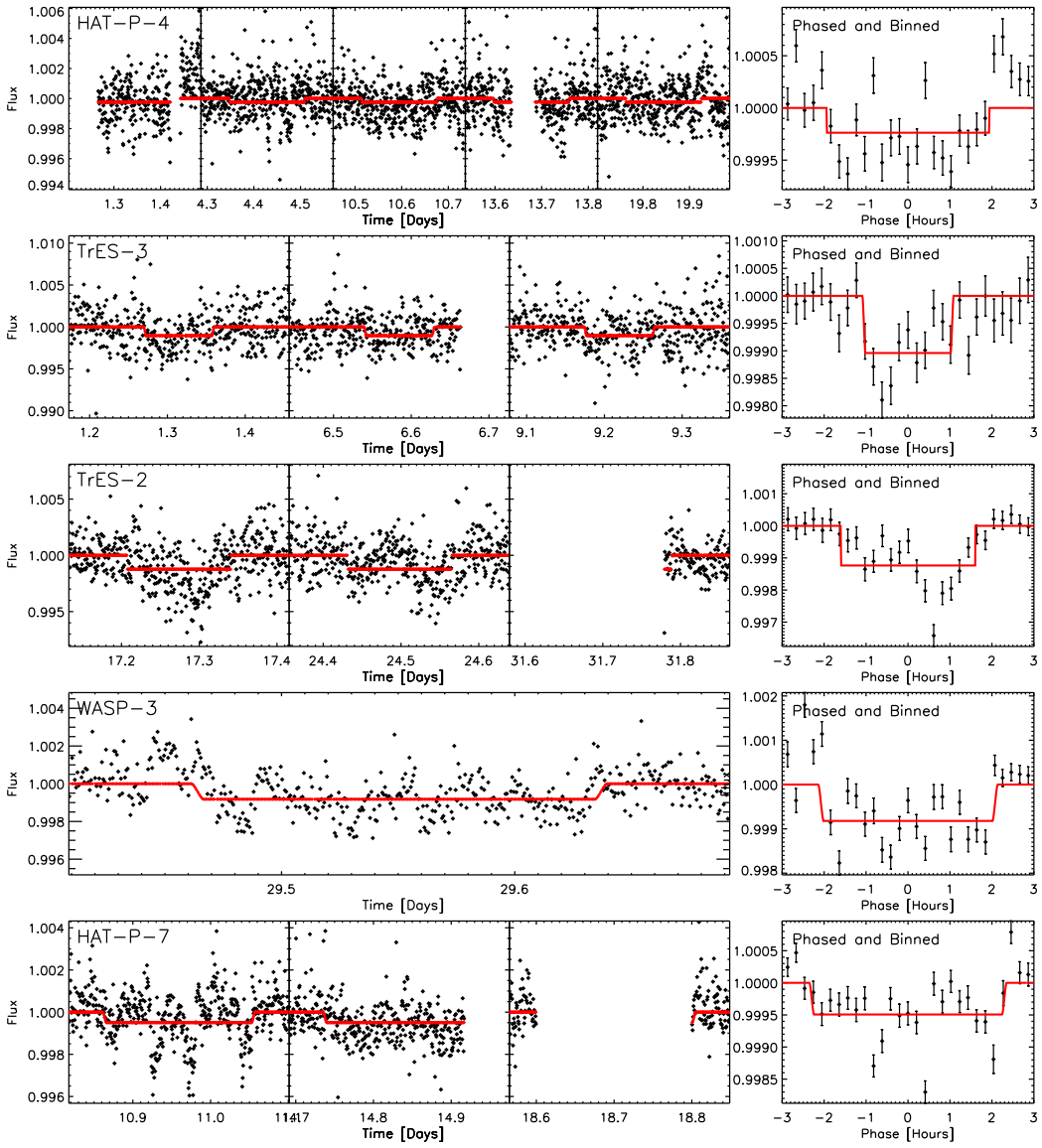

Figure 4.5.—: (Continued).

CCD that is never visited afterward; these data are therefore uncalibrated by the 2D spline flat field and are unreliable. Without the transit signal that occurs in the uncalibrated area of the CCD, the $\Delta\chi^2$ significance of the remaining transit is 80, which is well below the detection threshold of 200.

4.4.2 Radius constraints

From the results of our Monte Carlo analysis and phase coverage analysis, we can rule out transiting planets in the sub-Saturn radius range for HAT-P-4, TrES-3, and WASP-3, the Saturn-sized radius range for HAT-P-7, and Neptune-sized radius range for TrES-2. We consider in particular our sensitivity to additional planets in the dynamically favorable 3:2 and 2:1 resonance orbits with the known exoplanets. In Figure 4.4, we show the detection probability as a function of period for planets ranging in size from 3 to 10 $R_\oplus$, with positions of the exterior 3:2 and 2:1 resonances marked by vertical lines. We also indicate in Figure 4.4 the regions not guaranteed to be stable by Hill's criterion, per the formula given in Gladman (1993). Assuming an eccentricity of zero for both the known and putative additional planet, the planetary orbits are assumed to be stable if the following condition holds, where $\mu_1 = m_1/M_{star}$, $\mu_2 = m_2/M_{star}$, $\alpha = \mu_1 + \mu_2$, and $\delta = \sqrt{a_2/a_1}$:

$$\alpha^{-3}\left(\mu_1 + \frac{\mu_2}{\delta^2}\right)(\mu_1 + \mu_2\delta)^2 > 1 + 3^{4/3}\cdot\frac{\mu_1\mu_2}{\alpha^{4/3}}, \tag{4.2}$$

We solve numerically for the boundaries in δ of the stable region, using the

stellar masses and masses for the known planets given by Kovács et al. (2007) for HAT-P-4b, Sozzetti et al. (2009) for TrES-3b, Sozzetti et al. (2007) for TrES-2b, Pollacco et al. (2008) for WASP-3, and Pál et al. (2008) for HAT-P-7, and conservatively using a putative mass for the second body equal to the mass of Saturn. This results in an overestimate of the extent of the Hill-unstable region for the planets with masses smaller than Saturn; while we find we are sensitive to planets with radii well below that of Saturn, the mass of putative additional planets depends on their composition and is uncertain. However, the critical δ values vary slowly with increased mass of the putative additional planet, so that increasing the mass to that of Jupiter changes the periods associated with the closest Hill-stable orbits by only 7% at most for these systems. In some cases, the 3:2 orbital resonance is not guaranteed to be Hill-stable (though it may be stable); the exact boundary of the stable region depends on the mass we assume for the additional planet.

From the detection probabilities shown in Figure 4.4, in the HAT-P-4 system, we are sensitive to planets as small as 8 $R_\oplus$ in the 3:2 and 2:1 resonance with HAT-P-4b (with a period of 3.06 days) with 95% confidence. In the TrES-3 system, with the known exoplanet in a 1.3 day orbit, we would have detected a 5 $R_\oplus$ planet in the 3:2 and 1:2 resonance with 70% and 50% probability, respectively, and an 8 $R_\oplus$ in either orbit with nearly 100% probability. Around TrES-2 we are sensitive to the smallest planets, and would have detected a 4 $R_\oplus$ planet with 65% probability in the 3:2 resonance with TrES-2b (which has a period of 2.47 days). In both the 3:2 and 2:1 resonances, we had a high probability

of detecting a 5.0 $R_\oplus$ planet: >95% in the case of the 3:2 resonance, and 90% in the 2:1 resonance. Around WASP-3, we had 50% chance of detecting a 5.0 $R_\oplus$ planet in the 3:2 resonance with WASP-3b (which has a period of 1.85 days), and would have seen a planet as small as 8 $R_\oplus$ in either the 3:2 or 2:1 resonance with >95% probability. Around HAT-P-7, we would have detected a Saturn-sized 10 $R_\oplus$ planet in either the 3:2 or 2:1 resonances with 95% probability, and had a 70% chance of detecting an 8 $R_\oplus$ planet. If we assume an inclination equal to that of the known exoplanet, we can rule out additional transiting planets of HAT-P-4, WASP-3, and HAT-P-7 in the 3:2 and 2:1 resonances of the sizes stated above, as we still expect additional planets to transit at those orbital distances. However, the known exoplanets in both the TrES-3 and TrES-2 systems are already in grazing orbits, so additional planets in the exterior 3:2 and 2:1 resonances would not be expected to transit if they were strictly coplanar with the known exoplanet. However, if the orbits of additional planets were misaligned by 2.0° in the case of TrES-3 and 1.4° in the case of TrES-2 (using the planetary inclinations and stellar radii from Christiansen et al. 2010, 2011) then we would observe a transit in both of the 3:2 and 2:1 exterior resonances. The orbital inclinations of the ice and gas giants in our solar system vary by up to nearly 2° (Cox 2000), so it is feasible that an additional planet in these systems could transit.

4.5 Acknowledgments

We are extremely grateful to the *EPOXI* Flight and Spacecraft Teams that made these difficult observations possible. At the Jet Propulsion Laboratory, the Flight Team has included M. Abrahamson, B. Abu-Ata, A.-R. Behrozi, S. Bhaskaran, W. Blume, M. Carmichael, S. Collins, J. Diehl, T. Duxbury, K. Ellers, J. Fleener, K. Fong, A. Hewitt, D. Isla, J. Jai, B. Kennedy, K. Klassen, G. LaBorde, T. Larson, Y. Lee, T. Lungu, N. Mainland, E. Martinez, L. Montanez, P. Morgan, R. Mukai, A. Nakata, J. Neelon, W. Owen, J. Pinner, G. Razo Jr., R. Rieber, K. Rockwell, A. Romero, B. Semenov, R. Sharrow, B. Smith, R. Smith, L. Su, P. Tay, J. Taylor, R. Torres, B. Toyoshima, H. Uffelman, G. Vernon, T. Wahl, V. Wang, S. Waydo, R. Wing, S. Wissler, G. Yang, K. Yetter, and S. Zadourian. At Ball Aerospace, the Spacecraft Systems Team has included L. Andreozzi, T. Bank, T. Golden, H. Hallowell, M. Huisjen, R. Lapthorne, T. Quigley, T. Ryan, C. Schira, E. Sholes, J. Valdez, and A. Walsh.

Support for this work was provided by the *EPOXI* Project of the National Aeronautics and Space Administration's Discovery Program via funding to the Goddard Space Flight Center, and to Harvard University via Co-operative Agreement NNX08AB64A, and to the Smithsonian Astrophysical Observatory via Co-operative Agreement NNX08AD05A.

Chapter 5

The Kepler-19 System: A Transiting 2.2 $R_\oplus$ Planet and a Second Planet Detected via Transit Timing Variations

S. Ballard, D. Fabrycky, F. Fressin, D. Charbonneau, J.-M. Désert, G. Torres, G. Marcy, C. J. Burke, H. Isaacson, C. Henze, J. H. Steffen, D. R. Ciardi, S. B. Howell, W. D. Cochran, M. Endl, S. T. Bryson, J. F. Rowe, M. J. Holman, J. J. Lissauer, J. M. Jenkins, M. Still, E. B. Ford, J. L. Christiansen, C. K. Middour, M. R. Haas, J. Li, J. R. Hall, S. McCauliff, N. M. Batalha, D. G. Koch, & W. J. Borucki *The Astrophysical Journal*, Vol. 743, pp. 200-219, 2011

Abstract

We present the discovery of the Kepler-19 planetary system, which we first identified from a 9.3-day periodic transit signal in the *Kepler* photometry. From high-resolution spectroscopy of the star, we find a stellar effective temperature $T_{\rm eff}$=5541 ± 60 K, a metallicity [Fe/H]=-0.13 ± 0.06, and a surface gravity log(g)=4.59 ± 0.10. We combine the estimate of $T_{\rm eff}$ and [Fe/H] with an estimate of the stellar density derived from the photometric light curve to deduce a stellar mass of $M_\star = 0.936 \pm 0.040\ M_\odot$ and a stellar radius of $R_\star = 0.850 \pm 0.018\ R_\odot$ (these errors do not include uncertainties in the stellar models). We rule out the possibility that the transits result from an astrophysical false positive by first identifying the subset of stellar blends that reproduce the precise shape of the light curve. Using the additional constraints from the measured color of the system, the absence of a secondary source in the high-resolution spectrum, and the absence of a secondary source in the adaptive optics imaging, we conclude that the planetary scenario is more than three orders of magnitude more likely than a blend. The blend scenario is independently disfavored by the achromaticity of the transit: we measure a transit depth with *Spitzer* at 4.5 μm of 547^{+113}_{-110} ppm, consistent with the depth measured in the *Kepler* optical bandpass of 567±6 ppm (corrected for stellar limb-darkening). We determine a physical radius of the planet Kepler-19b of $R_p = 2.209 \pm 0.048\ R_\oplus$; the uncertainty is dominated by uncertainty in the stellar parameters. From radial-velocity observations of the star, we find an upper limit on the planet mass of 20.3 $M_\oplus$, corresponding to a maximum density of 10.4 g cm^{-3}. We report a significant sinusoidal deviation of the transit times from a

predicted linear ephemeris, which we conclude is due to an additional perturbing body in the system. We cannot uniquely determine the orbital parameters of the perturber, as various dynamical mechanisms match the amplitude, period, and shape of the transit timing signal and satisfy the host star's radial velocity limits. However, the perturber in these mechanisms has period $\lesssim$ 160 days and mass $\lesssim 6 M_{Jup}$, confirming its planetary nature as Kepler-19c. We place limits on the presence of transits of Kepler-19c in the available *Kepler* data.

5.1 Introduction

With the recent discoveries of the first transiting exoplanets intermediate in size between Earth and Neptune, namely CoRoT-7b (Léger et al. 2009), GJ 1214b (Charbonneau et al. 2009), Kepler-9d (Torres et al. 2011), Kepler-10bc (Batalha et al. 2011; Fressin et al. 2011), Kepler-11bcdf (Lissauer et al. 2011), and 55 Cancri b (Winn et al. 2011), astronomers have begun in earnest to probe this radius regime of exoplanets, for which no Solar System analog exists. Borucki et al. (2011) presents a catalog of 1235 transiting planetary candidates, of which nearly 300 have a radius estimate in the range $1.25 < R_p < 2.0\ R_\oplus$. While most of these candidates have not yet been confirmed as authentic planets, Morton & Johnson (2011) have shown that the rate of false positives is expected to be low for the *Kepler*-identified sample. The composition of such planets may be widely variable, as exemplified by the case of GJ 1214b (Charbonneau et al. 2009), for which the measured radius and mass were consistent with both a hydrogen

envelope or a pure CO_2 or H_2O atmosphere (Miller-Ricci & Fortney 2010). It was only with follow-up studies of the atmosphere in transmission that it became possible to distinguish among the various possibilities for the composition of GJ 1214b (Bean et al. 2010; Croll et al. 2011; Désert et al. 2011).

The limiting precision of the current state-of-the-art radial velocity observations (meters per second) presents a challenge for the dynamical confirmation of these small planets. In the case of the 1.42 $R_\oplus$ transiting planet Kepler-10b, Batalha et al. (2011) gathered 40 high-resolution spectra at the Keck telescope (Vogt et al. 1994) to determine a mass of $4.56^{+1.17}_{-1.29}$ $M_\oplus$. In the absence of radial velocity confirmation, however, it is still possible to make a statistical argument for the planetary nature of the candidate, if the combined likelihood of all false positive scenarios (namely, blends of stars containing an eclipsing member) is sufficiently smaller than the planet scenario. This process of "validation" for *Kepler*-identified planetary candidates has already been applied to three planets in the 1.5-3 $R_\oplus$ radius range: Kepler-9d (Torres et al. 2011), Kepler-11f (Lissauer et al. 2011), and Kepler-10c (Fressin et al. 2011).

Transiting planets are also of interest as they present an opportunity to identify yet more planets in the system by the method of transit timing variations (TTVs). Since this method was proposed (Holman & Murray 2005; Agol et al. 2005), the search for planets by TTVs has been a major activity in exoplanet research. Steffen & Agol (2005) applied a lack of significant TTV variations in the TrES-1 system to deduce constraints on the existence of additional, non-transiting planets. Subsequent works, such as Miller-Ricci et al. (2008a) for HD 189733,

using *MOST* observations, Bean (2009) for CoRoT-1, using the CoRoT satellite, Gibson et al. (2009) for TrES-3, using observations gathered at the Liverpool Telescope, and Ballard et al. (2010b) for GJ 436, using *EPOXI* observations, have also used transit times to rule out companions, specifically companions in resonances, for which the TTV method is particularly sensitive to low-mass planets. The *Kepler* team has presented two cases of transit timing variations in exoplanetary systems: Kepler-9 (Holman et al. 2010) and Kepler-11 (Lissauer et al. 2011). In both of these cases, the additional planet (or planets) responsible for the transit timing signal also transit, which enabled mutual constraints on the masses of the planets as predicted by Holman & Murray (2005). Over the past year, the *Kepler* team has also presented instances of single-transiting candidate systems showing transit timing variations, but has not confirmed the planetary nature of the candidates or perturbers (Ford et al. 2011). Meanwhile, using ground-based observations, several groups have described their transit times as being inconsistent with a linear ephemeris, though two such claims have been revisited by groups who could not confirm the result. In the case of HAT-P-13, while Pál et al. (2011) and Nascimbeni et al. (2011) found evidence for a companion from the transit times of HAT-P-13b, Fulton et al. (2011) demonstrated that the times were consistent with a linear ephemeris (with the exception of a single transit). In the case of OGLE-111b, Díaz et al. (2008) claimed that the transit times were inconsistent with a linear ephemeris, but an analysis by Adams et al. (2010) with additional transit observations found no evidence for TTVs or duration variations and pointed to systematic errors in

previous photometry. Maciejewski et al. (2010) and Fukui et al. (2011) presented evidence for transit timing variations in the WASP-3 and WASP-5 systems, respectively, but cautioned that additional transits are necessary to confirm or refute the signal (Fukui et al. 2011 expressed caution about unknown systematic effects). Maciejewski et al. (2011) presented evidence for TTVs of WASP-10b, and they reported a two-planet orbital solution that fit the TTVs and radial velocities better than alternative orbital models they found, which was not achieved in prior work.

In this paper, we present the discovery of two planets orbiting Kepler-19. The star, which has right ascension and declination 19h21m40.99s and +37d51m06.5s, *Kepler* magnitude Kp=11.90, and *Kepler* Input Catalog number 2571238, was identified to host a planetary candidate in the catalog of 1235 *Kepler* identified candidates published by Borucki et al. (2011). In that work, the star was identified by the *Kepler* Object of Interest (KOI) designation KOI-84. The first planet, identified by its transits, has a period of 9.3 days and a radius of 2.2 $R_{\oplus}$, as we discuss below. We validate the planetary nature of the transit signal by a blend analysis. The second planet, Kepler-19c, was identified by transit timing variations. We see no evidence for transits of Kepler-19c in the available *Kepler* data. This detection differs from the ones using ground-based data, summarized in the previous paragraph, in several ways. In the case of Kepler-19, the transiting object has a radius of only 2.2 $R_{\oplus}$, whereas other claims are for perturbations to the transit times of hot Jupiters. Additionally, as we show below, we have well-sampled the TTV signal, since we have measured the transit times

of Kepler-19b at a cadence 30 times shorter than the TTV period. Finally, the TTV signal reported here is a much higher signal-to-noise detection. In Section 2, we present the *Kepler* time series from which we detected the system. In Section 3, we present our characterization of the Kepler-19 system from the photometry. And in Section 4, we summarize our follow-up observations of the star. In Section 5, we present the validation of Kepler-19b as a planet. In Section 6, we discuss our constraints on the nature of the perturbing planet Kepler-19c from transit timing variations, as well as our inferred constraints on the composition of the transiting planet Kepler-19b.

5.2 *Kepler* Observations

The *Kepler* spacecraft, launched on 7 March 2009, will photometrically monitor 170,000 stars for 3.5 years for evidence of transiting planets. Argabright et al. (2008) gives an overview of the *Kepler* instrument, and Caldwell et al. (2010) and Jenkins et al. (2010b) provide a summary of its performance since launch. The *Kepler* observations of Kepler-19 that we present in this work were gathered from 5 May 2009 to 5 March 2011. This range spans *Kepler* "Quarters" 0–8; *Kepler* operations are divided into four quarters each year. At the end of each quarter, *Kepler* rotates the spacecraft by 90° to maintain illumination of the solar panels (though the Quarter 0 pre-science commissioning data were gathered in the same configuration as Quarter 1). For Quarters 3–8, the observations of Kepler-19 were gathered continuously with an exposure time of 58.8 seconds, corresponding to the

"short cadence" (SC) mode of the instrument, described by Jenkins et al. (2010b) and Gilliland et al. (2010), while data from Quarters 0, 1, and 2 were gathered in long-cadence mode (characterized by an exposure time of 29.5 minutes). The data contain gaps of approximately 3 days between quarters for scheduled downlinks. We used the raw light curves generated by the *Kepler* aperture photometry (PA) pipeline, described in Twicken et al. (2010), to which we add two additional steps. First, we remove the effects of baseline drift by individually normalizing each transit. We fit a line with time to the flux immediately before and after transit (specifically, from 9 hours to 20 minutes before first contact, equal to 2.5 transit durations, and an equivalent time after fourth contact). We divide this line from the observations spanning five transit durations and centered on the predicted transit time. For the observations gathered outside of transit, we apply a median filter, with width equal to one day, in order to remove baseline drift over timescales of days. We observed slight flux offsets between observations that occurred after gaps of larger than 1 hour (either for data download, quarterly rolls, or safe modes). The *Kepler* time series of Kepler-19 are shown in Figure 1.

Figure 5.1.—: (Following page) Kepler-19 relative photometry from Quarters 0-8, as a function of barycentric Julian Day. Data from quarters 0, 1, and 2 were gathered in long-cadence observing mode, while data from quarters 3-8 were gathered in the short-cadence mode. *Top panel:* The raw flux depicted in red (with bin size of 1/3 days). We have multiplied the short-cadence observations by a factor of 30 to account for the exposure time ratio between modes, so that all observations appear on the same scale. The gaps between quarters are depicted by dashed lines. To remove the flux offsets between quarterly rolls, we compare the mean brightness during the first two hours of each quarter to the mean of final two hours of the previous quarter, and divide this ratio value from the flux over the entire quarter. This corrected flux is shown in black. *Bottom panel:* the detrended *Kepler* light curve, after applying a median filter with width equal to one day and normalizing individual transits as described above. This light curve is depicted with a binsize of 1 hour, so that individual transit events are apparent. Gaps of longer than one hour in the observations are associated with instances of correlated noise in the corrected light curve.

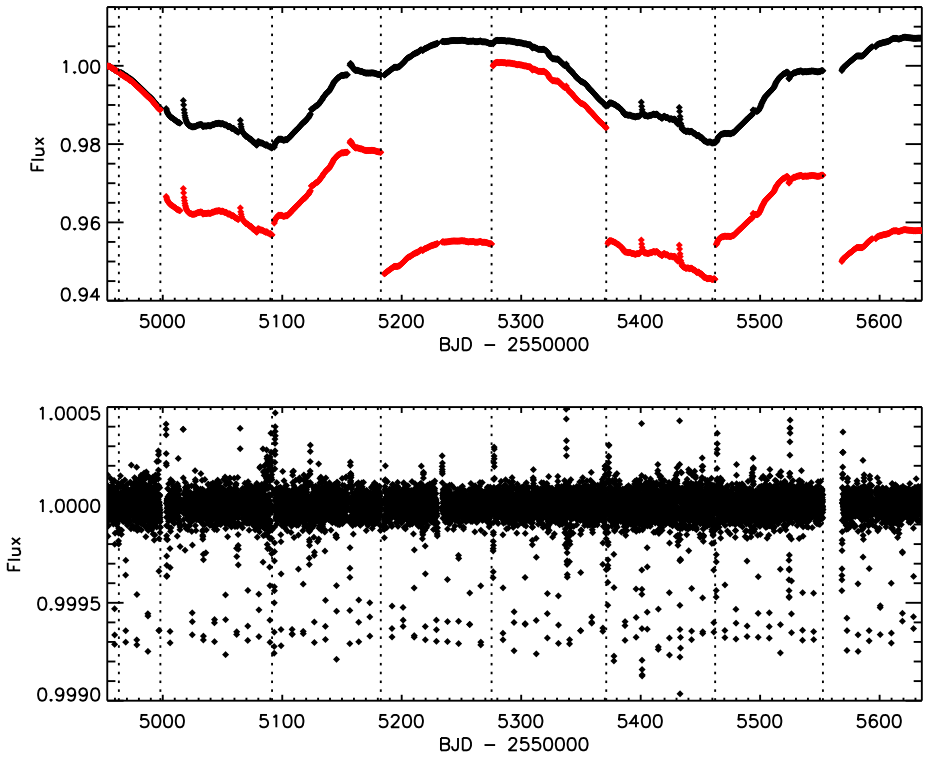

Figure 5.1.—: (Continued).

5.3 Analysis

5.3.1 Derivation of Planetary Parameters from the *Kepler* Light Curve

The traditional procedure for fitting the phased transit light curve relies on the assumption of a linear ephemeris. In this case, that assumption does not hold: the transit times deviate from a linear ephemeris in a nearly sinusoidal manner, with a period of about 316 days and an amplitude of about 5 minutes (as compared to a transit duration of 3.5 hours). We incorporated the transit timing deviations into the light curve parameter fit in an iterative sense, similar to the procedure described by Lissauer et al. (2011) for the transit times of the Kepler-11 planets: we first estimate the light curve parameters with an assumption of a linear ephemeris. We then fit for the epoch of each individual transit using these parameters in a manner that we describe below (with the exception of the epoch, which we allow to float for each transit). Finally, we shift the transits by their measured timing deviation, refold the light curve, and repeat the fit for the parameters. We repeat this process until all parameters converged, and found that it converged after only two iterations. We note that we employed only the subset of short cadence observations for fitting the light curve parameters themselves. The addition of the long cadence observations from Quarters 0-2 to the analysis would have contributed only a very modest improvement to our knowledge of the parameters.

We estimated the uncertainty in the parameters using the Markov Chain Monte Carlo (MCMC) method as follows, using a Metropolis-Hastings algorithm with Gibbs sampling Tegmark et al. (2004). We employ model light curves generated with the routines in Mandel & Agol (2002), which depend upon the period P, the epoch T_c, the planet-to-star radius ratio $R_p/R_\star$, the ratio of the semi-major axis to the stellar radius $a/R_\star$, the inclination of the orbit i, and two quadratic limb-darkening coefficients u_1 and u_2. We assume an eccentricity of zero for the orbit, which we discuss in further detail in Section 3.2. We choose randomly one parameter, perturb it, and evaluate the χ^2 of the solution. If the χ^2 is lower, we accept the new parameter value. If the χ^2 is higher, we evaluate the probability of accepting the jump as $p = e^{-\Delta\chi^2/2}$. We adjust the width of the distribution from which we randomly draw the jump sizes in each parameter until 20–25% of jumps are executed in each of the parameters. We created five chains, each of length 10^6 points, where each of the chains is begun from a different set of starting parameters (each parameter is assigned a starting position that is $+3\sigma$ or -3σ from the best-fit values). We discard the first 20% of jumps from each chain to remove the transient dependence of the chain on the starting parameters.

After the first iteration of the MCMC procedure, we locate the best solution in the χ^2 sense, and use these parameters to fit the individual times of transit for observations gathered in both short and long cadence observing mode. We fix all parameters with the exception of the center of transit time, which we allow to vary over a range of 30 minutes for each transit, centered on the predicted transit time from a linear ephemeris, in intervals of 6 seconds. In this case, we account

for the finite integration time by taking a numerical average of an oversampled model (evaluated at 6 second intervals) over a period corresponding to the exposure time (58.8 seconds for short-cadence observations, and 29.5 minutes for long-cadence observations). We determine the center of transit time from the epoch associated with the minimum χ^2 value, and the error from the range over which $\Delta\chi^2 < 1$ when compared to the minimum value. In practice, this results in asymmetric error bars for many of the individual transits. We also conduct an analysis to determine the contribution of quarter-by-quarter correlated noise to the transit time measurements, whereby we inject transits with the same light curve parameters as we derive for Kepler-19b into the *Kepler* light curve, and then fit for the transit times in an identical fashion to the authentic transits. Based upon a typical deviation of these times from the injected time (as compared to their error bars), we inflate the error bars for the short-cadence observations by factors of 1.32, 1.15, 1.45, 1.40, 1.18, and 1.20 for Quarters 3–8, respectively. These values are consistent with the larger scatter of the transit times in the latter quarters, as discussed in further detail in Section 6.1. The transits gathered in long cadence from Quarters 0–2 show errors that are consistent with Gaussian noise, and so we do not apply a scaling factor to these error bars. After two iterations of the steps described above, we found that the measured individuals transit times varied by less than 10 seconds between the two iterations. We fixed the average period to the one determined by the final fit to the transit times for the final MCMC analysis.

In Figure 5.2, we show the MCMC correlations between all free parameters

in the model fit, as well as the histograms corresponding to each parameter. In Figure 5.3, we show the *Kepler* transit light curve for Kepler-19b (which is phased to the best period after shifting the transit times by the values given in Table 5.6.5), with the best-fit transit light curve overplotted. We report the best-fit parameters and uncertainties in Table 5.3.2. The range of acceptable solutions for each of the light curve parameters ($R_p/R_\star$, $a/R_\star$, and i) is determined as follows. We report the "best" solution from the set of parameters that minimize the χ^2. The error bars are then given by the highest and lowest values that are within the 68% of points closest in χ^2 to the best value. We additionally calculate the transit duration, impact parameter, and ingress duration, using the formulae given in Seager & Mallén-Ornelas (2003) and Winn et al. (2010) to create the distribution in those quantities from the parameters in the MCMC chains. In some cases, the error bar is asymmetric (for $a/R_\star$ and i, which we expect from their asymmetrical MCMC distributions). We report the transit times, deviation from a linear ephemeris, and errors in Table 5.6.5. Figure 5.4 shows the individual timing deviations from the best linear ephemeris. In Figure 5.5, we show a binned subset of "late" and "early" transits, comprised of five transits each (corresponding to numbers 26–30 and numbers 39–43 listed in Table 5.6.5), over which we plot a model generated with a linear ephemeris. The deviation of the transit times from the predicted T_c of five minutes, which is equal to approximately one ingress time, is apparent.

We also performed the MCMC analysis with the two quadratic limb-darkening coefficients (LDCs), u_1 and u_2, fixed to theoretical values. We used the values for

the effective stellar temperature $T_{\rm eff}$, metallicity [Fe/H], and surface gravity log(g) derived from our Spectroscopy Made Easy (SME) analysis of the Keck HIRES spectra (see Section 4.2): $T_{\rm eff}$=5541 ±60 K, [Fe/H]=-0.13±0.06 dex, and log(g) of 4.59 ± 0.1 dex. In this case, the closest stellar model from the tables of theoretical limb-darkening coefficients generated for the *Kepler* bandpass by Prsa (2011) corresponded to a model with $T_{\rm eff}$=5500 K, log(g)=4.5, and [Fe/H]=0.0: these coefficients are u_1=0.5 and u_2=0.18. Our results for the planetary parameters were consistent with the values we obtained while allowing the limb-darkening coefficients to float, but the error bars were slightly smaller with fixed LDCs. In particular, the LDC derived from the light curve lie within 1σ of the theoretical values for u_1 and u_2, and the largest deviation in the derived parameters is 1.4σ for $R_p/R_\star$. The difference between the best χ^2 values (between fixing the LDCs or allowing them to float) is approximately equal to five, which is roughly consistent with the addition of two degrees of freedom.

Figure 5.2.—: (Following page) Markov Chain Monte Carlo probability distributions for light curve parameters of Kepler-19b. The dark grey area encloses 68% of the values in the chain, while the light grey area encloses 95% of the values. We assign the range of values corresponding to 1σ confidence from the area enclosing 68% of the values nearest to the parameters associated with the minimum χ^2 (as described in the text).

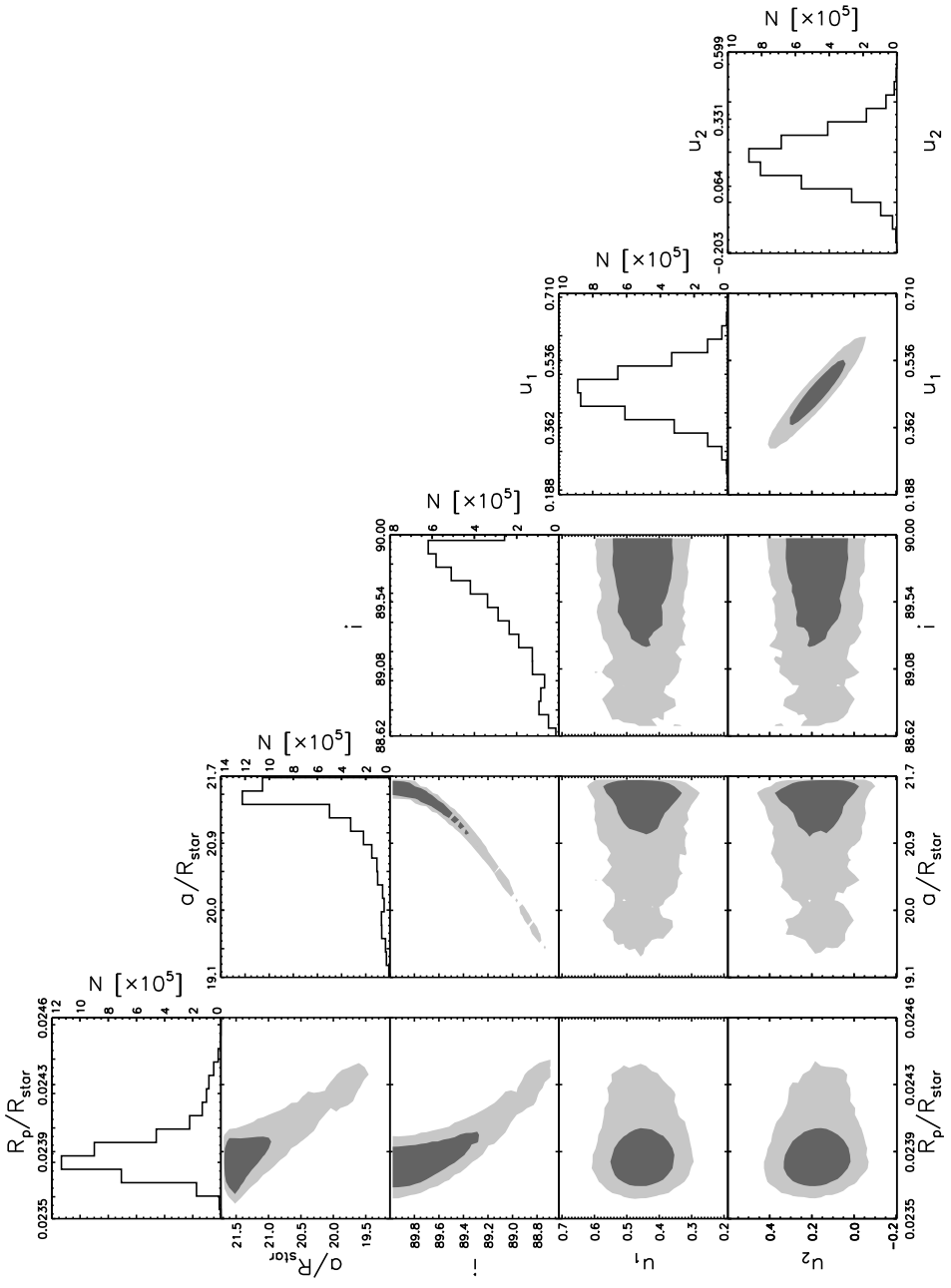

Figure 5.2.—: (Continued).

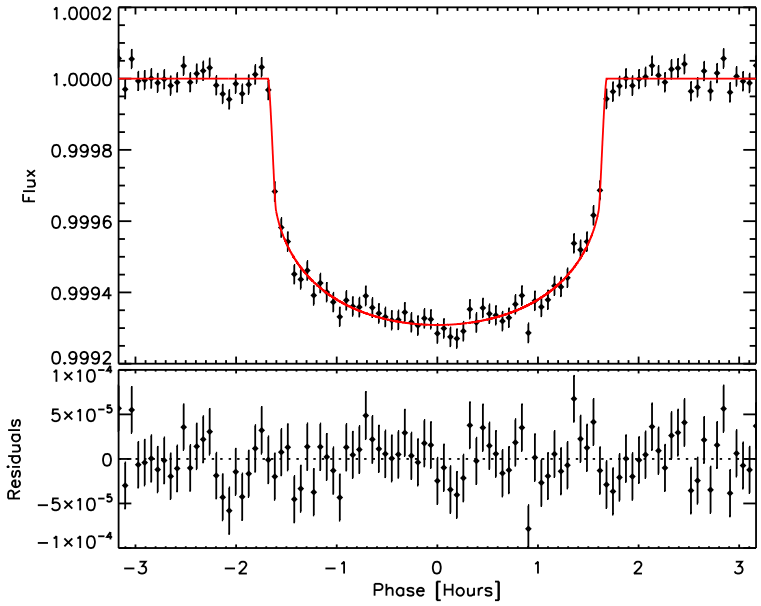

Figure 5.3.—: *Kepler* transit light curve for the short-cadence observations of Kepler-19, centered on time of transit, with transit timing variations removed, and binned by a factor of 40 (binsize of 4 minutes). Overplotted in red is the best transit model light curve, with parameters given in Table 5.3.2. The bottom panels shows the residuals of the light curve, after the model is subtracted.

5.3.2 Physical Parameters

We based our procedure for constraining the mass, radius, and age of the host star on the method described by Torres et al. (2008). Using the metallicity determined from SME (described in Section 4.2), we created a set of stellar evolution models from the Yonsei-Yale (Y^2) isochrone series by Yi et al. (2001), with corrections from Demarque et al. (2004). We employed the interpolation

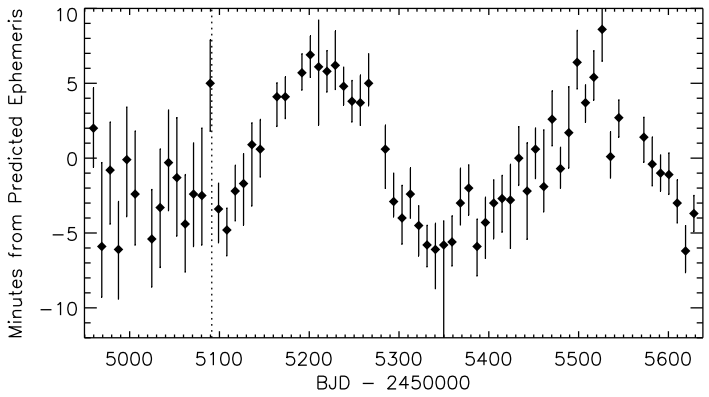

Figure 5.4.—: *Kepler* transit times for Kepler-19b from Quarters 0-8, as compared to the best linear ephemeris model. The linear ephemeris we use to generate these O-C values is given in Table 5.3.2, and the individual transit times are given in Table 5.6.5. The demarcation between long cadence and short cadence observations is shown with a dotted line.

software that accompanied that work, which accepts as inputs the age of the star, the iron abundance, and the abundance of α-elements relative to solar (for which we assume the solar value), and outputs a grid of stellar isochrones corresponding to a range of masses. We evaluated a set of isochrones over an age range of 0.1 to 14 Gyr (at intervals of 0.1 Gyr) and in [Fe/H] in 60 equally spaced increments from -3σ to $+3\sigma$ above and below the best-fit value of [Fe/H]$=-0.13 \pm 0.06$. We then performed a spline interpolation of each output table at a resolution of 0.005 $M_{\odot}$ in effective temperature $T_{\rm eff}$, the log of the surface gravity log(g), and the stellar luminosity $L_{\star}$. We evaluate the physical radius corresponding to each stellar model via log(g) and the mass of the star ($g = GM_{\star}/R_{\star}^2$), though it is

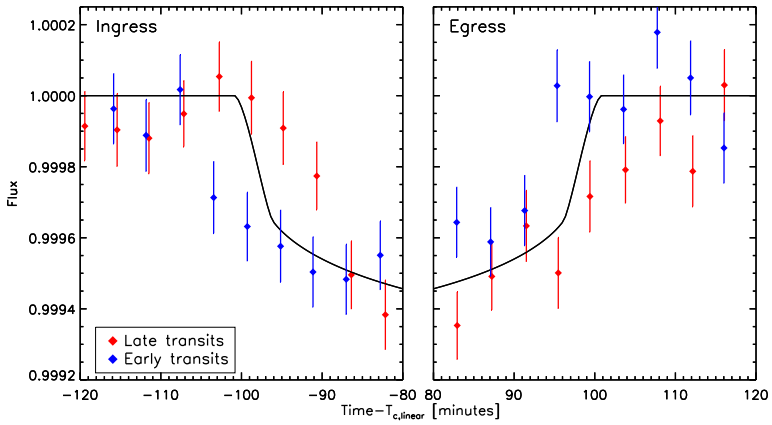

Figure 5.5.—: A binned subset of five "late" transits of Kepler-19b (in red, comprised of individual transit numbers 26–30 listed in Table 5.6.5) and five "early" transits (in blue, comprised of transit numbers 39-43), with best linear transit model overplotted. At left, we show the binned transits centered on time of ingress, and at right, centered on time of egress.

also possible to convert to physical radius using the model stellar luminosity and effective temperature (assuming $L_\star = 4\pi R_\star \sigma T^4$); in practice these conversions give identical results.

Rearranging Kepler's version of Newton's third law in the manner employed by Seager & Mallén-Ornelas (2003), Sozzetti et al. (2007) and Torres et al. (2008), we convert the period (derived from photometry), and the radius and mass of the host star (from isochrones) to a ratio of the semi-major axis to the radius of the host star, $a/R_\star$:

$$\frac{a}{R_\star} = \left(\frac{G}{4\pi^2}\right)^{1/3} \frac{P^{2/3}}{R_\star}(M_\star + M_p)^{1/3}, \tag{5.1}$$

where we assume that M_p is negligible when compared to the mass of the host star, and that the orbit is circular. Using the MCMC sequence of $a/R_\star$ and generating a series of Gaussian random realizations of [Fe/H] and $T_{\rm eff}$ using the values and error bars derived from spectroscopy, we locate the best isochrone fit at each realization using the χ^2 goodness-of-fit

$$\chi^2 = \left(\frac{\Delta a/R_\star}{\sigma_{a/R_\star}}\right)^2 + \left(\frac{\Delta T_{\rm eff}}{\sigma_{T_{\rm eff}}}\right)^2 + \left(\frac{\Delta[{\rm Fe/H}]}{\sigma_{[{\rm Fe/H}]}}\right)^2. \tag{5.2}$$

Using the output of the MCMC chain of $a/R_\star$ ensures that correlations between parameters, which are preserved in the chain, are properly incorporated into our estimate of the stellar parameters.

We then assign a weight to the likelihood of each stellar model in the chain by applying a prior for the initial mass function (IMF) that assumes a Salpeter index (Salpeter 1955). The number of stars of each mass and age, per 1000 stars, is generated by the interpolation software provided by Yi et al. (2001) for several IMF assumptions, including the Salpeter IMF. We designate the weight assigned to each stellar model in the chain by normalizing to the highest IMF value within the sample: in practice, the weights vary from 0.2 to 1 (from the least to most likely). We then incorporate this likelihood by discarding members of the chain according to their weight, where the weight is equal to the likelihood of remaining in the chain. About 50% of the original chain remains intact after this stage. The value for each stellar parameter is then assigned from the median of this weighted

distribution, with the formal error bars assigned from the nearest 68% of values above and below the median. We find $M_\star$= 0.936 ± 0.040 $M_\odot$, $R_\star$= 0.850 ± 0.018 $R_\odot$, and an age = 1.9 ± 1.7 Gyr. These uncertainties exclude possible systematic uncertainties in the stellar models. Using the modified MCMC chain in both stellar radius and $R_p/R_\star$ to determine the physical radius of the planet, we find R_p=2.209 ± 0.048 $R_\oplus$. The IMF prior changes the final answer by less than 1σ for all physical parameters, and by 0.1σ in the case of the planetary radius.

We note that we also recorded the log(g) of the best stellar model for each realization of $T_{\rm eff}$, [Fe/H], and $a/R_\star$, as described above. From this analysis, we find a log(g) of 4.54±0.02, which is consistent with the value inferred from spectroscopy of 4.59±0.10. We conclude that the assumption of zero orbital eccentricity for the transiting planet is consistent with the value of log(g) measured spectroscopically. However, using the analytic formulae presented in Carter et al. (2008), the derived log(g) would vary by only 0.04 dex if the eccentricity were as high as 0.15 (which Moorhead et al. 2011 found was typical for the sample of *Kepler* Objects of Interest), which is well below our measured uncertainty on log(g).

Table 5.1. Star and Planet Parameters for Kepler-19

Parameter	Value
Kepler-19 [star]	
Right ascension	19h21m40.99s
Declination	+37d51m06.5s
[Fe/H]	-0.13±0.06
log(g) [cgs]	4.59±0.10
$T_{\rm eff}$ [K]	5541±60
v sin i [km s^{-1}]	< 2
$M_\star$ [$M_\odot$]	0.936±0.040
$R_\star$ [$R_\odot$]	0.850±0.018
Age [Gyr]	1.9±1.7
Kepler-19b	
Period [days]	9.2869944±0.0000088[a]
T_c [BJD-2450000]	4959.70597±0.00036
$R_p/R_\star$	0.02379±0.00012
$a/R_\star$	$21.59^{+0.15}_{-0.37}$
i [degrees]	$89.94^{+0.06}_{-0.44}$
u_1	0.466±0.061
u_2	0.155±0.097
Impact parameter, b	$0.02^{+0.16}_{-0.02}$
Transit duration, τ [min]	201.91±0.47
Ingress duration, τ_{ing} [min]	$4.70^{+0.18}_{-0.57}$
R_p [$R_\oplus$]	2.209±0.048
M_p [$M_\oplus$]	<20.3[b]
Kepler-19c	
Period [days]	<160[c]
M_p [$M_{\rm Jupiter}$]	<6.0[c]

[a]The period and T_c values for Kepler-19b are determined from a linear fit to the transit times.

[b]The upper limit on the mass of Kepler-19b is determined from the radial velocity analysis in Section 4.2.

[c]The upper limit on the mass and period of Kepler-19c is described in the text of Section 6.1.2.

5.4 Follow-up Observations

5.4.1 Reconnaissance Spectroscopy

We gathered reconnaissance spectra of Kepler-19 on UT 2009 August 05 (orbital phase 0.596), 2009 August 29 (phase 0.161) and 2010 October 1 (phase 0.017) with the Tull coude spectrograph of the McDonald Observatory 2.7m telescope. We used these high resolution (R=60,000) spectra to verify the Kepler Input Catalog stellar classification and to search for evidence of any secondary stellar spectrum or binary orbital motion. We cross-correlated the spectra against a library of synthetic stellar spectra as described by Batalha et al. (2011). The spectra did not show any evidence of a secondary spectrum, and the absolute radial velocities, which cover both orbital quadratures, agree at the 0.75 km/s level. These spectra gave the best match to the synthetic templates with $T_{\rm eff}$ = 5750 K, log(g)= 4.5, and v sin i = 2 km s^{-1}, for an assumed solar metallicity. The height of the cross-correlation peaks was 0.98 for all of the spectra, indicating an excellent fit to the stellar template spectra.

5.4.2 High-resolution Spectroscopy

Between 2009 October 29 and 2011 June 10 we gathered 8 high-resolution spectra of Kepler-19 with the Keck HIRES spectrometer (Vogt et al. 1994). With these spectra, we conducted an analysis to determine the stellar parameters. We compared a high-resolution template spectrum to stellar models, generated

with the spectral synthesis package Spectroscopy Made Easy (SME; Valenti & Piskunov 1996; Valenti & Fischer 2005). We determine the effective temperature $T_{\rm eff}$ of the host star of 5541 ± 60 K, a metallicity [Fe/H] of -0.13 ± 0.06 dex, a log(g) of 4.59 ± 0.1 dex, and a v sin $i < 2$ km s^{-1}. We comment briefly here on the stellar activity. We find a value of the ratio of emission from the Ca II H and K lines to the total bolometric emission of log(R_{HK})=-4.95±0.05. The R_{HK} value is derived from a Mt. Wilson style S-value of 0.174±0.007 (Isaacson & Fischer 2010). The log(R_{HK}) value is low for main sequence stars of this temperature and is consistent with the slow stellar rotation we infer from the measured v sin i of <2 km s^{-1}. If we assume rigid body rotation of the star and a stellar spin axis aligned with the orbital spin axis of the planet, we find a lower limit on the stellar rotation period of 22 days. The rotation period derived from the R_{HK} value is 32 days (Noyes et al. 1984) which along with the lack of emission in the core of the Ca II H and K lines leads us to conclude that the star is relatively inactive.

We further used the spectra to derive estimates of the stellar radial velocity. The spectra were gathered with the same configuration of HIRES, described in Marcy et al. (2008), which was demonstrated to yield typical precisions of 1.0 to 1.5 m s^{-1} on nearby FGK stars. This method relies on the use of an iodine cell placed in front of the beam, which superimposes the iodine spectrum on the stellar spectrum with an identical instrumental profile. For each 100 pixel section of the spectrum, the iodine and stellar spectral lines are fit simultaneously. For the set of these observations, this treatment yields a typical internal error estimate on individual radial velocities of 1.5 m s^{-1}. We note also the use of the

"C2 decker" entrance aperture for all of these observations, which technique is described in greater detail in Batalha et al. (2011), and enables sky subtraction (as compared to the "B5 decker", for which sky subtraction is not possible). We list the measured radial velocities, with associated error bars (excluding stellar jitter), in Table 5.4.2. We gathered twelve additional observations prior to the ones listed in Table 5.4.2 but these were observed with the B5 configuration, and had a much higher scatter (15 m s^{-1} as opposed to 4 m s^{-1}). For this reason, we excluded them from the analysis.

We determine the upper mass limit on Kepler-19b from the radial velocities as follows. We employ the Bayesian MCMC technique described in Gregory (2007) to fit a radial velocity model to the observations. The free parameters in the model are the semi-amplitude velocity K of the star, the zero-point velocity γ, the eccentricity e of the planetary orbit, the argument of perihelion ω, and a stellar jitter term. The orbital period and transit epoch are also free parameters, however the precision of the Gaussian priors we place on them from the light curve analysis (see Table 5.3.2) effectively fixes their values. Additionally, we fix the inclination of the orbit to the value measured from the light curve of 89.94°. We first fit a model, assuming a circular orbit. In this case, we infer a stellar jitter contribution of 4.1 ± 1.7 m s^{-1}, and 1, 2 and 3σ upper limits on the semi-amplitude of 1.4, 3.3, and 4.9 m s^{-1}, respectively (these values are derived from integrating over the posterior distribution of semi-amplitude until 68%, 95%, and 99.73% of the area is enclosed). Applying the semi-amplitude toward a mass upper limit, we determine a 3σ upper limit on the mass of $< 15.2\ M_{\oplus}$, if the

orbit is circular (these upper limits are 4.3 and 10.2 $M_{\oplus}$ at 1 and 2σ confidence). The most likely fit (depicted as the solid line in Figure 5.6) has an amplitude of 0.5 m s^{-1} (corresponding to a mass of 1.6 $M_{\oplus}$), but this value is well below our detectability threshold. For comparison, we also show representative circular orbit at the 3σ upper limit for semi-amplitude (dashed line in Figure 5.6).

We also address the possibility of a non-zero eccentricity. If the orbit were significantly eccentric, then the transit duration of Kepler-19b would deviate from the predicted duration for the edge-on circular orbit scenario, unless the argument of perihelion conspired to mimic the circular transit duration. As eccentricity increases, there is an increasingly narrow range of ω that matches the transit duration of a circular orbit. As we demonstrate in Section 3, the assumption of a circular orbit is consistent with the well-constrained low impact parameter (high inclination) measured from the the *Kepler* light curve, as illustrated by the short ingress and egress times. In addition the log(g) inferred from the light curve analysis assuming zero eccentricity agrees with the independent spectroscopically determined value. We note that the planet is too small to constrain the eccentricity from secondary eclipse observations; we discuss this possibility further in Section 6.3. Therefore, we elected to impose a prior on e and ω from our knowledge of the transit duration, as follows. The ratio τ of the transit duration for an eccentric orbit to the transit duration for a circular orbit can be approximated by the following expression of the eccentricity and argument of perihelion (Burke 2008):

$$\tau = (1 - e^2)^{1/2}/(1 + e\cos(\omega - \pi/2)). \quad (5.3)$$

For each element of the MCMC chain, for which we now vary e and ω, we evaluate the transit duration ratio τ. We then assign a flat prior on τ, which is equal to one for $0.7 < \tau < 1.3$ (that is, the transit duration is within 30% of circular) and zero otherwise. Applying this transit duration prior during the radial velocity parameter estimates, we find a negligibly smaller estimate for the stellar jitter than the circular orbit case and semi-amplitude upper limits (again, with 1, 2, and 3σ confidence respectively) of 2.0, 9.2, and 23.5 m s^{-1}. These semi-amplitudes are associated with mass upper limits of 5.5, 20.3, and 50.3 $M_\oplus$, with the same stated confidences. Given the radius value for the planet determined from the *Kepler* photometry and the 2σ upper mass limit of 20.3 $M_\oplus$, we find an upper limit on the density of Kepler-19b of 10.4 g cm^{-3}. We comment further on the possible composition of the planet, given these upper limits, in Section 6.4.

5.4.3 Adaptive Optics Imaging

We gathered adaptive optics images in J band of Kepler-19 on UT 24 September 2009, using the PHARO near-infrared camera (Hayward et al. 2001) on the the Hale 200 inch telescope on Mt. Palomar, CA. Troy et al. (2000) give a complete description of the Palomar adaptive optics system. We employed a dither pattern for these observations similar to the technique described in Batalha et al. (2011), although we used an exposure time of 4.25 seconds. In Figure 5.7, we show the

Table 5.2. Relative Radial Velocities for Kepler-19

HJD -2450000	RV m s^{-1}	Unc. m s^{-1}
5134.805	0.9	2.1
5320.113	0.4	1.7
5402.956	5.9	1.5
5407.827	-6.5	1.4
5412.981	-0.2	1.6
5435.879	5.5	1.3
5723.074	2.0	1.5
5723.950	4.0	1.5

Note. — Uncertainties do not include stellar jitter, which is likely to be near 4 m s^{-1}.

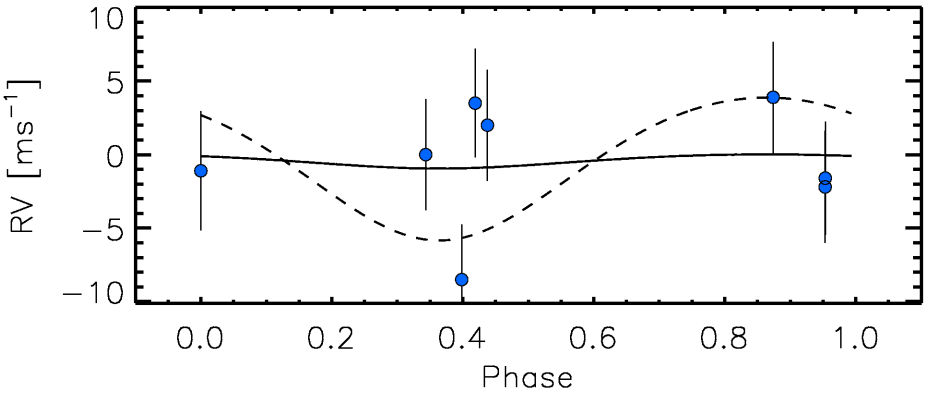

Figure 5.6.—: Measured radial velocities of Kepler-19, as a function of phase (assuming the orbital period and epoch of Kepler-19b, as stated in Table 5.3.2). We have depicted two radial velocity models with zero eccentricity, the first (dashed) corresponding to a planetary mass at the 3σ upper limit of 15.2 $M_{\oplus}$, and the second (solid) corresponding to the most likely amplitude of 0.5 m s^{-1} (or 1.6 $M_{\oplus}$). The error bar depicted include the effects of stellar jitter, which we conclude are near 4 m s^{-1}.

local neighborhood of Kepler-19 within 10 arcseconds.

We assess our sensitivity to additional sources using a similar procedure to that described by Batalha et al. (2011). We inject fake sources near the target star at random position angles, using steps in magnitude of 0.5 mag and varying the distance from the target star in increments of 1.0 FWHM of the point-spread function (PSF). We then attempt to identify the injected sources with the DAOPhot routine (Stetson 1987) and also by eye, and set our sensitivity limit, as a function of distance, at the magnitude where we are able to recover the

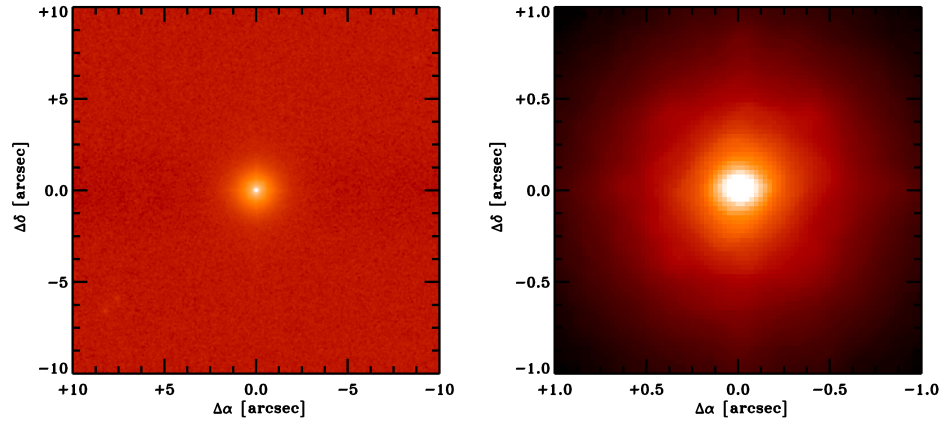

Figure 5.7.—: J-band adaptive optics image of the neighborhood of Kepler-19, within 10 arcseconds (left) and 1 arcsecond (right).

injected sources. The limit in Δm as a function of distance from the target star is shown in Figure 5.8. We then convert the Δm sensitivity limit in J band to a limit in *Kepler* magnitudes, by assuming a nominal *Kepler* magnitude-J color (using the value derived from a magnitude-limited sample of Kp-J=1.28±0.52 mag). We do not detect any additional sources within our sensitivity limits in the neighborhood of Kepler-19.

5.4.4 Speckle Imaging

We gathered speckle images of Kepler-19 using filters in both R and V band on UT 18 June 2010, using the Differential Speckle Survey Instrument located at the WIYN telescope (DSSI, Horch et al. 2009) A detailed discussion of the recent upgrades to DSSI is presented in Horch et al. (2010). We assess our

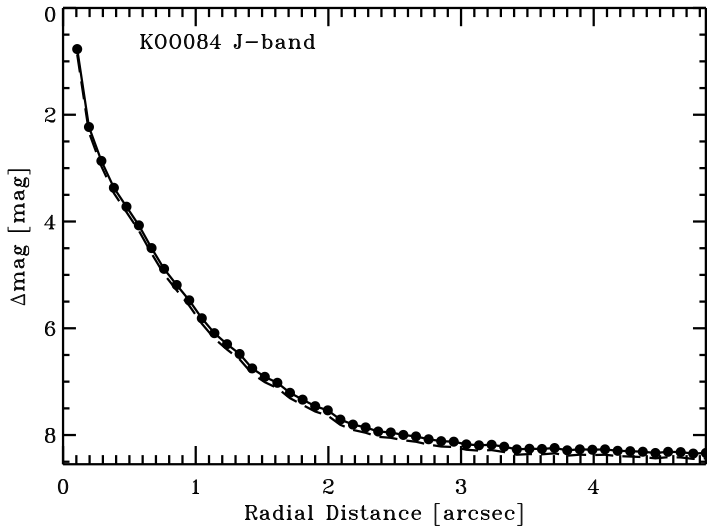

Figure 5.8.—: The sensitivity limits to additional point sources in the neighborhood of Kepler-19b as a function of radial distance from the primary target. The filled circles represent the J-band limits and each point represents a step in FWHM away from the primary target centroid peak. The dashed line underneath represents the J-band limits converted to *Kepler* magnitude limits if a star were to have a nominal Kp-J color, as described in the text.

sensitivity to the presence of additional stars near the *Kepler* target star as a function of angular distance. For concentric rings of varying radius, centered on the target star, we determine the magnitude difference between the target star itself and the local extrema of the sky background. Figure 5.9 shows the results of this procedure in both R and V band. We find that we would have detected a companion at a distance of 0.2" with a difference in magnitude smaller than Δm=3.48 in R band, and a companion at a distance of 0.25" with Δm <1.65 in

Figure 5.9.—: (Following page) *Top panel:* R band speckle sensitivity curve of Kepler-19. The magnitude difference between the target star and local extrema in the background are denoted by squares (local maxima) and points (local minima). The solid line denotes a flux that is 5σ brighter than the mean background brightness (where σ is the standard deviation of the extrema in the background), where we could confidently detected an additional source. No companions are detected within 1.8 arcseconds of the target star to a depth of 4 magnitudes. *Bottom panel:* V band speckle sensitivity curve of Kepler-19. No companions are detected within 1.8 arcseconds of the target star to a depth of 2 magnitudes.

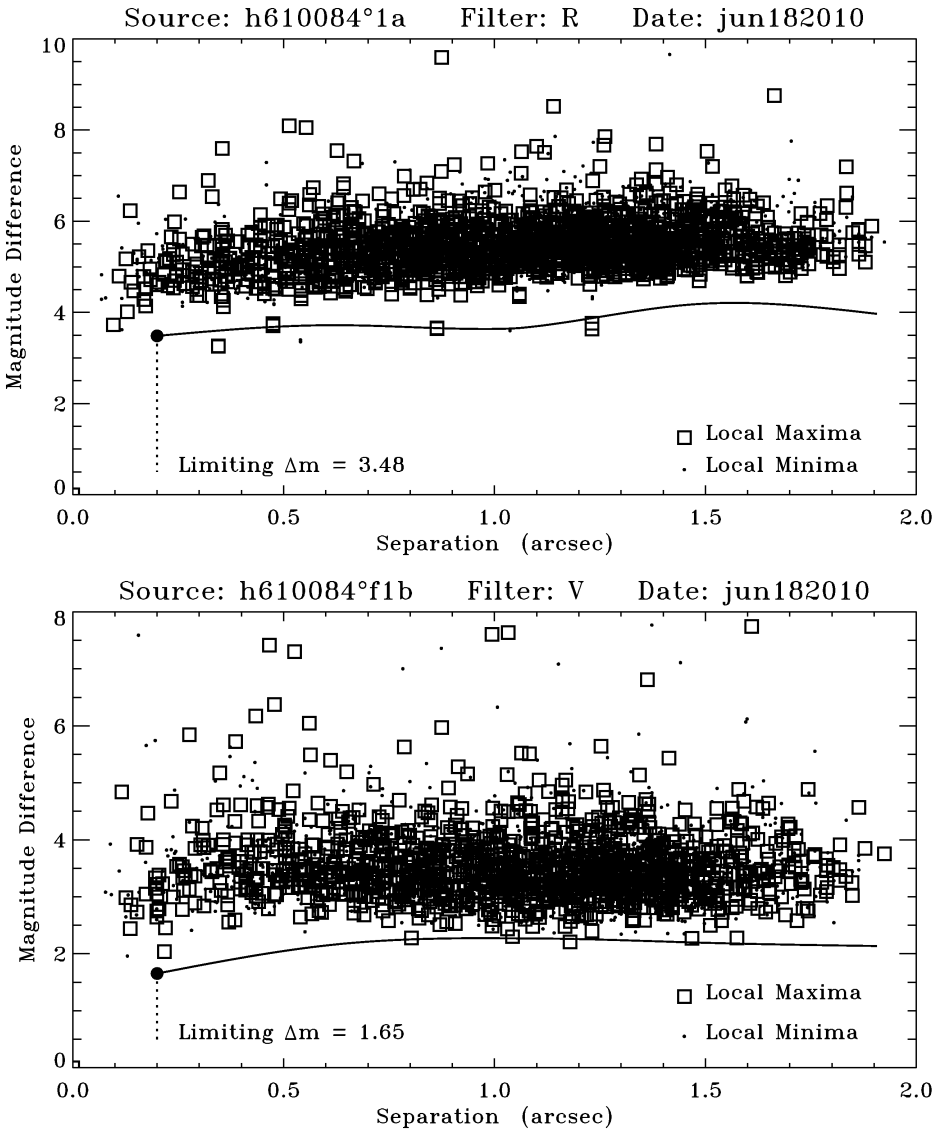

Figure 5.9.—: (Continued).

V band. Here again, as in the adaptive optics images, we detect no additional sources nearby to the *Kepler* target star.

5.5 Planetary Validation of Kepler-19b

5.5.1 Photocenter Tests

We use two methods to search for false positives due to background eclipsing binaries, based on examination of the pixels in the aperture of Kepler-19: direct measurement of the source location via difference images, and inference of the source location from photocenter motion associated with the transits. We employ two methods because of their different vulnerabilities to systematic bias; when the methods agree, we have increased confidence in their result.

Difference image analysis (Torres et al. 2011) takes the difference between average in-transit pixel images and average out-of-transit images. A fit of the Kepler pixel response function (PRF; Bryson et al. 2010) to both the difference and out-of-transit images directly provides the location of the transit signal relative to the host star. We measure difference images separately in each quarter, and estimate the transit source location as the robust uncertainty-weighted average of the quarterly results.

We measure photocenter motion by computing the flux-weighted centroid of the pixels in the optimal aperture, plus a one-pixel halo in every cadence, generating a centroid time series for row and column. We fit the modeled transit

to the whitened centroid time series transformed into sky coordinates. We perform a single fit for all quarters, and then infer the source location by scaling the difference of these two centroids by the inverse of the flux as described in Jenkins et al. (2010a).

The source as determined by the difference image method is offset from the nominal location of Kepler-19, as given in the *Kepler* Input Catalog, by 0.09 ± 0.11 arcsec = 0.80σ. The source as determined by the flux-weighted centroid method is offset from Kepler-19 by 0.10 ± 0.11 arcsec = 0.88σ. The location of the offsets is shown for both methods in Figure 5.10. Both methods show that the observed centroid location is consistent with the transit occurring at the location of Kepler-19.

5.5.2 *Spitzer* Observations

Warm *Spitzer* observations in the near-infrared can also prove useful toward validating *Kepler* candidates, as shown for Kepler-10c (Fressin et al. 2011). Unless a putative blend scenario is comprised of stars of nearly identical color, the transit depth in a blend scenario will depend upon the wavelength at which it is observed. Conversely, an authentic transiting planet will produce an achromatic transit depth.

We gathered observations using the Infrared Array Camera (IRAC) (Fazio et al. 2004) on Warm *Spitzer* at 4.5 μm of two consecutive transits of Kepler-19: one on UT 29 June 2010, and one on UT 9 July 2010. Both observations span

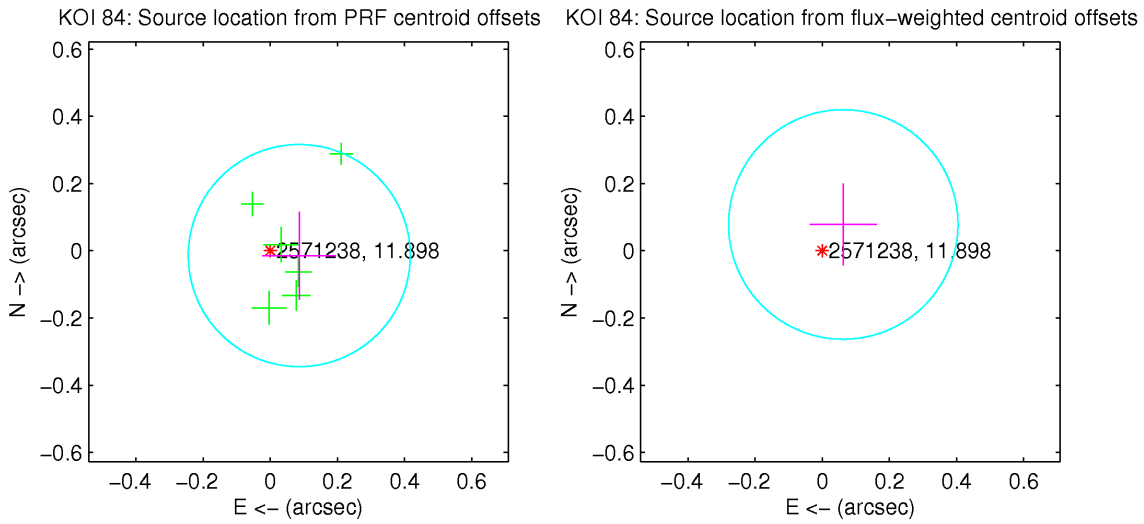

Figure 5.10.—: Quarterly and average reconstructed transit source locations relative to Kepler-19. *Left:* The green crosses show the individual quarter measurements using the difference image technique, and the magenta cross shows the uncertainty-weighted robust average of the quarterly results. *Right:* The magenta cross shows the transit source location reconstructed from the multi-quarter fit of the transit signal to the centroid motion. The length of the crosses show the 1σ uncertainty of each measurement in RA and Dec. The circles show the 3σ circle around the average source location. The location of Kepler-19 is shown by the red asterisk along with its Kepler ID and Kepler magnitude.

8 hours, centered on the 3.5-hour-long transit. We gathered the observations using the full-array mode of IRAC, with an integration time of 26.8 s/image. We employed the techniques described in Agol et al. (2010) for the treatment of the images before photometry. We first converted the Basic Calibrated Data products from the *Spitzer* IRAC pipeline (which applies corrections for dark

current, flat field variations, and detector non-linearity) from mega-Janskys per steradian to data number per second, using 0.1469 MJy·sr^{-1} per DN s^{-1}, and then to electrons per second, using the gain of 3.71 e DN^{-1}. We identified cosmic rays by performing a pixel-by-pixel median filter, using a window of 10 frames. We replace pixels that are $> 4\sigma$ outliers within this window with the running median value. We also corrected for a striping artifact in some of the Warm *Spitzer* images, which occurred consistently in the same set of columns, by taking the median of the pixel values in the affected columns (using only rows without an overlying star) and normalizing this value to the median value of neighboring columns.

We estimate the position of the star on the array using two techniques. First, we employed a flux-weighted sum of the position within a circular aperture of 3 pixels (we tested whether the size of this aperture made a difference by increasing the size to 4 pixels and repeating the analysis: we found that the position estimates were nearly identical). Additionally, we fit a Gaussian to the core of the PSF using the IDL routine `GCNTRD` (again using apertures of 3 and 4 pixels, and finding no significant difference between them). We then performed aperture photometry on the images, using both estimates for the position and variable aperture sizes between 2.1 and 4.0 pixels, in increments of 0.1 pixels up to 2.7 pixels, and then at 3.0 and 4.0 pixels. We decided to use the position estimates using a flux-weighted sum at an aperture of 2.6 pixels, which minimized the out-of-transit RMS. Alternatively, using the positions derived with `GCNTRD`, using a slightly smaller aperture, or using a slightly larger aperture, changed the

RMS by only a few percent at the most.

We remove the effect of the IRAC intrapixel sensitivity variations, or the "pixel-phase" effect (see eg. Charbonneau et al. 2005; Knutson et al. 2008) using two techniques. With the first technique, we assume a polynomial functional form for the intrapixel sensitivity (which depends upon the x and y position of the star on the array). We denote the transit light curve f (which depends upon time), and we hold all parameters constant except for the transit depth. We use the light curve software of Mandel & Agol (2002) to generate the transit models. The model for the measured brightness $f'(x, y)$ is given by:

$$f' = f(t, R_p/R_\star) \cdot (b_1 + b_2(x - \bar{x}) + b_3(x - \bar{x})^2 + b_4(y - \bar{y}) + b_5(y - \bar{y})^2), \quad (5.4)$$

where we include all of the observations (both in- and out-of-transit) to fit the polynomial coefficients and the transit depth simultaneously.

We included cross-terms in x and y, as well as higher order terms, but found that did not substantially decrease the RMS error of the out-of-transit residuals after the sensitivity function is divided from the flux. We fit for the polynomial coefficients b_1 through b_5 using a Levenberg-Marquardt χ^2 minimization. We also performed an MCMC analysis to fit the polynomial coefficients to determine whether fitting for the transit depth was degenerate with any other free parameters, and determined that about 20% of the error in the best-fit transit depth is due to a degeneracy with the strongest polynomial dependence of the intrapixel sensitivity, which is the linear coefficient in y.

However, the Spitzer light curve contains significant correlated noise even after the best intrapixel sensitivity model is removed. We incorporate the effect of remaining correlated noise with a residual permutation analysis of the errors as described by Winn et al. (2008), wherein we find the best-fit model f' to the light curve as given by Equation 5.4, subtract this model from the light curve, shift the residuals by one step in time, add the same model back to the residuals, and refit the depth and pixel sensitivity coefficients. We wrap residuals from the end of the light curve to the beginning, and in this way we cycle through every residual permutation of the data. We determine the best value from the median of this distribution, and estimate the error from the closest 68% of values to the median. We gathered 4.5 hours of observations outside transit, which is sufficient to sample the systematics on the same timescale as the 3.5 hour transit. Using the residual permutation method on the light curve treated with a polynomial, we find a best-fit transit $R_p/R_\star$ to be 0.0226 ± 0.0039 for the visit on 29 June, which is consistent with the best solution using MCMC, although the error bars are inflated by 40% when compared to the MCMC error bars. For the visit on 9 July, we find 0.0280 ± 0.0027 with the rosary-beading analysis; these error bars are 20% larger than the corresponding MCMC error bars. The larger error on the transit depth measured on the first visit is attributable to the larger area on the pixel over which the star wanders during the observations: the smaller this area, the better we are able to fit the polynomial sensitivity model. While the extent of the pointing oscillations in the x direction are comparable between the two visits (0.1 pixels), they differ substantially in the y direction. The star wanders 0.15

pixels in y on the 29 June visit and 0.08 pixels in y on the 9 July visit.

We also treated the light curve with the weighted sensitivity function used in Ballard et al. (2010a), which proved in that work to produce a time series with lower RMS residuals. For this procedure, we do not assume any *a priori* functional form for the intrapixel sensitivity; rather, we perform a weighted sum over neighboring points for each flux measurement, and use this sum to correct each flux measurement individually. In this way, we build up a map of the intrapixel sensitivity point-by-point. We use same widths, σ_x=0.017 pixels and σ_y=0.0043, for the weighting function (which is a Gaussian in x and y) as we used in Ballard et al. (2010a). We therefore have only one free parameter in this case, which is $R_p/R_\star$. We correct each observation using all other flux measurements, but we did not bin the data, as was done in Ballard et al. (2010a). With this treatment, we also use the residual permutation method to fit the transit depth at each residual permutation. We find $R_p/R_\star$=0.0242±0.0032 for the 29 June visit and $R_p/R_\star$=0.0233±0.0033 for the 9 July visit. These errors are larger by 20% and 30%, respectively, as compared to the MCMC-derived errors. The out-of-transit RMS of the light curve is slightly lower in both cases using the weighted sensitivity function treatment, so in this case we defer to the weighting-function-derived values for $R_p/R_\star$. Combining the two measurements, we find a radius ratio $R_p/R_\star$ at 4.5 μm of 0.0238±0.0023, which translated to a transit depth of 547^{+113}_{-110} ppm. This value is in excellent agreement with the depth in the *Kepler* bandpass of 567±6 ppm (corrected for limb-darkening). In Figure 5.11, we show the combined and binned *Spitzer* light curve, with the best-fit

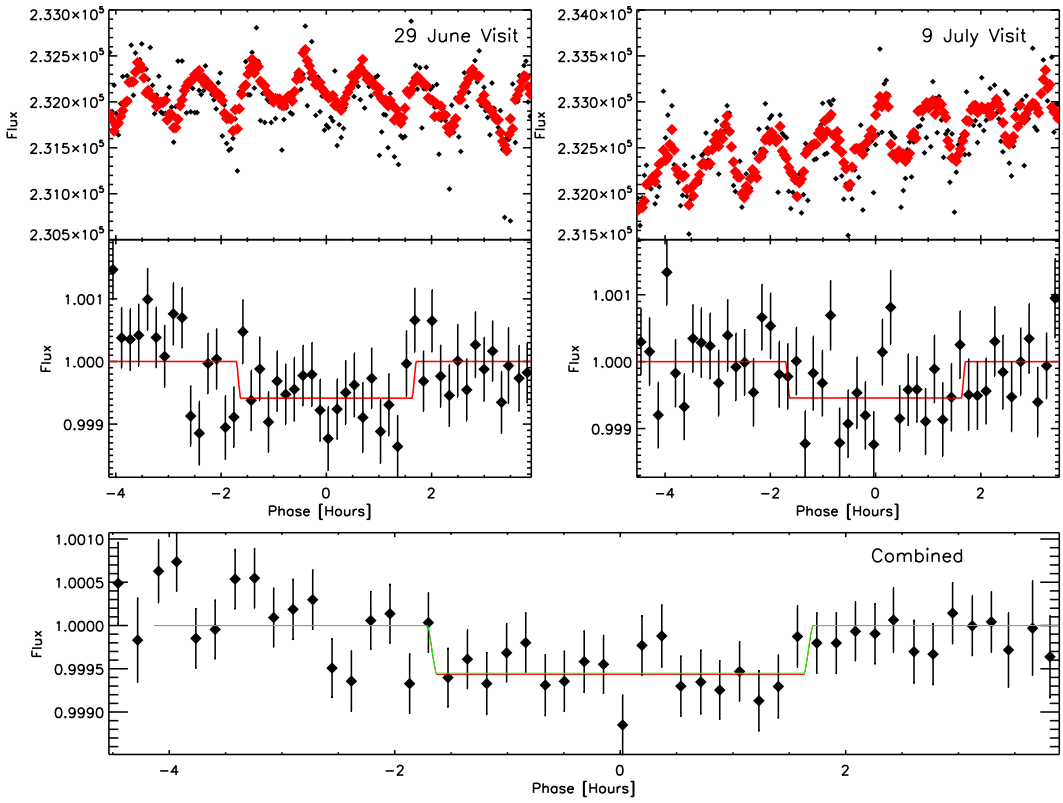

Figure 5.11.—: Both transits of KOI-084 gathered with Warm *Spitzer* at 4.5 μm. The top panels show the raw flux, binned by a factor of 4, with the intrapixel sensitivity variation (obtained with the weighted sensitivity function, as described in the text) overplotted in red. The middle panels show the individual transits with this intrapixel sensitivity removed, binned by a factor of 16, with the best models overplotted. The bottom panel shows the combined transit light curves gathered with *Spitzer*. The best-fit transit model with depth derived from the *Spitzer* observations is shown in red, while the *Kepler* transit model (corrected for limb darkening) is shown in green. The *Spitzer* and *Kepler* transit depths are in excellent agreement.

transit model derived from the *Spitzer* observations and the best-fit *Kepler* transit model (corrected for limb-darkening) overplotted. We comment further on the types of blends we rule out with *Spitzer* (and their complementarity with blends ruled out by `BLENDER`) in the following section.

5.5.3 `BLENDER` Analysis

In the absence of a radial velocity confirmation and mass measurement of the planet Kepler-19b, we instead investigate the likelihood that the transit signal is a false positive. Possible false positive scenarios involve another eclipsing system lying within the same photometric aperture as the *Kepler* target star. This binary system could comprise two stars, or a star and a gas giant planet, and could be physically associated or unassociated with the host star (in the foreground or background). In a false positive scenario, the presence of the *Kepler* target star dilutes the depth of the transit to appear planetary (or attributable to a smaller planet, if the binary system comprises a star and a Jupiter-size planet). We employ the `BLENDER` software package (Torres et al. 2004, 2011), which produces synthetic light curves corresponding to eclipsing binary blend scenarios and attempts to replicate the detailed shape of the *Kepler* transit light curve. The `BLENDER` technique has been applied previously toward validating three *Kepler* planets: Kepler-9d (Torres et al. 2011), Kepler-11f (Lissauer et al. 2011), and Kepler-10c (Fressin et al. 2011). Model blend light curves are compared with the *Kepler* photometry in a χ^2 sense, with models considered poor fits accordingly deemed unlikely to explain the transit. By exploring the parameter space of mass,

impact parameter, orbital eccentricity, and distance from the host star, BLENDER amasses knowledge of the range of possible blends that are consistent with the shape of the transit, and the range of blends that are inconsistent. The BLENDER nomenclature defines the objects within the binary to be the "secondary" and "tertiary", while the *Kepler* target star is defined to be the "primary". In the case of hierarchical triples, BLENDER uses the best isochrone parameters for the *Kepler* target star (derived from SME) as input constraints to the secondary and tertiary stars: these stars are assumed to have formed concurrently and are therefore assumed to be the same age. When the secondary and tertiary are physically unassociated with the *Kepler* target star, BLENDER assumes an age of 3 Gyr (a representative age for the field, per Torres et al. 2011) and a solar metallicity to model the putative binary system.

In order to validate Kepler-19b as a planet, we evaluate the probability of false positive scenarios allowable by BLENDER and compare these probabilities to that of the authentic 2.2 $R_\oplus$ planet hypothesis. First, we address the probability of a physically unassociated binary in the foreground or background of the target star. In the case of Kepler-19b, all false positive scenarios consisting of a background or foreground eclipsing binary (comprising two stars) are ruled out at the 10σ level from the shape of the transit alone. That is, the best planet model furnishes a solution that is a 10σ improvement over the best blend model in this case. This result is attributable to the sharp ingress and egress of the transit light curve, which is not well reproduced by blend models involving a binary system consisting of two stars. We therefore confidently conclude that this scenario

cannot replicate the *Kepler* transit signal.

For scenarios consisting of a foreground/background star orbited by a larger (Jupiter-size) planet, there exists a region of parameter space in which an eclipsing binary model provides a comparably good fit, as compared to the single star and planet model. The `BLENDER` constraints are represented by contours of equal goodness of fit in Figure 5.12. The 3σ contour is shown with a heavy white line, and blend scenarios under this curve are considered viable. In additional to the goodness-of-fit of the blend models to the *Kepler* light curve, there are regions of parameter space that are disallowed by the color of the star (as measured by 2MASS and in Sloan r band), as well as the spectrum (in which a secondary star within a certain magnitude range would be apparent). These constraints are depicted in Figure 5.12 as blue cross-hatching (within which region blends are disallowed) and a solid green line (below which an additional star would have appeared in the spectrum). We comment briefly on this spectroscopy constraint, which we measured by injecting additional stellar spectra (in this case, solar-type) into the spectrum of Kepler-19 at varying brightnesses and relative velocities, and then determining the limits on detectability via a cross-correlation of the spectrum with a template. We determine that any star within 10% the flux of Kepler-19 would be detectable in the cross-correlation function down to relative velocities of 5 km s^{-1}, which translates conservatively to a $\Delta m < 2$ constraint. A velocity variation of $<$5 km s^{-1} would be unlikely for a random unassociated background star, and we comment on the hierarchical triple case further below. Furthermore, the angular separation of this star and planet system must also be sufficiently

small as to be undetectable by adaptive optics imaging for which limits are given in Section 5.4.3. While an unassociated binary might be resolvable by adaptive optics, for a hierarchical triple the possibility of an unresolved companion remains.

We proceed to evaluate the frequency of the remaining allowable blends as follows: We estimate *a priori* the frequency of stars in the background or foreground of the target star. We evaluate a theoretical number density of neighboring stars, per square degree, using Galactic structure models given by Robin et al. (2003). We record this number density in half-magnitude bins (shown in Table 5.5.3), and show both the number density of stars and their allowed mass values in Columns 3 and 4, based on the constraints constraints imposed by the `BLENDER` contours, additional color constraints, and brightness constraints. For the magnitude bins in which no blend furnishes a solution within 3σ of the planetary model, we have left these columns blank. The maximum angular separation at which these stars might have remained undetected in adaptive optics imaging (the limits are provided in Section 5.4.3) is listed in Column 5. The number of stars in each magnitude bin is then listed in Column 6. In order to evaluate the transiting planet prior, we rely on the reported *Kepler* planet candidate sample to date, presented in Borucki et al. (2011). While the majority of these candidates have not yet been confirmed to be planets, the false positive rate is expected to be quite small (as reported by Morton & Johnson 2011) and so will not substantially change our results. We also assume that the sample presented in the Borucki et al. (2011) candidate list is complete.

The second feasible blend scenario is an additional star and transiting

Jupiter-size planet, which are physically associated with the *Kepler* target star. We present the results of `BLENDER` for this case in Figure 5.13. While there exists a range of hierarchical triples whose light curve shape is consistent with the *Kepler* transit (depicted by the χ^2 contours), these are all ruled out by either the color constraint on blends (shown in blue cross-hatching) or the brightness constraint on blends from the spectrum (shown in green cross-hatching). There exists the remaining possibility of a true twin to the target star: a star that has an identical color, and whose position is either at a distance > 20 AU (at which position the predicted radial velocity is equal to 5 km s^{-1}) or whose tangential velocity is <5 km s^{-1} relative to the target star during the time of our observations. Even if this scenario were to be true, the planet's inferred radius would only be greater by a factor of $\sqrt{2}$. Therefore, we conclude that the only possible blends belong to the unassociated planet and star scenario.

Combining the probabilities associated with all background or foreground star and planet pairs, we find a total blend frequency of 1.08×10^{-7}. This frequency corresponds to the likelihood of a blend that is capable of producing a transit light curve that is no worse ($< 3\sigma$) than the best model corresponding to a transiting planet around a single star within the aperture.

Next, we estimate the *a priori* frequency of a true planet with the characteristics implied by the *Kepler* transit light curve. Using the planetary radius range of 2.209 ± 0.048 $R_\oplus$, we identify 119 planet candidates from the Borucki et al. (2011) catalog with sizes that are within 3σ of this measured value. The planet prior is equal to 7.6×10^{-4} (119 divided by the total number of *Kepler*

targets, 156,453), which is more than 3 orders of magnitudes larger than the blend frequency. We therefore find that the planetary scenario corresponding to a 2.2 $R_\oplus$ planet is 7000 times as likely as the blend scenario, and conclude with very high confidence that the transit signal is due to a planet, Kepler-19b.

For comparison, the constraint from *Spitzer* in this case provides an independent means of ruling out a subset of blends which are also ruled out by `BLENDER`. If we impose the constraint that a putative additional star may not produce a transit depth at 4.5 μm which is 3σ deeper than measured, such a star cannot be less massive than 0.7 $M_\odot$ (otherwise, the additional star would be so red as to produce a significantly deeper transit depth in the near-infrared). As shown in Figures 5.12 and 5.13, `BLENDER` independently rules out blends consisting of a star in this mass range from the shape of the transit light curve.

Table 5.3. Blend frequency estimate for KOI-084.01.

		Blends Involving Planetary Tertiaries				
Kp Range (mag)	ΔKp (mag)	Stellar Mass Range ($M_\odot$)	Stellar Density (per sq. deg)	$\rho_{\max}$ ($''$)	Stars ($\times 10^{-6}$)	Transiting Planets 0.36–2.00 $R_{\rm Jup}$, $f_{\rm planet} = 0.20\%$ ($\times 10^{-6}$)
(1)	(2)	(3)	(4)	(5)	(6)	(7)
11.9–12.4	0.5	···	···	···	···	···
12.4–12.9	1.0	···	···	···	···	···
12.9–13.4	1.5	···	···	···	···	···
13.4–13.9	2.0	···	···	···	···	···
13.9–14.4	2.5	0.88–1.40	444	0.22	5.21	0.011
14.4–14.9	3.0	0.91–1.40	505	0.29	10.3	0.021
14.9–15.4	3.5	0.95–1.40	436	0.38	15.3	0.031
15.4–15.9	4.0	1.00–1.30	327	0.53	22.3	0.045
15.9–16.4	4.5	···	···	···	···	···
16.4–16.9	5.0	···	···	···	···	···
16.9–17.4	5.5	···	···	···	···	···
17.4–17.9	6.0	···	···	···	···	···
17.9–18.4	6.5	···	···	···	···	···
18.4–18.9	7.0	···	···	···	···	···
18.9–19.4	7.5	···	···	···	···	···
19.4–19.9	8.0	···	···	···	···	···
19.9–20.4	8.5	···	···	···	···	···
Totals			1712		53.11	0.108

Total frequency (BF) = $(0.108) \times 10^{-6} = 1.08 \times 10^{-7}$

Note. — Magnitude bins with no entries correspond to brightness ranges in which `BLENDER` excludes all blends.

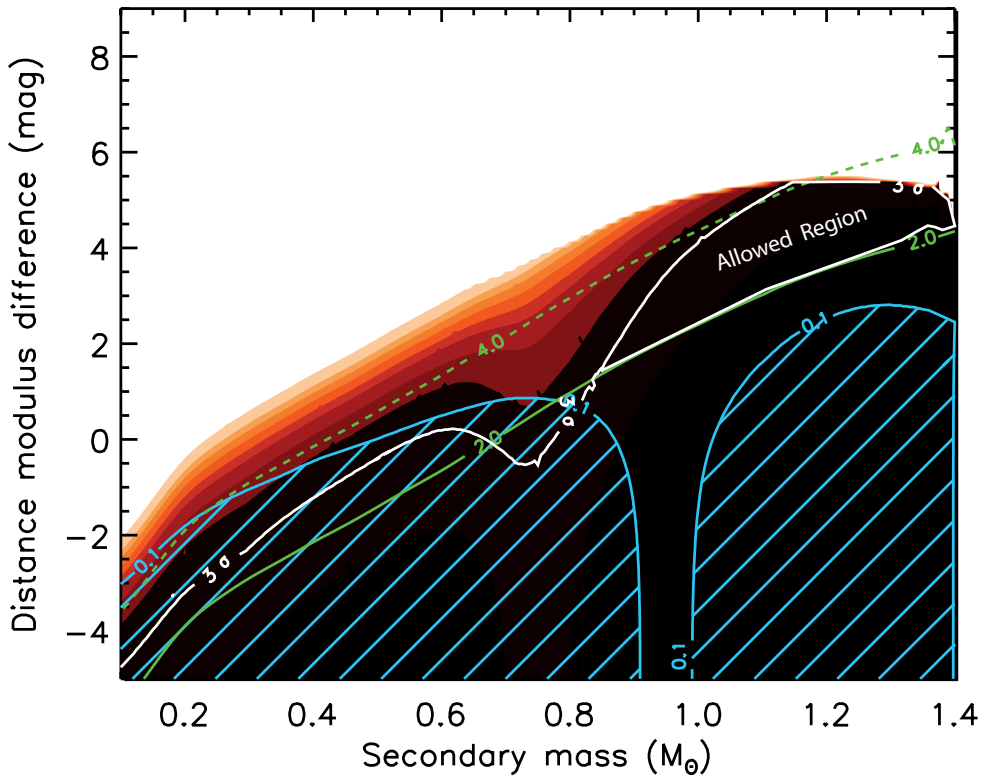

Figure 5.12.—: BLENDER χ^2 goodness-of-fit contours corresponding to blend models with background/foreground (physically unassociated) secondary star and planetary tertiary, as a function of distance modulus and mass of the secondary. Viable blend scenarios lie below the 3σ contour, depicted with a heavy white line. The blue cross-hatching shows the region of parameter space for which the blend model is the wrong color to be consistent with the measured 2MASS and Sloan r colors of the star, while models that lie below the solid green line have a small enough magnitude difference that the secondary would have been detected in the spectrum of the star ($\Delta m < 2.0$). The dashed green line shows location of the Δm contrast limit corresponding to the faintest allowable blend. The remaining allowed parameter space is denoted "Allowed Region."

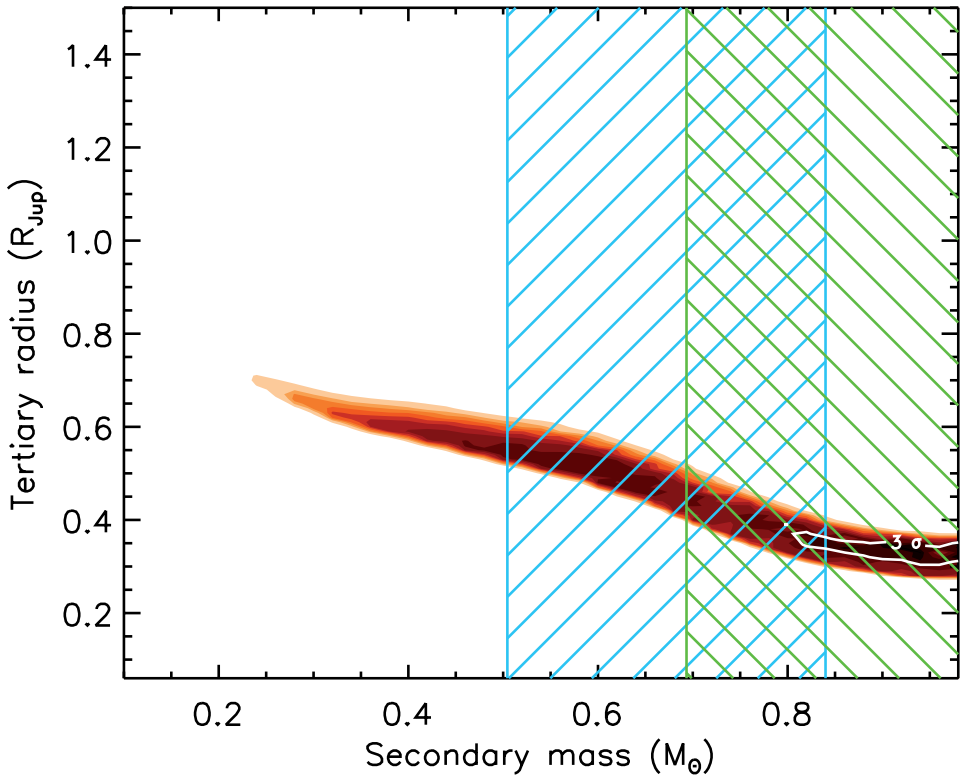

Figure 5.13.—: BLENDER χ^2 goodness-of-fit contours corresponding to hierarchical triple blend models (with physically associated secondary star and planetary tertiary). As in Figure 5.12, viable blend scenarios lie within the 3σ contour, depicted with a heavy white line. The color-coding is similar to the previous figure, with blends of the wrong color depicted in blue cross-hatching, and blends that are ruled out spectroscopically depicted in green cross-hatching.

5.6 Discussion and Conclusions

5.6.1 Interpretation of Transit Timing Variations

Our analysis of the transit timing variation of Kepler-19b comprises two sections. In Section 5.6.1, we argue that there must exist a second planet in the Kepler-19 system, since the TTVs cannot originate from astrophysical effects or a stellar mass perturber. Then, in Section 5.6.1, we describe the dynamical properties of planetary perturbers that could account for the observed TTV pattern of planet b.

Demonstration of Planethood of Perturber

In Figure 4 we presented a strongly detected and nearly sinusoidal variation (period $P_{\rm ttv} = 316$ days and amplitude $A_{\rm ttv} = 5$ min) in the times of transits of planet b. Here we discuss four potential interpretations of the signal which do not invoke a perturbing planet, and demonstrate that the signal cannot originate from these scenarios. The first two scenarios consider a system of only the star and the transiting planet, while the latter two allow for the presence of a third, non-planetary, body. Because these scenarios are disallowed, the only viable alternative is that the signal is a dynamical variation caused by a second planet (planet c), which we discuss in the next subsection.

First, we consider the possibility that the signal is due to stellar activity. The most plausible candidate for dynamical interaction with the star causing the TTV

signal is the Applegate (1992) effect from the eclipsing binary literature, which Watson & Marsh (2010) recently applied to exoplanets. In this mechanism, the star undergoes a magnetic cycle, which varies the rotational bulge's gravitational pull on the planet, slightly varying its orbital period. For this effect to produce the observed TTV signal, the magnetic cycle would need to have an exceptionally short period of 316 days. This is problematic because the stellar activity in the spectra is low, as we describe in Section 4.2, suggesting a magnetically inactive star with a long spin period. For magnetic dynamos typical of solar-type stars like Kepler-19, Watson & Marsh (2010) calculate TTV variations of less than 1 second over timescales of several years, much too small to explain our data. Apart from this dynamical interaction, activity could cause apparent TTV via the planet transiting over starspots (Silva-Valio 2008; Alonso et al. 2008). For instance, Knutson et al. (2011) recently found transit timing deviations for GJ 436b that are greater in optical photometry, where spots are pronounced, than in near-infrared photometry, where spots are relatively muted. However, in our case, even with excellent *Kepler* photometry, no spots are detected, either in out-of-transit stellar modulation or in excess residuals during transit due to spot crossings.

Second, the signal could be due to rotation of the planetary orbit's apsidal line about the star (Heyl & Gladman 2007). The eccentricity need not be large ($e_b \simeq 2\pi A_{\rm ttv}/P_b = 0.0023$), but the apse must be precessing very quickly to be consistent with the TTV period ($P_{\rm ttv} = 316$ days). Using expressions for realistic apsidal motion rates (Fabrycky 2010, section 3.1.1), we demonstrate that the

periods associated with possible precession mechanisms are too long by several orders of magnitude, as follows. General relativistic precession has a period of 7.9×10^4 yr. A star made oblate by rotation, alternatively, would cause precession with a period of 7×10^6 yr $\times (P_{\rm rot}/10 \text{ days})^2$, if the star has an apsidal motion constant of $k_{\rm L}/2 = 0.02$ (Claret & Gimenez 1992). Finally, tidal distortion of the planet would cause precession with a period of $\sim 10^8$ yr, if the planet has a Love number of $k_{\rm L} = 0.3$ (Mardling & Lin 2004). We conclude that general relativity dominates the putative precession rate, but it is inconsistent by orders of magnitude with $P_{\rm ttv}$ and is probably undetectable (Ragozzine & Wolf 2009).

Third, the signal could originate from light time delay, owing to reflex motion of the system as it is orbited by a third body with an orbital period of $P_2 = P_{\rm ttv} \simeq 316$ days. It is conceivable that this putative body moves the barycenter of the Kepler-19 / Kepler-19 b system by ± 5 light minutes, causing a time-variable light-time delay (e.g., Irwin 1952; Sybilski et al. 2010). In creating such a large displacement in the radial direction, a radial velocity signal – its derivative – would also be created. The semi-amplitude would be $2\pi(0.6\text{AU})/(316\text{days}) \simeq 17$ km s^{-1}, ruled out by orders of magnitude given our radial velocity measurements. Moreover, to induce this motion, the additional body must have a mass of at least $1.0 M_{\odot}$, and would likely impart a second set of lines on the spectra, which are not detected.

Finally, the signal could be dynamical, owing to perturbations from another body in the system such as a second star or a brown dwarf. The orbital period of such a body cannot be too long; otherwise, the gravitational potential it

induces on planet b would result in a period longer than the observed $P_{\rm ttv}$. In fact, the longest period the body could have is $2P_{\rm ttv}$ (Borkovits et al. 2003), as the dominant part of the perturbation of a distant body is its "tidal" term, which has a frequency of twice the body's orbital frequency[1]. The lack of large radial velocity variation means that additional bodies must have masses in the planetary regime (a case handled in the next subsection) on nearly any orbit with $P_2 \leq 2P_{ttv}$. An exception is for nearly face-on orbits with a small component of radial motion. To our knowledge, there is only one such configuration that could explain the timing data, as follows. A circular orbit of period $2P_{ttv}$, mutually perpendicular to the orbit of planet b, causes a timing signature (Borkovits et al. 2003, eq. 46) :

$$O - C_b \approx \frac{3}{8\pi} \frac{M_2}{M_\star + M_b + M_2} \frac{P_b^2}{P_2} \sin 2f_2 \tag{5.5}$$

where M_2 is the perturber's mass and f_2 is its true anomaly measured with respect to the plane of planet b's orbit. The perturbing orbit must be nearly circular in the case of Kepler-19, as we have measured two full $O - C$ cycles and found them to be nearly identical, rather than different either in amplitude or phase as would result from an eccentric perturber (e.g., run A13 of Figure 2 in Borkovits et al. 2003). To fit A_{ttv}, we have $M_2 \approx 0.25 M_\odot$. The radial velocity limit (at 99.73% confidence) on circular orbits at $P_2 = 2P_{ttv}$ is $K < 22$ m s^{-1}, so the orbit would need to be inclined by $i_2 < 0.2^\circ$ to the plane of the sky. Given an isotropic prior, this configuration has a probability of $1 - \cos i_2 = 6.0 \times 10^{-6}$, i.e.

[1]Planet b would also speed up and down twice per orbit due to a static tidal term, but this is not observable, as transits occur only once per orbit.

it is too finely tuned toward face-on to be plausible.

Having thus demonstrated that the TTV signal cannot be created by any known mechanism other than a second planet, we interpret the transit timing effect of planet b to be due to a second planet in the system, which we call Kepler-19c.

Possible orbits of planet c

In this subsection we discuss the possible orbits of planet c, consistent with the TTV data for planet b. We take as constraints a sinusoidal transit timing signal as well as radial velocity upper limit of $M_c < 0.44 M_{\rm Jup} \times (P_c/P_b)^{1/3}$ (99.73% confidence limit on a second orbit of arbitrary eccentricity). This assumes $\sin i_c > 0.5$, as we consider a mutual inclination $i_m > 60^\circ$ to be physically implausible[2]. These planetary scenarios fall broadly into five categories: orbits with the period of the TTV signal, resonant perturbers, orbits near first-order mean-motion resonances, orbits near higher-order resonances (in which category we assign an upper limit on the mass of the perturber), and satellite scenarios. The latter three are favored, under circumstances that we elucidate below.

Our first consideration is the possibility that planet c could have a period $P_c = P_{\rm ttv} = 316$ days and a large eccentricity, such that it produces a time-

[2]A large mutual inclination would likely drive large-amplitude eccentricity cycles (Kozai 1962) in the innermost planet, which would in turn trigger rapid tidal orbital decay (Fabrycky & Tremaine 2007; Mardling 2010).

variable tidal force on the Kepler-19 / Kepler-19 b pair, accounting for the TTVs (Borkovits et al. 2003; Agol et al. 2005; Borkovits et al. 2011). However, radial velocity constraints require its mass is $M_c \lesssim 1.4 M_{\rm Jupiter}$, so to generate a TTV signal with amplitude $A_{\rm ttv} = 5$ min, its eccentricity would need to be > 0.99 (Agol et al. 2005). This would be unstable with respect to planet b because the orbits would cross. Moreover, a smaller amplitude could be generated at $0.5 < e_c < 0.9$, but the signal would have a saw-toothed shape, which is inconsistent with the measured transit times. Therefore, any putative planet with period 316 days that is massive enough to create the TTV signal would be inconsistent with the observed radial velocities.

Another possibility is that the TTV curve of b is driven by a resonant perturber. In this case, the amplitude can be substantial, even for a low-mass perturber (Agol et al. 2005),

$$\delta t \approx \frac{P_b}{p} \frac{M_c}{M_b + M_c}, \tag{5.6}$$

where p refers to the period ratio of the transiting planet to the perturbing planet p/q, $\mu \equiv \max(M_b, M_c)/M_\star$, and δt is the amplitude of the TTV signal. The libration (and TTV) period is of order $P_{\rm lib} \simeq e^{-1/2} \mu^{-1/2} P/p$ (Agol et al. 2005). This consideration determines whether such a resonance is a possible site for planet c, as the mass of c must be large enough so that this libration period equals the rather short TTV period. For low eccentricities ($e_b, e_c \lesssim 0.1$), the mass of the perturbing planet must be ~ 1 Jupiter mass, which is ruled out by the radial velocities. For high eccentricities, lower masses are allowed, but then the region of stability becomes more constrained, such that the proposed system would need to

be finely tuned. Orbits near the Lagrange points of b (the 1:1 resonance; Ford & Holman 2007) fail for the same reason: $P_{\rm lib} \simeq P_b\sqrt{27/4 \times M_\star/(M_b + M_c)}$ (Ford & Holman 2007), which means $M_c \simeq 3M_{\rm Jup}$, in violation of the radial velocity constraint. For these reasons, we do not favor resonant orbits for planet c.

Next, we consider perturbers near period commensurabilities. If two planets are near to, but offset from, a period commensurability, they can generate a large TTV signal (Agol et al. 2005; Holman & Murray 2005), as in the interaction between planets Kepler-11 b and c (Lissauer et al. 2011). In this scenario, the orbital frequency ratio of the known planet to the perturbing planet, P_b/P_c, is slightly offset from a ratio of integers, p/q. Then, as long as the planets' eccentricities are moderate, the transit timing signature will have a dominant frequency equal to:

$$1/P_{\rm ttv} = |p/P_b - q/P_c|. \tag{5.7}$$

The absolute value sign above means we can postulate a perturber on one side or the other of each resonance, that is responsible for the TTV signal. The strength of the resonance must be finely tuned, so that a 5 minute amplitude signal is possible, yet the radial velocity amplitude also lies within the observed upper limit. If the resonance is spaced too closely to the transiting planet, the planets will generate timing variations on the conjunction timescale (Nesvorný & Morbidelli 2008; Holman et al. 2010) which are not observed, or else the two planets will not be stable with respect to one another (Wisdom 1980).

The absolute value sign above means we can postulate a perturber on one side or the other of each resonance, that is responsible for the TTV signal. The

resonance must be strong enough that a perturber small enough to fulfill the radial velocity constraints can produce the 5 minute amplitude timing signal. However, if the resonance is spaced too closely to the transiting planet, the planets will generate timing variations on the conjunction timescale (Nesvorný & Morbidelli 2008; Holman et al. 2010) which are not observed, or else the two planets will not be stable with respect to one another (Wisdom 1980).

For first-order resonances in which $q = p \pm 1$, Agol et al. (2005) developed an order of magnitude estimate for TTV signals which depends on the fractional offset from the resonance $\epsilon \equiv |1 - qP_b/(pP_c)|$ and the mass ratio $\mu \equiv \max(M_b, M_c)/M_\star$:

$$\delta t_b = \left\{ \begin{array}{cc} (M_c/M_\star)\epsilon^{-1}P_b, & \epsilon \geq \mu^{1/2} \\ \min(M_c/M_b, 1)\mu^2\epsilon^{-3}P_b, & \epsilon \leq \mu^{1/2}. \end{array} \right\} \tag{5.8}$$

In the current case, presuming planetary masses of $\lesssim 10M_\oplus$, the upper expression of Equation 5.8 holds for $p \lesssim 5$. In particular, for exterior first-order resonances q:p = (2:1, 3:2, 4:3), to produce $A_{\rm ttv} = 5$ min we have $M_c \sim (4, 2, 1)M_\oplus$. Of course, these values are only good to order-of-magnitude, but they demonstrate that a reasonable planetary mass just offset from first-order resonances can indeed cause the observed TTV signal.

A planet near a second-order (e.g., 3:1, 5:3) or higher-order (e.g., 4:1, 5:1) resonance can also be responsible for the TTV signal. However, in these cases the strengths of the resonances are smaller, and they depend on a higher power of the eccentricities. Therefore, planetary-mass perturbers that satisfy the radial velocity constraints might need to have substantial eccentricities to match $A_{\rm ttv}$. For $n : 1$ resonances of exterior perturbers with $n \gg 1$, e_c must be large, and

the timing signal would be a series of constant-period segments with kicks at the outer body's periastron passage. The scaling relation of the radial velocity limit quoted above breaks down at high eccentricity, as periaston passages can appear as spikes which fall in data gaps, but we still wish to limit M_c. We therefore set 99.73% confidence limits on $M_c \sin i_c$ by (1) introducing a 4.8 $M_\oplus$, circular and edge-on planet b, and (2) sampling the orbit of planet c on a grid with P_c drawn from equation 5.7 for all $n:1$ resonances with $n = 3$ to 16 (28 cases); e_c drawn from 0.1, 0.2 ... until the orbit crossed with planet b's; ω drawn from 0°, 45°, ... 315°; $T_{0,c}$ drawn from 10 values uniformly spaced between BJD 2455200 and $2455200 + P_c$; and M_c spaced logarithmically by 0.25 dex from $0.32 M_{\rm Jup}$ to $18 M_{\rm Jup}$. The total grid sampled 150120 trials, and not one of the cases at or above $5.6 M_{\rm Jup}$ fit the radial velocities (allowing for a constant offset). Apparently, although a high-mass perturber can be fine-tuned to not induce large radial velocity at the times of the data, its mass is limited even at arbitrary eccentricity. For concreteness, let us describe the end-member of this set of n:1 resonances. It has $P_c = 153.2$ days $\approx P_{ttv}/2$, and the $O - C$ signal would be a zig-zag, only marginally consistent with the apparently sinusoidal shape. At each periastron passage of planet c, P_b would need to change by 0.6 minutes to match A_{ttv}. A consistent set of parameters according to (Holman & Murray 2005, eqn. 2) is 1 $M_{\rm Jupiter}$ and $e_c \gtrsim 0.8$. The periastron of planet c would thus be at $\lesssim 1.3 a_b$, only marginally stable with respect to the inner planet. This scenario is also barely allowable according to the radial velocities. Therefore we set an upper limit of $P_c \lesssim 160$ days. Again, this corresponds to $M_c \lesssim 6 M_{\rm Jupiter}$, according to our grid

search.

The final possibility that we consider is a satellite orbit, which could also cause TTVs (e.g., Kipping 2009). The amplitude of 5 minutes translates to a displacement along the orbit of $2.1R_p$. A prograde orbit for such a satellite would lie between R_p and $\sim 7R_p$ (0.4 of the Hill sphere, if $M_b \simeq 5M_{\rm Earth}$) to be stable (Domingos et al. 2006). Since the putative satellite lies so close to the planet in this case, its mass would have to be $\gtrsim 0.6M_b$ cause the TTVs observed for the transiting planet. Therefore, it would probably be big enough to be seen in transit. We examined each transit by eye, to see if any deviated significantly from the single-planet model, as mutual events of the co-orbiting planets would cause shallower transits (Szabó et al. 2006; Simon et al. 2007; Ragozzine & Holman 2010), but we found no features of interest. Furthermore, in this scenario, the b-c mutual orbital period would need to be near-resonant with the pair's orbital period around the star, so that the TTV signal aliases to the long $P_{\rm ttv} = 316$ day signal. We find this scenario unlikely.

A retrograde orbit for a satellite could be stable to much larger distances, even beyond the Hill sphere (Jackson 1913; Shen & Tremaine 2008). In fact, planet c could follow an independent Keplerian orbit which resonates with planet b, keeping their periods and orbital phases the same (Laughlin & Chambers 2002). The allowable M_c could be much lower in this case, down to of order $0.1M_{\rm Earth}$ if the eccentricity is $e_c \sim 0.1$. The TTV could be caused by either the resonant libration or by the two orbits precessing together at a swift rate. If the latter, then as in Section 5.6.1, e_b would be ~ 0.0023; unlike in that section, an apsidal

motion period of 316 days is plausible because of the proximity of the perturber.

We compiled examples of our favored orbits for planet c into Figure 5.14. Foremost are orbits nearby first-order mean motion resonances, which can fit the TTVs with masses which comfortably obey the RV constraints, and have near-circular orbits. Second, we consider orbits nearby higher order resonances to be possible, particularly if eccentricities are non-zero. Third, a retrograde satellite is a possibility, but we recognize this option as an exotic one. There is clearly profound degeneracy of interpretation. Such degeneracies are intrinsic to the TTV method of planet discovery, in the case that the signal is well-characterized by a single sinusoid (Nesvorný & Morbidelli 2008) and the radial velocity data cannot pinpoint the perturber (Meschiari & Laughlin 2010).

Figure 5.14.—: (Following page) Possible orbits for Kepler-19c. Orbits near first-order mean-motion resonances (eq. 5.7) may fit the TTV signal and RV constraints even on circular orbits; shown are $P_c = 6.129$ days (*bright green*) and 6.256 days (*blue*), flanking the interior 2:3 resonance, and $P_c = 18.033$ days (*olive green*), next to the exterior 2:1 resonance. Orbits near higher-order resonances likely need eccentricity to produce the TTV signal with masses low enough to satisfy the radial velocities; shown are $P_c = 3.065$ days (*pink*) near the interior 1:3 resonance, $P_c = 15.326$ days (*purple*) near the exterior 5:3 resonance, $P_c = 27.036$ days (*aqua blue*) near the exterior 3:1 resonance, and $P_c = 38.310$ days (*brown*) near the exterior 4:1 resonance. Finally, a co-orbital planet (or distant retrograde satellite) is shown at $P_c = 9.287$ days (*red*) – in such an orbit very small masses are possible, so the dot representing the planet is drawn small. Other possible orbits are within mean motion resonances (including the 1:1 at Lagrange points), or a prograde satellite, but these are disfavored (see text).

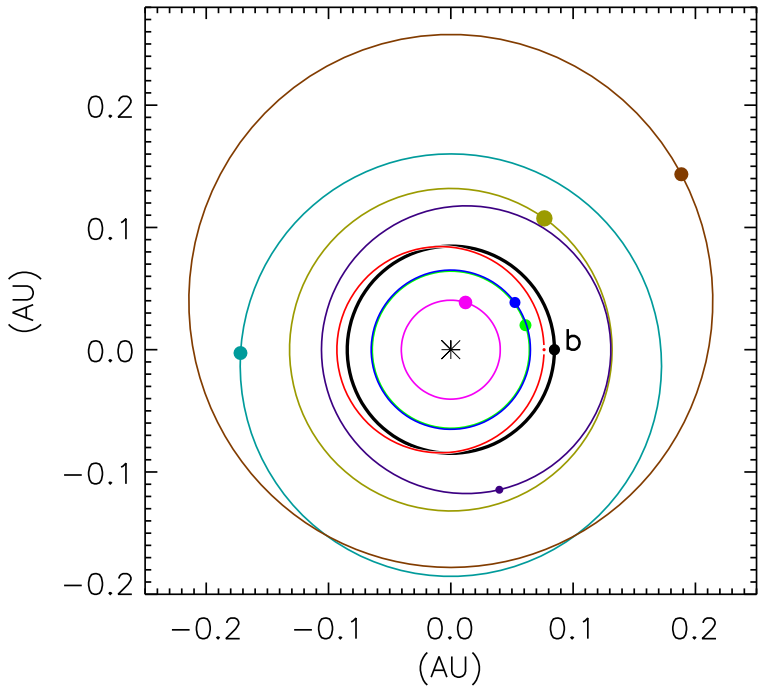

Figure 5.14.—: (Continued).

5.6.2 Constraints on Transits of Perturber

The *Kepler* team searches for transit signatures using the Transiting Planet Search pipeline module (Jenkins et al. 2010b). This has already been applied to the Kepler-19 light curve, and it identified transits of Kepler-19b. We analyzed the size of the planet we could have detected in the *Kepler* photometry by injecting signals at random phases and at varying planetary radii and attempting to blindly recover them. While the mass of Kepler-19c is highly uncertain, we can rule out the transits of at least some putative perturbers, as we describe here. The degeneracy of interpretation of the TTV signal means that we cannot address an exhaustive list of potential planets, but we comment here on the representative cases shown in Figure 5.14. The perturbing planet Kepler-19c may also not transit, in which case its orbit may be significantly misaligned from the transiting planet. Because Kepler-19b resides in a near-equatorial orbit (with $i >$88.62 with 3σ confidence), the orbit of Kepler-19c may also be misaligned by at least 0.27°, or 3.6σ in the exterior 2:1 resonance, for example, if it does not transit. In contrast, in the interior 1:2 resonance at 4.57 days, the planet would have to have $i <$85.7 to avoid transit. The planets would have to be misaligned by nearly 3 degrees in that case, if the orbits are circular.

First, we consider the orbits of 19c in second-order mean-motion or higher-order resonances. The planets depicted in Figure 5.14 range from 1.6 to 13.8 $M_\oplus$. We evaluate a minimum physical radius for the 1.6 $M_\oplus$ planet, assuming maximum collisional stripping of the planet during formation, from

the relationship derived by Marcus et al. (2010). At the maximum possible iron fraction, a 1.6 $M_\oplus$ planet would have a radius of 1 $R_\oplus$. At a period of 30 days (which range encloses mean-motion resonances up to 3:1 with Kepler-19c) we achieve 95% completeness at 1.0 $R_\oplus$. At 40 days, which includes the example perturber in Figure 5.14 in the 4:1 mean-motion resonance, we would still have detected a 1.0 $R_\oplus$ planet at 90% of phases.

If the planet Kepler-19c were instead coorbital with 19b, or if it resides in a satellite orbit, its mass could be much smaller, as described in the previous section: this mass could be as smaller as 0.1 $M_\oplus$ (equivalent to the mass of Mars) if its eccentricity were equal to 0.1. The models of Seager et al. (2007) show that a 0.1 $M_\oplus$ planet could be as small as 0.4 $R_\oplus$ if it comprised 70% iron and 30% silicate by mass (which is plausible, given the maximum iron fractions determined by Marcus et al. 2010). Its predicted transit depth would be 20 ppm, which might be barely detectable when compared to the error bar on the transit depth of Kepler-19b (with a necessarily similar orbital period) of 6 ppm. However, even if such a planet transited, its detection would be extremely challenging.

However, though the representative cases (with the exception of the coorbital scenario) depicted in Figure 5.14 would all have been readily detectable, we note that the perturbing planet could easily be smaller than 1 $R_\oplus$ in the mean-motion or higher-order resonance cases, in which case it might have eluded detection even in orbits with periods shorter than 30 days. However, we note that we achieve 95% completeness for 0.7 $R_\oplus$-sized planets up to 10 days, so such a world would have to be less massive than 0.7 $M_\oplus$ for $P < 10$ days, referring again to the

maximum iron fraction models derived by Marcus et al. (2010).

5.6.3 Search for Secondary Eclipse of Kepler-19b

If we assume the planet reradiates isotropically the energy it receives from its star, then the equilibrium temperature of Kepler-19b is given by:

$$T_p = (1 - A_B)^{1/4} T_\star \sqrt{\frac{R_\star}{2a}}, \tag{5.9}$$

where $T_\star$ is the temperature of the star, $a/R_\star$ is the orbital radius to stellar radius ratio, and A_B is the albedo of the planet. If we assume a Bond albedo A_B of 0.3 and ignore atmospheric effects in order to obtain a rough estimate for the equilibrium temperature, we may employ the MCMC chain of $a/R_\star$ (and the corresponding values for $T_{\rm eff}$ of the star identified from the nearest stellar isochrone, per the analysis in Section 3.2) to find the allowable range of planetary temperature. The range that encompasses 68% of realizations of planetary temperature is $T_P = 770 \pm 10$ K, rounded to the nearest 10 Kelvin.

There are two contributing sources to the occultation depth, namely the reflected starlight, and the emitted light from the planet itself. Both of these are dependent upon the unknown albedo of the planet. Assuming again the Bond albedo of 0.3, the expected depth due to reflected light is given by $\delta_{ref} = A_B(R_p/a)^2$; this value lies between 3 and 4 parts in 10^7. The expected occultation depth due to the emitted light of the planet is given by $\delta_{em} = (R_p/R_\star)^2 \cdot B_\lambda(T_p)/B_\lambda(T_\star)$. Using a wavelength of 700 nm (in the middle of

the *Kepler* bandpass) to estimate $B_\lambda(T)$, δ_{em} is of order 10^{-13} and so contributes negligibly to the expected eclipse depth.

To assess our sensitivity to the secondary eclipse, we fit a line to either side of each expected eclipse, and divided this line from the data during eclipse (centered on a phase of 0.5 and spanning 2.5 eclipse durations on either side), in a manner similar to the method we employed for data in transit. We then evaluated a model with epoch and duration set by the transit parameters given in Table 5.3.2, but with variable depth, from 0 to 20 ppm (considerably larger than the expected eclipse depth), and compared to the phase-folded light curve. We neglect the possibility that the transiting planet resides in an eccentric orbit, and thus that the secondary eclipse may not occur at a phase of 0.5. We find that our sensitivity is yet too low to detect the secondary eclipse at any phase. Values as high as 9 ppm are statistically indistinguishable from a depth of zero (furnishing a χ^2 difference less than 9). A planet with a maximal Bond albedo of 1 would produce a decrement of 1.2 ppm, which is still considerably below detectability with *Kepler*. Figure 5.15 shows the χ^2 improvement associated with adding an eclipse of variable depth at a phase of 0.5. The dotted line shows the expected depth for an extreme albedo of 1, which is indistinguishable from a flat line.

5.6.4 Composition of Kepler-19b

While we cannot estimate the mean density of Kepler-19b without a measurement of its mass, we can still draw meaningful conclusions about its composition from

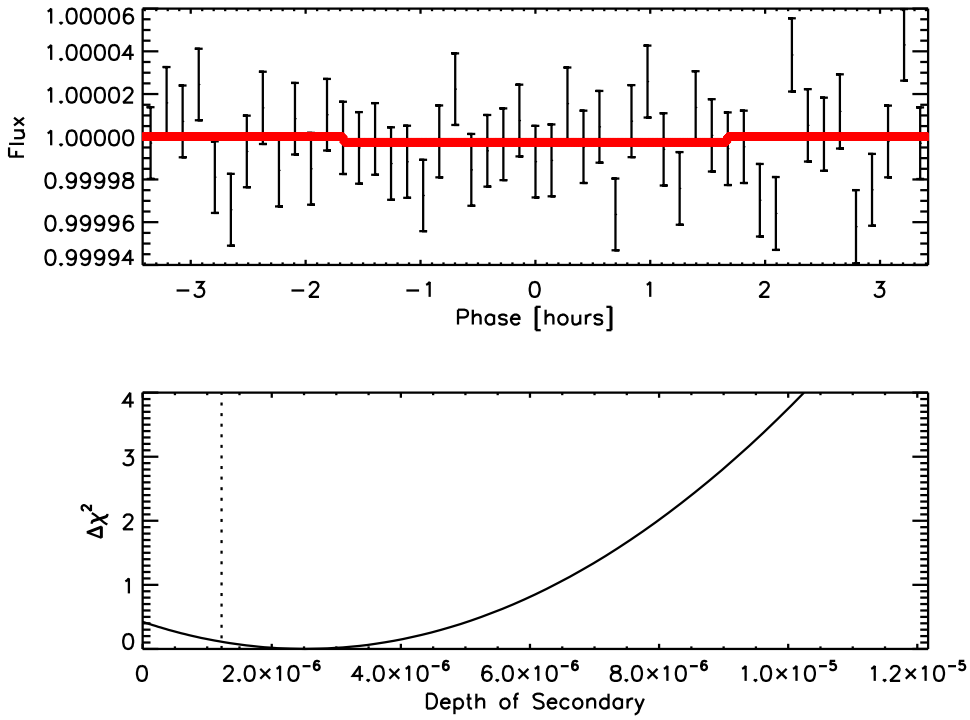

Figure 5.15.—: The Kepler-19 light curve at a phase of 0.5. The best eclipse light curve is shown overplotted, but this solution is statistically indistinguishable from a flat line. The expected depth for planet with an albedo of one is shown by the dashed line.

the upper limit mass value, as was done by Fressin et al. (2011) in the similar case of Kepler-10c. We first address whether we can rule out solid compositions at the highest density: a planet made of pure iron at a radius of 2.2 $R_\oplus$ would have a mass of 100 $M_\oplus$ (Seager et al. 2007). However, such a high fraction of iron is unphysical, even with maximal collisional stripping during the planet's formation; a 2.2 $R_\oplus$ planet with the largest possible iron fraction would have a mass of 30 $M_\oplus$ (Marcus et al. 2010). This maximum density is ruled out with

95% confidence by the mass upper limit from radial velocities of 20.3 $M_\oplus$. A planet composed of pure silicate at the measured radius, however, would have a mass of 15 $M_\oplus$ (Seager et al. 2007), which lies within the allowable mass range for Kepler-19b. In contrast, a 2.2 $R_\oplus$ planet with a homogeneous composition of water ice would have a mass of 4.5 $M_\oplus$ (Seager et al. 2007): mixtures of water ice and silicate in any fraction are therefore consistent with the measured mass upper limit. We consider also whether a substantial H/He envelope is possible for Kepler-19b. This scenario brackets the lower range of possible densities. Rogers et al. (2011) present theoretical models for planets in the radius range of 2-6 $R_\oplus$ and the temperature range 500-1000 K (in which sample Kepler-19b, with radius of 2.2 $R_\oplus$ and temperature near 700 K, is included), given different formation histories. If Kepler-19b formed by a nucleated core-accretion scenario beyond the snow line, a core of ice and rock surrounded by an H/He envelope would not be tenable even at the cooler equilibrium temperature of 500 K: such an envelope would have been lost in a timescale of <1 Gyr. An outgassed hydrogen envelope, by comparison, is a plausible scenario over a timescale greater than 1 Gyr, although the mass fraction of such an envelope would be less than 0.01 the mass of the planet (Rogers et al. 2011).

5.6.5 Future Prospects

In light of the dynamical study of Section 6.1, which combined transit time variations and radial velocities to characterize a perturber in the Kepler-19 system, we may ask whether we can expect to measure the precise orbital parameters of

planet 19c. The two main issues causing ambiguity among the perturber scenarios are: (i) the transit variations are consistent with a smooth sinusoid down to the noise level, with no additional hints of the perturber's identity such as "chopping" (Holman et al. 2010) on the conjunction timescale, (ii) the radial velocities, while essential to ruling out massive, non-planetary perturbers, simply do not have the precision sufficient to distinguish between the various planetary scenarios. The former issue might be resolved with much more data. The *Kepler* collaboration intends to keep Kepler-19 on its short cadence mode (demonstrated here to result in superior timing accuracy) for the remainder of the mission. Furthermore, in numerical simulations, chopping signals can wax and wane over secular cycles, so a detection of this effect is possible in future quarters. The latter issue requires more radial velocity data to resolve, which could allow us to further address the degeneracy of interpretation of the TTV signal, or could point to even more planets that are not clearly detected by transit timing variations.

We would like to thank the Spitzer team at IPAC and in particular Nancy Silbermann for scheduling the Spitzer observations of this program. This work is based on observations made with the Spitzer Space Telescope, which is operated by the Jet Propulsion Laboratory, California Institute of Technology under a contract with NASA. Support for this work was provided by NASA through an award issued by JPL/Caltech. This work is also based on observations made with Kepler, which was competitively selected as the tenth Discovery mission. Funding for this mission is provided by NASA's Science Mission Directorate. The authors would like to thank the many people who generously gave so much their time to

make this Mission a success. Some of the data presented herein were obtained at the W.M. Keck Observatory, which is operated as a scientific partnership among the California Institute of Technology, the University of California and the National Aeronautics and Space Administration. The Observatory was made possible by the generous financial support of the W.M. Keck Foundation.

Table 5.4. Transit Times for Kepler-19b From Q0-Q8

Transit Number	Transit Time [BJD-2450000]	Predicted Time (from linear ephemeris)	O-C [min]	-1σ [min]	$+1\sigma$ [min]
1	4959.70744	4959.70605	2.0	2.6	2.7
2	4968.98895	4968.99305	-5.9	3.4	5.6
3	4978.27949	4978.28004	-0.8	3.6	3.2
4	4987.56280	4987.56704	-6.1	3.3	3.2
5	4996.85396	4996.85403	-0.10	3.8	3.5
6	5006.13936	5006.14102	-2.4	3.4	4.2
8	5024.71126	5024.71501	-5.4	3.2	3.3
9	5033.99971	5034.00201	-3.3	4.0	3.9
10	5043.28879	5043.28900	-0.30	3.2	3.5
11	5052.57509	5052.57599	-1.3	3.9	4.0
12	5061.85993	5061.86299	-4.4	3.2	3.3
13	5071.14832	5071.14998	-2.4	3.5	3.4
14	5080.43524	5080.43698	-2.5	3.3	4.5
15	5089.72744	5089.72397	5.0	3.2	2.9
16	5099.00860	5099.01096	-3.4	2.2	1.7
17	5108.29463	5108.29796	-4.8	1.7	1.5
18	5117.58342	5117.58495	-2.2	2.0	1.7
19	5126.87077	5126.87195	-1.7	2.8	2.0
20	5136.15957	5136.15894	0.9	4.1	1.5
21	5145.44635	5145.44593	0.6	1.8	2.0
23	5164.02277	5164.01992	4.1	2.0	0.9
24	5173.30976	5173.30692	4.1	1.5	1.3
26	5201.17269	5201.16790	6.9	1.5	1.3
27	5210.45913	5210.45489	6.1	3.9	3.1
28	5219.74591	5219.74189	5.8	1.4	1.4
29	5229.03319	5229.02888	6.2	1.6	2.3
30	5238.31921	5238.31587	4.8	1.3	1.3
31	5247.60551	5247.60287	3.8	1.4	1.4
32	5256.89243	5256.88986	3.7	1.5	1.8
33	5266.18033	5266.17686	5.0	1.5	2.0
34	5284.75126	5284.75084	0.6	2.6	1.6
36	5294.03582	5294.03784	-2.9	1.0	1.9
37	5303.32205	5303.32483	-4.0	1.7	2.2
38	5312.61016	5312.61183	-2.4	1.6	1.7
39	5321.89569	5321.89882	-4.5	2.0	1.3
40	5331.18179	5331.18581	-5.8	1.5	1.3
41	5340.46857	5340.47281	-6.1	2.6	1.7
42	5349.75577	5349.75980	-5.8	8.7	1.6
43	5359.04291	5359.04680	-5.6	1.6	1.7
44	5368.33171	5368.33379	-3.0	1.5	2.3
45	5377.61939	5377.62078	-2.0	1.8	1.5
46	5386.90368	5386.90778	-5.9	2.0	1.8
47	5396.19179	5396.19477	-4.3	2.4	1.7
48	5405.47968	5405.48177	-3.0	2.4	1.5
49	5414.76688	5414.76876	-2.7	2.2	1.5
50	5424.05381	5424.05575	-2.8	3.2	2.4
51	5433.34275	5433.34275	0.0	1.8	2.1

Table 5.4—Continued

Transit Number	Transit Time [BJD-2450000]	Predicted Time (from linear ephemeris)	O-C [min]	-1σ [min]	$+1\sigma$ [min]
52	5442.62821	5442.62974	-2.2	3.2	3.2
53	5451.91715	5451.91674	0.6	2.0	1.4
54	5461.20241	5461.20373	-1.9	1.7	3.8
55	5470.49253	5470.49072	2.6	1.8	1.9
56	5479.77723	5479.77772	-0.7	1.3	1.4
57	5489.06589	5489.06471	1.7	2.4	3.1
58	5498.35615	5498.35171	6.4	1.8	2.1
59	5507.64127	5507.63870	3.7	1.3	1.2
60	5516.92944	5516.92569	5.4	1.5	1.8
61	5526.21866	5526.21269	8.6	2.1	1.8
62	5535.49975	5535.49968	0.1	1.4	1.7
63	5544.78855	5544.78668	2.7	1.3	1.2
64	5572.64863	5572.64766	1.4	1.7	1.3
67	5581.93437	5581.93465	-0.4	1.4	1.8
68	5591.22095	5591.22165	-1.0	1.2	1.2
69	5600.50788	5600.50864	-1.1	1.3	1.4
70	5609.79355	5609.79563	-3.0	1.3	1.6
71	5619.07832	5619.08263	-6.2	1.4	1.7
72	5628.36705	5628.36962	-3.7	1.2	1.2

Note. — Transits with numbers < 16 were gathered at long cadence (with an exposure time of 29.5 minutes), while transits with numbers ≥ 16 were gathered at short cadence (with an exposure time of 58.8 seconds).

Chapter 6

KOI 1361: A Transiting 2.0 $R_\oplus$ Planet Candidate in the Habitable Zone of a Low-Mass Star

S. Ballard, D. Charbonneau, J.-M. Désert, G. Torres, J. Irwin, S. T. Bryson, D. R. Ciardi, & S. B. Howell

Abstract

We present evidence toward the validation of KOI 1361.01: a super-Earth-sized planet in the habitable zone of a low-mass star. We combine published

spectroscopic characterization of the star with *Kepler* photometry to deduce a planetary radius of $2.02^{+0.38}_{-0.32}$ $R_\oplus$ and an equilibrium temperature of 257^{+10}_{-5} K (assuming a planetary albedo of 0.3), and a stellar mass and radius of 0.57±0.10 $M_\odot$ and 0.55±0.08 $R_\odot$, respectively. From a year of *Kepler* photometry, we find a stellar rotation period of 36 days, which implies a stellar age of > 1 Gyr. We summarize the evidence for the planetary nature of KOI 1361.01, which includes a published *a priori* false positive probability of $< 5\%$, centroid motion analysis, and *Spitzer* photometry. Finally, we discuss possible compositions for KOI 136.01 with a comparison to theoretical models as well as to known exoplanets with similar radii and dynamically measured masses. We find that, given the known exoplanets with radii smaller than 3 $R_\oplus$, a mean density greater than 7 g cm^3 is unlikely. Assuming a maximum density of 7 g cm^3, the planetary mass must be less than 10 $M_\oplus$. We consider habitability concerns for super-Earths orbiting M dwarfs. These effects include spin synchronization, which we we conclude has likely occurred for KOI 1361.01, and tidal heating, which in this case is insufficient to induce plate tectonics. Although stellar activity is also a concern for planets orbiting M dwarfs, given the mass and age of the KOI 1361 we consider it unlikely to be active.

6.1 Introduction

With the discoveries of exoplanets Kepler-22b (Borucki et al. 2011), Kepler-20e & f (Fressin et al. 2012), and KOI 961.01–961.03 (Muirhead et al. 2012), astronomers

are encroaching upon the regime of terrestrial exoplanets in their stellar habitable zones. Kepler 22b is the first super-Earth-sized exoplanet with a measured radius to reside in the habitable zone of a sun-like star, though its radius of 2.4 $R_\oplus$ does not necessitate a terrestrial composition. The Kepler-20 and KOI 961 exoplanetary systems each comprise multiple planets that are Earth-sized or smaller (as small as Mars in the case of KOI 961.03). However, these planets orbit too close to their host stars to lie within the habitable zone. The most recent release of *Kepler* exoplanetary candidates (Batalha et al. 2012) contains 10 members <2 $R_\oplus$ and with equilibrium temperatures between 185 and 303 K. This temperature range is a generous definition of the habitable zone proposed by Kasting (2012). However, these candidates are as-yet unvalidated as authentic planets.

KOI 1361.01, a transiting exoplanet candidate 2.0 $R_\oplus$ in size with an equilibrium temperature of 257 K (assuming an Earth-like albedo of 0.3), comprises another member of the set of exoplanets that edge toward the Earth-like, habitable-zone planet marker. Kaltenegger & Sasselov (2011) define the range of planetary equilibrium temperatures from 175–270 K to consistute the "habitable zone", which definition we employ here. The high-temperature cutoff of this range accounts for the presence of atmospheric warming (above 270 K, a runaway greenhouse effect occurs). This planet candidate is also reflective of another result of the *Kepler* mission to date, which is that small planets (within the 2–4 $R_\oplus$ range) are more common around M dwarfs than around solar-type stars (within the period range <50 days studies by Howard et al.

2011a). KOI 1361.01, which orbits an M0 star (among the coolest observed by *Kepler*) lies within its habitable zone even with a 60 day period. The suggestion of small planets being more common around M dwarfs is a promising one, since M dwarfs are the most common stellar type and exist in abundance in our stellar neighborhood. However, the concept of habitability around M dwarf is complicated by the same factor that makes small planets in their habitable zones more amenable to transit detection: the close position of the habitable zone to its star. This fact has implications for spin-synchronization and tidal heating of planets in the habitable zones of M dwarfs. Additionally, the magnetic activity of M dwarfs, coupled with the proximity of the habitable zone to the star, poses questions about the lifetimes of planetary atmospheres in the presence of possibly intense UV radiation.

The composition of KOI 1361.01, for which we have no mass measurement, is also uncertain. While we are able to validate its authentic planetary nature with a statistical argument about the likelihood of the planet scenario in comparison to false-positive scenarios with `BLENDER` which machinery has already been applied to validate Kepler-9d (Torres et al. 2011), Kepler-11f (Lissauer et al. 2011), Kepler-10c (Fressin et al. 2011), Kepler-10b (Ballard et al. 2011), Kepler-22b (Borucki et al. 2012), and Kepler-20 e & f (Fressin et al. 2012), without a mass measurement we can provide only theoretical limitations on the bulk density of the planet. However, a rocky composition is a plausible one among others, as we describe below, in which case the planet could have a solid surface and a temperature that could support an atmosphere and liquid water. It is also

possible that KOI 1361.01 is more like a "mini-Neptune" (Rogers et al. 2011), in which case it would possess a hydrogen and helium atmosphere and have a much lower density.

In Section 2, we describe the *Kepler* observations of KOI 1361.01. In Section 3 we describe our characterization of the transit light curve and the physical parmeters of the star, which folds in published spectroscopic information. In Section 4, we describe follow-up imaging observations of the star to characterize any additional stars within the *Kepler* photometric aperture of KOI 1361. In Section 5, we describe the validation efforts to date. In Section 6, we comment on the stellar rotation of KOI 1361 and transit times of KOI 1361.01. We also discuss the nature of the planet from a habitability standpoint. Finally, in Section 7, we describe future prospects.

6.2 *Kepler* Observations

The *Kepler* spacecraft, launched on 7 March 2009, will photometrically monitor 170,000 stars for 3.5 years for evidence of transiting planets. Argabright et al. (2008) provides an overview of the *Kepler* instrument, and Caldwell et al. (2010) and Jenkins et al. (2010b) provide a summary of its performance since launch. The *Kepler* observations of KOI 1361 that we present in this work were gathered from 13 May 2009 to 28 September 2011, spanning *Kepler* "Quarters" 1–10. All data for this star were gathered in long-cadence mode (characterized by an exposure time of 29.5 minutes). The data contain gaps of approximately 3 days

between quarters for scheduled downlinks. We used the raw light curves generated by the *Kepler* aperture photometry (PA) pipeline, described in Twicken et al. (2010), to which we add an additional step. We remove the effects of baseline drift by individually normalizing each transit as follows. We fit a line with time to the flux immediately before and after transit (specifically, from 9 hours to 20 minutes before first contact, equal to 2.5 transit durations, and an equivalent time after fourth contact).

6.3 Analysis

6.3.1 Derivation of Planetary Parameters from the *Kepler* Light Curve

We estimated the uncertainty in the parameters using the Markov Chain Monte Carlo (MCMC) method as follows. We employ model light curves generated with the routines in Mandel & Agol (2002), which depend upon the period P, the epoch T_c, the planet-to-star radius ratio $R_p/R_\star$, the ratio of the semi-major axis to the stellar radius $a/R_\star$, the inclination of the orbit i, the eccentricity e, and the longitude of periastron, ω. We fixed two quadratic limb-darkening coefficients (LDCs), u_1 and u_2, to theoretical values based on published spectral classification of KOI 1361 from Muirhead et al. (2012) (we consider the stellar characterization in greater detail in Section 4.1 using both optical spectra and the stellar colors, but these analyses corroborate the published characterization).

We compared the effective stellar temperature $T_{\rm eff}$ of 3929^{+66}_{-135} and metallicity [Fe/H] of -0.02±0.11 to the grid of stellar model from the tables of theoretical limb-darkening coefficients generated for the *Kepler* bandpass by Claret & Bloemen (2011), and found that the closest match corresponded to a model with $T_{\rm eff}$=4000 K, [Fe/H]=0.0 (we additionally specified a log(g) of 5.0 and an intermediate turbulent velocity value of 2 km s^{-1}): these coefficients are u_1=0.473 and u_2=0.2546. We accounted for the 29.5 minute integration time of the *Kepler* photometry, which is comparable in this case to the ingress and egress duration of the planet candidate, by evaluating the light curve model at intervals of 1 minute, and then summing the model over the long cadence integration time.

To generate the MCMC chain, we randomly choose one parameter, perturb it, and evaluate the χ^2 of the solution. If the χ^2 is lower, we accept the new parameter value. If the χ^2 is higher, we evaluate the probability of accepting the jump as $p = e^{-\Delta\chi^2/2}$. We adjust the width of the distribution from which we randomly draw the jump sizes in each parameter until 20–30% of jumps are executed in each of the parameters. We created five chains, each of length 4×10^5 points, where each of the chains is begun from a different set of starting parameters (each parameter is assigned a starting position that is $+3\sigma$ or -3σ from the best-fit values). We discard the first 20% of jumps from each chain to remove the transient dependence of the chain on the starting parameters. We first conducted this analysis, as described, using only the *Kepler* light curve to inform our value of χ^2. However, the allowable stellar densities we infer from the light curve alone is much broader than the range of stellar densities consistent with

our spectroscopic information about the star. Because KOI 1361 is an M star, its range of theoretical densities is tightly constrained for ages < 14 Gyr. In Figure 6.1, we show the Dartmouth stellar evolutionary models (Dotter et al. 2008) for ages from 0.2–14 Gyr and a metallicity of -0.02 (from the Muirhead et al. 2012 stellar classification). We have indicated the allowable range of $a/R_\star$ which is permitted from the light curve alone, and the range of effective temperature permitted by Muirhead et al. (2012), both with 1σ confidence. In this case, the range of allowable stellar densities from the Dartmouth stellar evolutionary models is much tighter than the range allowed by the light curve; or, stated differently, the light curve allows for values of $a/R_\star$ which are not physically plausible given our prior knowledge of the star KOI 1361.

In this case, we take advantage of the fact that M stars are slowly evolving to set a prior on $a/R_\star$ as follows. We based our procedure for constraining the mass, radius, and age of the host star on the method described by Torres et al. (2008). Using the metallicity determined by Muirhead et al. (2012), we created a set of stellar evolution models from the Dartmouth isochrone series (Dotter et al. 2008). We employed the interpolation software that accompanied that work, which accepts as inputs the age of the star, the iron abundance, and the abundance of α-elements relative to solar (for which we assume the solar value), and outputs a grid of stellar isochrones corresponding to a range of masses. We evaluated a set of isochrones over an age range of 0.2 to 14 Gyr (at intervals of 0.1 Gyr) and in [Fe/H] in 60 equally spaced increments from -3σ to $+3\sigma$ above and below the best-fit value of [Fe/H]$=-0.02 \pm 0.11$. We evaluate the physical

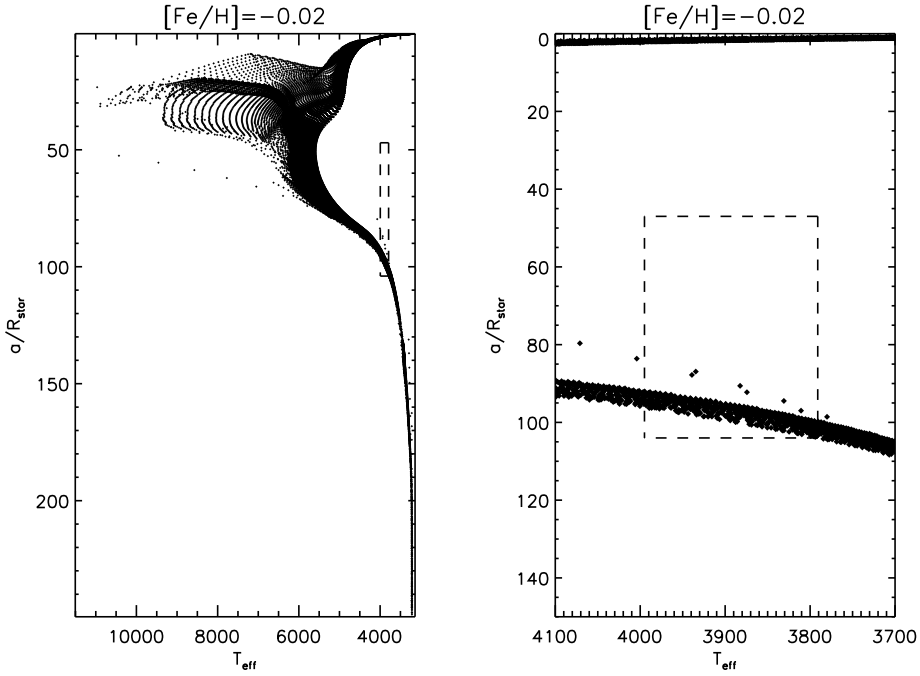

Figure 6.1.—: Comparison between Dartmouth stellar isochrones and allowable region from photometry and spectroscopy. The panel at right is an inset, in the allowable temperature range of the star KOI 1361, of the larger figure at left.

radius corresponding to each stellar model via log(g) and the mass of the star ($g = GM_\star/R_\star^2$), though it is also possible to convert to physical radius using the model stellar luminosity and effective temperature (assuming $L_\star = 4\pi R_\star \sigma T^4$); in practice these conversions give identical results.

Rearranging Kepler's version of Newton's third law in the manner employed by Seager & Mallén-Ornelas (2003), Sozzetti et al. (2007) and Torres et al. (2008), we convert the period (derived from photometry), and the radius and mass of the host star (from isochrones) to a ratio of the semi-major axis to the radius of the host star, $a/R_\star$:

$$\frac{a}{R_\star} = \left(\frac{G}{4\pi^2}\right)^{1/3} \frac{P^{2/3}}{R_\star}(M_\star + M_p)^{1/3}, \tag{6.1}$$

where we assume that M_p is negligible when compared to the mass of the host star.

We calculate the corresponding value of $a/R_\star$ for each stellar model. We then generate the MCMC chain as follows. We implement our prior on $a/R_\star$ by varying the quantities [Fe/H] and $T_{\rm eff}$ in the chain, in addition to the light curve parameters. For each set of [Fe/H] and $T_{\rm eff}$, we locate the closest stellar model associated with these values and record its corresponding stellar density, $a/R_\star$. It is this value of $a/R_\star$ that is used to generate the light curve model, along with the other light curve parameters, which are permitted to vary independently. In this way, we are sampling only values of $a/R_\star$ that are consistent with the spectroscopically-derived parameters, but values of $a/R_\star$ that are not as well

matched to the light curve are penalized by the χ^2 term corresponding to the photometry. We penalize values of [Fe/H] and $T_{\rm eff}$ that are inconsistent with the measured spectra by including them as terms in the χ^2 that we evaluate at every step of of the chain (where $\mathbf{P}$ corresponds to the vector of light curve parameters at each iteration).

$$\chi^2 = \sum_{i=1}^{n} \left(\frac{f_i - m(\mathbf{P})_i}{\sigma_i} \right)^2 + \left(\frac{\Delta T_{\rm eff}}{\sigma_{T_{\rm eff}}} \right)^2 + \left(\frac{\Delta [{\rm Fe/H}]}{\sigma_{[{\rm Fe/H}]}} \right)^2 . \tag{6.2}$$

In Figure 6.2, we show the MCMC correlations between all free parameters in the model fit, as well as the histograms corresponding to each parameter. In Figure 6.3, we show the phased *Kepler* transit light curve for KOI 1361.01, with the best-fit transit light curve overplotted. We report the best-fit parameters and uncertainties in Table 6.3.2. The range of acceptable solutions for each of the light curve parameters is determined as follows. We report the "best" solution from the set of parameters that minimize the χ^2. The error bars are then given by the highest and lowest values that are within the 68% of points closest in χ^2 to the best value.

Figure 6.2.—: (Following page) Markov Chain Monte Carlo probability distributions for light curve parameters of KOI-1361.01. The dark grey area encloses 68% of the values in the chain, while the light grey area encloses 95% of the values. We assign the range of values corresponding to 1σ confidence from the area enclosing 68% of the values nearest to the parameters associated with the minimum χ^2 (as described in the text).

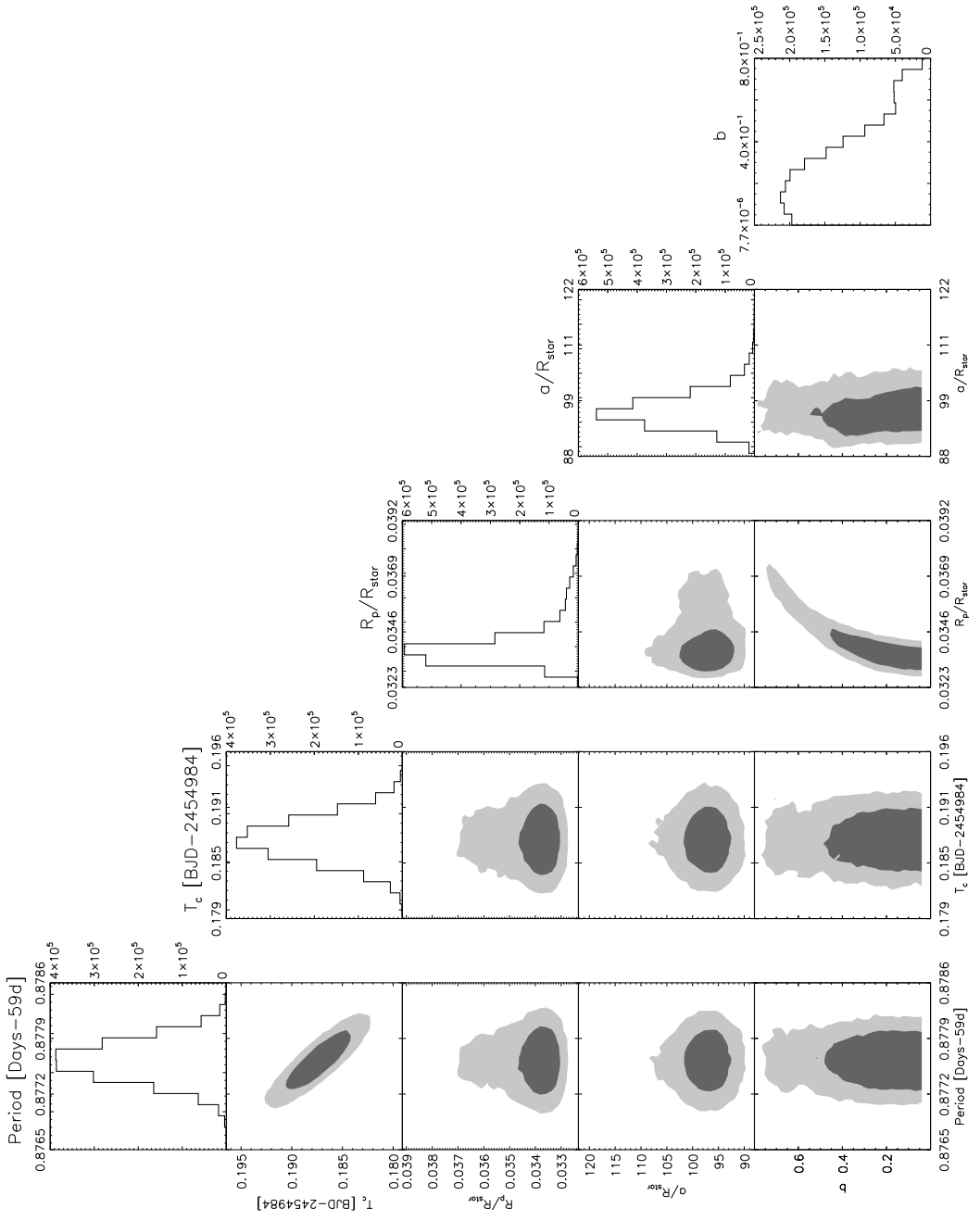

Figure 6.2.—: (Continued).

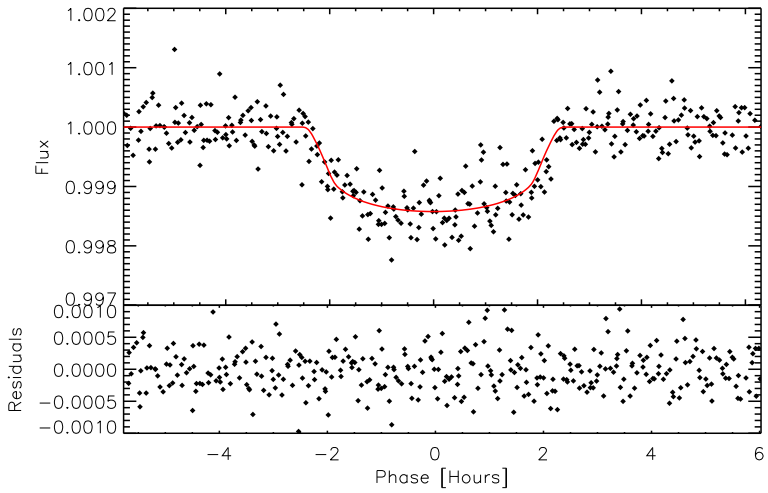

Figure 6.3.—: *Kepler* transit light curve for Quarters 1–10 of KOI 1361.01, centered on time of transit. Overplotted in red is the best transit model light curve, with parameters given in Table 6.3.2. The bottom panels shows the residuals of the light curve, after the model is subtracted.

6.3.2 Physical Parameters

This procedure described in Section 1.1 is also advantageous in that, in addition to recording the value of $a/R_\star$ at each iteration of the MCMC chain, we may also record the other traits of the star at that value of [Fe/H] and $T_{\rm eff}$, including its mass, radius, luminosity, and age. At the conclusion of the MCMC analysis, therefore, we have accumulated a chain not only for the light curve parameters, but for the physical parameters as well. The correlations between parameters, both physical parameters and those associated with the light curve, are therefore preserved in the chain and incorporated into our estimate of the stellar parameters.

In Figure 6.4, we show the posterior distributions for the stellar radius, mass, and age, as well as the planetary radius (which we calculate from multiplying the elements of the $R_p/R_\star$ by the chain of $R_\star$). The posterior distribution for stellar age reflects a weak preference for young stars, peaking at 1 Gyr. However, the stellar rotation period (36 days, described in Section 6.1) indicates a star older than 1 Gyr. We consider the stellar age posterior distribution to be too broad to make these two age indications necessarily contradictory: by integrating the posterior distribution, we find rather that ages > 1 Gyr account for 80% of the probability.

It's also possible to evaluate the posterior distribution of planetary equilibrium temperatures from the MCMC analysis. In the case of a circular orbit, we require only the stellar radius and temperature, the planetary semimajor axis, and the planetary albedo. However, in the case of an eccentric orbit, the planet receives time-variable stellar insolation. In order to evaluate the equilibrium temperature of the planet in the case of non-zero eccentricity, we evaluate the time-averaged equilibrium temperature by performing an integral over the mean anomaly from 0 to 2π, using the formalism detailed in Murray & Correia (2010):

$$\frac{1}{2\pi}\int_0^{2\pi} T_{eq}\mathrm{d}M = \frac{1}{2\pi}(1-A)^{1/4}\int_0^{2\pi}\sqrt{\frac{R_\star}{2d}}T_\star \mathrm{d}M \tag{6.3}$$

In Figure 6.5, we show both the planetary temperatures based on the apastron and periastron isolation from the star, as well as the time-averaged temperature of the planet, for each element of the MCMC chain.

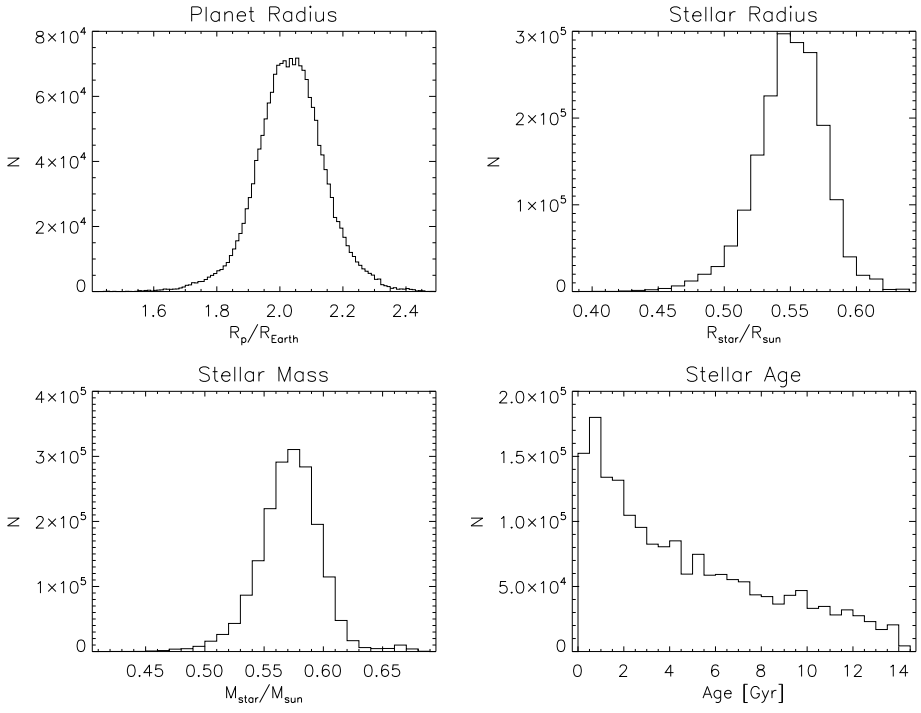

Figure 6.4.—: MCMC histograms of physical parameters. *Top:* Planetary and stellar radius, in units of Earth and solar radii. *Bottom:* Stellar mass and age, in solar mass and Gyr, respectively.

We did not impose a prior on the eccentricity of KOI 1361.01, so the posterior distribution on e includes values as high as 0.95 (such a large eccentricity still matches the transit duration at finely-tuned values of ω). Indeed, the circularization timescale for KOI 1361.01 has not yet elapsed if we assume it did not possess a large initial eccentricity. We consider the expression for circularization time (for modest initial e) given by Goldreich & Soter (1966), where a is the semimajor axis of the planet, R_p is the planetary radius, M_p is the planetary mass, $M_\star$ the stellar mass, Q is the tidal quality factor for the planet

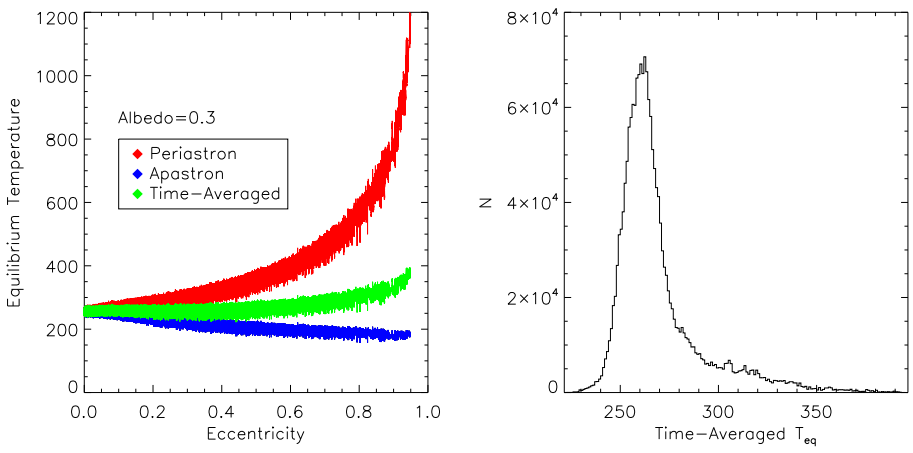

Figure 6.5.—: *Left:* For each iteration of the MCMC chain, we calculate the temperature of the planet at apastron (blue), periastron (red) and the time-averaged equilibrium temperature (green). We have assumed an albedo of 0.3. *Right:* Histogram of time-averaged equilibrium temperatures for KOI 1361.01. The long tail of temperatures higher than 300 K is contributed entirely from orbital eccentricities > 0.6.

(which is highly uncertain, but which we take to be in the range 10–100 for the assumption of a terrestrial composition, per Goldreich & Soter 1966) and G is the gravitational constant:

$$t_{circ} = \frac{4}{63} \frac{1}{\sqrt{GM_\star^3}} \frac{M_p a^{13/2} Q}{R_p^5} \tag{6.4}$$

We find that the circularization timescale is 312 Gyr in the shortest case (for a 10 $M_\oplus$ planet, with Q of 10, orbiting a 0.67 $M_\odot$ star, which is 1σ higher than the predicted stellar mass) at 0.25 AU. It's therefore plausible that the planet

resides in an eccentric orbit, even if its age were on the higher end of the allowable range. However, if KOI 1361.01 began with a large initial eccentricity, then terms of order (1-e^2) become relevant and the circularization timescale decreases (as elucidated in Equations 7–9 of Socrates et al. 2011). It's therefore also possible that the circularization timescale has indeed elapsed, dependent upon the initial eccentricity of the planet. However, the uncertainty of our knowledge about its initial eccentricity (coupled with the uncertainty about the correct value of tidal Q for KOI 1361.01 in particular) is such that we believe a flat prior on e to be appropriate.

6.4 Follow-up Observations

6.4.1 Optical Spectroscopy

On 22 March 2012 we gathered an optical spectrum of KOI 1361 with the FAST spectrograph (Fabricant et al. 1998), mounted on the 1.5 m Tillingham telescope at Mt. Hopkins, AZ. We employed the 600 grooves mm^{-1} grating, which has a spectral coverage of 2000 $\mathring{A}$ centered at 5500 $\mathring{A}$, and the 2" slit. With an integration time of 20 minutes, we achieve a signal-to-noise ratio of 30 per pixel (with resolution of 0.75 Å per pixel). We use the Hammer spectral typing algorithm (Covey et al. 2007) to determine a spectral type of K7, which we conclude is consistent with the spectral type (M0) and temperature (3929^{+66}_{-135} K) determined by Muirhead et al. (2012) for three reasons. First, the Hammer is

Table 6.1. Star and Planet Parameters for KOI-1361

Parameter	Value	$+1\sigma$	-1σ
KOI 1361 [star]			
Right ascension	19h41m13.09s		
Declination	+42d28m31.0s		
$T_{\rm eff}$[a]	3929	66	135
[Fe/H][a]	-0.02	0.11	0.11
$M_\star$ [Solar masses]	0.57	0.10	0.10
$R_\star$ [Solar radii]	0.553	0.082	0.092
Age [Gyr]	$\leq$14.0		
KOI 1361.01 [candidate planet]			
Period [Days]	59.87762	0.00066	0.00062
T_0 [BJD-2450000]	4984.1875	0.0066	0.0065
$R_p/R_\star$	0.03360	0.00470	0.00081
Depth [ppm]	1403	73	65
a/$R_\star$	96.9	13.	7.7
inc [deg]	$\geq$89.055		
u_1	0.4730		
u_2	0.2546		
e	$\leq$0.95		
e cos(ω)	-0.01	0.76	0.71
Impact Parameter	$\leq$0.76		
Total Duration [min]	280.4	18.	8.1
Ingress Duration [min]	9.29	17.	0.46
R_p [Earth radii]	2.02	0.38	0.32
T_{eq} [K]	257	10	5

[a]Stellar effective temperature and metallicity are derived from near-infrared spectroscopy by Muirhead et al. (2012).

accurate to ±1 spectral subtype, and does not include K8 or K9 spectral types, since they are not included in the spectral sequence produced by Kirkpatrick et al. (1991). Therefore, a type of K7 from optical spectra is consistent with a type of M0 from the near-infrared spectrum, allowing for the ±1 spectral type accuracy achieved by the Hammer. Secondly, comparison between spectral type and temperature as in Boyajian et al. (2010) shows that K7 stars span a range of temperatures between 3750 and 4100 K, which is consistent with the value of 3929 K found by Muirhead et al. (2012). Thirdly, we are inclined to give additional confidence to the H2O-K2 index determination of the temperature of KOI-1361.01 based upon the results of Rojas-Ayala et al. (2012), who found that the H2O-K2 index is still a good predictor of optical spectral type down to M0.

6.4.2 UKIRT Imaging

We gathered moderate resolution images in J band of KOI 1361 on 13 July 2009, using the Wide Field Camera (WFCAM) on the United Kingom Infra-Red Telescope (UKIRT) (Hayward et al. 2001) on Mauna Kea, HI. Casali et al. (2007) give a complete description of WFCAM. We employed a 5 s integration time to gather the image shown in Figure 6.6, which depicts the local neighborhood of KOI 1361 within 1 arcminute.

We assess our sensitivity to additional sources using a similar procedure to that described by Batalha et al. (2011). We inject fake sources near the target star at random position angles, using steps in magnitude of 0.5 mag and

varying the distance from the target star in increments of 1.0 FWHM of the point-spread function (PSF). We then attempt to identify the injected sources with the DAOPhot routine (Stetson 1987) and also by eye, and set our sensitivity limit, as a function of distance, at the magnitude where we are able to recover the injected sources. The limit in Δm as a function of distance from the target star is shown in Figure 6.6. We then convert the Δm sensitivity limit in J band to a limit in *Kepler* magnitudes, by assuming a nominal *Kepler* magnitude-J color (using the value derived from a magnitude-limited sample of Kp-J=1.28±0.52 mag). We do not detect any additional sources within our sensitivity limits in the neighborhood of KOI 1361.

6.4.3 Speckle Imaging

We gathered speckle images of KOI 1361 at 880 nm on UT 11 June 2011, using the Differential Speckle Survey Instrument located at the WIYN telescope (DSSI, Horch et al. 2009). We assess our sensitivity to the presence of additional stars near the *Kepler* target star as a function of angular distance. For concentric rings of varying radius, centered on the target star, we determine the magnitude difference between the target star itself and the local extrema of the sky background. Figure 6.7 shows the results of this procedure at 880 nm. We find that we would have detected a companion at a distance of 0.2" with a difference in magnitude greater than Δm=2.5. We detect no additional sources nearby to the *Kepler* target star.

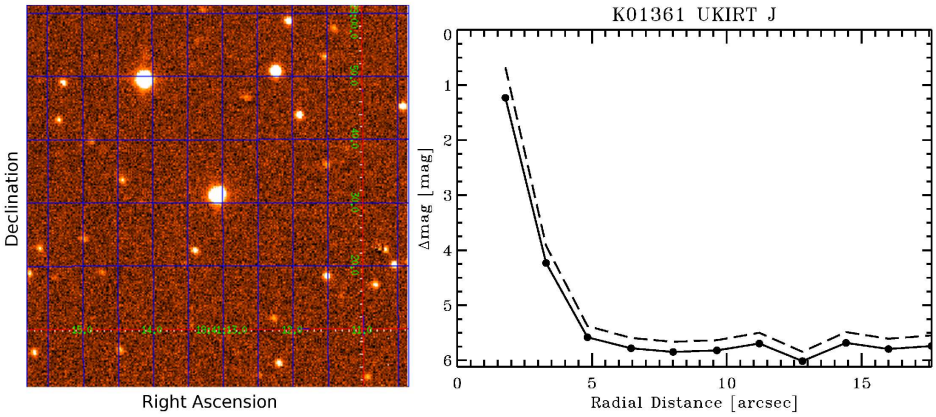

Figure 6.6.—: *Left:* UKIRT image of the neighborhood of KOI 1361, within 1 arcminute. *Right:*The sensitivity limits to additional point sources in the neighborhood of Kepler-19b as a function of radial distance from the primary target. The filled circles represent the J-band limits and each point represents a step in FWHM away from the primary target centroid peak. The dashed line underneath represents the J-band limits converted to *Kepler* magnitude limits if a star were to have a nominal Kp-J color, as described in the text.

6.5 Planetary Validation of Kepler-19b

Morton & Johnson (2011) provide *a priori* false positive probabilities for the *Kepler* planetary candidates published by Borucki et al. (2011), within which sample KOI 1361.01 is included. They cite the vetting of candidates by the *Kepler* software (detailed by Batalha et al. 2010) as being already sufficient to produce a robust list of candidates, and combine stellar population synthesis and galactic structure models to demonstrate that nearly all of these 1235 candidates have a false positive probability <10%. KOI 1361.01, with a *Kepler* magnitude of 14.995

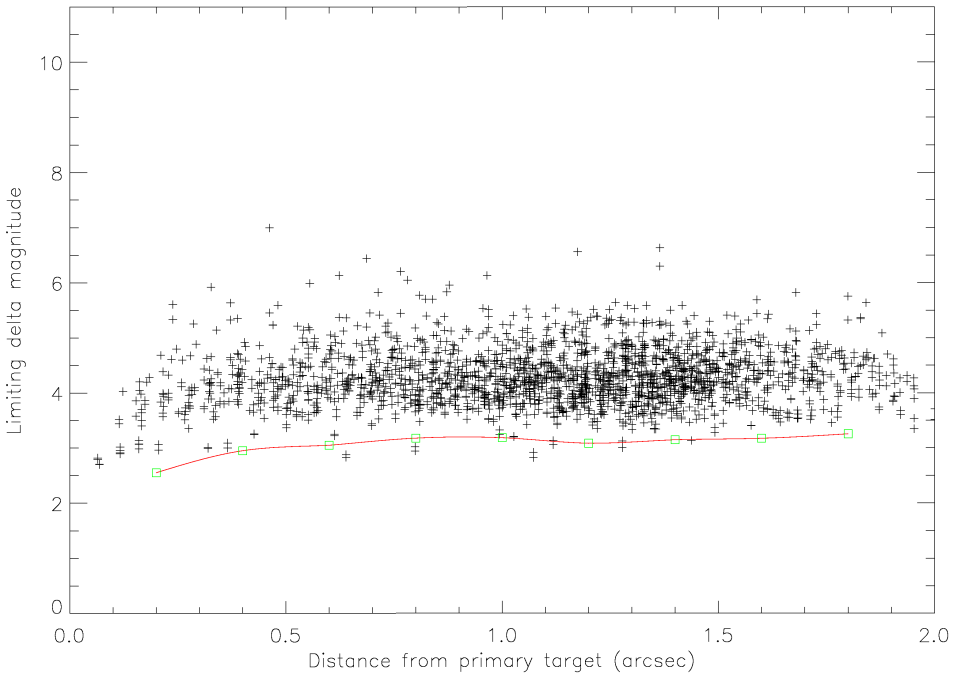

Figure 6.7.—: 880 nm speckle sensitivity curve of KOI 1361. The magnitude difference between the target star and local extrema in the background are denoted by crosses. The solid line denotes a flux that is 5σ brighter than the mean background brightness (where σ is the standard deviation of the extrema in the background), where we could confidently detected an additional source. No companions are detected within 1.8 arcseconds of the target star to a depth of 2.5 magnitudes.

and a galactic latitude of 9.6°, has an *a priori* false positive probability of 4.8%.

6.5.1 Photocenter Tests

We use two methods to search for false positives due to background eclipsing binaries, based on examination of the pixels in the aperture of KOI 1361: direct measurement of the source location via difference images, and inference of the

source location from photocenter motion associated with the transits. We employ two methods because of their different vulnerabilities to systematic bias; when the methods agree, we have increased confidence in their result.

Difference image analysis (Torres et al. 2011) takes the difference between average in-transit pixel images and average out-of-transit images. A fit of the Kepler pixel response function (PRF; Bryson et al. 2010) to both the difference and out-of-transit images directly provides the location of the transit signal relative to the host star. We measure difference images separately in each quarter, and estimate the transit source location as the robust uncertainty-weighted average of the quarterly results.

We measure photocenter motion by computing the flux-weighted centroid of the pixels in the optimal aperture, plus a one-pixel halo in every cadence, generating a centroid time series for row and column. We fit the modeled transit to the whitened centroid time series transformed into sky coordinates. We perform a single fit for all quarters, and then infer the source location by scaling the difference of these two centroids by the inverse of the flux as described in Jenkins et al. (2010a).

The source as determined by the difference image method is offset from the nominal location of Kepler-19, as given in the *Kepler* Input Catalog, by 0.09 ± 0.29 arcsec $= 0.68\sigma$. The source as determined by the flux-weighted centroid method is offset from Kepler-19 by 0.32 ± 0.37 arcsec $= 0.86\sigma$. The location of the offsets is shown for both methods in Figure 6.8. Both methods show that the

observed centroid location is consistent with the transit occurring at the location of Kepler-19.

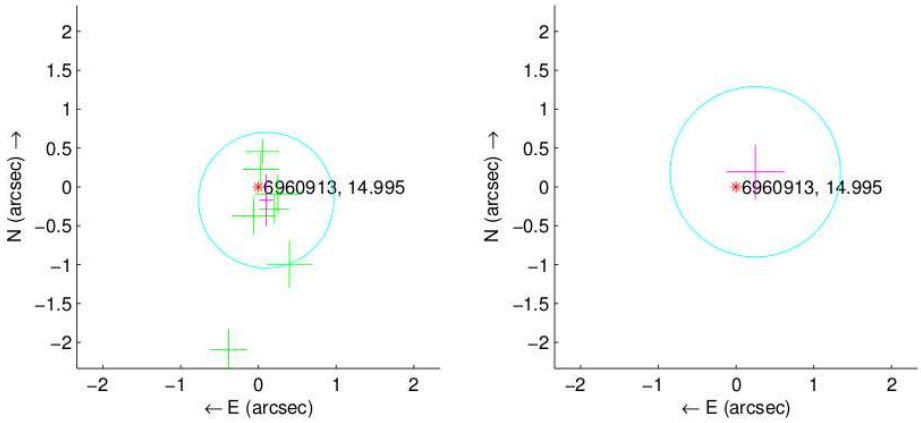

Figure 6.8.—: Quarterly and average reconstructed transit source locations relative to KOI 1361. *Left:* The green crosses show the individual quarter measurements using the difference image technique, and the magenta cross shows the uncertainty-weighted robust average of the quarterly results. *Right:* The magenta cross shows the transit source location reconstructed from the multi-quarter fit of the transit signal to the centroid motion. The length of the crosses show the 1σ uncertainty of each measurement in RA and Dec. The circles show the 3σ circle around the average source location. The location of KOI 1361 is shown by the red asterisk along with its Kepler ID and Kepler magnitude.

6.5.2 *Spitzer* Observations

Warm *Spitzer* observations in the near-infrared can also prove useful toward validating *Kepler* candidates, as shown for Kepler-10c (Fressin et al. 2011),

Kepler-18c & d (Cochran et al. 2011), Kepler-19b (Ballard et al. 2011), Kepler-22b (Borucki et al. 2011), and Kepler-20c, d, e, & f (Gautier et al. 2012; Fressin et al. 2012) Unless a putative blend scenario is comprised of stars of nearly identical color, the transit depth in a blend scenario will depend upon the wavelength at which it is observed. Conversely, an authentic transiting planet will produce an achromatic transit depth.

We gathered observations using the Infrared Array Camera (IRAC) (Fazio et al. 2004) on Warm *Spitzer* at 4.5 μm of the UT 17 September 2011 transit of KOI 1361.01. The observations span 10 hours, centered on the 4.75-hour-long transit. We gathered the observations using the full-array mode of IRAC, with an integration time of 12 s/image. We employed the techniques described in Agol et al. (2010) for the treatment of the images before photometry. We first converted the Basic Calibrated Data products from the *Spitzer* IRAC pipeline (which applies corrections for dark current, flat field variations, and detector non-linearity) from mega-Janskys per steradian to data number per second, using 0.1469 MJy·sr^{-1} per DN s^{-1}, and then to electrons per second, using the gain of 3.71 e DN^{-1}. We identified cosmic rays by performing a pixel-by-pixel median filter, using a window of 10 frames. We replace pixels that are $> 4\sigma$ outliers within this window with the running median value. We also corrected for a striping artifact in the Warm *Spitzer* images, which occurred in the same set of columns, by taking the median of the pixel values in the affected columns (using only rows without an overlying star) and normalizing this value to the median value of neighboring columns.

We discuss several means of performing the Warm *Spitzer* IRAC photometric reduction for similar observations in Ballard et al. (2011), and make use of the conclusions from that work. First, we estimate the position of the star on the array with a flux-weighted sum of the position within a circular aperture of 3 pixels We then performed aperture photometry on the images, using both estimates for the position and variable aperture sizes between 2.1 and 4.0 pixels, in increments of 0.1 pixels up to 2.7 pixels, and then at 3.0 and 4.0 pixels. We decided to use the position estimates using a flux-weighted sum at an aperture of 2.6 pixels, which minimized the out-of-transit RMS.

We remove the effect of the IRAC intrapixel sensitivity variations, or the "pixel-phase" effect (see eg. Charbonneau et al. 2005; Knutson et al. 2008) using a polynomial functional form for the intrapixel sensitivity (which depends upon the x and y position of the star on the array). We denote the transit light curve f (which depends upon time), and we hold all parameters constant except for the transit depth. We use the light curve software of Mandel & Agol (2002) to generate the transit models. The model for the measured brightness $f'(x, y)$ is given by:

$$f' = f(t, R_p/R_\star) \cdot [b_1 + b_2(x - \bar{x}) + b_3(x - \bar{x})^2 + b_4(y - \bar{y}) + b_5(y - \bar{y})^2], \quad (6.5)$$

where we include all of the observations (both in- and out-of-transit) to fit the polynomial coefficients and the transit depth simultaneously.

We fit for the polynomial coefficients b_1 through b_5 using a Levenberg-

Marquardt χ^2 minimization. However, the Spitzer light curve contains significant correlated noise even after the best intrapixel sensitivity model is removed. We incorporate the effect of remaining correlated noise with a residual permutation analysis of the errors as described by Winn et al. (2008), wherein we find the best-fit model f' to the light curve as given by Equation 6.5, subtract this model from the light curve, shift the residuals by one step in time, add the same model back to the residuals, and refit the depth and pixel sensitivity coefficients. We wrap residuals from the end of the light curve to the beginning, and in this way we cycle through every residual permutation of the data. We determine the best value from the median of this distribution, and estimate the error from the closest 68% of values to the median. Using the residual permutation method on the light curve treated with a polynomial, we find $R_p/R_\star$=0.0315±0.0069. This value corresponds to a best-fit transit depth δ=990^{+482}_{-387}, in excellent agreement with the *Kepler* depth of 1403^{+73}_{-65}.

We note that the use of the weighted sensitivity function proposed in Ballard et al. (2010a) made a negligable difference to the photometric residuals in this case, so for reasons of computational time, we deferred to the polynomial reduction technique. In Figure 6.9, we show the combined and binned *Spitzer* light curve, with the best-fit transit model derived from the *Spitzer* observations and the best-fit *Kepler* transit model (with the quadratic limb darkening coefficients for the *Spitzer* 4.5 μm filter, drawn from Claret & Bloemen 2011 as similarly described in Section 1) overplotted.

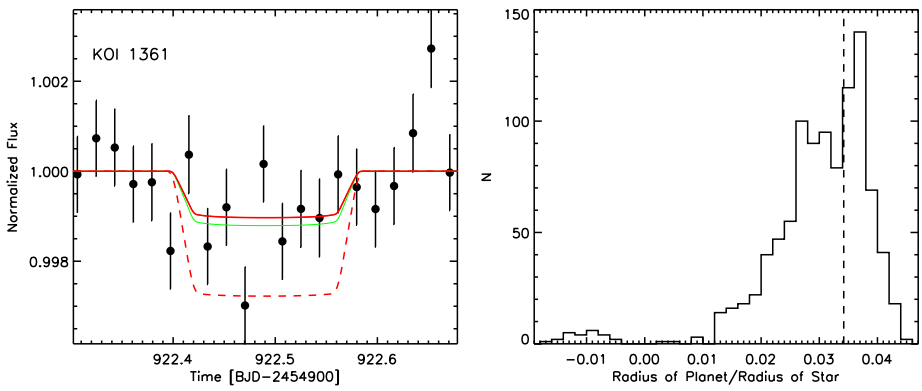

Figure 6.9.—: *Left:* Transit of KOI 1361.01 gathered with Warm *Spitzer* at 4.5 μm, binned by a factor of 16. The best-fit transit model with depth derived from the *Spitzer* observations is shown in red, while the *Kepler* transit model (with *Spitzer* 4.5 μm channel limb darkening) is shown in green. The *Spitzer* and *Kepler* transit depths are in excellent agreement. *Right:* The results of a residual permutation analysis on the *Spitzer* transit of KOI 1361.01. We detect the transit with 3σ confidence, and the depth inferred from the *Kepler* light curve lies within one standard deviation of the depth inferred from *Spitzer*.

6.6 Discussion and Conclusions

6.6.1 Stellar Rotation

While the age of KOI 1361.01 is largely unconstrained from spectroscopy and the *Kepler* photometry, given the very slowly-evolving nature of M stars, the rotational period of the star may offer some insight into its age. In Figure 6.10, we depict the first four quarters of *Kepler* observations of KOI 1361, or approximately

one year of continuous observation. These observations have been processed using the Presearch Data Conditioning (PDC) module of the Kepler data analysis pipeline, with the Bayesian Maximum A Posteriori (MAP) approach applied (described in Smith et al. 2012). The use of highly correlated and quiet stars to create a set of co-trending basis vectors enables the removal of non-astrophysical artifacts from the *Kepler* time series, and the preservation of astrophysically interesting signals such as stellar rotation. PDC-MAP has not yet been applied to the entirety of the KOI 1361.01 light curve, and so we have displayed the longest contiguous portion of the treated light curve in Figure 6.10. We apply the discrete correlation function of Edelson & Krolik (1988), similarly applied by Fabrycky et al. (2012b) on the time series of Kepler-30 and Queloz et al. (2009) on CoRoT-7, on this portion of the KOI 1361 light curve. We test lags from 1 to 100 days, which is sufficient to identify the 36±4 day stellar rotation period which is also visible by eye in the top panel of Figure 6.10.

Irwin et al. (2011) recently published a compliation of the known rotation periods of M dwarfs from the literature, including those he measured for the MEarth sample (which comprises much lower mass stars than had previous populated the relationship between stellar mass and rotation period). The rotation periods are drawn from open clusters of stars with derived ages from 1–650 Gyr (which ages are measured by comparing the Hertzsprung-Russell diagrams of these clusters to stellar evolutionary models), and then also from field stars with ages >1 Gyr. Among the clusters with ages less than 1 Gyr, all of the stars with masses >0.5 $M_{\odot}$ have rotation periods shorter than 30 days,

with the exception of a single star in NGC 2516 (although longer rotation periods are observed for fully convective stars with younger ages, as described in greater detail in Irwin et al. 2011). Only after 1 Gyr do M dwarfs appear to spin down enough to produce 36 day rotation periods, and stars with masses between 0.5 and 0.7 $M_{\odot}$ and ages between 8 and 10 Gyr are more likely to have rotation periods in the tens of days (they observed values <30 days for field stars in the 1-2 Gyr range). We exercise caution however, in estimating the age of KOI 1361.01 using these metrics, as the rotation period as a function of age and mass for M dwarfs is still very undersampled.

6.6.2 Transit Times

We depict the transit times of KOI 1361.01 in Figure 6.11. We report no significant deviation from a linear ephemeris.

6.6.3 Theoretical Composition and Habitability of KOI 1361.01

Bulk Composition and Atmosphere

While we cannot estimate the mean density of KOI 1361.01 without a measurement of its mass, we can still discuss plausible compositions, given its equilibrium temperature and radius. While the theoretical compositions of Fortney et al. (2007) allow for pure iron compositions (in which case a 2.0 $R_{\oplus}$ planet would

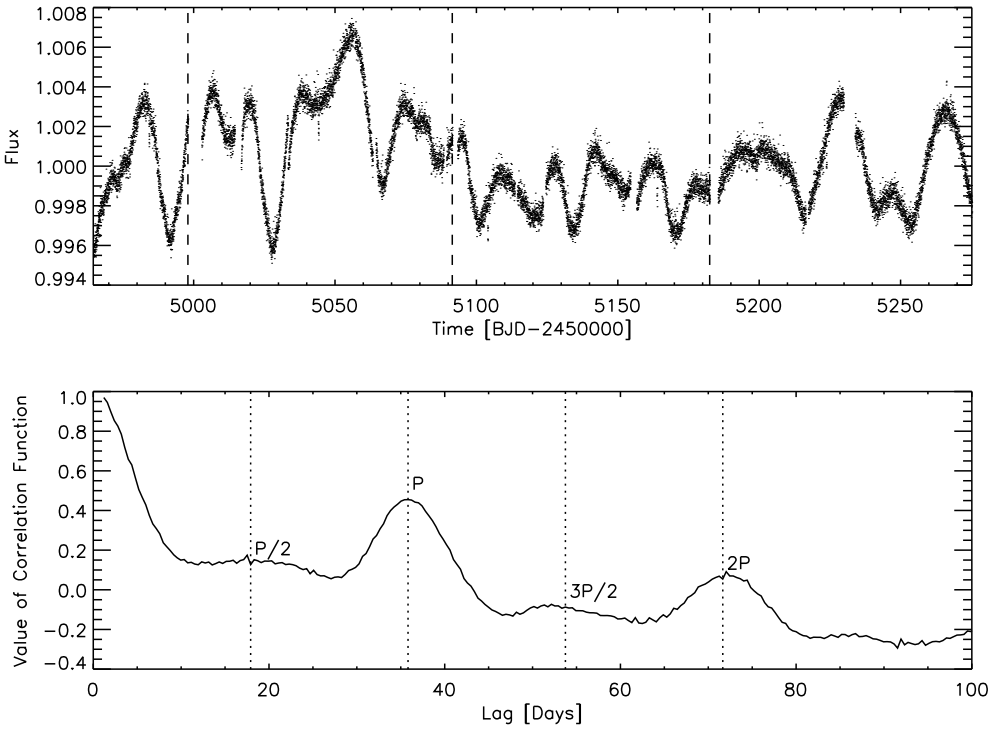

Figure 6.10.—: *Top:* Quarters 1–4 of *Kepler* observations of KOI 1361. Dashed lines denote the intervals between quarters. *Bottom:* The results of the discrete correlation function applied to this portion of the light curve. The strongest peak corresponds to 36 days, which variability is present by eye in the 300 days of observations depicted in the top panel. Dotted lines indicate the strongest period and its harmonics.

have a mass of 64 $M_\oplus$), the models of Marcus et al. (2010), which address the iron content of planets with maximal collisional stripping, find that a 2 $R_\oplus$ planet should have a mass < 21 $R_\oplus$. Employing again the Fortney et al. (2007) models, we would infer a mass of 9.6 $M_\oplus$ for a pure rock planet, and a mass of 2.3 $R_\oplus$ for a pure ice planet. There now exist a sizeable set of exoplanets with radii in the

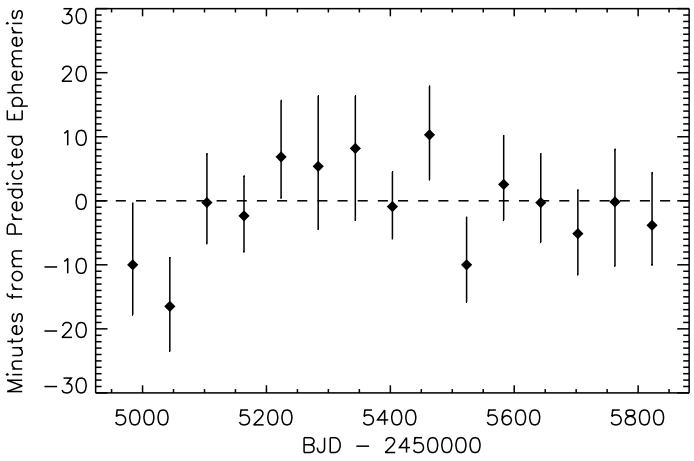

Figure 6.11.—: *Kepler* transit times for Kepler-19b from Quarters 1-10, as compared to the best linear ephemeris model.

1.4–3.0 $R_\oplus$ range with dynamically measured masses, though these span a large range of bulk densities from 0.7 g cm^{-3} in the case of Kepler-11f to 10.4 cm^{-3} in the case of CoRoT-7b. We list published masses, radii, and mean densities from the literature in Table 6.6.3. The four planets nearest to KOI 1361.01 in radius are Kepler-20b (Gautier et al. 2012), Kepler-11b (Lissauer et al. 2011), Kepler-18b (Cochran et al. 2011), and 55 Cancri e (Winn et al. 2011), the radii of which are lie within 0.10 $R_\oplus$ of the radius of KOI 1361. The densities of these four planets span the range from 3.1–6.9 g cm^{-3}, all of which lie within the range bracketed by solid ice and solid rock (Seager et al. 2007). We therefore conclude that a mass larger than 10 $M_\oplus$ is unlikely for KOI 1361, given its radius and comparatively low stellar insolation.

We also consider the possible atmospheric content of a 2.0 $R_\oplus$ planet. Rogers

Table 6.2. Properties of Transiting Planets from 1.4–3.0 $R_\oplus$ with Dynamically-Measured Masses

Name	Radius $[R_\oplus]$	Mass $[M_\oplus]$	Mean Density [g cm^{-3}]	Reference
Kepler-10b	$1.416^{+0.033}_{-0.036}$	$4.56^{+1.17}_{-1.29}$	$8.8^{+2.1}_{-2.9}$	Batalha et al. (2011)
CoRoT-7b	1.58±0.10	7.42±1.21	10.4±1.8[a]	Bruntt et al. (2010), Hatzes et al. (2011)
Kepler-20b	$1.91^{+0.12}_{-0.21}$	8.7±2.2	$6.9^{+5.3}_{-2.6}$[b]	Gautier et al. (2012)
Kepler-11b	1.97±0.19	$4.3^{+2.2}_{-2.0}$	$3.1^{+2.1}_{-1.5}$	Lissauer et al. (2011)
Kepler-18b	2.00±0.10	6.9±3.4	4.9±2.4	Cochran et al. (2011)
55 Cnc e	2.00±0.14	8.63±0.35	$5.9^{+1.5}_{-1.1}$	Winn et al. (2011)
Kepler-11f	2.61±0.25	$2.3^{+2.2}_{-1.2}$	$0.7^{+0.7}_{-0.4}$	Lissauer et al. (2011)
GJ 1214	2.678±0.13	6.55±0.98	1.87±0.4	Charbonneau et al. (2009)
HD 97658b	2.93±0.28	6.4±0.7	$1.40^{+0.53}_{-0.36}$	Henry et al. (2011), Howard et al. (2011b)

[a]Differing mass measurements of CoRoT-7b (Queloz et al. 2009; Pont et al. 2011) furnish different mean densities; we have stated the most recently published values.

[b]Mean density calculated from stated 1σ limits in radius and mass.

[c]We have omitted planets here within the same radius range 1.4–3 $R_\oplus$ that are validated, but for which there exist only upper limits in mass. These include Kepler-21b (Howell et al. 2012), Kepler-9d (Holman et al. 2010; Torres et al. 2011), Kepler-23b (Ford et al. 2012), Kepler-19b (Ballard et al. 2011), Kepler-22b (Borucki et al. 2011), Kepler-24b (Ford et al. 2012), Kepler-25b (Steffen et al. 2012), Kepler-24c (Ford et al. 2012), Kepler-20d (Gautier et al. 2012), and Kepler-25c (Fabrycky et al. 2012b).

et al. (2011) considers two scenarios (core accretion and outgassing) by which planets in the 2–4 $R_\oplus$ regime might retain a substantial hydrogen and helium envelope; half of the posterior distribution for the radius of KOI 1361.01 lies within this radius range. Though that work focuses on temperatures > 500 K, a cooler temperature still would extend still longer the lifetime of a putative hydrogen/helium envelope. For example, if KOI 1361.01 formed by core-nucleated accretion beyond the snow line, at 500 K (substantially warmer), a hydrogen helium envelope fraction of 0.1% by mass is plausible for timescales <1 Gyr. Alternatively, it the hydrogen content of the atmosphere is outgassed from the planet (assumed to be formed from iron enstatite), a mass fraction of 1% by mass is plausible for timescales as long as 100 Gyr. These timescales (and their corresponding atmospheric mass fractions) should be considered lower bounds, given these formation scenarios, since a cooler planet will retain an atmosphere for a longer duration, all else being equal. While these scenarios, necessarily poor ones from the habitability standpoint, cannot be ruled out from the radius and temperature of KOI 1361.01 alone, a truly "Neptune-like" scenario (where the atmosphere comprises 5-10% of the mass of planet) less likely here than for a larger super-Earth.

There also exist theoretical constraints on the sustainability of super-Earth atmospheres with higher mean molecular weights. In particular, Heng & Kopparla (2012) consider the stability of high mean molecular weight atmospheres belonging to super Earths orbiting M dwarfs in particular. The proximity of the habitable zone to the star means that many super Earths will be spin-synchronized,

with a permanent day and night side. In particular, the timescale for spin synchronization is given by Bodenheimer et al. (2001) and stated in terms of orbital frequency Ω by Heng & Kopparla (2012):

$$t_{syn} = \frac{8Q}{45\Omega}\left(\frac{\omega}{\Omega}\right)\left(\frac{M_p}{M_\star}\right)\left(\frac{a}{R_p}\right)^3 \tag{6.6}$$

where the planet's initial rotational frequency is given by w, Q is the tidal quality factor (and is believed to lie within the range of 10–100 for rocky exoplanets, and in the 10^5–10^6 range for gas giants, as stated in Goldreich & Soter 1966). Even with extremely rapid inital rotational periods of the planet (e.g. 0.1 day) and values for Q which approach that of gas giants, KOI 1361.01 is close enough to its host star where the spin sychronization timescale is less than 1 Myr.

This poses a problem for atmospheric stability unless the zonal winds' ability to redistribute heat in the atmosphere outstrips the radiative timescale of the atmosphere. If this condition (namely, that the advective timescale is shorter than the radiative timescale) does not hold, then the low temperature of "night side" of the planet can allow heavier elements can condense out, leaving the atmosphere unstable. An atmosphere comprising heavier elements has a longer advective timescale, since the wind speed is slowed as mean molecular weight increases (similarly to the sound speed). For this reason, Earth-like atmospheres (with mean molecular weights of 30) are particularly suspectible to instability. The fact that KOI 1361 is a very earlier M dwarf translates to a radiative timescale for a super Earth residing in the habitable zone that is longer than the advective

timescale (Heng & Kopparla 2012), so an Earth-like atmosphere would remain stable. For later M stars (for example, an M 3.5V star, as adopted as a trial case by Heng & Kopparla 2012), the radiative timescale at 0.25 AU is shorter, so a 2 $R_\oplus$ planet possessing an atmosphere with mean molecular weight of 30 would be potentially unstable.

Tidal Heating and Plate Tectonics

Jackson et al. (2008a) consider whether tidal heating is sufficient to induce plate tectonics in terrestrial planets orbiting M stars, where the habitable zone is close enough that tides play an important role in habitability concerns. In particular, though the heat source for plate tectonics on Earth is the decay of radionuclides, in other potentially habitable terrestrial planets orbiting M dwarfs, this role could be played by tidal heating even for modest eccentricities. However, in the extreme case of a satellite such as Jupiter's moon Io, tidal heating is responsible for extreme vulcanism that would hinder habitability. Therefore, there exists a range of tidal heating considered favorable for habitability, which translates to a range of favorable eccentricity values as a function of stellar and planetary mass. These values of "habitable" heating per unit area, offered by Jackson et al. (2008a), are 0.04–2 W m^{-2}, which brackets at the lower end the heating on Mars (which likely had plate tectonics in the past) and at the higher end on Io. KOI 1361.01 likely resides near the edge of the ranges in both planetary and stellar mass considered by Jackson et al. (2008a), who examined tidal heating for planetary systems with stellar masses up to 0.5 $M_\odot$ and planets as massive as 10 $M_\oplus$. However, they

find that the maximal tidal heating received by a 10 $M_\oplus$ planet in the habitable zone of a 0.5 $M_\odot$ star peaks near 0.01 W m^{-2}: likely too lower to contribute to tectonic activity. However, the possibility of other heat sources (such as those on Earth, for which tidal heating is negligable) remains.

Stellar Activity and Age

We first address the possible effect of stellar activity on the putative habitability of KOI 1361.01. For example, Khodachenko et al. (2007) found that coronal mass ejections around active M dwarfs have the capability to strip exoplanetary atmosphere, and that the spin synchronization of planets in the habitable zones of M dwarfs precludes their developing a protective planetary magnetosphere such as Earth's. However, West et al. (2008), from a survey of activity in 38,000 low-mass stars observed by the Sloan Digital Sky Survey, found that $< 10\%$ of M0 stars are chromospherically "active" (based upon $H\alpha$ emission line strength), and that the active period of M0 stars takes place before they reach an age of 1.4 Gyr (0.8±0.6 Gyr). We conclude that the KOI 1361, as an early M dwarf that is likely older than 1 Gyr, is unlikely to be active.

Second-order questions of habitability might concern the age of the star, and whether sufficient time has elapsed to allow relevent evolutionary timescales to occur. While we have only very wide constraints on the stellar age from spectroscopy and the *Kepler* photometry, its rotation period may indicate an age older at least than 1 Gyr. While the first cells are believed to have formed on Earth about a Gyr after its creation, the timescales for evolution on other worlds

(in addition to our broad lack of information about habitability around M stars) are sufficiently uncertain that we can draw no definitive conclusions.

6.7 Future Prospects

We comment briefly on the feasibility of atmospheric characterization of KOI 1361.01. It orbits a small star and may possess a hydrogen and helium atmosphere, both of which are favorable circumstances for transmission spectroscopy. To perform a basic estimation of the expected change in transit depth at an optically thick wavelength, we consider the atmosphere to be a ring with scale height H, where $H = kT_p/\mu_m g$ (and k is Boltzmann's constant, T_p is the temperature of the planet, μ_m is the mean molecular weight of the atmosphere, and g is the surface gravity of the planet). If we use a mass estimate of 10 $M_\oplus$ for KOI 1361.01, then we expect a surface gravity of 25 m s^{-2}. If we assume the most optimistic case from a detectability standpoint, we also use molecular weight of 2 (corresponding to the hydrogen-rich scenario). Employing the the same equation to estimate the change in transit depth attributable to the atmosphere as Miller-Ricci et al. (2009), we expect a change in transit depth given by:

$$\Delta D \approx \frac{2\pi R_p H}{\pi R_\star^2} = \frac{2R_p H}{R_\star^2} \tag{6.7}$$

which equates to ΔD=7 ppm, if we employ the values for R_p and $R_\star$ given in Table 6.3.2. If the planet is less massive, and we select a stellar radii from the

lower end of the acceptable range of values, it's possible for achieve depths of dozens of ppm (for example, if KOI 1361 had a mass of 3.1 $M_\oplus$ like Kepler-11b and the true stellar radius was the -1σ value of 0.47 $R_\odot$, the signal would be 30 ppm). If we define several factors of the scale height to constitute the extent of the atmosphere, we acheive values approaching hundreds of ppm. However, even this signal is 10 times shallower than the 0.5 mmag values which might have been detectable in the atmosphere of GJ 1214 by Berta et al. (2012) using the Wide Field Camera 3 on board the *Hubble* Space Telescope, which is itself a factor of 25 times brighter in K band, for example. The launch of JWST, could enable the detection of 100 ppm features in the spectrum of GJ 1214 (Berta et al. 2012), but again, this star is much brighter than KOI 1361.01.

Similarly, the radial velocity amplitude of KOI 1361.01 is increased by the small mass of the host star. In this case, assuming again a mass of 10 $M_\oplus$ for the planet and a mass of 0.57 $M_\odot$ for the star, the planet induces a 2.4 m s^{-1} motion of its star (this value is 1.2 m s^{-1} if the planet is only 5 $M_\oplus$). However, though measuring a radial velocity signature of several meters-per-second has been acheived for dozens of exoplanets, these are all around very nearby stars. KOI 1361.01, with its R magnitude of 14.9, is probably too dim for such study with current instruments.

However, gathering additional *Kepler* observations of KOI 1361.01 will be helpful, particularly given the fact that it will be observed in short cadence mode for Quarter 11 onward. With short cadence observations, we may be able to measure the shape of ingress and egress with accuracy that enables us to rule out

a number of eccentricities which are allowable fits to the long cadence light curve.

We would like to thank the *Spitzer* team at the Infrared Processing and Analysis Center in Pasadena, California, and in particular Nancy Silbermann for scheduling the *Spitzer* observations of this program. This work is based in part on observations made with the Spitzer Space Telescope, which is operated by the Jet Propulsion Laboratory, California Institute of Technology under a contract with NASA. Support for this work was provided by NASA through an award issued by JPL/Caltech. This work is also based on observations made with *Kepler*, which was competitively selected as the tenth Discovery mission. Funding for this mission is provided by NASA's Science Mission Directorate. The authors would like to thank the many people who generously gave so much their time to make this Mission a success.

References

Adams, E. R., López-Morales, M., Elliot, J. L., Seager, S., & Osip, D. J. 2010, ApJ, 714, 13

Agol, E., Cowan, N. B., Knutson, H. A., Deming, D., Steffen, J. H., Henry, G. W., & Charbonneau, D. 2010, ApJ, 721, 1861

Agol, E., Steffen, J., Sari, R., & Clarkson, W. 2005, MNRAS, 359, 567

Agol, E., & Steffen, J. H. 2007, MNRAS, 374, 941

Alonso, R., Barbieri, M., Rabus, M., Deeg, H. J., Belmonte, J. A., & Almenara, J. M. 2008, A&A, 487, L5

Alonso, R., Guillot, T., Mazeh, T., Aigrain, S., Alapini, A., Barge, P., Hatzes, A., & Pont, F. 2009a, A&A, 501, L23

Alonso, R., et al. 2009b, A&A, 506, 353

Applegate, J. H. 1992, ApJ, 385, 621

Argabright, V. S., et al. 2008, in Society of Photo-Optical Instrumentation Engineers (SPIE) Conference Series, Vol. 7010, Society of Photo-Optical Instrumentation Engineers (SPIE) Conference Series

Bakos, G. Á., et al. 2010, ApJ, 710, 1724

Ballard, S., et al. 2010a, PASP, 122, 1341

—. 2010b, ApJ, 716, 1047

—. 2011, ApJ, 743, 200

Banfield, D., & Murray, N. 1992, Icarus, 99, 390

Batalha, N. M., et al. 2010, ApJ, 713, L109

—. 2011, ApJ, 729, 27

—. 2012, submitted to ApJS (arXiv: 1202:5852)

Batygin, K., Laughlin, G., Meschiari, S., Rivera, E., Vogt, S., & Butler, P. 2009, ApJ, 699, 23

Bean, J. L. 2009, A&A, 506, 369

Bean, J. L., Miller-Ricci Kempton, E., & Homeier, D. 2010, Nature, 468, 669

Bean, J. L., & Seifahrt, A. 2008, A&A, 487, L25

Bean, J. L., et al. 2008, A&A, 486, 1039

—. 2011, ApJ, 743, 92

Berger, D. H., et al. 2006, ApJ, 644, 475

Berta, Z. K., et al. 2012, ApJ, 747, 35

Blume, W. H. 2005, Space Science Reviews, 117, 23

Bodenheimer, P., Lin, D. N. C., & Mardling, R. A. 2001, ApJ, 548, 466

Borkovits, T., Csizmadia, S., Forgács-Dajka, E., & Hegedüs, T. 2011, A&A, 528, A53

Borkovits, T., Érdi, B., Forgács-Dajka, E., & Kovács, T. 2003, A&A, 398, 1091

Borucki, W. J., et al. 2010, Science, 327, 977

—. 2011, ApJ, 736, 19

—. 2012, ApJ, 745, 120

Boyajian, T. S., et al. 2010, Proceedings of Cool Stars 16 (arXiv:1012.0542)

Brown, T. M. 2003, ApJ, 593, L125

Bruntt, H., et al. 2010, A&A, 519, A51+

Bryson, S. T., et al. 2010, ApJ, 713, L97

Burke, C. J. 2008, ApJ, 679, 1566

Bursa, M. 1992, Earth Moon and Planets, 59, 239

Butler, R. P., Vogt, S. S., Marcy, G. W., Fischer, D. A., Wright, J. T., Henry, G. W., Laughlin, G., & Lissauer, J. J. 2004, ApJ, 617, 580

Caceres, C., Ivanov, V. D., Minniti, D., Naef, D., Melo, C., Mason, E., Selman, F., & Pietrzynski, G. 2009, ArXiv e-prints

Caldwell, D. A., et al. 2010, in Society of Photo-Optical Instrumentation Engineers (SPIE) Conference Series, Vol. 7731, Society of Photo-Optical Instrumentation Engineers (SPIE) Conference Series

Carter, J. A., Yee, J. C., Eastman, J., Gaudi, B. S., & Winn, J. N. 2008, ApJ, 689, 499

Carter, J. A., et al. 2011, Science, 331, 562

Casali, M., et al. 2007, A&A, 467, 777

Charbonneau, D., Knutson, H. A., Barman, T., Allen, L. E., Mayor, M., Megeath, S. T., Queloz, D., & Udry, S. 2008, ApJ, 686, 1341

Charbonneau, D., et al. 2005, ApJ, 626, 523

—. 2009, Nature, 462, 891

Chatterjee, S., Ford, E. B., Matsumura, S., & Rasio, F. A. 2008, ApJ, 686, 580

Christiansen, J. L., et al. 2010, ApJ, 710, 97

—. 2011, ApJ, 726, 94

Claret, A. 2000, A&A, 363, 1081

Claret, A., & Bloemen, S. 2011, A&A, 529, A75

Claret, A., & Gimenez, A. 1992, A&AS, 96, 255

Cochran, W. D., et al. 2011, ApJS, 197, 7

Coughlin, J. L., Stringfellow, G. S., Becker, A. C., López-Morales, M., Mezzalira, F., & Krajci, T. 2008, ApJ, 689, L149

Covey, K. R., Lada, C. J., Román-Zúñiga, C., Muench, A. A., Forbrich, J., & Ascenso, J. 2010, ApJ, 722, 971

Covey, K. R., et al. 2007, AJ, 134, 2398

Cox, A. N. 2000, Allen's Astrophysical Quantities, ed. A. N. Cox

Croll, B., Albert, L., Jayawardhana, R., Miller-Ricci Kempton, E., Fortney, J. J., Murray, N., & Neilson, H. 2011, ApJ, 736, 78

Croll, B., et al. 2007a, ApJ, 658, 1328

—. 2007b, ApJ, 671, 2129

Crossfield, I. J. M., Barman, T., & Hansen, B. M. S. 2011, ApJ, 736, 132

Demarque, P., Woo, J.-H., Kim, Y.-C., & Yi, S. K. 2004, ApJS, 155, 667

Deming, D., Harrington, J., Laughlin, G., Seager, S., Navarro, S. B., Bowman, W. C., & Horning, K. 2007, ApJ, 667, L199

Demory, B.-O., Gillon, M., Waelkens, C., Queloz, D., & Udry, S. 2009, in IAU Symposium, Vol. 253, IAU Symposium, 424–427

Demory, B.-O., et al. 2007, A&A, 475, 1125

Désert, J.-M., et al. 2011, ApJ, 731, L40

Díaz, R. F., Rojo, P., Melita, M., Hoyer, S., Minniti, D., Mauas, P. J. D., & Ruíz, M. T. 2008, ApJ, 682, L49

Domingos, R. C., Winter, O. C., & Yokoyama, T. 2006, MNRAS, 373, 1227

Dotter, A., Chaboyer, B., Jevremović, D., Kostov, V., Baron, E., & Ferguson, J. W. 2008, ApJS, 178, 89

Doyle, L. R., et al. 2011, Science, 333, 1602

Edelson, R. A., & Krolik, J. H. 1988, ApJ, 333, 646

Fabricant, D., Cheimets, P., Caldwell, N., & Geary, J. 1998, PASP, 110, 79

Fabrycky, D., & Tremaine, S. 2007, ApJ, 669, 1298

Fabrycky, D. C. 2010, Non-Keplerian Dynamics of Exoplanets, ed. Seager, S., 217–238

Fabrycky, D. C., et al. 2012a, submitted to ApJ (arXiv: 1202:6328)

—. 2012b, submitted to ApJ (arXiv: 1201:5415)

Fazio, G. G., et al. 2004, ApJS, 154, 10

Ford, E. B., & Gaudi, B. S. 2006, ApJ, 652, L137

Ford, E. B., & Holman, M. J. 2007, ApJ, 664, L51

Ford, E. B., et al. 2011, ApJS, 197, 2

—. 2012, ApJ, accepted (arXiv:1201.5409)

Fortney, J. J., Marley, M. S., & Barnes, J. W. 2007, ApJ, 659, 1661

Freistetter, F., Süli, Á., & Funk, B. 2009, Astronomische Nachrichten, 330, 469

Fressin, F., Knutson, H. A., Charbonneau, D., O'Donovan, F. T., Burrows, A., Deming, D., Mandushev, G., & Spiegel, D. 2010, ApJ, 711, 374

Fressin, F., et al. 2011, ApJS, 197, 5

—. 2012, Nature, 482, 195

Fukui, A., et al. 2011, PASJ, 63, 287

Fulton, B. J., Shporer, A., Winn, J. N., Holman, M. J., Pál, A., & Gazak, J. Z. 2011, ArXiv e-prints

Gautier, III, T. N., et al. 2012, ApJ, 749, 15

Gibson, N. P., et al. 2009, ApJ, 700, 1078

Gilliland, R. L., et al. 2010, ApJ, 713, L160

Gillon, M., et al. 2007a, A&A, 471, L51

—. 2007b, A&A, 472, L13

Gladman, B. 1993, Icarus, 106, 247

Goldreich, P., & Soter, S. 1966, Icarus, 5, 375

Gregory, P. C. 2007, MNRAS, 374, 1321

Hampton, D. L., Baer, J. W., Huisjen, M. A., Varner, C. C., Delamere, A., Wellnitz, D. D., A'Hearn, M. F., & Klaasen, K. P. 2005, Space Science Reviews, 117, 43

Hatzes, A. P., et al. 2011, ApJ, 743, 75

Hauschildt, P. H., Allard, F., & Baron, E. 1999, ApJ, 512, 377

Hayward, T. L., Brandl, B., Pirger, B., Blacken, C., Gull, G. E., Schoenwald, J., & Houck, J. R. 2001, PASP, 113, 105

Heng, K., & Kopparla, P. 2012, submitted to ApJ (arXiv: 1203:1922)

Henry, G. W., Howard, A. W., Marcy, G. W., Fischer, D. A., & Johnson, J. A. 2011, submitted to ApJ (arXiv: 1109:2549)

Heyl, J. S., & Gladman, B. J. 2007, MNRAS, 377, 1511

Holman, M. J., & Murray, N. W. 2005, Science, 307, 1288

Holman, M. J., et al. 2006, ApJ, 652, 1715

—. 2007, ApJ, 664, 1185

—. 2010, Science, 330, 51

Horch, E. P., Falta, D., Anderson, L. M., DeSousa, M. D., Miniter, C. M., Ahmed, T., & van Altena, W. F. 2010, AJ, 139, 205

Horch, E. P., Veillette, D. R., Baena Gallé, R., Shah, S. C., O'Rielly, G. V., & van Altena, W. F. 2009, AJ, 137, 5057

Howard, A. W., et al. 2010, Science, 330, 653

—. 2011a, submitted to ApJ (arXiv: 1103:2541)

—. 2011b, ApJ, 730, 10

Howell, S. B., et al. 2012, ApJ, 746, 123

Ida, S., & Lin, D. N. C. 2004, ApJ, 604, 388

Irwin, J., Berta, Z. K., Burke, C. J., Charbonneau, D., Nutzman, P., West, A. A., & Falco, E. E. 2011, ApJ, 727, 56

Irwin, J., Charbonneau, D., Nutzman, P., & Falco, E. 2009, in IAU Symposium, Vol. 253, IAU Symposium, 37–43

Irwin, J. B. 1952, ApJ, 116, 211

Isaacson, H., & Fischer, D. 2010, ApJ, 725, 875

Jackson, B., Barnes, R., & Greenberg, R. 2008a, MNRAS, 391, 237

Jackson, B., Greenberg, R., & Barnes, R. 2008b, ApJ, 678, 1396

Jackson, J. 1913, MNRAS, 74, 62

Jenkins, J. M., et al. 2010a, ApJ, 724, 1108

—. 2010b, ApJ, 713, L120

Jordán, A., & Bakos, G. Á. 2008, ApJ, 685, 543

Kaltenegger, L., & Sasselov, D. 2011, ApJ, 736, L25

Kasting, J. 2012, in American Astronomical Society Meeting Abstracts, Vol. 219, American Astronomical Society Meeting Abstracts, 206.02

Khodachenko, M. L., et al. 2007, Astrobiology, 7, 167

Kipping, D., & Bakos, G. 2011a, ApJ, 730, 50

—. 2011b, ApJ, 733, 36

Kipping, D. M. 2009, MNRAS, 392, 181

Kipping, D. M., & Spiegel, D. S. 2011, MNRAS, 417, L88

Kirkpatrick, J. D., Henry, T. J., & McCarthy, Jr., D. W. 1991, ApJS, 77, 417

Klaasen, K. P., Carcich, B., Carcich, G., Grayzeck, E. J., & McLaughlin, S. 2005, Space Science Reviews, 117, 335

Klaasen, K. P., et al. 2008, Review of Scientific Instruments, 79, 091301

Knutson, H. A., Charbonneau, D., Allen, L. E., Burrows, A., & Megeath, S. T. 2008, ApJ, 673, 526

Knutson, H. A., Charbonneau, D., Burrows, A., O'Donovan, F. T., & Mandushev, G. 2009a, ApJ, 691, 866

Knutson, H. A., Charbonneau, D., Cowan, N. B., Fortney, J. J., Showman, A. P., Agol, E., & Henry, G. W. 2009b, ApJ, 703, 769

Knutson, H. A., Howard, A. W., & Isaacson, H. 2010, ApJ, 720, 1569

Knutson, H. A., et al. 2011, ApJ, 735, 27

Kopal, Z. 1959, Close binary systems (London: Chapman & Hall)

Kovács, G., et al. 2007, ApJ, 670, L41

Kozai, Y. 1962, AJ, 67, 591

Kurucz, R. 1994, Solar abundance model atmospheres for 0,1,2,4,8 km/s. Kurucz CD-ROM No. 19. Cambridge, Mass.: Smithsonian Astrophysical Observatory, 1994, 19

Kurucz, R. L. 2005, Memorie della Societa Astronomica Italiana Supplement, 8, 14

Laughlin, G., & Chambers, J. E. 2002, AJ, 124, 592

Léger, A., et al. 2009, A&A, 506, 287

Lissauer, J. J., et al. 2011, Nature, 470, 53

Machalek, P., McCullough, P. R., Burke, C. J., Valenti, J. A., Burrows, A., & Hora, J. L. 2008, ApJ, 684, 1427

Maciejewski, G., et al. 2010, MNRAS, 407, 2625

—. 2011, MNRAS, 411, 1204

Madhusudhan, N., Mousis, O., Johnson, T. V., & Lunine, J. I. 2011a, ApJ, 743, 191

Madhusudhan, N., et al. 2011b, Nature, 469, 64

Mandel, K., & Agol, E. 2002, ApJ, 580, L171

Mandell, A. M., Raymond, S. N., & Sigurdsson, S. 2007, ApJ, 660, 823

Maness, H. L., Marcy, G. W., Ford, E. B., Hauschildt, P. H., Shreve, A. T., Basri, G. B., Butler, R. P., & Vogt, S. S. 2007, PASP, 119, 90

Marcus, R. A., Sasselov, D., Hernquist, L., & Stewart, S. T. 2010, ApJ, 712, L73

Marcy, G. W., et al. 2008, Physica Scripta Volume T, 130, 014001

Mardling, R. A. 2010, MNRAS, 407, 1048

Mardling, R. A., & Lin, D. N. C. 2004, ApJ, 614, 955

Meschiari, S., & Laughlin, G. P. 2010, ApJ, 718, 543

Miller-Ricci, E., & Fortney, J. J. 2010, ApJ, 716, L74

Miller-Ricci, E., Seager, S., & Sasselov, D. 2009, ApJ, 690, 1056

Miller-Ricci, E., et al. 2008a, ApJ, 682, 593

—. 2008b, ApJ, 682, 586

Miralda-Escudé, J. 2002, ApJ, 564, 1019

Moorhead, A. V., et al. 2011, ApJS, 197, 1

Morton, T. D., & Johnson, J. A. 2011, ApJ, 738, 170

Muirhead, P. S., Hamren, K., Schlawin, E., Rojas-Ayala, B., Covey, K. R., & Lloyd, J. P. 2012, ApJ, 750, L37

Murray, C. D., & Correia, A. C. M. 2010, Keplerian Orbits and Dynamics of Exoplanets, ed. Seager, S., 15–23

Murray, C. D., & Dermott, S. F. 1999, Solar System Dynamics, ed. Murray, C. D. & Dermott, S. F.

Nascimbeni, V., Piotto, G., Bedin, L. R., Damasso, M., Malavolta, L., & Borsato, L. 2011, A&A, 532, A24+

Nelder, J. A., & Mead, K. 1965, Computer Journal, 7, 308

Nesvorný, D., & Morbidelli, A. 2008, ApJ, 688, 636

Noyes, R. W., Hartmann, L. W., Baliunas, S. L., Duncan, D. K., & Vaughan, A. H. 1984, ApJ, 279, 763

O'Donovan, F. T., et al. 2006, ApJ, 651, L61

—. 2007, ApJ, 663, L37

Ogilvie, G. I., & Lin, D. N. C. 2004, ApJ, 610, 477

Pál, A., & Kocsis, B. 2008, MNRAS, 389, 191

Pál, A., Sárneczky, K., Szabó, G. M., Szing, A., Kiss, L. L., Mező, G., & Regály, Z. 2011, MNRAS, 413, L43

Pál, A., et al. 2008, ApJ, 680, 1450

Pollacco, D., et al. 2008, MNRAS, 385, 1576

Pont, F., Aigrain, S., & Zucker, S. 2011, MNRAS, 411, 1953

Pont, F., Gilliland, R. L., Knutson, H., Holman, M., & Charbonneau, D. 2009, MNRAS, 393, L6

Prsa, A. 2011, Kepler Limb Darkening Coefficients

Queloz, D., et al. 2009, A&A, 506, 303

Rabus, M., Deeg, H. J., Alonso, R., Belmonte, J. A., & Almenara, J. M. 2009, A&A, 508, 1011

Raetz, S., et al. 2009, Astronomische Nachrichten, 330, 459

Ragozzine, D., & Holman, M. J. 2010, submitted to ApJ (arXiv:1006.3727)

Ragozzine, D., & Wolf, A. S. 2009, ApJ, 698, 1778

Raymond, S. N., Mandell, A. M., & Sigurdsson, S. 2006, Science, 313, 1413

Reach, W. T., et al. 2005, PASP, 117, 978

Ribas, I. 2006, Ap&SS, 304, 89

Ribas, I., Font-Ribera, A., & Beaulieu, J.-P. 2008, ApJ, 677, L59

Robin, A. C., Reylé, C., Derrière, S., & Picaud, S. 2003, A&A, 409, 523

Rogers, L. A., Bodenheimer, P., Lissauer, J. J., & Seager, S. 2011, ApJ, 738, 59

Rojas-Ayala, B., Covey, K. R., Muirhead, P. S., & Lloyd, J. P. 2010, ApJ, 720, L113

—. 2012, ApJ, 748, 93

Rowe, J. F., et al. 2008, ApJ, 689, 1345

Salpeter, E. E. 1955, ApJ, 121, 161

Seager, S., Kuchner, M., Hier-Majumder, C. A., & Militzer, B. 2007, ApJ, 669, 1279

Seager, S., & Mallén-Ornelas, G. 2003, ApJ, 585, 1038

Ségransan, D., Kervella, P., Forveille, T., & Queloz, D. 2003, A&A, 397, L5

Shen, Y., & Tremaine, S. 2008, AJ, 136, 2453

Shporer, A., Mazeh, T., Pont, F., Winn, J. N., Holman, M. J., Latham, D. W., & Esquerdo, G. A. 2009, ApJ, 694, 1559

Silva-Valio, A. 2008, ApJ, 683, L179

Simon, A., Szatmáry, K., & Szabó, G. M. 2007, A&A, 470, 727

Smith, A. M. S., et al. 2009, MNRAS, 398, 1827

Smith, J. C., et al. 2012, submitted to PASP (arXiv:1203:1383)

Smith, M. W., et al. 2010, in Society of Photo-Optical Instrumentation Engineers (SPIE) Conference Series, Vol. 7731, Society of Photo-Optical Instrumentation Engineers (SPIE) Conference Series

Snellen, I. A. G., de Mooij, E. J. W., & Albrecht, S. 2009, Nature, 459, 543

Socrates, A., Katz, B., Dong, S., & Tremaine, S. 2011, submitted to ApJ (arXiv: 1110:1644)

Southworth, J. 2008, MNRAS, 386, 1644

Sozzetti, A., Torres, G., Charbonneau, D., Latham, D. W., Holman, M. J., Winn, J. N., Laird, J. B., & O'Donovan, F. T. 2007, ApJ, 664, 1190

Sozzetti, A., et al. 2009, ApJ, 691, 1145

Steffen, J. H., & Agol, E. 2005, MNRAS, 364, L96

Steffen, J. H., et al. 2012, MNRAS, 2482

Stetson, P. B. 1987, PASP, 99, 191

Sudarsky, D., Burrows, A., & Pinto, P. 2000, ApJ, 538, 885

Swain, M. R., Vasisht, G., & Tinetti, G. 2008, Nature, 452, 329

Sybilski, P., Konacki, M., & Kozłowski, S. 2010, MNRAS, 405, 657

Szabó, G. M., Szatmáry, K., Divéki, Z., & Simon, A. 2006, A&A, 450, 395

Tegmark, M., et al. 2004, Phys. Rev. D, 69, 103501

Tittemore, W. C., & Wisdom, J. 1989, Icarus, 78, 63

Torres, G. 2007, ApJ, 671, L65

—. 2011, Proceedings of the Astronomical Society of the Pacific (arXiv:1107:3088)

Torres, G., Konacki, M., Sasselov, D. D., & Jha, S. 2004, ApJ, 614, 979

Torres, G., Winn, J. N., & Holman, M. J. 2008, ApJ, 677, 1324

Torres, G., et al. 2011, ApJ, 727, 24

Troy, M., et al. 2000, in Society of Photo-Optical Instrumentation Engineers (SPIE) Conference Series, Vol. 4007, Society of Photo-Optical Instrumentation Engineers (SPIE) Conference Series, ed. P. L. Wizinowich, 31–40

Twicken, J. D., Clarke, B. D., Bryson, S. T., Tenenbaum, P., Wu, H., Jenkins, J. M., Girouard, F., & Klaus, T. C. 2010, in Society of Photo-Optical Instrumentation Engineers (SPIE) Conference Series, Vol. 7740, Society of Photo-Optical Instrumentation Engineers (SPIE) Conference Series

Valenti, J. A., & Fischer, D. A. 2005, ApJS, 159, 141

Valenti, J. A., & Piskunov, N. 1996, A&AS, 118, 595

Vogt, S. S., et al. 1994, in Society of Photo-Optical Instrumentation Engineers (SPIE) Conference Series, Vol. 2198, Society of Photo-Optical Instrumentation Engineers (SPIE) Conference Series, ed. D. L. Crawford & E. R. Craine, 362–+

Watson, C. A., & Marsh, T. R. 2010, MNRAS, 405, 2037

Werner, M. W., et al. 2004, ApJS, 154, 1

West, A. A., Hawley, S. L., Bochanski, J. J., Covey, K. R., Reid, I. N., Dhital, S., Hilton, E. J., & Masuda, M. 2008, AJ, 135, 785

Winn, J. N., Fabrycky, D., Albrecht, S., & Johnson, J. A. 2010, ApJ, 718, L145

Winn, J. N., Johnson, J. A., Albrecht, S., Howard, A. W., Marcy, G. W., Crossfield, I. J., & Holman, M. J. 2009, ApJ, 703, L99

Winn, J. N., et al. 2008, ApJ, 683, 1076

—. 2011, ApJ, 737, L18

Wisdom, J. 1980, AJ, 85, 1122

Yi, S., Demarque, P., Kim, Y., Lee, Y., Ree, C. H., Lejeune, T., & Barnes, S. 2001, ApJS, 136, 417